THE UNIVERSITY of EDINBURGH

This thesis has been submitted in fulfilment of the requirements for a postgraduate degree (e.g. PhD, MPhil, DClinPsychol) at the University of Edinburgh. Please note the following terms and conditions of use:

- This work is protected by copyright and other intellectual property rights, which are retained by the thesis author, unless otherwise stated.
- A copy can be downloaded for personal non-commercial research or study, without prior permission or charge.
- This thesis cannot be reproduced or quoted extensively from without first obtaining permission in writing from the author.
- The content must not be changed in any way or sold commercially in any format or medium without the formal permission of the author.
- When referring to this work, full bibliographic details including the author, title, awarding institution and date of the thesis must be given.

Experimental Studies on Pore Wetting and Displacement of Fluid by CO_2 in Porous Media

Xingxun LI

A thesis submitted for the Degree of Doctor of Philosophy

The University of Edinburgh

2015

Declaration

The author declares that the work undertaken in this thesis has been carried out and composed by him unless stated or acknowledged otherwise. This work has not been submitted or accepted in the fulfillment of any other degree or qualification, at any other university.

Xingxun LI

Abstract

The study of multiphase flow in porous media is highly relevant to many problems of great scientific importance, such as CO_2 storage and enhanced oil recovery. Even though significant progress has been made in these areas, many challenges still remain. For instance, the leakage of stored CO_2 may occur due to the capillary trapping failure of cap rock. Approximately 70% of oil cannot be easily recovered from underground, because the oil is held in tight porous rocks. Although CO_2 storage and enhanced oil recovery are engineering processes at a geological scale, they are predominantly controlled by the transport and displacement of CO_2 and reservoir fluids in aquifers and reservoirs, which are further controlled by wetting and fluid properties at pore scale. This work focuses on experimental investigations of pore-scale wetting and displacement of fluids and CO_2 in porous core samples.

Pore wetting, which has been measured based on contact angle, is a principal control on multiphase flow through porous media. However, contact angle measurement on other than flat surfaces still remains a challenge. In order to indicate the wetting in a small pore, a new pore contact angle measurement technique is developed in this study to directly measure the contact angles of fluids and CO_2 in micron-sized pores. The equilibrium and dynamic contact angles of various liquids are directly measured in single glass capillaries, by studying the effects of surface tension, viscosity and chemical structure. The pore contact angles are compared with the contact angles on a planar substrate. The pore contact angle of a confined liquid in a glass capillary differs from the contact angle measured on a flat glass surface in an open space. Surface tension is not the only dominant factor affecting contact angle. The static contact angle in a glass pore also varies with liquid chemical structure. Viscosity and surface tension can significantly affect the dynamic pore contact angle. A new empirical correlation is developed based on our experimental data to describe

dynamic pore wetting.

The CO_2-fluid contact angle in porous media is an important factor affecting the feasibility of long-term permanent CO_2 storage. It determines CO_2 flow and distribution in reservoirs or aquifers, and thus ultimately finally the storage capacity. CO_2-fluid contact angles were measured in small water-wet pores and oil-wet pores, investigating the effect of CO_2 phase (gas/liquid/supercritical). The CO_2 phase significantly affects the CO_2-fluid contact angle in an oil-wet pore. Supercritical CO_2-fluid contact angles are larger than gas CO_2-fluid contact angles, but are smaller than liquid CO_2-fluid contact angles. However, this significant CO_2 phase effect on contact angle was not observed in a water-wet pore.

Another key issue considered in this study is two-phase flow displacement in porous media. This strongly relates to the important macroscopic parameters for multiphase flow transport in porous media, such as capillary pressure and relative permeability. Here CO_2-water displacements are studied by conducting CO_2 flooding experiments in a sandstone core sample, considering the effects of CO_2 phase, pressure and CO_2 injection rate. The capillary pressure-saturation curve, water production behaviour and relative permeability are investigated for gas CO_2-water, liquid CO_2-water and supercritical CO_2-water displacements in porous media. The pressure-dependant drainage capillary pressures are obtained as a result of CO_2-water interfacial tension. Various water production behaviours are obtained for gas CO_2-water and liquid CO_2-water displacements, mainly due to the effect of CO_2 dissolution. The significant irregular capillary pressure-saturation curves and water production behaviors can be observed for the supercritical CO_2-water displacements. The water and CO_2 relative permeabilities for CO_2-water displacements in a porous media are then predicted.

Contents

DECLARATION I

ABSTRACT II

LIST OF FIGURES VIII

LIST OF TABLES XV

ACKNOWLEDGMENTS XVI

PUBLICATIONS AND PRESENTATIONS XVIII

CHAPTER 1: INTRODUCTION 1

1.1 PROJECT BACKGROUND AND MOTIVATION 1

1.2 THESIS STRUCTURE 4

1.3 REFERENCE 6

CHAPTER 2: THEORETICAL BACKGROUND AND LITERATURE REVIEW 9

2.1 ENHANCED OIL RECOVERY 9

2.2 CO_2 STORAGE 11

2.3 WETTING 16

2.3.1 Surface Tension *16*

2.3.2 Fundamentals of Wetting and Contact Angle *17*

2.3.2.1 Young's Equation 17

2.3.2.2 Modified Young's Equation 20

2.3.2.3 Spreading Coefficient 22

2.3.2.4 Equilibrium Spreading Pressure 23

2.3.3 Dynamic Wetting *24*

2.3.4 Pore Wetting *27*

2.3.5 Interfacial Phenomena in a CO_2-fluid-mineral System *29*

2.3.5.1 CO_2-water/brine Interfacial Tension 29

2.3.5.2 CO_2-water/brine Contact Angle 31

2.4 MULTIPHASE FLOW IN POROUS MEDIA 37

2.4.1 Capillary Pressure 37

2.4.2 Two-phase Flow Displacement in Porous Media 39

2.4.2.1 Imbibition and Drainage 39

2.4.2.2 CO_2-fluid Displacement 42

2.4.3 Permeability 43

2.5 REFERENCES 46

CHAPTER 3: METHODS AND MATERIALS 61

3.1 EXPERIMENTAL METHODOLOGIES 61

3.1.1 Pendant Drop Method for Surface Tension Measurements 61

3.1.2 Sessile Drop Method for Contact Angle Measurement on a Flat Surface 63

3.1.3 Microscopic Imaging Technique for Contact Angle Measurement in a Micron-sized Pore 64

3.1.3.1 Contact Angle Measurements in a Pore at Ambient Conditions 64

3.1.3.2 Contact Angle Measurements in a Pore at High Pressure 67

3.1.4 CO_2 Core Flooding Experimental Set-up 69

3.2 MATERIALS 72

3.2.1 Liquids 72

3.2.1.1 Basic Reservoir Fluids 72

3.2.1.2 Liquids with Various Surface Tensions and Viscosities 72

3.2.1.3 Organic Liquids with Various Chemical Structures 75

3.2.2 CO_2 77

3.2.3 Capillaries 79

3.2.3.1 Manufacturing and Cleaning Capillary Tubes 79

3.2.3.2 Polymeric Capillary 79

3.2.4 Sandstone 81

3.3 REFERENCES 82

CHAPTER 4: STATIC PORE WETTING 85

4.1 INTRODUCTION 85

4.2 EQUILIBRIUM CONTACT ANGLE IN A SINGLE GLASS CAPILLARY 86

4.3 COMPARISON OF PORE CONTACT ANGLE WITH THE CONTACT ANGLE MEASURED ON A FLAT SURFACE AND IN AN OPEN SPACE 92

4.4 SUMMARY 95

4.5 REFERENCES 96

CHAPTER 5: DYNAMIC PORE WETTING 101

5.1 INTRODUCTION 101

5.2 DYNAMIC CONTACT ANGLES IN GLASS CAPILLARIES 102

5.3 EFFECTS OF SURFACE TENSION AND VISCOSITY ON THE DYNAMIC CONTACT ANGLE IN A PORE 105

5.3.1 Effect of Surface Tension 105

5.3.2 Effect of Viscosity 107

5.4 A NEW EMPIRICAL CORRELATION FOR DYNAMIC PORE CONTACT ANGLE 111

5.5 PREDICTION OF DYNAMIC PORE WETTING BY MOLECULAR-KINETIC THEORY 116

5.6 SUMMARY 119

5.7 REFERENCES 120

CHAPTER 6: EFFECT OF CHEMICAL STRUCTURE OF ORGANICS ON PORE WETTING 122

6.1 INTRODUCTION 122

6.2 PORE CONTACT ANGLE OF PURE AMPHIPHILE 124

6.3 EFFECTS OF FUNCTIONAL GROUP AND ALKYL CHAIN OF AMPHIPHILE ON PORE WETTING 129

6.4 EFFECTS OF STRUCTURAL ISOMER AND SYMMETRICAL STRUCTURE ON PORE WETTING 132

6.5 CONTACT ANGLE OF AMPHIPHILE AQUEOUS SOLUTION 135

6.6 SUMMARY 140

6.7 REFERENCES 142

CHAPTER 7: GAS/LIQUID/SUPERCRITICAL CO_2-FLUIDS CONTACT ANGLES IN OIL-WET AND WATER-WET PORES 144

7.1 INTRODUCTION 144

7.2 CO_2-FLUID CONTACT ANGLES IN AN OIL-WET PORE 146

7.3 CO_2-FLUID CONTACT ANGLES IN A WATER-WET PORE 152

7.4 DISCUSSION 154

7.4.1 Hydrophobic Surface 156

7.4.2 Hydrophilic Surface 157

7.5 SUMMARY 159

7.6 REFERENCES 161

CHAPTER 8: CO_2-WATER DISPLACEMENTS IN A SANDSTONE CORE SAMPLE 164

8.1 INTRODUCTION 164

8.2 CAPILLARY PRESSURE-SATURATION CURVE AND WATER PRODUCTION BEHAVIOUR 165

8.2.1 Experimental Results on Gas CO_2-water and Liquid CO_2-water Displacements 171

8.2.1.1 Capillary Pressure-Saturation Curve 171

8.2.1.2 Water Production 173

8.2.2 Experimental Results on Supercritical CO_2-water Displacement 175

8.2.2.1 Capillary Pressure-Saturation Curve 175

8.2.2.2 Water Production 178

8.3 CO_2-WATER RELATIVE PERMEABILITY CURVES 183

8.4 SUMMARY 189

8.5 REFERENCES 191

CHAPTER 9: CONCLUSIONS AND FURTHER WORK 194

9.1 PORE WETTING OF RESERVOIR FLUIDS 194

9.2 GAS/LIQUID/SUPERCRITICAL CO_2-FLUIDS PORE WETTING 195

9.3 GAS/LIQUID/SUPERCRITICAL CO_2-WATER DISPLACEMENTS IN SANDSTONE CORE SAMPLE 196

9.4 FUTURE WORKS 197

List of Figures

Figure 1.1 Overview of Geological Storage Options [7] 2

Figure 1.2 Carbon Storage – Geologic sequestration in deep saline formation [8] 2

Figure 2.1 Oil recovery defined by the Society of Petroleum Engineering (SPE) [9, 10] 10

Figure 2.2 Concept of CO_2 geological storage [14] 11

Figure 2.3 CO_2 storage mechanisms at various timescales [16] 12

Figure 2.4 CO_2 structural trapping: the buoyant CO_2 is trapped by low-permeability layers [19] 13

Figure 2.5 CO_2 capillary trapping in rock pores (a) [19] and in a single glass capillary (b) 13

Figure 2.6 CO_2 Solubility trapping: CO_2 dissolves into brine and sinks down to the bottom of formation for storage [19] 14

Figure 2.7 Rocks lock CO_2 into stable mineral forms [31] 14

Figure 2.8 Schematic illustration of surface tension for a drop of liquid in air [36]. 16

Figure 2.9 Pictorial representation of Young's equation. 18

Figure 2.10 (a) Advancing and receding contact angles induced by the drop method; (b) advancing and receding contact angles captured by the tilting base method; (c) dynamic contact angles of the water meniscus in the exposure head. 20

Figure 2.11 Drop size dependence of (a) octane contact angles [52] and (b) organic contact angles [53] on self-assembled monolayer (SAM) surface..... 22

Figure 2.12 (a) Interfacial tension between water/brine and gas/liquid CO_2 at ambient temperature (20 ℃) [35, 121, 123, 126, 127]; (b) interfacial tension between water and gas/supercritical CO_2 at elevated temperatures [119, 120] 31

Figure 2.13 Glass micromodel: (a) gaseous CO_2 (P = 57.9 bars, T = 20 ℃), (b) supercritical CO_2 (P = 105.4 bars, T = 60 ℃), (c) liquid CO_2 (P = 100 bars, T =

23 ℃). [129] 32

Figure 2.14 CO_2-water contact angle data on quartz substrate during first and second measurement cycles [128] 33

Figure 2.15 CO_2-water contact angles on a PTFE substrate as CO_2 pressure increases from 0.1 to 18.5 MPa [35] 34

Figure 2.16 Stable CO_2-water/brine contact angles for the effectively oil-wet rock (saturated and aged with crude B, SB-5 and SB-6) and partially water-wet rock (saturated and aged with crude A, SB-1 and SB-4) substrates at various pressures [132] 35

Figure 2.17 Effect of brine concentration on CO_2-brine wetting [140] 36

Figure 2.18 Illustration of capillary pressure: water rise in a capillary (water is a wetting fluid, air is a non-wetting fluid) [143] 38

Figure 2.19 (a) Imbibition for water; (b) Drainage between oil and water in a single capillary and rock [36] 40

Figure 2.20 A typical capillary pressure-saturation curve for a non-wetting/wetting fluids (oil/water) displacement system. It can be assumed that water and oil are the wetting and non-wetting fluids respectively (P_c: capillary pressure, P_0: capillary entry pressure, S_w: water saturation, S_{cw}: residual water saturation, S_{spw}: spontaneous water imbibition saturation, S_{or}: residual oil saturation) [148] 41

Figure 2.21 Drainage capillary pressure curves for CO_2-water displacements in coarse sand at various pressure and CO_2 phase conditions [151] 43

Figure 2.22 A two-phase water-oil relative permeability curve ($k_{r,w}$: wetting fluid relative permeability, $k_{r,nw}$: non-wetting fluid relative permeability, $S_{w,ir}$: residual water saturation)[160] 45

Figure 3.1 (a) Experimental set-up (FTA 32, First Ten Angstroms) for investigation of surface tension and contact angle measurement on a flat substrate. (1) light source, (2) syringe, (3) substrate holder, (4) camera; Pendant drop methods for surface

tension measurements of water (b) and n-decane (c). 62

Figure 3.2 Sessile drop method for contact angle measurement on a flat surface; sessile drop image of water on a flat glass surface. 63

Figure 3.3 Experimental setup for the study of dynamic contact angles in a capillary: (a) microscopic imaging of contact angle of liquid in a pore (the vector g shows the direction of gravity); (b) dynamic contact angles (meniscus movements) under a microscope equipped with a camera 65

Figure 3.4 Experimental setup for CO_2- fluids pore contact angle measurements: (a) CO_2 cylinder; (b) CO_2 filter; (c) ISCO CO_2 pump; (d) fluid injector; (e) capillary tube; (f) hot water bath chamber; (g) optical microscope (Olympus, BHW) with a 10X objective; (h) digital camera (AM7023, Dino- Eye); (i) data acquisition computer; (j) CO_2-water pore contact angle image; 1~5: ball valve, 6: needle valve 68

Figure 3.5 Experimental set-up developed for CO_2-water core flooding experiments. 70

Figure 3.6 (a) shrinkable Teflon sleeve; (b) stainless steel core holder; (c) cross-section view of core holder..... 71

Figure 3.7 CO_2 phase diagram [18]..... 78

Figure 3.8 A glass capillary coated with a FEP tube for CO_2-fluid contact angle measurements in a glass capillary under high pressure 80

Figure 3.9 Sandstone rock core sample..... 81

Figure 4.1 l^2/t vs r for water capillary imbibition. (×) Experimental points [15]; (—) theoretical line from Lucas-Washburn equation by assuming $\theta=0^0$; (---) Lucas-Washburn equation with our measured air-water pore contact angle $\theta=30^0$ ... 87

Figure 4.2 Static water contact angles in glass capillaries with a pore size from 100 to 250 μm. 87

Figure 4.3 Static pore contact angles for DI water, 1-propanol, n-decane and crude oil in glass capillaries with a pore size ranging from 100 to 1000 μm. 88

Figure 4.4 Static pore contact angles at unit surface tension (θ/γ) for water, 1-propanol, n-decane and crude oil 91

Figure 4.5 Comparison of pore contact angles with contact angles on a flat surface. (a) water; (b) 1-propanol; (c) n-decane; (d) crude oil 94

Figure 5.1 Experimental data of dynamic contact angles of silicone oil (η=9.30×10^{-3} Pa s) in glass capillaries, and data calculated using empirical correlations [1, 5, 6]102

Figure 5.2 Dynamic contact angles of DI water, 1-propanol, n-decane, crude oil and silicone oil (η=9.30×10^{-3} Pa s) in a pore 104

Figure 5.3 (a) Dynamic contact angle; and (b) contact angle variation from 0 to 0.0012 m/s of water (γ=72.0 mN/m; η=8.94×10^{-4} Pa s), 1-propanol (γ=24.4 mN/m; η=1.94×10^{-3} Pa s), 5wt% 1-propanol aqueous solution (γ=46.2 mN/m; η=1.10×10^{-3} Pa s) and 10wt% 1-propanol aqueous solution (γ=37.3 mN/m; η=1.34×10^{-3} Pa s) 106

Figure 5.4 (a) Dynamic contact angle; and (b) contact angle variation ($\cos\theta_s$-$\cos\theta_d$) from 0 to 0.0012 m/s of silicone oils with different viscosities of 9.30×10^{-3} Pa s, 4.80×10^{-2} Pa s, 9.60×10^{-2} Pa s, 4.85×10^{-1} Pa s and 9.70×10^{-1} Pa s and similar surface tensions of 19.4 mN/m, 20.8 mN/m, 20.9 mN/m, 21.2 mN/m and 21.2 mN/m respectively. The scale in the x-axis (the viscosity of silicone oil) of (b) is logarithmic with base 10. 109

Figure 5.5 Comparison of empirical correlations (Table 5.1) with the experimental data in the present study in a low capillary number (Ca) range 113

Figure 5.6 Wetting line friction coefficients of various liquids 118

Figure 6.1 Contact angles in a glass pore and on a flat glass surface and the surface tensions for the organics used in this study 125

Figure 6.2 Comparison of contact angles measured in a glass pore and a PMMA pore 126

Figure 6.3 Contact angles in a pore and on a flat surface and vapor pressures at 20 ℃

for all amphiphiles used in this study 128

Figure 6.4 Contact angles of pentane, propionic acid, propylamine and 1-propanol in a glass pore 129

Figure 6.5 Pore contact angles of alkanes, alkanols, alkylamines and alkyl carboxyl acid with different straight alkyl chain lengths 131

Figure 6.6 Contact angles of structural isomers of 1-propanol and 1-butanol in a glass pore 133

Figure 6.7 Pore contact angles of ethanol, ethylene glycol, 1-propanol and glycerol 134

Figure 6.8 Contact angles of methanol, ethanol and 1-propanol aqueous solutions in a (a) PMMA pore and (b) glass pore 137

Figure 6.9 Contact angles of 1-propanol, propylamine and propionic acid aqueous solutions in a (a) PMMA pore and (b) glass pore 139

Figure 7.1 CO_2-water contact angle in a FEP pore versus pressure at 20 ℃ (small diagram: contact angle data from 50 to 60 bar) 147

Figure 7.2 Contact angles for water-CO_2, brine-CO_2 and decane-CO_2 in a FEP pore at 20 ℃ (a) and 40 ℃ (b) 149

Figure 7.3 Contact angles for water-CO_2, brine-CO_2 and decane-CO_2 in a glass pore at two different temperatures: (a) 20 ℃; (b) 40 ℃ 153

Figure 7.4 Comparison of our experimental contact angles measured in a FEP pore with values recently reported in the literature [4, 6] 157

Figure 7.5 Comparison of our experimental contact angles measured in a glass pore with values recently reported in the literature [1, 4, 6, 7] 158

Figure 8.1 CO_2-water core flooding 166

Figure 8.2 (a) Pressures at the inlet (CO_2) and outlet (water) of the core holder and the differential pressure (capillary pressure) between the two ends of the core as a

function of time; (b) Capillary pressure curve as a function of water saturation, at 75 bar and 20 ℃..... 168

Figure 8.3 Cumulative volumes of liquid CO_2 injection and water production at 75 bar and 20 ℃..... 170

Figure 8.4 Capillary pressure-water saturation curves for gas CO_2-water displacements at 10 bar and 30 bar and liquid CO_2-water displacement at 75 bar.. 171

Figure 8.5 Drainage capillary pressures normalized by the interfacial tension (P_c/γ) for different CO_2 pressures..... 172

Figure 8.6 Cumulative volumes of CO_2 injection and water production at 10 bar, 30 bar and 75 bar at a CO_2 injection rate of 0.2 ml/min 174

Figure 8.7 Plug and Bruining's experimental data for cumulative volumes of water production for gas CO_2 injection (atmospheric conditions) and liquid CO_2 injection (85 bar), with both gas CO_2 and liquid CO_2 at an injection rate of 0.5ml/h [6] 174

Figure 8.8 Capillary pressure-water saturation curves for supercritical CO_2-water displacement (75 bar, 40 ℃), gas CO_2-water displacement (10 bar, 20 ℃) and liquid CO_2-water displacement (75 bar, 20 ℃)..... 175

Figure 8.9 Capillary pressure-water saturation curves for a supercritical CO_2-water system at CO_2 injection rates of 0.1, 0.2, 0.4 and 0.6 ml/min..... 177

Figure 8.10 Water production behaviour during supercritical CO_2-water displacement. (a) comparison of water production behaviour of gas CO_2-water, liquid CO_2-water and supercritical CO_2-water systems; (b) water production behaviour and capillary pressure as a function of time for supercritical CO_2-water displacement. 179

Figure 8.11 Densities of liquid CO_2 and supercritical CO_2 from 20 to 40 ℃ at 75 bar [9] 180

Figure 8.12 Cumulative water production and CO_2 injection for the supercritical CO_2-water system at various supercritical CO_2 injection rates of 0.1, 0.2, 0.4 and 0.6 ml/min 181

Figure 8.13 Normalized water production rates of gas CO_2-water, liquid CO_2-water

and supercritical CO_2-water systems against water saturation 182

Figure 8.14 Experimental capillary pressure data and curve fitting using the van Genuchten (VG) equation for: (a) gas CO_2-water, liquid CO_2-water and supercritical CO_2-water systems at injection rate of 0.2 ml/min; and (b) supercritical CO_2-water system at various CO_2 injection rates of 0.1, 0.2, 0.4 and 0.6 ml/min..... 185

Figure 8.15 Relative permeability curves for gas CO_2-water, liquid CO_2-water and supercritical CO_2-water displacements 187

Figure 8.16 Relative permeability curves predicted based on Plug and Bruining's experimental data [6] for gas CO_2-water, liquid CO_2-water and supercritical CO_2-water displacement..... 188

List of Tables

Table 2.1 Brooks-Corey (BC) and van Genuchten (VG) capillary pressure models for wetting and nonwetting phase relative permeability 44

Table 3.1 The physical properties of liquids for dynamic pore contact angle measurements 73

Table 3.2 Surface tensions of amphiphile aqueous solutions 74

Table 3.3 Physical and structural properties of organic liquids with various chemical structures 76

Table 3.3 (Continued) Physical and structural properties of organic liquids with various chemical structures 77

Table 4.1 Static contact angles on flat glass surface for water, 1-propanol, n-decane and crude oil 92

Table 5.1 Empirical correlations and fitting parameters for dynamic contact angle in the literature 112

Table 5.2 The fitting parameters (κ_0, λ) in molecular-kinetic theory for various liquids 118

Table 7.1 Summary of materials and operating conditions in the studies on CO_2-liquid-mineral system from literatures 155

Table 8.1 Relative permeability function parameters 186

Acknowledgments

First of all, I owe my deepest gratitude to my PhD supervisor, Dr Xianfeng Fan, for his extremely responsible supervision of my PhD project. The PhD work, publications and the thesis would not have been possible without the support he has generously given, and I am deeply appreciative of this PhD project opportunity he offered to me. I feel very lucky to have had such a supervisor who has not only given me tremendous help in my research, but has also taught me how to become a qualified researcher with a genuine scientific spirit. Dr Fan's patience, motivation, enthusiasm, and immense knowledge of science and engineering constantly encouraged me and gave me so much confidence to overcome difficulties at the hardest time. All of the publications stemming from this work would not be possible without Dr Fan's patient revisions and supervision. All the things I have learned from Dr Fan will be invaluable to me for the rest of my life.

I would like to express my appreciations to Prof. Brandani for his contribution of my experimental apparatus and advice on the work. I am also thankful to and acknowledge Prof. Sefiane, Dr Koutsos and Dr Askounis for their effort, useful suggestions and guidance on the relevant published work from Chapter 5 of this thesis. In Chem. Eng. Sci. 104 (2013) 988-997, Prof. Sefiane contributed to the description of interface deformation by Crispation number and important advices on the article structure and theory. Dr Koutsos and Dr Askounis provided AFM images and analysis, gave helpful advices and suggestions. Dr Wu made an effort on work plan. I would also like to express my appreciation for the electric and mechanical technical support for my experimental apparatus commissioning and starting-up from the technicians in the school. They are Kevin Tierney, Derek Jardine, Steve Gourlay, Paul Aitken, Douglas and others. Also, I would like to thank Mr Len Shaw for his professional English proofreading on the thesis.

I would also like to thank the Carnegie Trust and the University of Edinburgh. They offered me the Carnegie Scholarship and the University of Edinburgh Research Scholarship. Without their financial support, it would have been difficult for me to complete this PhD project.

I would also like to thank the reviewers and editors from the Journals of Chemical Engineering Science, Langmuir and International Journal of Greenhouse Gas Control. The very constructive and helpful suggestions given by these experts improved my work, and finally led to some of the content of Chapters 4, 5 and 7 to be published.

Lastly, I express many thanks to my dear parents, relatives and all my friends and colleagues of the University of Edinburgh and Imperial College London for always supporting me in terms of academic communication and experimental apparatus.

Publications and Presentations

Journal Papers:

1. **Li, X.**, Fan, X., **2015.** Effect of CO_2 Phase on Contact Angle in Oil-wet and Water-wet Pores. **International Journal of Greenhouse Gas Control**, 36, 106-113.

2. **Li, X.**, Fan, X., Brandani, S., **2014**. Difference in Pore Wetting and the Wetting Measured on a Flat Surface and in an Open Space. **Chemical Engineering Science** 117, 137-145.

3. **Li, X.**, Fan, X., Askounis, A., Wu, K., Sefiane, K., Koutsos, V., **2013**. An Experimental Study on Dynamic Pore Wettability. **Chemical Engineering Science** 104, 988-997.

4. **Li, X.**, Fan, X., Effect of Chemical Structure of Organics on Pore Wetting. **Chemical Engineering Science** (submitted).

International Conference Papers/Presentations:

1. **Li, X.**, Fan, X., **2014.** Pore Wetting Phenomena: Implications to Enhanced Oil Recovery and Geologic Carbon Storage. **International Conference on Applied Energy, ICAE 2014**, Taiwan, published in **Energy Procedia** 61, 2712-2715.

2. **Li, X.**, Fan, X., **2014.** Pore Wetting and Its Effect on Breakthrough Pressure in Water-Wet and Oil-Wet Pores. **International Conference on Biological and Chemical Science – ICBCS, 2014,** Shanghai, China, published in **International Journal of Chemical Engineering and Applications** 5, 359-362.

3. **Li, X.**, Fan, X., Fluids in Pores. **Geochemical processes during CO_2 storage meeting 2014, Cambridge, UK**

4. **Li, X.**, Fan, X., Mathematical Modelling of Two-Phase Flow Imbibition through a Pore Neck. **the 20th Joint Annual Conference of CSCST-SCI 2013**, London, UK.

5. **Li, X.**, Fan, X., **2013.** Experimental Studies on Multiphase Flow in Porous Media and Pore Wettability. **International Conference on Chemical and Environmental Engineering 2013**, Barcelona, Spain, published in **World Academy of Science, Engineering and Technology** 74, 739-743.

Chapter 1: Introduction

1.1 Project Background and Motivation

The geological storage of CO_2 has become one of the most promising technologies with the potential to mitigate CO_2 from the combustion of fossil fuel to greenhouse gas control (Figure 1.1) [1]. Saline aquifers and oil reservoirs have been estimated to have the largest CO_2 storage capacities world-wide. If the depleted oil reservoir is considered for CO_2 storage, the injected CO_2 will enhance the recovery of oil trapped in porous rock. This will reduce the cost of CO_2 storage and make it much more feasible [2].

The geological storage of CO_2 and enhanced oil recovery involve engineering at a geological scale, but the important mechanisms and operation are controlled by colloid and interfacial phenomena at pore scale [3]. For these processes, injected CO_2 and other fluids must be delivered not only to large geological cracks, but also micron-sized or even nano-sized pore space (Figure 1.2). The transport of CO_2 and reservoir fluids in confined spaces is governed by fluid-fluid and rock-fluid interactions, wettability, fluid surface tension and viscosity, the chemical properties of fluids and pore surfaces, reservoir conditions, such as temperature and pressure, and pore structure [4-6]. Most of these factors are interrelated. We do not exactly know the impact of individual factors on the transport of CO_2 and reservoir fluids, and neither is the relative importance of the various factors mentioned above known. A proper understanding of the significance of these factors could enhance the understanding of the long-term subsurface storage of CO_2 and improve oil recovery efficiency.

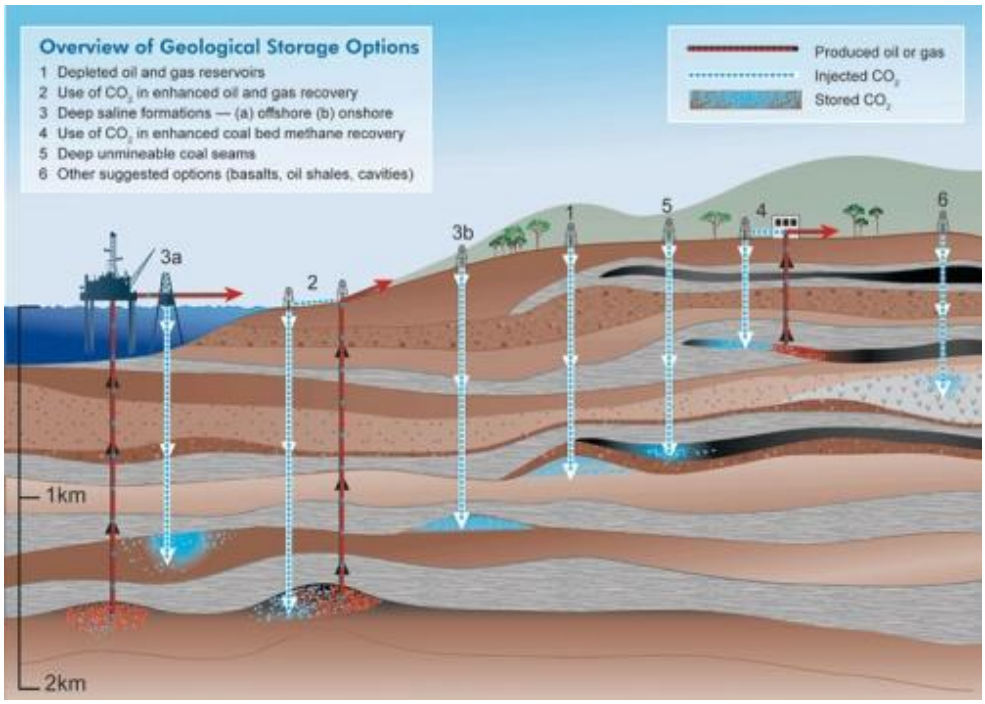

Figure 1.1 Overview of Geological Storage Options [7]

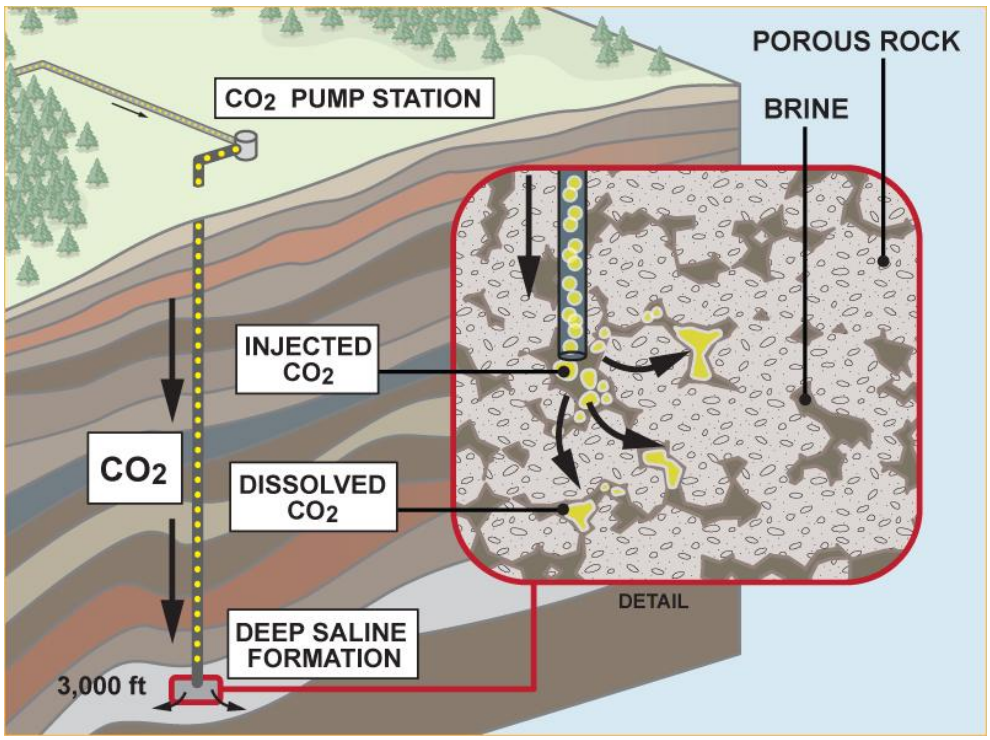

Figure 1.2 Carbon Storage – Geologic sequestration in deep saline formation [8]

A deep geological formation can be regarded as a capillary system, since fluid-fluid

transport is mainly governed by capillary action. The magnitude of capillary force is not usually large, but its effect could be considerable. For instance, CO_2-water capillary pressure characteristics in porous media have a dominant effect on the relative permeabilities of CO_2 and water, and thus control how fluids flow and distribute in the porous-structured subsurface. In addition, capillary forces are responsible for fluid-fluid displacement mechanisms at a pore scale, and therefore then determine CO_2 injectability and the sealing capacity of geological formations.

Capillary force is associated with interfacial tension and the contact angle in fluid-rock systems. They are two of the most important macroscopic parameters for multiphase flow transport in porous media. For instance, because the interfacial tension and contact angle of fluids in hydrocarbon/water systems are greatly different from those in CO_2/water systems, the sealing capacity of the caprock is significantly altered once its original hydrocarbons in a reservoir are replaced by CO_2 [9, 10]. The fluid-fluid interfacial tensions under various reservoir conditions have been thoroughly investigated by considering the effects of CO_2 phase, brine composition, pressure and temperature. Consistent findings concerning interfacial tension have been obtained by most previous studies [4, 11-18]. However, the wetting behaviour of CO_2-fluids is controversial [4, 12, 16, 19-25]. Moreover, because of wetting (contact angle) measurements on other than planar substrates still remains a challenge, it is commonly assumed that the contact angle on a flat surface can represent the wetting conditions in a pore. This might be true in some cases, but deserves to be properly assessed [26]. In order to indicate the pore wetting correctly and to avoid the use of inappropriate contact angles in cases of porous surfaces, a new experimental method [27, 28] has been developed in this PhD project to directly measure the contact angles of fluids and CO_2 in micro-size pores, by considering the effects of surface tension, viscosity, chemical structure and CO_2 phase. In addition, the capillary pressures, displacement behaviours and relative permeabilities of CO_2

(gas, liquid and supercritical)-water-sandstone systems are also studied using two-phase core flooding experiments.

1.2 Thesis Structure

This thesis contains 9 chapters.

Chapter 1 gives an introduction to the thesis in terms of the project background, motivation and objectives. The scientific merit and significance of the work is briefly discussed. Chapter 2 provides the relevant theoretical background and literature review of this project. Concepts of wetting, interfacial phenomenon, capillary actions and multiphase flow in porous media and related fundamental theoretical equations are explained. Chapter 3 describes the materials and the main experimental methodologies used, such as a novel micron-sized pore wetting measurement technique developed in this project and a two-phase core flooding experimental apparatus.

The main body of the thesis is from Chapter 4 to Chapter 8. These five chapters present the micron pore-scale experimental results and discussions of the pore wetting of fluids and CO_2, and CO_2-water displacement behaviour in porous media.

Chapter 4 investigates the static contact angles of various liquids directly measured in single glass capillaries, and indicates that the contact angles measured in a glass pore differ from those measured on a flat glass surface in an open space.

In Chapter 5, dynamic wetting behaviour in a glass pore is studied. The dynamic contact angles for various liquids imbibed into single glass capillaries are measured, in order to describe the dependence of the dynamic contact angle on imbibition rate

(interfacial velocity) and the effects of surface tension and the viscosity of liquid on the dynamic contact angle in a pore. A new empirical correlation is developed to describe the dynamic wetting in a pore in a low capillary number regime. Blake's molecular-kinetic theory is also used to explain our experimental dynamic pore contact angle results.

Some of the results in Chapters 4 and 5 imply that the chemical structure of liquids might affect glass pore wetting. Thus, the effect of the chemical structure of organic substances on glass pore wetting is discussed in detail in Chapter 6. Contact angles of a range of pure amphiphilies and amphiphilie aqueous solutions in a glass pore are measured, in order to reveal the effect of the chemical structure of organics on glass pore wetting in terms of functional group, alkyl chain length and chain structural isomer.

In Chapter 7, the gas/liquid/supercritical CO_2-fluid contact angles in single oil-wet and water-wet pores are directly measured, by considering the effect of CO_2 phase (gas, liquid and supercritical). The results can significantly advance the understanding of pore wetting phenomena for the CO_2 storage process.

Chapter 8 presents the experimental results for gas CO_2-water, liquid CO_2-water and supercritical CO_2-water displacements in a sandstone core sample. The effects of CO_2 phase, pressure and CO_2 injection rate are considered. Several important macroscopic parameters in geological carbon storage, such as capillary pressure, water production behaviour and relative permeability, are investigated.

Chapter 9 presents the main findings and highlights the significance of the study. The limitations, weaknesses and flaws of the work are addressed and emphasized, and future work is also proposed.

1.3 Reference

[1] Benson S, Cook P. IPCC Special Report on Carbon dioxide Capture and Storage. Underground geological storage. 2010;Chapter 5:181 and 203.

[2] Kokal S, Al-Kaabi A. Enhanced oil recovery: challenges & opportunities. World Petroleum Council: Official Publication. 2010:64-9.

[3] Andrew M, Bijeljic B, Blunt MJ. Pore-scale contact angle measurements at reservoir conditions using X-ray microtomography. Advances in Water Resources. 2014;68:24-31.

[4] Chalbaud C, Robin M, Lombard JM, Martin F, Egermann P, Bertin H. Interfacial tension measurements and wettability evaluation for geological CO_2 storage. Adv Water Resour. 2009;32:98-109.

[5] Gaus I. Role and impact of CO_2–rock interactions during CO_2 storage in sedimentary rocks. International Journal of Greenhouse Gas Control. 2010;4:73-89.

[6] Plug WJ, Bruining J. Capillary pressure for the sand–CO_2–water system under various pressure conditions. Application to CO_2 sequestration. Advances in Water Resources. 2007;30:2339-53.

[7] Overview of Geological Storage Options 2013 http://www.southwestclimatechange.org/figures/geological-storage. Last Accessed Date: 06/12/2014

[8] Carbon Storage and Sequestration 2014 http://www.fossiltransition.org/pages/carbon_storage_and_sequestration/30.php. Last Accessed Date: 06/12/2014

[9] Li Z, Dong M, Li S, Huang S. CO_2 sequestration in depleted oil and gas reservoirs—caprock characterization and storage capacity. Energy Conversion and Management. 2006;47:1372-82.

[10] Younger PL. Hydrogeological challenges in a low-carbon economy. Quarterly Journal of Engineering Geology and Hydrogeology. 2014;47:7-27.

[11] Hebach A, Oberhof A, Dahmen N, Kögel A, Ederer H, Dinjus E. Interfacial Tension at Elevated PressuresMeasurements and Correlations in the Water + Carbon Dioxide System. Journal of Chemical & Engineering Data. 2002;47:1540-6.

[12] Saraji S, Goual L, Piri M, Plancher H. Wettability of Supercritical Carbon Dioxide/Water/Quartz Systems: Simultaneous Measurement of Contact Angle and Interfacial Tension at Reservoir Conditions. Langmuir. 2013;29:6856-66.

[13] Chun B-S, Wilkinson GT. Interfacial tension in high-pressure carbon dioxide mixtures. Industrial & Engineering Chemistry Research. 1995;34:4371-7.

[14] Chiquet P, Daridon J-L, Broseta D, Thibeau S. CO_2/water interfacial tensions under pressure and temperature conditions of CO_2 geological storage. Energy Conversion and Management. 2007;48:736-44.

[15] Sutjiadi-Sia Y, Jaeger P, Eggers R. Interfacial phenomena of aqueous systems in dense carbon dioxide. The Journal of Supercritical Fluids. 2008;46:272-9.

[16] Espinoza DN, Santamarina JC. Water-CO_2-mineral systems: Interfacial tension, contact angle, and diffusion—Implications to CO_2 geological storage. Water Resour Res. 2010;46:W07537.

[17] Li X, Ross DA, Trusler JPM, Maitland GC, Boek ES. Molecular Dynamics Simulations of CO_2 and Brine Interfacial Tension at High Temperatures and Pressures. The Journal of Physical Chemistry B. 2013;117:5647-52.

[18] Li X, Boek ES, Maitland GC, Trusler JPM. Interfacial Tension of (Brines + CO_2): $CaCl_2$(aq), $MgCl_2$(aq), and Na_2SO_4(aq) at Temperatures between (343 and 423) K, Pressures between (2 and 50) MPa, and Molalities of (0.5 to 5) mol·kg^{-1}. Journal of Chemical & Engineering Data. 2012;57:1369-75.

[19] Bikkina PK. Contact Angle Measurements of CO_2–water–quartz/calcite systems in the Perspective of Carbon Sequestration. Int J Greenh Gas Con. 2011;5:1259-71.

[20] Jung J-W, Wan J. Supercritical CO_2 and Ionic Strength Effects on Wettability

of Silica Surfaces: Equilibrium Contact Angle Measurements. Energy & Fuels. 2012;26:6053-9.

[21] Ameri A, Kaveh NS, Rudolph ESJ, Wolf KH, Farajzadeh R, Bruining J. Investigation on Interfacial Interactions among Crude Oil–Brine–Sandstone Rock–CO_2 by Contact Angle Measurements. Energy & Fuels. 2013;27:1015-25.

[22] Dickson JL, Gupta G, Horozov TS, Binks BP, Johnston KP. Wetting Phenomena at the CO_2/Water/Glass Interface. Langmuir. 2006;22:2161-70.

[23] Li Y, Pham JQ, Johnston KP, Green PF. Contact Angle of Water on Polystyrene Thin Films: Effects of CO_2 Environment and Film Thickness. Langmuir. 2007;23:9785-93.

[24] Yang D, Gu Y, Tontiwachwuthikul P. Wettability Determination of the Reservoir Brine−Reservoir Rock System with Dissolution of CO_2 at High Pressures and Elevated Temperatures. Energy & Fuels. 2007;22:504-9.

[25] Yang D, Gu Y, Tontiwachwuthikul P. Wettability Determination of the Crude Oil−Reservoir Brine−Reservoir Rock System with Dissolution of CO_2 at High Pressures and Elevated Temperatures. Energy & Fuels. 2008;22:2362-71.

[26] Gomez F, Denoyel R, Rouquerol J. Determining the Contact Angle of a Nonwetting Liquid in Pores by Liquid Intrusion Calorimetry. Langmuir. 2000;16:4374-9.

[27] Li X, Fan X, Askounis A, Wu K, Sefiane K, Koutsos V. An Experimental Study on Dynamic Pore Wettability. Chem Eng Sci. 2013;104:988-97.

[28] Li X, Fan X, Brandani S. Difference in pore contact angle and the contact angle measured on a flat surface and in an open space. Chem Eng Sci. 2014;117:137-45.

Chapter 2: Theoretical Background and Literature Review

2.1 Enhanced Oil Recovery

Global oil demand has been rising progressively for the past five decades. The barrels of oil equivalent per day (boe/d) significantly increased from 55 million boe/d in 1960 to 227 million boe/d in 2008 [1]. This increase will continue due to rapid economic development and increased energy consumption. By 2030, world energy demand is predicted to be 40% higher than present demand [1]. Currently, the main oil sources are mobile oil in mature oil reservoirs recovered by conventional methods (primary and secondary recoveries). The world average oil recovery factor from hydrocarbon reservoirs remains at only around 30%. If the oil recovery factor can be enhanced beyond the current level, this would significantly boost the global energy supply.

Primary and secondary oil recoveries mainly aim to extract mobile oil in oil fields. As shown in Figure 2.1, less than 30% of oil can be readily extracted from the reservoir at the primary recovery stage [1]. The oil can be driven up to the surface by significant underground surplus pressure. For secondary recovery, water flooding and increasing reservoir pressure would be applied to recover more oil. However, at least 50% of the original oil in place (OOIP) cannot be recovered and is still left in the reservoirs [2].

Enhanced oil recovery (EOR), also termed tertiary recovery, is a generic concept for techniques used to improve crude oil extraction from hydrocarbon reservoirs [3-5].

EOR processes attempt to continue to recover the immobile oil stuck in the reservoir rocks beyond the secondary recovery. Since EOR can enhance the average oil recovery factor to more than 50%, or even up to 80%, it is closely related to oil prices and overall economics [6]. EOR methods involve thermal treatment, gas or chemical injection and others (Figure 2.1).

The oil reservoir has a porous-structured architecture, containing reservoir fluids and gas, such as oil, water, CO_2, air, and methane. During the recovery process, the efficiency of fluid displacement is predominately determined by interactions among the multiphase flows in porous media. The interactions among the fluids in porous rocks are mainly reflected by interfacial tension and wettability (contact angle) [7, 8], which ultimately affect oil recovery processes. The interfacial tensions among reservoir fluids have been widely investigated, but the experimental research on wettability in small pores is sparse. Thus this study focuses on the experimental investigation of the contact angles of fluids and CO_2 in micron-sized pores, as well as their displacement characteristics in porous media.

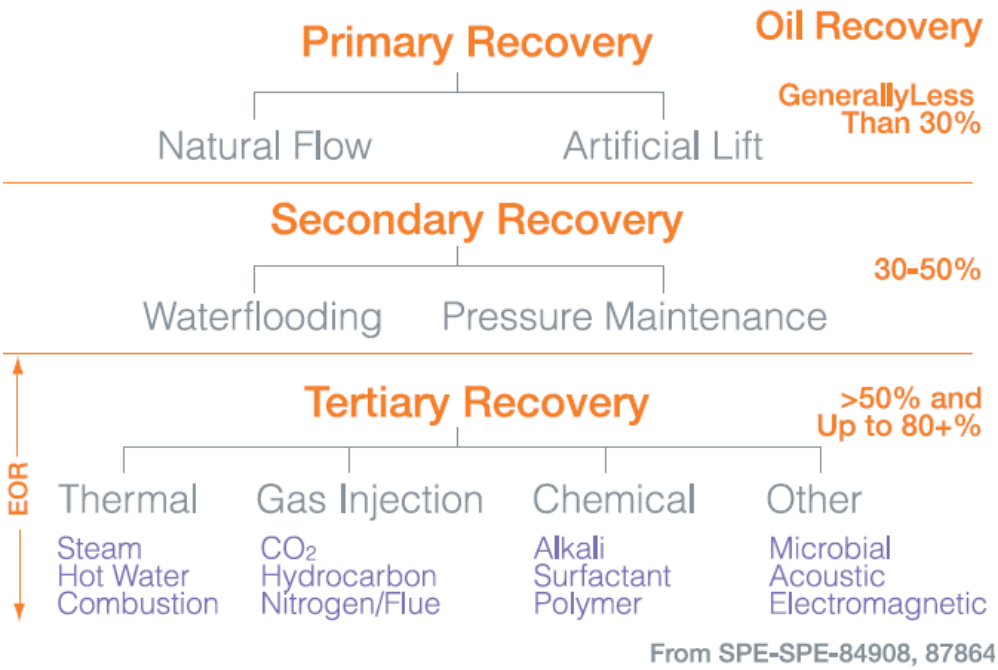

Figure 2.1 Oil recovery defined by the Society of Petroleum Engineering (SPE) [9, 10]

2.2 CO_2 Storage

The geological storage of anthropogenic CO_2 has been regarded as one of the most important technologies potentially to mitigate greenhouse gas emissions [11]. Here, CO_2 is injected into deep subsurface repositories, typically saline aquifers and depleted oil reservoirs, for safe and permanent storage [12, 13] (Figure 2.2). In depleted oil reservoirs, the injected CO_2 performs as a solvent which is miscible with oil. The solution of CO_2 can swell the oil, make crude oil lighter, reduce surface tension and viscosity, detach the oil from the rock surface, and thus favour the displacement of unrecovered residual crude oil. A joint field-scale project for a combination of CO_2 enhanced oil recovery and CO_2 storage has been undertaken in the Weyburn oilfield [3].

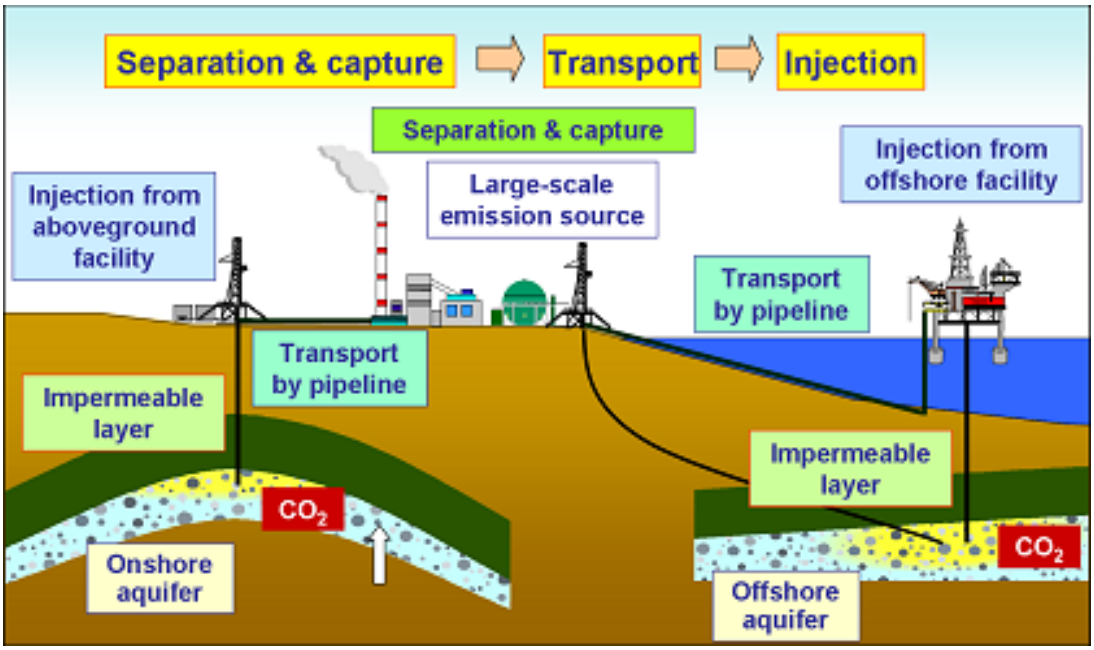

Figure 2.2 Concept of CO_2 geological storage [14]

A variety of tapping mechanisms could keep the underground CO_2 immobilized and securely stored, which are structural trapping, residual/capillary trapping, solubility trapping and mineral trapping. However, these act at various timescales and with

different trapping contributions [15], as shown in Figure 2.3.

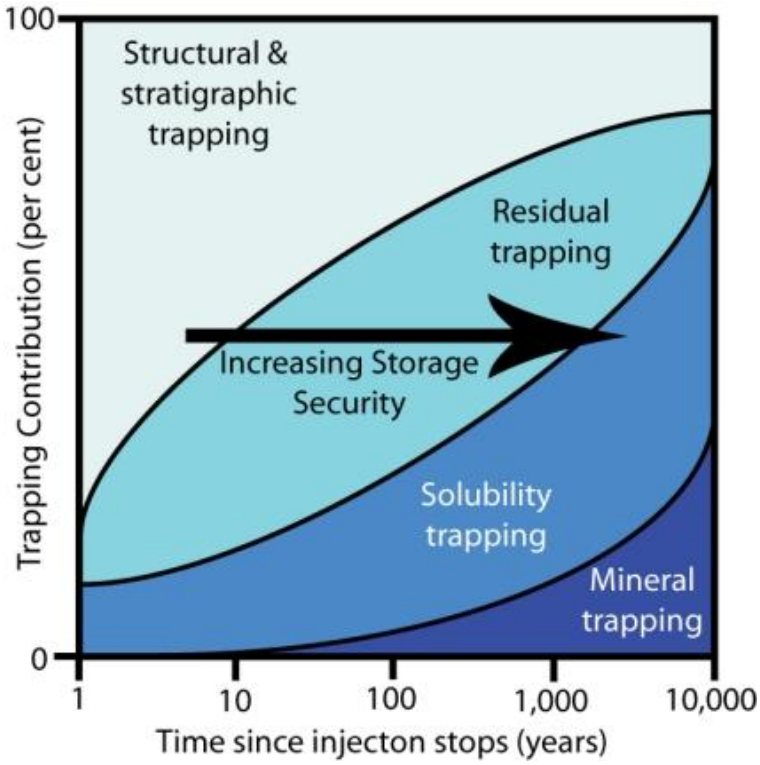

Figure 2.3 CO_2 storage mechanisms at various timescales [16]

- In structural trapping, also called hydrodynamic trapping, the buoyant CO_2 is suppressed by low-permeability layers, and this is generally regarded as one of the most dominant trapping mechanisms involving a physical trap [17, 18]. Once the CO_2 is injected, it will perform less dense and more buoyant than the other fluids. Thus, the CO_2 will percolate up through the porous rock until it reaches the low permeability layer or impermeable layer of rock which is able to curtail upward CO_2 migration. The low permeability layer at the top of the aquifer is usually called cap rock, which plays the role of a closed dome to prevent any lateral escape, as shown in Figure 2.4.

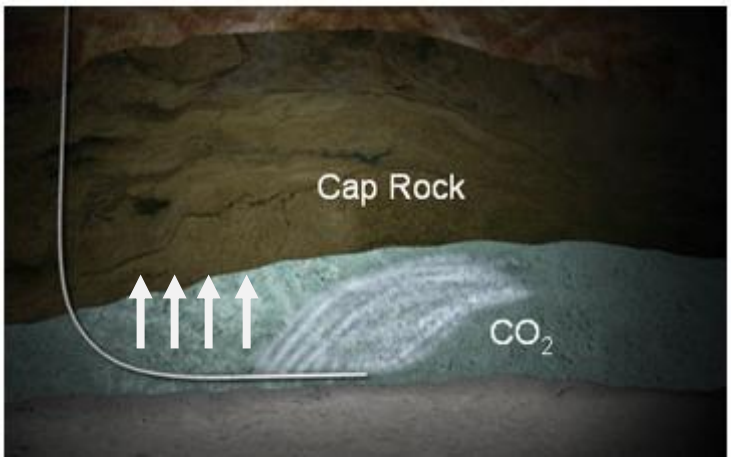

Figure 2.4 CO_2 structural trapping: the buoyant CO_2 is trapped by low-permeability layers [19]

- In residual trapping, also termed 'capillary trapping', CO_2 breaks up into small ganglia that are immobilized by capillary forces [18, 20-22]. As the CO_2 is injected into the formation, a plume of CO_2 displaces fluids (such as water or brine) from the porous rock. Sometimes the displaced water re-enters the pore at the trailing edge of the CO_2 plume. Consequently, CO_2 is disconnected and trapped in pores by capillary pressure (Figure 2.5). Capillary trapping is of great significance for securing CO_2 storage on a short timescale. Hesse and Tchelepi state that most of the injected CO_2 can be immobilized by capillary trapping [20]. Capillary trapping and structural trapping happen over short timescales, and are dominated by two-phase flow dynamics [23].

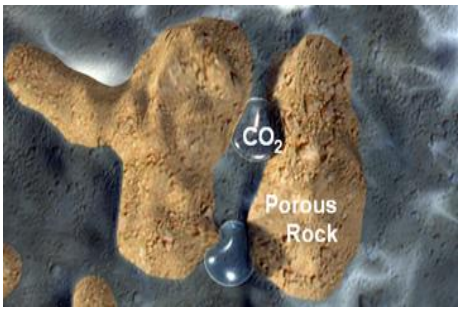

(a)

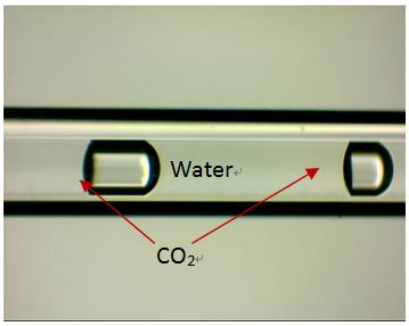

(b)

Figure 2.5 CO_2 capillary trapping in rock pores (a) [19] and in a single glass capillary (b)

- In solubility trapping, CO_2 dissolves in the formation of the aqueous phase or residue oil [18, 24, 25] (Figure 2.6). As CO_2 dissolves in fluids, the salt water (eg. Brine) containing CO_2 is denser, compared with the surrounding fluids. It therefore sinks down to the bottom of the rock along with time rather than rising upwards, trapping the CO_2 even more securely.

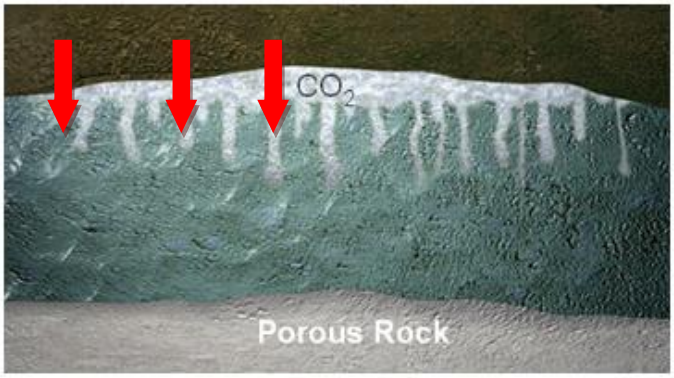

Figure 2.6 CO_2 Solubility trapping: CO_2 dissolves into brine and sinks down to the bottom of formation for storage [19]

- Mineral trapping is where the dissolved CO_2 reacts with carbonate or silicate minerals to form solid precipitation [18, 26-30] (Figure 2.7).

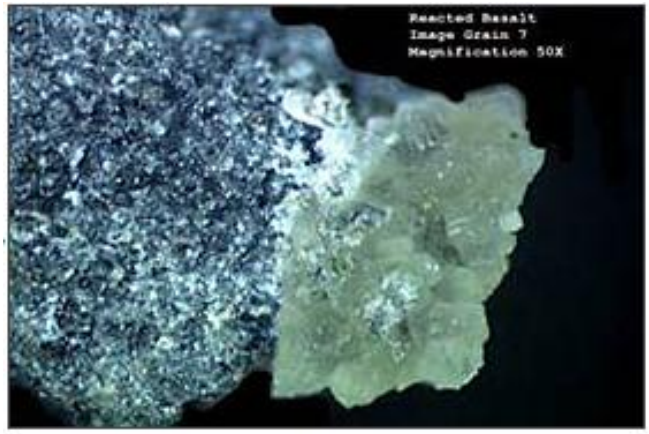

Figure 2.7 Rocks lock CO_2 into stable mineral forms [31]

Before being feasible for safe CO_2 storage, a number of technical issues must be

comprehensively understood; otherwise, premature leakage may occur. It is accepted that interfacial interactions among CO_2, reservoir fluids and minerals initially determine the success of CO_2 storage [23, 32-34]. Most interfacial interaction relates to wettability, interfacial tension, capillarity and interface mass transfer. Among these factors, wettability has a dominant effect on capillary pressure [23, 34], phase distribution [7] and relative permeability [23]. These are of major significance for the CO_2-fluid displacement mechanism [7]. For instance, long-term CO_2 storage is a quasi-static condition which is closely controlled by the capillary breakthrough pressure at the pore throat. For a given pore structure or size (d^*), the CO_2 breakthrough pressure ($Pc^* = 4\gamma\cos\theta/d^*$) is determined by fundamentally important parameters: interfacial tension (γ) and contact angle (θ) [35].

2.3 Wetting

2.3.1 Surface Tension

Surface tension is the one of the most significant properties in interfacial and colloid phenomenon. It stems from the cohesive nature of liquid matter, showing a contractive tendency of the liquid surface. In the bulk of the liquid, each molecule is surrounded by sufficient molecules and pulled equally by neighbouring molecules in every direction, so that the net force is entirely balanced and equals zero. However, there is no molecule above the surface molecule; the force balance is broken at the surface, which leads to an attractive force pulling the surface inwards (Figure 2.8). In other words, surface tension is caused by the imbalance of molecular force at the interface between two immiscible fluids.

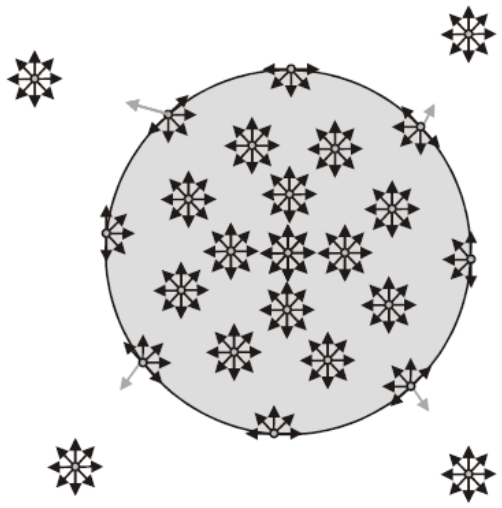

Figure 2.8 Schematic illustration of surface tension for a drop of liquid in air [36]

In order to increase the surface area of a drop, external work must be done to move the interior molecules to the new surface. The surface tension (energy) (γ) is defined as the work consumed (ΔW) per unit of new surface area formed (ΔA):

$$\gamma = \frac{\Delta W}{\Delta A} = \frac{F\Delta R}{\Delta A} = \frac{F\Delta R}{2\pi R\Delta R} = \frac{F}{2\pi R} = \frac{F}{L} \tag{2.1}$$

where γ is surface tension in dynes/cm or N/m, F is the force acting on the surface (dynes or N), R is the drop circle radius (m), and L is the length of the line that the force acts on perpendicularly (m).

2.3.2 Fundamentals of Wetting and Contact Angle

Wettability, or the degree of wetting, is the tendency of a liquid to keep contact with or adhere to a solid surface. Wetting is one of the most common interfacial phenomena in nature and in technological applications. In addition to their applications to colloids, membranes, metallurgic powders and biophysical media and some fundamental practical processes, such as cleaning, coating, drying and adhesion [37-42], the wetting phenomena of fluids within porous media have been intensively investigated for oil/gas recovery from reservoir rocks and carbon storage [43, 44].

2.3.2.1 Young's Equation

The wetting process can be characterized by the three-phase (solid-liquid-vapor) contact line as a consequence of the combination of adhesive and cohesive forces. The three-phase contact line generates a contact angle. The contact angle is regarded as the primary parameter in wettability studies, or it indicates the degree of wetting when a liquid and solid interact. In general, a small contact angle of less than 90° represents high wettability, while a large contact angles larger than 90° correspond to

low wettability. Once an equilibrium status is reached, the three-phase contact line no longer moves at this state of the minimal excess of the total free energy of the system. The contact angle at equilibrium is defined as the equilibrium contact angle (θ_e), which relates the surface energies (solid, liquid-solid and liquid surface tensions) according to Young's equation (Equation 2.2) [45] (Figure 2.9). The contact angle ranges from 0 °(completely spreading) to 180 °(completely nonspreading).

$$\gamma_{LV} \cos\theta_e = \gamma_{SV} - \gamma_{SL} \tag{2.2}$$

where γ_{SV} (mN/m), γ_{LV} (mN/m) and γ_{SL} (mN/m) are the solid-vapor, liquid-vapor and solid-liquid interfacial tensions respectively.

For the static case, the work of adhesion (W) can be expressed in terms of the surface tension [46] and equals the change in free energy of the system,

$$W = \gamma_{SV} + \gamma_{LV} - \gamma_{SL}, \tag{2.3}$$

Substituting equation (2.2) into (2.3), the work of adhesion (W) can be obtained as a function of the contact angle [47]:

$$W(\theta) = \gamma_{LV} (1 + \cos\theta), \tag{2.4}$$

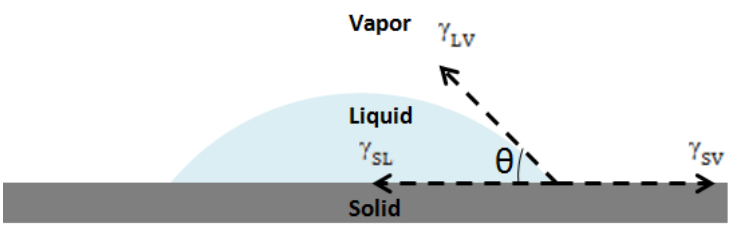

Figure 2.9 Pictorial representation of Young's equation.

However, Young's equation has been the subject of much controversy [48]. It is necessary to note that Young's equation has limitations in describing the contact angle of liquids due to the non-ideal nature of surfaces, even though this equation is well established thermodynamically. Young's equation is not valid unless the following assumptions are satisfied for surfaces [49]:

- The surface should be ideal, smooth and homogenous.
- The surface should be physically and chemically inert to the liquid and sufficiently hydrophobic to produce an apparent contact angle to be accurately measured.
- The line tension contribution can be neglected.
- All interfacial tensions are unchanged.

Based on Young's equation, the wettability of an ideal certain solid flat surface is fixed, since the three thermodynamic parameters γ_{SV}, γ_{LV} and γ_{SL} can give a unique contact angle. However, due to the existence of many metastable states of a droplet of liquid on a solid surface, observed contact angles are usually not equivalent to the Young contact angle. The static/equilibrium contact angle is not adequate to describe the wetting behaviour in some cases. On a non-ideal surface, the contact angle formed by expanding the liquids would be different from that generated by contracting the liquid. These two contact angles under unsteady status are called dynamic contact angles. (Figure 2.10) The former is termed the advancing contact angle; and the latter is called the receding contact angle. They represent the maximum and minimum contact angles when the advancing and receding contact lines respectively begin to move. The difference between the advancing contact angle (θ_A) and receding contact angle (θ_R) is termed the contact angle hysteresis [50].

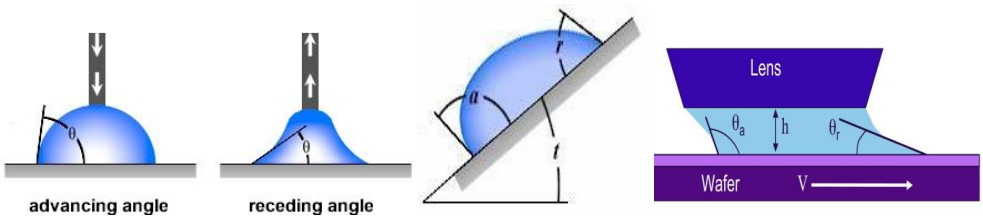

(a) (b) (c)

Figure 2.10 (a) Advancing and receding contact angles induced by the drop method; (b) advancing and receding contact angles captured by the tilting base method; (c) dynamic contact angles of the water meniscus in the exposure head.

2.3.2.2 Modified Young's Equation

The classic Young's equation shows that the contact angle of a liquid drop does not depend on drop size. Nevertheless, the significant size dependence of the contact angle has been extensively observed and studied for various solid surfaces in experiments [51-59]. The effect of three-phase line tension is considered influencing the key factor for the dependence of contact angle on drop size. The line tension is defined as the free energy per unit length of the contact line between three coexisting phases [55]. A modified Young's equation predicts a size-dependent contact angle [55]:

$$\gamma_{lv} \cos\theta + \sigma\kappa_{gs} = \gamma_{sv} - \gamma_{sl} \tag{2.5}$$

where σ is the line tension (mN/m), and κ_{gs} is the geodesic curvature of the

three-phase contact line, which equals the reciprocal of the three-phase contact line circle radius (R) (m). When R is infinite, the modified Young's equation could be reduced to the classic Young's equation:

$$\gamma_{lv}\cos\theta_{\infty} = \gamma_{sv} - \gamma_{sl} \tag{2.6}$$

Combing equations (2.5) and (2.6):

$$\cos\theta = \cos\theta_{\infty} - \frac{\sigma}{\gamma_{lv}}\frac{1}{R} \tag{2.7}$$

It is clear that the contact angle is relevant to the three-phase contact size from this modified Young's equation (Equation 2.7). A lot of studies have considered contact angle dependence on drop size by determining the effect of three-phase line tension [51-57]. All of these studies suggest that the contact angle of a liquid does significantly depend on the system size due to the line tension effect. In general, the contact angle increases as the drop size decreases (Figure 2.11). In addition, Kaveh et al. also observed a strong dependence of CO_2-water static contact angle on bubble size [60]. However, they observed that the effect of bubble radius on contact angle became insignificant as the bubble size became small [60].

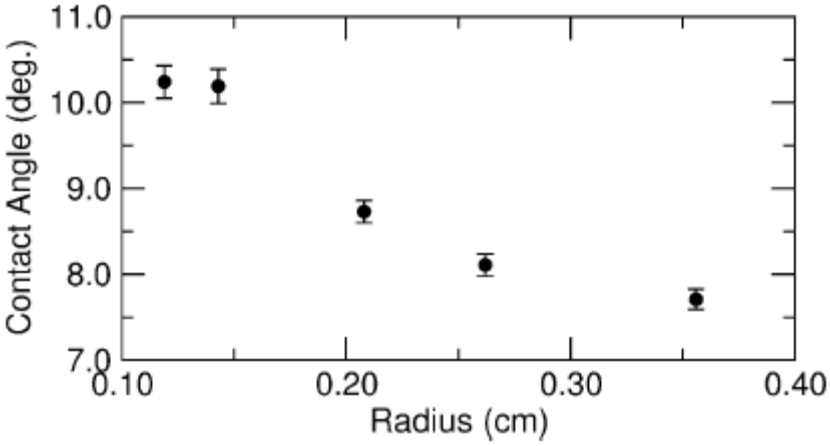

(a)

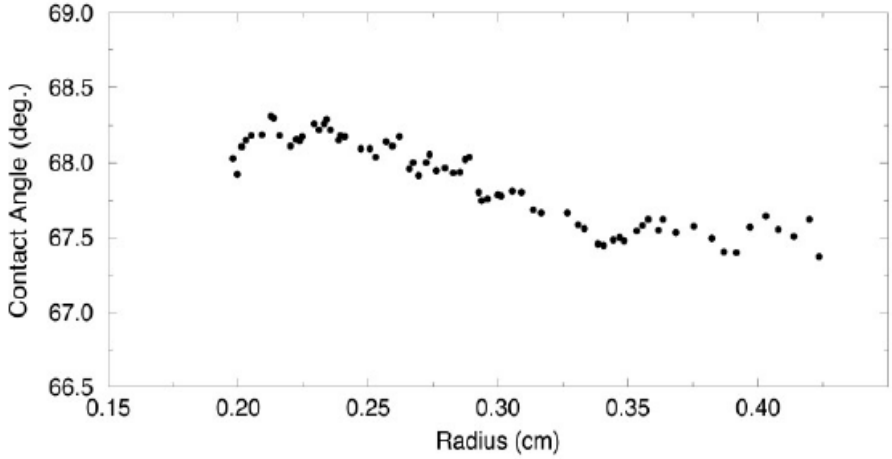

(b)

Figure 2.11 Drop size dependence of (a) octane contact angles [52] and (b) organic contact angles [53] on self-assembled monolayer (SAM) surface

2.3.2.3 Spreading Coefficient

The spreading coefficient (S) is defined as [61]:

$$S = \gamma_{sv}-(\gamma_{lv}+\gamma_{sl})= \gamma_{lv}(\cos\theta -1)$$

$$=W_{SL}^{adh} - W_{LL}^{coh} \quad (2.8)$$

This parameter can be used to predict whether or not a droplet will spread on a surface. If S≥0, the work of solid-liquid adhesion (W_{SL}^{adh}) is larger than liquid cohesion(W_{LL}^{coh}), and thus spreading or complete wetting occurs. On the other hand, if the spreading coefficient (S) is negative, then adhesion is smaller than cohesion. The liquid would partially spread on the surface and give a finite contact angle at equilibrium.

2.3.2.4 Equilibrium Spreading Pressure

When some liquids spread on a solid substrate, the intrinsic solid surface energy (γ_S) would be reduced due to vapor adsorption. The theoretical explanation for this phenomenon is termed equilibrium spreading pressure or film pressure, π_e. Thus, Young's equation can be re-expressed as:

$$\gamma_S = \gamma_{LV}\cos\theta + \gamma_{SL} + \pi_e \tag{2.9}$$

where $\pi_e = \gamma_S - \gamma_{SV}$.

On a low-energy surface, the insignificant vapor adsorption leads to negligible spreading pressure (π_e) [62, 63]. Wu proposed that the spreading pressure can be neglected on a low-energy surface when the contact angle is over 10°[64]. Yildirim and Fowkes et al. demonstrated experimentally that the vapors of water and other high-energy liquids cannot be adsorbed onto low-energy surfaces [65, 66].

On the other hand, the vapor of some low-energy liquids can be adsorbed onto some

high-energy surfaces, such as mica, metal and glass surfaces. The vapor adsorption may turn a high-energy surface into a low-energy one. Thus, low-surface-tension liquids can form large contact angles under their own saturated vapor instead of complete spreading [67, 68]. Zisman and co-workers noted that some amphiphilic organic compounds with low surface tension did not completely spread on high-energy solid surfaces [69, 70]. An oriented monolayer of amphiphilic molecules forms on the high-energy solid surface because of the sufficiently strong surface interaction between the solid surface and the liquid molecules. This leads to the incomplete spreading of the amphiphilic liquid on its own monolayers, which is called autophobing [70, 71]. Luckham and Matar observed that a surfactant adsorbed onto a solid-liquid interface rendered the initially hydrophilic substrate hydrophobic, which causes unstable droplet spreading, dewetting and retraction [72-75]. Sharma et al. investigated the mechanism of autophobing in pure amphiphilic organics and amphiphilic solutions on high-energy liquid subphases [76]. Kumar et al. stated that the surfactant reduced the local solid-vapor surface tension, increased the contact angle, and then caused unusual wetting conditions on a hydrophilic surface [77]. This is due to the autophobic effect [77].

2.3.3 Dynamic Wetting

Dynamic wetting on a smooth surface is characterized by a dynamic three-phase moving contact line [78] and is mainly measured by the spreading of liquids onto flat solid substrates. For instance, Bayer and Megaridis measured dynamic contact angles during the spontaneous spreading and recoiling of water droplets on planar substrates with different wetting conditions [79]. Keller et al. used the Wihelmy plate technique to measure the dynamic contact angles of petroleum hydrocarbons at various advancing velocities [80]. Previous studies on flat surfaces have indicated that

dynamic contact angle depends on the velocity of the solid-liquid-gas contact line, and varies with drop volume, viscosity, surfactant concentration, flow geometry, fluid composition and solid surface properties [81-86].

The dynamic wetting of liquids can be described by several hydrodynamic theories, such as those proposed by Cox [87], Voinov [88] and Dussan [89]. Combined models have also been developed by Petrov et al. to describe the contact line motion of spreading liquids [90]. According to the hydrodynamic model, the spreading process is dominated by the driving force per unit triple line length ($F \sim \gamma(\cos\theta_s - \cos\theta_d)$) and viscous dissipation (η). The Cox-Voinov equation is a simple description of contact line motion and the driving force as the deviation of the contact angle from equilibrium):

$$v = \frac{\gamma}{9\eta \ln\left(\frac{\ell}{a}\right)}(\theta_d^3 - \theta_s^3) \tag{2.7}$$

where θ_d is the dynamic contact angle, θ_s is the static (equilibrium) contact angle, η is the liquid viscosity (Pa s), γ is the liquid-vapor surface tension (mN/m), and $\frac{\ell}{a}$ is the ratio of macroscopic to microscopic length scales.

Brochart-Wyart and de Gennes derived an equivalent expression by considering spreading as an irreversible process and calculating the energy dissipation per length of unit line [91]. The velocity of the contact line is then given by:

$$v = \frac{\theta\gamma}{6\eta \ln\left(\frac{\ell}{a}\right)}(\cos\theta_s - \cos\theta_d) \tag{2.8}$$

Blake developed a molecular-kinetic theory of the three-phase moving line [92] based on Eyring's activated-rate theory [93] with an adsorption/desorption model.

The imbibition rate or penetration velocity is given by:

$$v = \frac{dL}{dt} = 2\kappa_0\, \lambda \sinh\left[\frac{\gamma(\cos\theta_s - \cos\theta_d)}{2nk_BT}\right] \quad (2.9)$$

where κ_0 is the frequency of molecular displacement (s^{-1}), which is related to the natural molar activation free energy of wetting ($\kappa_0 = \left(\frac{k_BT}{h}\right)\exp\left(\frac{-\Delta G_W^*}{Nk_BT}\right)$, where ΔG_W^* is activation free energy of wetting (J), T is temperature (K), h is Planck constant (h = 6.626 $\times 10^{-34}$ J s), N is Avogadro constant (N = 6.022 $\times 10^{-23}$) , k_B denotes the Boltzmann constant (k_B = 1.381$\times 10^{-23}$ J K^{-1})). n denotes the number of adsorption sites per unit area ($n^{-1}=\lambda^2$) (m^{-2}), λ is the average length of each molecular displacement (m). The term $\gamma(\cos\theta_s - \cos\theta_d)$ can be regarded as the nonequilibrated surface tension force needed to drive the motion of the wetting line.

The effects of viscosity and interfacial tension can be basically reflected in molecular-kinetic theory [93] and hydrodynamic theories [87-89], so that any increase in bulk viscosity or a decrease in interfacial tension leads to a decrease in contact line velocity.

A number of empirical correlations [94-96] and semi-empirical correlations [97-99] have been proposed to predict the dynamic contact angle (θ_d) by using the static contact angle (θ_s) and the capillary number (Ca). The capillary number (Ca) is defined as the ratio of viscous forces to interfacial forces:

$$Ca = \frac{v\eta}{\gamma} \quad (2.10)$$

where v is the interface velocity (m/s), η is the liquid viscosity (Pa s) and γ is the liquid-vapor surface tension (mN/m).

For instance, Jiang et al. presented an empirical correlation to describe the dependence of dynamic contact angle on capillary number (Ca) and static contact angle (θ_s) based on Hoffman's data through a study of the spreading of non-polar liquids [94]. Bracke et al. proposed a similar empirical correlation by drawing polymer strips into liquid [95]. Because Ca and θ_s can be easily measured, the correlations from Jiang et al. and Bracke et al. can be applied to most three-phase dynamic wetting phenomena when the capillary number is less than 0.01 [94, 95]. Seebergh and Berg examined the dynamic contact angle at a low capillary number regime via force measurements using a dynamic microtensiometer [96]. The correlation proposed by Seebergh and Berg is a function of contact-line velocity, and have the same functional form as the correlations from Jiang et al. and Bracke et al. at low capillary numbers, but with different constants (A, B) [94-96]:

$$\frac{\cos\theta_s - \cos\theta_d}{\cos\theta_s + 1} = \mathrm{ACa}^{\mathrm{B}} \tag{2.11}$$

where θ_s and θ_d are static and dynamic contact angles, and A and B are correlation constants.

2.3.4 Pore Wetting

It is well known that pore wetting is of significance in many practical processes, such as fuel cells, nanofluidics, nanolubrication, CO_2 storage and oil recovery. Due to the difficulty of directly measuring the contact angle in a small pore, and the common assumption that the external flat surface represents the internal surface of the pore [100], the pore contact angle has simply been estimated by either using the contact angle measured on a flat surface by a sessile drop experiment [7, 101-103], or

indirect measurements such as the capillary rise technique, liquid intrusion calorimetry, thin-layer wicking technique, or distance-time and weight-time imbibition techniques based on the Young-Laplace and Lucas-Washburn equations [104-109]. For example, Gomez et al. determined the contact angle of a nonwetting liquid within a mesoporous solid using a microcalorimetric method [106]. Xue et al. and Galet et al. estimated the contact angles of liquids in capillary tubes and the wettability of powders by the relationship between the liquid front height and time based on the modified Lucas-Washburn equation using a capillary rise method [105, 109]. Yang et al. and Ishakoglu and Baytas estimated the contact angle in porous media by measuring the contact angle on spherical surfaces [44, 110].

In many studies, the pore contact angle is oversimplified and simply treated as zero. For example, Popescu et al. applied an equilibrium contact angle of zero not only to a complete wetting case in a number of theoretical and empirical expressions for dynamic contact angle in the water/glass capillary rise, but also to the silicone oil/glass capillary rise [111]. Siebold et al. treated alkanes in capillary rise as total wetting liquids in order to assume their contact angles on silica or glass as zero at equilibrium [112]. Xue et al. stressed that a common way to solve the problem is by using a perfect liquid ($\theta_e=0^0$), but that a perfect wetting liquid is hard to find in practice [109]. Fisher and Lark experimentally studied capillary rise using the Washburn equation and concluded that the capillary rise plotted by assuming pore contact angle of zero was significantly different from their experimental data for water rising in a glass capillary [113]. Thus, it is necessary to measure and study the contact angle in pores to correctly indicate the pore wetting and avoid the use of inappropriate contact angles for the case of a porous surface case.

In most dynamic contact angle studies, the Lucas-Washburn equation is used to calculate the contact angle in a pore by using the measured capillary imbibition

distance and imbibition time [104, 109, 112, 114], but the contact angle calculated from the Lucas-Washburn equation is static. To describe the imbibition dynamics, Joos et al. used a velocity-dependent contact angle (θ_v) which was derived from an empirical expression to replace the static contact angle (θ_s) in the classic Lucas-Washburn equation [115]. Martic et al. modified the classic Lucas-Washburn equation by using Blake's molecular-kinetic theory [114]. Girardo et al. used the molecular-kinetic model to describe the microcapillary imbibition dynamics considering the effect of friction on the three-phase moving line, and the modeling results matched the experimental data well [116]. Stukan et al. investigated the effect of roughness on the spontaneous imbibition of liquid in nanopores using molecular dynamics simulation, and used Blake's molecular-kinetic theory to describe the effect of dynamic contact angle on liquid imbibitions [117].

Because of the lack of experimental techniques to measure the contact angle in a small pore, most experimental or theoretical studies on pore wetting have been based on the data measured from a planar solid plate, strip or cylindrical rod rather than in pores [96]. All these previous studies for the estimation of wetting in porous media might be valid but need to be further assessed and confirmed [106].

2.3.5 Interfacial Phenomena in a CO_2-fluid-mineral System

2.3.5.1 CO_2-water/brine Interfacial Tension

Safe and permanent CO_2 geological storage has become one of the most promising technologies which could potentially control greenhouse gas emission. The efficiency and safety of this process depend on fluid-fluid and rock-fluid interactions inside porous media. For example, the final storage capacity and total amount of

capillary/structural-trapped CO_2 in the porous reservoir are highly controlled and affected by the interfacial tension (γ) and contact angle (θ) in pores in CO_2-fluid-rock mineral surface system [118].

CO_2 injection pressure and storage capacity could be significantly affected if the rock wettability changes or the CO_2-fluid interaction phenomenon alters during CO_2 storage. Thus, accurate measurements of the interface tension and contact angle between CO_2 and reservoir fluids in a pore can greatly contribute to the estimation of reservoir storage capacity, and the capillary-sealing efficiency of cap rock [118, 119]. The surface tension of CO_2 in reservoir fluids under various reservoir conditions has been investigated by considering the effects of CO_2 phase, brine composition, pressure and temperature [34, 35, 119-125]. Consistent observations have been obtained in most of these studies, as shown in Figure 2.12.

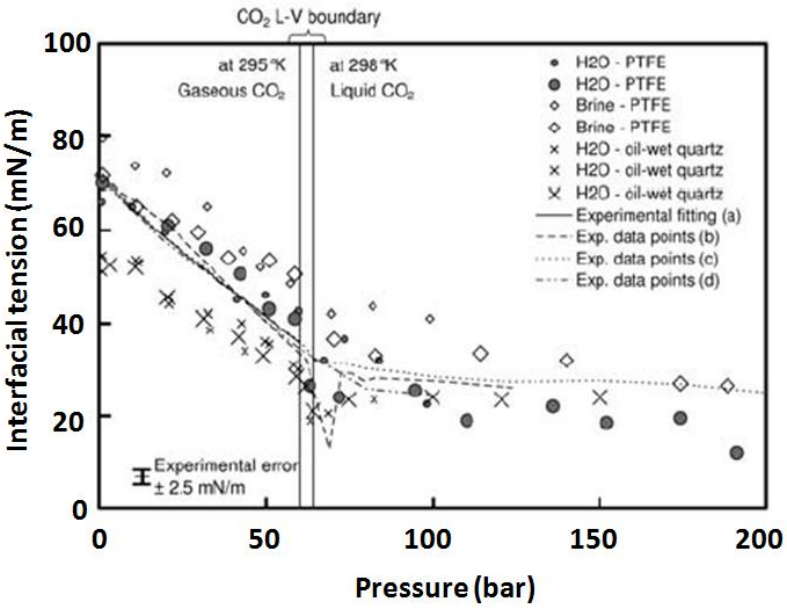

(a)

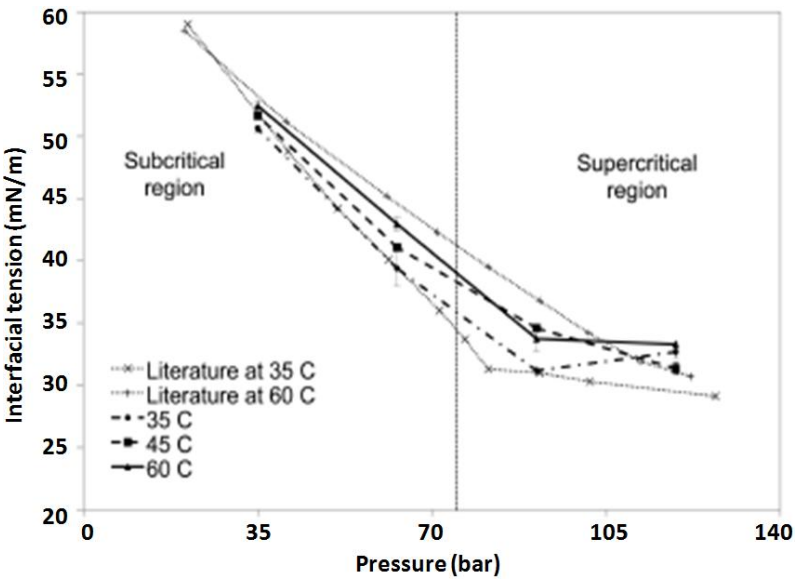

(b)

Figure 2.12 (a) Interfacial tension between water/brine and gas/liquid CO_2 at ambient temperature (20 ℃) [35, 121, 123, 126, 127]; (b) interfacial tension between water and gas/supercritical CO_2 at elevated temperatures [119, 120]

2.3.5.2 CO_2-water/brine Contact Angle

The CO_2-water/brine contact angle on a mineral surface has been a subject of

controversy [119]. Some studies state that there is no dependence of the wetting of the substrate on the CO_2 phase change or pressure [34, 128]. Chalbaud et al. emphasized that CO_2 did not affect the wetting of a solid surface when increasing pressure up to 100 bar using glass micromodels for water-CO_2 systems [34]. They observed no wetting transition phenomena with the increasing pressure, elevated temperature or CO_2 phase change, as shown in Figure 2.13. This is consistent with the wettability indices deduced by Egermann et al.[129] when performing CO_2 injection in carbonate samples. Bikkina also observed no clear CO_2-water contact angle trends with pressure (200-3000 psi) or temperature (25-50 ℃) on quartz and calcite substrate surfaces (Figure 2.14) [128]. A more recent study by Kaveh et al. also demonstrated no significant effects of pressure and CO_2 phase on the contact angle of a CO_2-water-sandstone system, and a strong dependence of contact angle on bubble size [60].

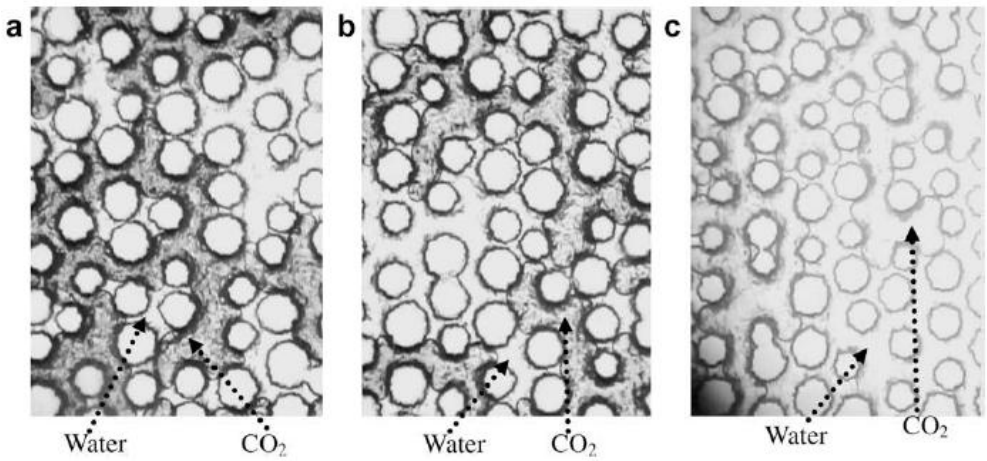

Figure 2.13 Glass micromodel: (a) gaseous CO_2 (P = 57.9 bars, T = 20 ℃), (b) supercritical CO_2 (P = 105.4 bars, T = 60 ℃), (c) liquid CO_2 (P = 100 bars, T = 23 ℃). [129]

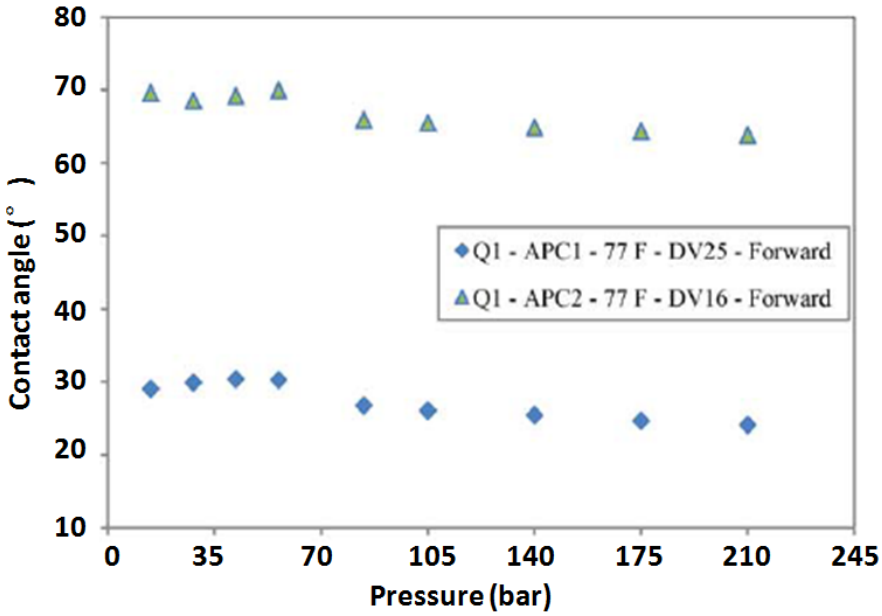

Figure 2.14 CO_2-water contact angle data on quartz substrate during first and second measurement cycles [128]

On the other hand, other studies have proposed that the CO_2 phase or pressure does affect surface wetting conditions. Some of them suggest that the wettability of a mineral surface was only altered in the CO_2 phase transition zone and that there is no significant pressure effect on contact angle when there is no phase change [35, 119, 130]. For instance, Espinoza and Santamarina found that the CO_2-water contact angle steeply increased at the CO_2 gas-liquid boundary when conducting sessile drop experiments were conducted on PTFE (polytetrafluoroethylene) in the pressure range 0−200 bar at ambient temperature (Figure 2.15). Jung and Wan observed that the static contact angle increased only at a narrow pressure range around the CO_2 phase transition region [130]. Chi et al. found that the water contact angle on the coal surface increased from 84° to 145° as the CO_2 changed from gas to liquid [131]. However, others have reported a gradual variation in contact angle with changes in pressure in both a particular CO_2 phase and phase transition zones [132-138]. For example, Sutjiadi-Sia et al. observed that the gas CO_2-water contact angle increased gradually with increasing pressure on PTFE, stainless steel and glass surfaces, but

this dependence of wetting on pressure was negligible for a supercritical CO_2-water system [123].

Ameri et al. investigated CO_2-water/brine contact angles on oil-wet and water-wet sandstone rock substrates [132]. They observed that the stable CO_2-water/brine contact angle on a water-wet substrate remained nearly constant with pressure or CO_2 phase change, but the contact angle on an oil-wet substrate significantly increased around the critical CO_2 state [132], as shown in Figure 2.16. Due to the observed discrepancies in the literature, it is necessary to work on this further.

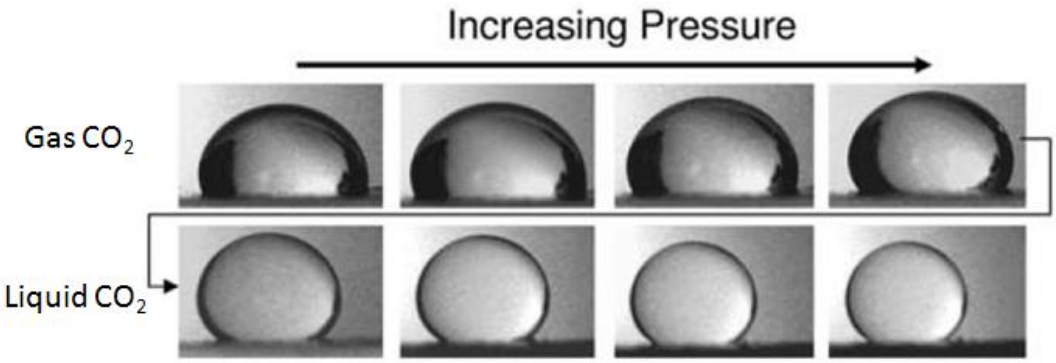

Figure 2.15 CO_2-water contact angles on a PTFE substrate as CO_2 pressure increases from 0.1 to 18.5 MPa [35]

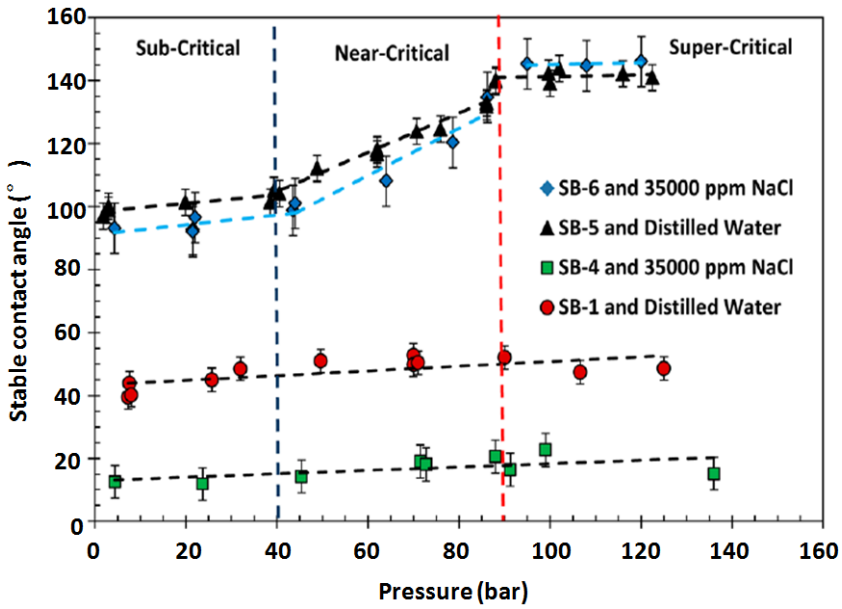

Figure 2.16 Stable CO_2-water/brine contact angles for the effectively oil-wet rock (saturated and aged with crude B, SB-5 and SB-6) and partially water-wet rock (saturated and aged with crude A, SB-1 and SB-4) substrates at various pressures [132]

Some studies have tried to explain the changes or lack of change in contact angle at various CO_2 pressures by considering Young's equation ($\gamma_{wc} \cos\theta = \gamma_{sc} - \gamma_{sw}$) [35, 130], where θ is the contact angle, γ_{wc} is the interfacial tension (IFT) between water and CO_2, γ_{sc} is the interfacial tension (IFT) between the solid and CO_2, and γ_{sw} is the interfacial tension (IFT) between solid and water. Among these three interfacial tensions only γ_{wc} can be determined by experiment. Furthermore, the interpretation of interfacial force balances using Young's equation still remains controversial because γ_{sc} and γ_{sw} cannot be directly measured [139]. In addition, CO_2 is not an ideal gas, so more consideration needs to be given to Young's theory for CO_2-water systems.[133]

In addition to wettability studies of CO_2-water systems, CO_2-brine contact angles have also been investigated in several studies. It has been reported that the significant contact angle increases with brine concentration on hydrophilic surfaces [35, 130, 140]. For instance, Kim et al. studied the pore-scale wettability of supercritical

CO_2-brine systems in silica micro-models, considering the effect of NaCl concentration in brine. They observed that the CO_2-brine contact angle significantly increases with increasing ionic strength increase (Figure 2.17). Sghaier et al. proved that the contact angle of an NaCl aqueous solution in air significantly increased with NaCl concentration on hydrophilic surfaces, but the variation in contact angle was much less marked on hydrophobic surfaces [141].

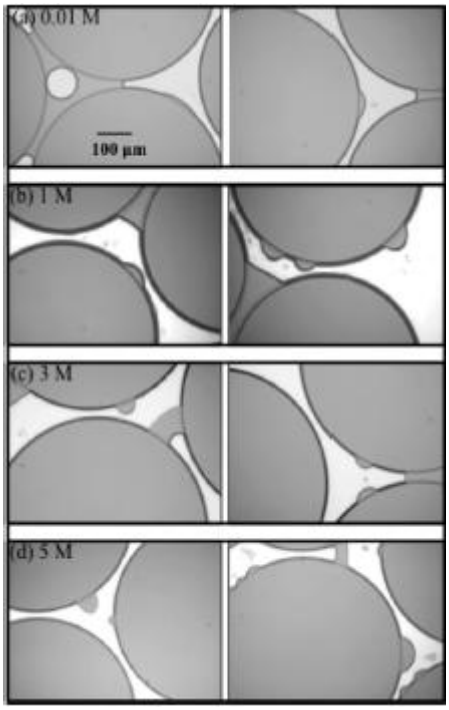

Figure 2.17 Effect of brine concentration on CO_2-brine wetting [140]

2.4 Multiphase Flow in Porous Media

2.4.1 Capillary Pressure

Depleted oil reservoirs or saline aquifers geologically store immiscible reservoir fluids, such as oil (hydrocarbons), water (brines) and gas (air, CO_2 and natural gas). The forces keeping these multiphase fluids in equilibrium in porous-structured reservoirs are commonly recognized as capillary forces. In CO_2 storage and enhanced oil recovery (EOR) processes, capillary force plays a dominant role in multiphase flow behaviours and fluid displacement, controlling the phase distribution in porous media [142].

Capillary pressure is generally defined as the difference in pressure across the interface between two kinds of immiscible fluids. Capillary pressure then refers to the pressure difference between non-wetting and wetting phases (Figure 2.18):

$$P_c = P_{nw} - P_w \tag{2.12}$$

where P_c is capillary pressure (Pa), P_{nw} is the pressure in the non-wetting phase (Pa) and P_w is the pressure in the wetting phase (Pa).

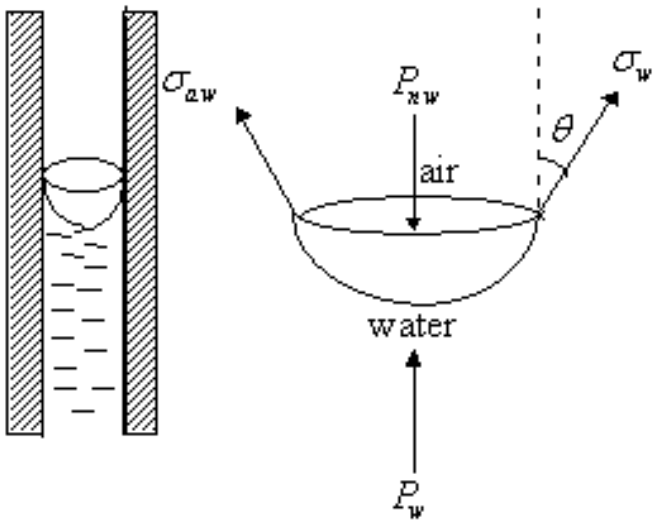

Figure 2.18 Illustration of capillary pressure: water rise in a capillary (water is a wetting fluid, air is a non-wetting fluid) [143]

The interfacial tension existing between the two immiscible fluids leads to capillary pressure. The Young-Laplace equation (Equation 2.13) shows that capillary pressure (pressure difference) is inversely proportional to the effective radius and proportional to the surface tension, and is also related to the wetting contact angle [45, 144].

$$P_c = \frac{2\gamma\cos\theta}{r} \tag{2.13}$$

where P_c is capillary pressure (Pa), γ is surface tension (mN/m), θ is the contact angle on the surface of the capillary and r is the effective radius (m).

This equation is also called the breakthrough pressure equation for the estimation of the CO_2 sealing capacity of a cap rock. From this equation, a high sealing capacity for gas or oil in a reservoir can be achieved for large interface tension, small contact angle and extremely small pore size.

2.4.2 Two-phase Flow Displacement in Porous Media

2.4.2.1 Imbibition and Drainage

The displacement processes in porous media can be generally categorized in two types, which are drainage and imbibition, based on the wetting properties of the fluids. When a single capillary or porous rock is saturated with 100% of a non-wetting fluid like gas or oil, and a wetting fluid (such as water) is introduced into the end, the wetting fluid will be spontaneously imbibed into the capillary to displace the non-wetting fluid by capillary force. This is called imbibition (Figure 2.19 (a)). Lucas and Washburn derived an analytical equation to describe the imbibition process of a liquid flow by its own capillary force in a horizontal cylindrical capillary [145, 146], and Bell first proposed the proportionality between l^2 and t [147]:

$$l^2 = \frac{\gamma r t \cos\theta}{2\eta} \tag{2.14}$$

where l is the distance (m) imbibed by the liquid at time t (s), η is the viscosity of the liquid (Pa s), r is the radius of the capillary (m), γ is the liquid-vapor interfacial tension (mN/m), and θ is the contact angle between the liquid and the capillary inner surface. The Lucas-Washburn equation was derived from Poiseuille's law for viscous flow by assuming that the pressure difference (ΔP) across the invading liquid meniscus can be given by the Young-Laplace equation [45, 144].

If the capillary or rock is fully filled with a wetting fluid (e.g. water), a non-wetting fluid (e.g. gas, oil) cannot spontaneously invade into the capillary pore or rock since the capillary force holds the wetting fluid in the pores. An external force must be introduced to overcome this capillary force, in order to use a wetting fluid to displace

a non-wetting fluid. This process is defined as drainage (Figure 2.19 (b)).

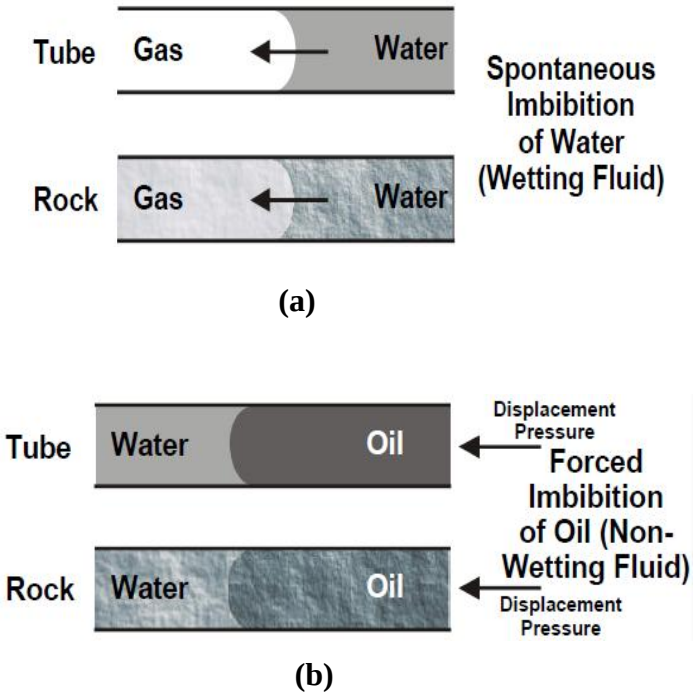

Figure 2.19 (a) Imbibition for water; (b) Drainage between oil and water in a single capillary and rock [36]

Capillary pressure is a very important parameter in both processes, and is generally expressed as a function of the saturation of the wetting-phase fluid in the porous medium. Figure 2.20 (1) gives a typical capillary pressure-saturation curve for oil invading a porous medium which is initially fully saturated with water. This is a primary drainage process, which refers to the decrease in water saturation. The capillary pressure (P_c) is defined as the pressure difference between oil (non-wetting, P_{nw}) and water (wetting, P_w). It is believed that it is difficult to penetrate oil until the capillary pressure reaches a critical pressure (P_0), which is also called the capillary entry pressure. This threshold pressure might be affected by the pore wetting and size and the porous structure of the pore sample. When the pressure exceeds the critical pressure (P_0), a plateau is reached. The capillary pressure slightly increases with decreasing water saturation during this plateau region.

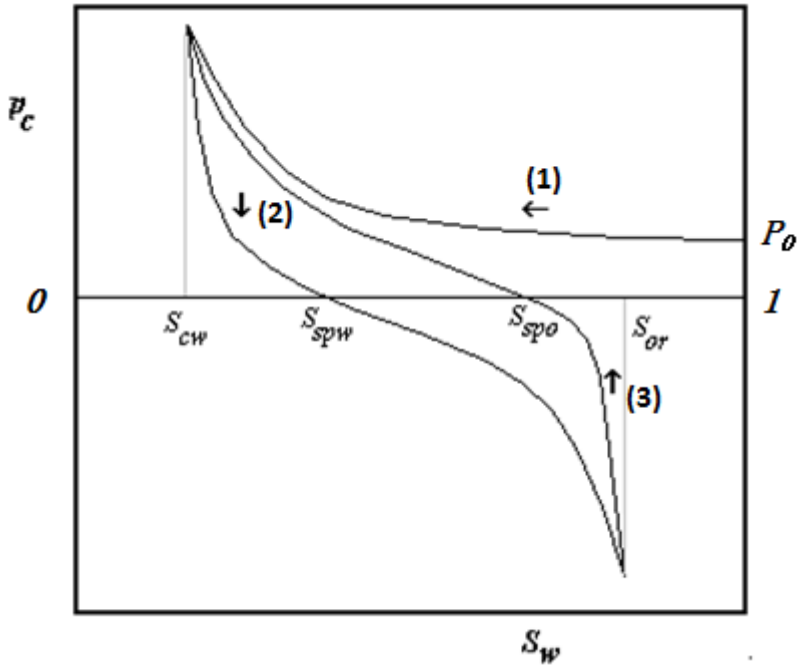

Figure 2.20 A typical capillary pressure-saturation curve for a non-wetting/wetting fluids (oil/water) displacement system. It can be assumed that water and oil are the wetting and non-wetting fluids respectively (P_c: capillary pressure, P_0: capillary entry pressure, S_w: water saturation, S_{cw}: residual water saturation, S_{spw}: spontaneous water imbibition saturation, S_{or}: residual oil saturation) [148]

As the water saturation decreases further, the capillary pressure rises significantly, and reaches very high levels as water saturation approaches an irreducible value of residual water saturation (S_{cw}). The direction of saturation can be reversed by imbibition, which is shown in Figure 2.20 (2). If the pressure of oil is reduced, the wetting fluid will be spontaneously imbibed to saturate the porous medium. This is called primary imbibitions, and it causes the capillary pressure to decrease, but it is smaller than the drainage capillary pressure at the same saturation. This is due to the capillary hysteresis effect. The capillary pressure decreases to zero when the oil pressure equals the water pressure. This saturation point is called spontaneous water imbibition saturation (S_{spw}). Beyond this point, additional force has to be applied for water to displace oil. The capillary pressure is hence negative. A very high

non-wetting fluid pressure is required to displace the next bit of non-wetting fluid until the saturation reaches the level of residual oil saturation (S_{or}). When the water pressure decreases, the non-wetting fluid will spontaneously invade into the porous media and the saturation decreases. This is defined as secondary drainage, which is shown in Figure 2.20 (3). The capillary pressure in secondary drainage is larger than that of primary imbibition for the same saturation due to capillary hysteresis. Spontaneous oil imbibition saturation (S_{spo}) is reached when P_c is zero. The oil pressure needs to be increased to overcome the water capillary pressure (forced drainage). The capillary pressure would rise infinitely at S_{cw}.

2.4.2.2 CO_2-fluid Displacement

CO_2-fluid displacements are crucial in predicting the CO_2 flow, mobility, capillary trapping and pressure distribution within reservoirs [18, 149, 150]. Some experimental studies of CO_2-fluids displacement in porous media are ongoing and results have recently become available. For instance, Plug and Bruining measured the imbibition and drainage behaviour of CO_2-water displacement in an unconsolidated sand system, proposing an increase of capillary pressure by reducing CO_2 pressure and observing significant capillary pressure fluctuations and instability in supercritical CO_2-water displacement (Figure 2.21) [151]. Tokunaga et al. measured the drainage and wetting behaviour of supercritical CO_2-brine and air-brine in a homogenous silica sand pack, and stressed that their results did not agree with the predictions [152]. Apart from conducting core flooding experiments, the CO_2 and fluid saturation and distribution in core rock under reservoir conditions have also been studied using a pore network micro model and high-resolution Magnetic Resonance Imaging (MRI), X-ray CT scanning techniques [153-157].

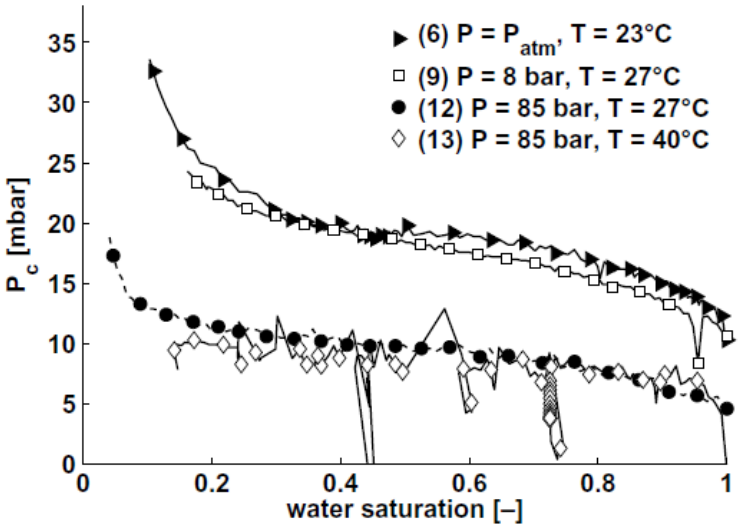

Figure 2.21 Drainage capillary pressure curves for CO_2-water displacements in coarse sand at various pressure and CO_2 phase conditions [151]

2.4.3 Permeability

A fluid moving through a porous medium can be described by Darcy's law, which forms the scientific basis of fluid permeability in earth sciences. Permeability (intrinsic permeability) is defined by the general form of Darcy's law:

$$q = -\frac{k}{\mu} \nabla P \tag{2.15}$$

where q is fluid velocity (m/s), μ is fluid viscosity (Pa s), ∇P is the pressure gradient vector (for a horizontal bed with length of L), $\nabla P = \Delta P/L$ and k is the intrinsic permeability of the medium (m^2 or D (darcy), 1D =1000 mD ≈10^{-12} m^2).

Relative permeability is defined as a dimensionless measure of the effective permeability of a certain phase in a multiphase flow in porous media. It is the ratio of

the effective permeability of this certain phase to the intrinsic permeability:

$$k_{r,i} = \frac{k_i}{k} \qquad i = 1, \dots, N_p \tag{2.16}$$

Thus, the equation (2.15) can be rearranged as

$$q_i = -\frac{k_{r,i}k}{\mu_i}\nabla P_i \tag{2.17}$$

The relative permeability of a fluid phase (i) is commonly described as a function of the saturation of that phase (S_i), $k_{r,i}=k_{r,i}(S_i)$. Models proposed by Brooks-Corey [158] and van Genuchten [159] have been extensively useful in characterizing the capillary pressure $P_c(S_w)$ and relative permeability $K_r(S_w)$ (Table 2.1).

Table 2.1 Brooks-Corey (BC) and van Genuchten (VG) capillary pressure models for wetting and nonwetting phase relative permeability

	Brooks-Corey (BC)[158]	***van Genuchten (VG)[159]***
Capillary pressure	$P_c = P_0 S_w^{*\,-1/\lambda}$	$P_c = P_0(S_w^{*\,-m} - 1)^{1-1/m}$
Relative permeability	$k_{r,w} = (S_w^*)^{3+2/\lambda}$ $k_{r,nw} = (1 - S_w^*)^2[1 - (S_w^*)^{1+\frac{2}{\lambda}}]$	$k_{r,w} = (S_w^*)^2\left\{1 - [1 - (S_w^*)^m]^{\frac{1}{m}}\right\}$ $k_{r,nw} = (1 - S_w^*)^2[1 - (S_w^*)^m]^{\frac{1}{m}}$

In Table 2.1, $k_{r,w}$ and $k_{r,nw}$ are the relative permeabilities of the wetting phase and non-wetting phase, respectively, the effective water saturation $S_w^* = \frac{S_w - S_{w,ir}}{1 - S_{w,ir}}$, $S_{w,ir}$ is the irreducible saturation, P_0 is capillary entry pressure, and λ is the so-called pore-size distribution index. P_0, λ and m are fitting parameters. These two models can be effectively applied to measure the relative permeability of multiphase flows in the petroleum and hydrology fields.

Figure 2.22 shows a typical set of wetting fluid and non-wetting fluid relative permeability curves in a porous media. As wetting-phase drainage starts and wetting-phase saturation decreases, the relative permeability of the wetting fluid (k_{rw}) decreases, while the relative permeability of the nonwetting fluid (k_{rnw}) increases. The wetting phase curve has a residual saturation (S_{wr}) of 0.2. Since the flow of each phase is inhibited by the other one, the sum of relative permeabilites is thus generally less than one.

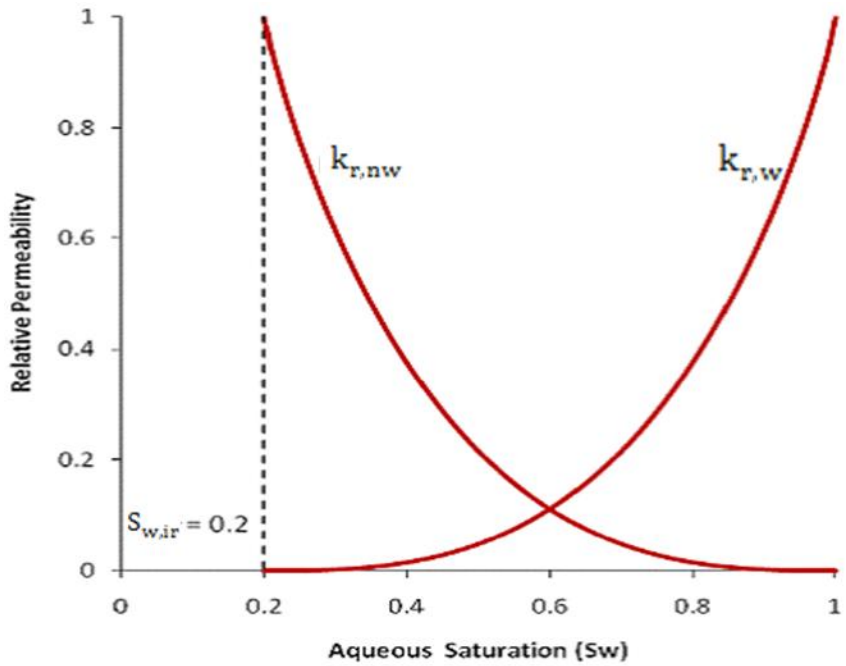

Figure 2.22 A two-phase water-oil relative permeability curve ($k_{r,w}$: wetting fluid relative permeability, $k_{r,nw}$: non-wetting fluid relative permeability, $S_{w,ir}$: residual water saturation)[160]

This chapter provides the relevant theoretical background and literature review for the chapter 3, 4, 5, 6, 7 and 8, such as concepts of contact angle, wetting, interfacial phenomenon, capillary actions, multiphase flow and displacement in porous media and related fundamental theoretical equations.

2.5 References

[1] Enhanced Oil Field Recovery Survey-Worldwide-EOR. Oil Gas J. 2010.

[2] Shedid SA. Influences of fracture orientation on oil recovery by water and polymer flooding processes: An experimental approach. Journal of Petroleum Science and Engineering. 2006;50:285-92.

[3] Moritis G. EOR Continues to Unlock Oil Resources. Oil Gas J. 2004;102:45-65.

[4] Moritis G. CO_2 injection gains momentum. Oil Gas J. 2006;104:37-57.

[5] Nobakht M, Moghadam S, Gu Y. Effects of Viscous and Capillary Forces on CO_2 Enhanced Oil Recovery under Reservoir Conditions. Energy & Fuels. 2007;21:3469-76.

[6] Kokal S, Al-Kaabi A. Enhanced oil recovery: challenges & opportunities. World Petroleum Council: Official Publication. 2010:64-9.

[7] Morrow NR. Wettability and Its Effect on Oil Recovery. J Pet Technol. 1990;42:1476-84.

[8] Rao DN. Fluid-fluid and solid-fluid interfacial interactions in petroleum reserviors. Pet Sci Technol. 2001;19:157-88.

[9] Stosur GJ. EOR: Past, Present and What the Next 25 Years May Bring. the SPE IOR Conference in Asia Pacific. Kuala Lumpur, Malaysia 2003.

[10] Stosur GJ, Hite JR, Carnahan NF. The Alphabet Soup of IOR, EOR and AOR: Effective Communication Requires a Definition of Terms. the SPE International IOR Conference in Asia Pacific. Kuala Lumpur, Malaysia 2003.

[11] Orr Jr. FM. Storage of carbon dioxide in geologic formations. J Pet Technol. 2004;56:90-7.

[12] Bruant RG, Celia MA, Guswa AJ, Peters CA. Safe storage of CO_2 in deep saline aquifiers. Environ Sci Technol. 2002;36:240-5.

[13] Li Z, Dong M, Li S, Huang S. CO_2 sequestration in depleted oil and gas reservoirs—caprock characterization and storage capacity. Energy Conversion

and Management. 2006;47:1372-82.

[14] Concept of CO_2 geological storage 2007 http://www.rite.or.jp/English/lab/geological/overview.html. Last Accessed Date: 06/12/2014

[15] Bandara UC, Tartakovsky AM, Palmer BJ. Pore-scale study of capillary trapping mechanism during CO_2 injection in geological formations. International Journal of Greenhouse Gas Control. 2011;5:1566-77.

[16] CO_2 storage mechanisms http://www.sosclima.org/5-argumentos-contra-la-captura-y-almacenamiento-de-carbono. Last Accessed Date: 06/12/2014

[17] Bachu S, Gunter WD, Perkins EH. Aquifer disposal of CO_2: Hydrodynamic and mineral trapping. Energy Conversion and Management. 1994;35:269-79.

[18] Bensons SM, Cole DR. CO_2 Sequestration in deep sedimentary formations. Elements. 2008;4:325-31.

[19] CO_2 Trapping Mechanisms 2008 http://www.co2captureproject.org/co2_trapping.html. Last Accessed Date: 06/12/2014

[20] Hesse MA, Orr Jr FM, Tchelepi HA. Gravity currents with residual trapping. Energy Procedia. 2009;1:3275-81.

[21] Kumar K, Dao E, Mohanty KK. AFM study of mineral wettability with reservoir oils. Journal of Colloid and Interface Science. 2005;289:206-17.

[22] Spiteri E, Juanes R, Blunt MJ, Orr FM. Relative-Permeability Hysteresis: Trapping Models and Application to Geological CO_2 Sequestration. Society of Petroleum Engineers, SPE-96448-MS; 2005

[23] Juanes R, Spiteri EJ, Orr FM, Blunt MJ. Impact of relative permeability hysteresis on geological CO_2 storage. Water Resources Research. 2006;42:W12418.

[24] Ennis-King JP, Paterson L. Role of Convective Mixing in the Long-Term

Storage of Carbon Dioxide in Deep Saline Formations, Society of Petroleum Engineers, SPE-84344-PA; 2005

[25] Riaz A, Hesse M, Tchelepi HA, Orr FM. Onset of convection in a gravitationally unstable diffusive boundary layer in porous media. Journal of Fluid Mechanics. 2006;548:87-111.

[26] Xu T, Apps JA, Pruess K. Reactive geochemical transport simulation to study mineral trapping for CO_2 disposal in deep arenaceous formations. Journal of Geophysical Research: Solid Earth. 2003;108:2071.

[27] Matter JM, Kelemen PB. Permanent storage of carbon dioxide in geological reservoirs by mineral carbonation. Nature Geosci. 2009;2:837-41.

[28] Gunter WD, Wiwehar B, Perkins EH. Aquifer disposal of CO_2-rich greenhouse gases: Extension of the time scale of experiment for CO2-sequestering reactions by geochemical modelling. Mineralogy and Petrology. 1997;59:121-40.

[29] Pruess K, Xu T, Apps J, Garcia J. Numerical Modeling of Aquifer Disposal of CO_2.

[30] Knauss KG, Johnson JW, Steefel CI. Evaluation of the impact of CO_2, co-contaminant gas, aqueous fluid and reservoir rock interactions on the geologic sequestration of CO2. Chemical Geology. 2005;217:339-50.

[31] Fighting climate change by turning CO_2 to stone .

[32] Arendt B, Dittmar D, Eggers R. Interaction of interfacial convection and mass transfer effects in the system CO_2–water. International Journal of Heat and Mass Transfer. 2004;47:3649-57.

[33] Arts R, Eiken O, Chadwick A, Zweigel P, van der Meer L, Zinszner B. Monitoring of CO_2 injected at Sleipner using time-lapse seismic data. Energy. 2004;29:1383-92.

[34] Chalbaud C, Robin M, Lombard JM, Martin F, Egermann P, Bertin H. Interfacial tension measurements and wettability evaluation for geological

CO_2 storage. Adv Water Resour. 2009;32:98-109.

[35] Espinoza DN, Santamarina JC. Water-CO_2-mineral systems: Interfacial tension, contact angle, and diffusion—Implications to CO_2 geological storage. Water Resour Res. 2010;46:W07537.

[36] Glover P. Fluid Saturation and Capillary Pressure. Department of Geology and Petroleum Geology, University of Aberdeen. p. 43.

[37] Holly FJ. Wetting, Spreading and Adhesion. New York: American Press; 1978.

[38] Huaung ST, Kammermeyer K. Membranes in Separation. New York: Wiley; 1975.

[39] Voyutsky S. Colloid Chemistry: Central Books Ltd; 1978.

[40] Wooding RA, Morel-Seytoux HJ. Multiphase Fluid Flow Through Porous Media. Annu Rev Fluid Mech. 1976;8:233-74.

[41] Mittal KL. Contact Angle, Wettability and Adhesion. Utrecht: VSP; 1993.

[42] Chen XX, Gao J, Song B, Smet M, Zhang X. Stimuli-responsive wettability of nonplanar substrates: pH controlled floatation and supporting force. Langmuir. 2010;26:104.

[43] Padday JF. Wetting, Spreading and Adhesion. New York: Academic Press; 1978.

[44] Yang Y-W, Zografi G, Miller EE. Capillary Flow Phenomena and Wettability in Porous Media: I. Static Characteristics. J Colloid Interface Sci. 1988;122:24-34.

[45] Young T. An Essay on the Cohesion of Fluids. Phil Trans Roy SocLond. 1805;95:65-87.

[46] Adamson AW. Physical Chemistry of Surfaces,. 3rd ed. New York: Wiley; 1976.

[47] Tenan MA, Hackwood S, Beni G. Friction in capillary systems. Journal of Applied Physics. 1982;53:6687-92.

[48] Marmur A. Equilibrium and spreading of liquids on solid surfaces. Advances in Colloid and Interface Science. 1983;19:75-102.

[49] Spelt JK, Li D, Neumann AW. The Equation of State Approach to Interfacial Tensions. In: Schrader M, Loeb G, editors. Modern Approaches to Wettability: Springer US; 1992. p. 101-42.

[50] Gong M-G, Liu Y-Y, Xu X-L. A new model for the formation of contact angle and contact angle hysteresis. Chinese Physics B. 2010;19.

[51] Amirfazli A, Chatain D, Neumann AW. Drop size dependence of contact angles for liquid tin on silica surface: line tension and its correlation with solid–liquid interfacial tension. Colloids and Surfaces A: Physicochemical and Engineering Aspects. 1998;142:183-8.

[52] Amirfazli A, Keshavarz A, Zhang L, Neumann AW. Determination of line tension for systems near wetting. Journal of Colloid and Interface Science. 2003;265:152-60.

[53] Amirfazli A, Kwok DY, Gaydos J, Neumann AW. Line Tension Measurements through Drop Size Dependence of Contact Angle. Journal of Colloid and Interface Science. 1998;205:1-11.

[54] Amirfazli A, Neumann AW. Status of the three-phase line tension: a review. Advances in Colloid and Interface Science. 2004;110:121-41.

[55] Duncan D, Li D, Gaydos J, Neumann AW. Correlation of Line Tension and Solid-Liquid Interfacial Tension from the Measurement of Drop Size Dependence of Contact Angles. Journal of Colloid and Interface Science. 1995;169:256-61.

[56] Gaydos J, Neumann AW. The dependence of contact angles on drop size and line tension. Journal of Colloid and Interface Science. 1987;120:76-86.

[57] David R, Park MK, Kalantarian A, Neumann AW. Drop size dependence of contact angle on two fluoropolymers. Colloid Polym Sci. 2009;287:1167-73.

[58] Lin FYH, Li D, Neumann AW. Effect of Surface Roughness on the

Dependence of Contact Angles on Drop Size. J Colloid Interface Sci. 1993;159:86-95.

[59] Dredich J, Miller JD, Huplca J. The Effect of Drop Size on Contact Angle over a Wide Range of Drop Volumes. J Colloid Interface Sci. 1993;155:379-85.

[60] Kaveh NS, Rudolph ESJ, van Hemert P, Rossen WR, Wolf KH. Wettability Evaluation of a CO2/Water/Bentheimer Sandstone System: Contact Angle, Dissolution, and Bubble Size. Energy & Fuels. 2014;28:4002-20.

[61] de Gennes PG. Wetting statics and dynamics. Rev Mod Phys. 1985;57:827-63.

[62] Chaudhury MK. Short Range and Long-range Forces in Colloidal and Macroscopic Systems: UMI; 1984.

[63] Good RJ. Contact angle, wetting, and adhesion: a critical review. Journal of Adhesion Science and Technology. 1992;6:1269-302.

[64] Wu S. Interfacial Thermodynamics, in Polymer Interface and Adhesion. New York: Marcel Dekker; 1982.

[65] Yildirim I. Surface free energy characterization of powders: Virginia Polytechnic Institute and State University; 2001.

[66] Fowkes FM, McCarthy DC, Mostafa MA. Contact angles and the equilibrium spreading pressures of liquids on hydrophobic solids. Journal of Colloid and Interface Science. 1980;78:200-6.

[67] Bangham DH, Saweris Z. The Behaviour of Liquid Drops and Adsorbed Films at Cleavage Surfaces of Mica. Transactions of the Faraday Society. 1938;34:554-70.

[68] Hardy WB. The Spreading of Fluids on Glass. Philos Mag. 1919;38:49-55.

[69] Fox HW, Hare EF, Zisman WA. Wetting Properties of Organic Liquids on High Energy Surfaces. JPhysChem. 1955;59:1097-106.

[70] Hare EF, Zisman WA. Autophobic Liquids and the Properties of Their

Adsorbed Films. J Phys Chem. 1955;59:335-40.

[71] Zisman WA. Relation of the Equilibrium Contact Angle to Liquid and Solid Constitution. Contact Angle, Wettability, and Adhesion: American Chemical Society; 1964. p. 1-51.

[72] Afsar-Siddiqui AB, Luckham PF, Matar OK. Unstable Spreading of Aqueous Anionic Surfactant Solutions on Liquid Films. Part 1. Sparingly Soluble Surfactant. Langmuir. 2003;19:696-702.

[73] Afsar-Siddiqui AB, Luckham PF, Matar OK. Unstable Spreading of Aqueous Anionic Surfactant Solutions on Liquid Films. 2. Highly Soluble Surfactant. Langmuir. 2003;19:703-8.

[74] Afsar-Siddiqui AB, Luckham PF, Matar OK. Dewetting Behavior of Aqueous Cationic Surfactant Solutions on Liquid Films. Langmuir. 2004;20:7575-82.

[75] Craster RV, Matar OK. On Autophobing in Surfactant-Driven Thin Films. Langmuir. 2007;23:2588-601.

[76] Sharma R, Kalita R, Swanson ER, Corcoran TE, Garoff S, Przybycien TM, et al. Autophobing on Liquid Subphases Driven by the Interfacial Transport of Amphiphilic Molecules. Langmuir. 2012;28:15212-21.

[77] Kumar N, Varanasi K, Tilton RD, Garoff S. Surfactant Self-Assembly ahead of the Contact Line on a Hydrophobic Surface and Its Implications for Wetting. Langmuir. 2003;19:5366-73.

[78] Latva-Kokko M, Rothman DH. Static Contact Angle in Lattice Boltzmann Models of Immiscible Fluids. Phys Rev E. 2005;72:046701.

[79] Bayer IS, Megaridis CM. Contact angle dynamics in droplets impacting on flat surfaces with different wetting characteristics. J Fluid Mech. 2006;558:415-49.

[80] Keller AA, Broje V, Setty K. Effect of advancing velocity and fluid viscosity on the dynamic contact angle of petroleum hydrocarbons. J Pet Sci Technol 2007;58:201-6.

[81] Carré A, Eustache F. Dynamique d'étalement d'un liquide rhéofluidifiant. Comptes Rendus de l'Académie des Sciences - Series IIB - Mechanics-Physics-Chemistry-Astronomy. 1997;325:709-18.

[82] Carré A, Eustache F. Spreading Kinetics of Shear-Thinning Fluids in Wetting and Dewetting Modes. Langmuir. 2000;16:2936-41.

[83] Dezellus O, Hodaj F, Eustathopoulos N. Chemical reaction-limited spreading: the triple line velocity versus contact angle relation. Acta Materialia. 2002;50:4741-53.

[84] Min Q, Duan Y-Y, Wang X-D, Liang Z-P, Si C. Does macroscopic flow geometry influence wetting dynamic? J Colloid Interface Sci. 2011;362:221-7.

[85] Roques-Carmes T, Mathieu V, Gigante A. Experimental contribution to the understanding of the dynamics of spreading of Newtonian fluids: Effect of volume, viscosity and surfactant. J Colloid Interface Sci. 2010;344:180-97.

[86] Wang XD, Lee DJ, Peng XF, Lai JY. Spreading Dynamics and Dynamic Contact Angle of Non-Newtonian Fluids. Langmuir. 2007;23:8042-7.

[87] Cox RG. The dynamics of the spreading of liquids on a solid surface. Part 1. Viscous flow. J Fluid Mech. 1986;168:169-94.

[88] Voinov OV. Hydrodynamics of wetting. Fluid Dynamics (English Translation of Izvestiya Akademii Nauk SSSR, Mekhanika Zhidkosti i Gaza). 1976;11:714-21.

[89] Dussan VEB. On the difference between a bounding surface and a material surface. J Fluid Mech. 1976;75:609-23.

[90] Petrov PG, Petrov JG. A Combined Molecular-Hydrodynamic Approach to Wetting Kinetics. Langmuir. 1992;8:1762-7.

[91] Brochard-Wyart F, de Gennes PG. Dynamics of partial wetting. Advances in Colloid and Interface Science. 1992;39:1-11.

[92] Blake TD. Dynamic contact angles and wetting kinetics. in Wettability.

1993:251-309.

[93] Glasstone S, Laidler KJ, Eyring HJ. The theory of rate processes. 1941.

[94] Jiang TS, Oh SG, Slattery JC. Correlation for dynamic contact angle. J Colloid Interface Sci. 1979;69:74-7.

[95] Bracke M, De Voeght F, Joos P. The kinetics of wetting: the dynamic contact angle. Prog Colloid Polym Sci. 1989;79:142-9.

[96] Seebergh JE, Berg JC. Dynamic Wetting in the Low Capillary Number Regime. Chem Eng Sci 1992;47:4455-64.

[97] Ishimi K, Hikita H, Esmail MN. Dynamic contact angles on moving plates. AIChEJ. 1986;32:486-92.

[98] Rillaerts E, Joos P. The Dynamic contact angle. Chem Eng Sci. 1980;35:883-7.

[99] Ström G, Fredriksson M, Stenius P, Radoev B. Kinetics of steady-state wetting. J Colloid Interface Sci. 1990;134:107-16.

[100] Patro D, Bhattacharyya S, Jayaram V. Flow Kinetics in Porous Ceramics: Understanding with Non-Uniform Capillary Models. J Am Ceram Soc. 2007;90:3040-6.

[101] Anderson WG. Wettability Literature Survey. Part 2: Wettability Measurement. JPT (Nov 1986). 1986;38:1246-62.

[102] Buckley JS. Mechanisms and Consequences of Wettability Alteration by Crude Oils (dissertation) [PhD Thesis]: Edinburgh, Scotland; 1996.

[103] Kwok DY, Lin R, Mui M, Neumann AW. Low-rate Dynamic and Static Contact Angles and the Determination of Solid Surface Tensions. Colloids and Surf A: Physicochem Eng Asp. 1996;116:63-77.

[104] Chibowski E, Hoysz L. On the use of Washburn's equation for contact angle determination. J Adhesion Sci Technol. 1997;11:1289-301.

[105] Galet L, Patry S, Dodds J. Determination of the wettability of powders by the Washburn capillary rise method with bed preparation by a centrifugal packing

technique. J Colloid Interface Sci. 2010;346:470-5.

[106] Gomez F, Denoyel R, Rouquerol J. Determining the Contact Angle of a Nonwetting Liquid in Pores by Liquid Intrusion Calorimetry. Langmuir. 2000;16:4374-9.

[107] Kwok DY, Budziak CJ, Neumann AW. Measurements of Static and Low Rate Dynamic Contact Angles by Means of an Automated Capillary Rise Technique. J Colloid Interface Sci. 1995;173:143-50.

[108] Labajos-Broncano L, Gonzalez-Martin ML, Bruque JM, Gonzalez-Garcia CM. Comparison of the use of Washburn's equation in the distance-time and weight-time imbibition techniques. J Colloid Interface Sci. 2001;233:356-60.

[109] Xue HT, Fang ZN, Yang Y, Huang JP, Zhou LW. Contact Angle Determined by Spontaneous Dynamic Capillary Rises with Hydrostatic Effects: Experiment and Theory. Chem Phy Lett. 2006;432:326-30.

[110] Ishakoglu A, Baytas AF. The influence of contact angle on capillary pressure–saturation relations in a porous medium including various liquids. International Journal of Engineering Science. 2005;43:744-55.

[111] Popescu MN, Ralston J, Sedev R. Capillary Rise with Velocity-Dependent Dynamic Contact Angle. Langmuir. 2008;24:12710-6.

[112] Siebold A, Nardin M, Schultz J, Walliser A, Oppliger M. Effect of dynamic contact angle on capillary rise phenomena. Colloids Surf A: Physicochemical and Engineering Asp. 2000;161:81-7.

[113] Fisher LR, Lark PD. An Experimental Study of the Washburn Equation for Liquid Flow in Very Fine Capillaries. J Colloid Interface Sci. 1979;69:486-92.

[114] Martic G, Gentner F, Seveno D, Coulon D, De Coninck J, Blake TD. A Molecular Dynamics Simulation of Capillary Imbibition. Langmuir. 2002;18:7971-6.

[115] Joos P, van Remoortere P, Bracke M. The kinetics of wetting in a capillary. J Colloid Interface Sci. 1990;136:189-97.

[116] Girardo S, Palpacelli S, De Maio A, Cingolani R, Succi S, Pisignano D. Interplay between Shape and Roughness in Early-Stage Microcapillary Imbibition. Langmuir. 2012;28:2596-603.

[117] Stukan MR, Ligneul P, Crawshaw JP, Boek ES. Spontaneous Imbibition in Nanopores of Different Roughness and Wettability. Langmuir. 2010;26:13342-52.

[118] Chiquet P, Broseta D, Thibeau S. Wettability alteration of caprock minerals by carbon dioxide. Geofluids. 2007;7:112-22.

[119] Saraji S, Goual L, Piri M, Plancher H. Wettability of Supercritical Carbon Dioxide/Water/Quartz Systems: Simultaneous Measurement of Contact Angle and Interfacial Tension at Reservoir Conditions. Langmuir. 2013;29:6856-66.

[120] Hebach A, Oberhof A, Dahmen N, Kögel A, Ederer H, Dinjus E. Interfacial Tension at Elevated PressuresMeasurements and Correlations in the Water + Carbon Dioxide System. Journal of Chemical & Engineering Data. 2002;47:1540-6.

[121] Chun B-S, Wilkinson GT. Interfacial tension in high-pressure carbon dioxide mixtures. Industrial & Engineering Chemistry Research. 1995;34:4371-7.

[122] Chiquet P, Daridon J-L, Broseta D, Thibeau S. CO_2/water interfacial tensions under pressure and temperature conditions of CO_2 geological storage. Energy Conversion and Management. 2007;48:736-44.

[123] Sutjiadi-Sia Y, Jaeger P, Eggers R. Interfacial phenomena of aqueous systems in dense carbon dioxide. The Journal of Supercritical Fluids. 2008;46:272-9.

[124] Li X, Ross DA, Trusler JPM, Maitland GC, Boek ES. Molecular Dynamics Simulations of CO_2 and Brine Interfacial Tension at High Temperatures and Pressures. The Journal of Physical Chemistry B. 2013;117:5647-52.

[125] Li X, Boek ES, Maitland GC, Trusler JPM. Interfacial Tension of (Brines + CO_2): $CaCl_2$(aq), $MgCl_2$(aq), and Na_2SO_4(aq) at Temperatures between (343 and 423) K, Pressures between (2 and 50) MPa, and Molalities of (0.5 to 5)

mol kg^{-1}. Journal of Chemical & Engineering Data. 2012;57:1369-75.

[126] Kvamme B, Kuznetsova T, Hebach A, Oberhof A, Lunde E. Measurements and modelling of interfacial tension for water+carbon dioxide systems at elevated pressures. Computational Materials Science. 2007;38:506-13.

[127] Massoudi R, King AD. Effect of pressure on interfacial tension of aqueous solutions in equilibrium with compressed gases. Abs Pap Am Chem Soc. 1974:179.

[128] Bikkina PK. Contact Angle Measurements of CO_2–water–quartz/calcite systems in the Perspective of Carbon Sequestration. Int J Greenh Gas Con. 2011;5:1259-71.

[129] Egermann P, Chalbaud CA, Duquerroix J, Le Gallo Y. An Integrated Approach to Parameterize Reservoir Models for CO_2 Injection in Aquifers. The annual technical conference and exhibition. San Antonio: Society of Petroleum Engineers, SPE 102308; 2006.

[130] Jung J-W, Wan J. Supercritical CO_2 and Ionic Strength Effects on Wettability of Silica Surfaces: Equilibrium Contact Angle Measurements. Energy & Fuels. 2012;26:6053-9.

[131] Chi SM, Morsi BI, Klinzing GE, Chiang SH. Study of interfacial properties in the liquid carbon dioxide-water-coal system. Energy & Fuels. 1988;2:141-5.

[132] Ameri A, Kaveh NS, Rudolph ESJ, Wolf KH, Farajzadeh R, Bruining J. Investigation on Interfacial Interactions among Crude Oil–Brine–Sandstone Rock–CO_2 by Contact Angle Measurements. Energy & Fuels. 2013;27:1015-25.

[133] Dickson JL, Gupta G, Horozov TS, Binks BP, Johnston KP. Wetting Phenomena at the CO_2/Water/Glass Interface. Langmuir. 2006;22:2161-70.

[134] Li Y, Pham JQ, Johnston KP, Green PF. Contact Angle of Water on Polystyrene Thin Films: Effects of CO_2 Environment and Film Thickness. Langmuir. 2007;23:9785-93.

[135] Yang D, Gu Y, Tontiwachwuthikul P. Wettability Determination of the Reservoir Brine−Reservoir Rock System with Dissolution of CO_2 at High Pressures and Elevated Temperatures. Energy & Fuels. 2007;22:504-9.

[136] Yang D, Gu Y, Tontiwachwuthikul P. Wettability Determination of the Crude Oil−Reservoir Brine−Reservoir Rock System with Dissolution of CO_2 at High Pressures and Elevated Temperatures. Energy & Fuels. 2008;22:2362-71.

[137] Shojai Kaveh N, Rudolph ESJ, Wolf K-HAA, Ashrafizadeh SN. Wettability determination by contact angle measurements: hvbB coal–water system with injection of synthetic flue gas and CO_2. Journal of Colloid and Interface Science. 2011;364:237-47.

[138] Shojai Kaveh N, Wolf KH, Ashrafizadeh SN, Rudolph ESJ. Effect of coal petrology and pressure on wetting properties of wet coal for CO_2 and flue gas storage. International Journal of Greenhouse Gas Control. 2012;11, Supplement:S91-S101.

[139] Hiemenz PC. Principles of Colloid and Surface Chemistry. New York: Marcel Dekker; 1997.

[140] Kim Y, Wan J, Kneafsey TJ, Tokunaga TK. Dewetting of Silica Surfaces upon Reactions with Supercritical CO_2 and Brine: Pore-Scale Studies in Micromodels. Environ Sci Technol. 2012;46:4228-35.

[141] Sghaier N, Prat M, Ben Nasrallah S. On the influence of sodium chloride concentration on equilibrium contact angle. Chemical Engineering Journal. 2006;122:47-53.

[142] Aker E, Måløy KJ. Simulating temporal evolution of pressure in two-phase flow in porous media. Phys Rev E. 1998;58:2217-26.

[143] Pc In terms of radius of capillary tube http://web.mst.edu/~numbere/cp/chapter%203.htm#_Toc506795446. Last Accessed Date: 06/12/2014

[144] Laplace PS. "Theory of Capillary Attraction," Supplements to the 10th book

of "Celestial Mechanics" (1806, 1807), translated and annotated by N. Bowditch (1893). Paris1806.

[145] Lucas R. Ueber das Zeitgesetz des Kapillaren Aufstiegs von Flussigkeiten. Kolloid Z. 1918;23:15-22.

[146] Washburn EW. The dynamics of capillary flow. Phys Rev. 1921;17:273-83.

[147] Bell JM, Cameron FK. The flow of liquids through capillary spaces. JPhysChem. 1906;10:658-74.

[148] Fluids in porous media: facts http://www.jgmaas.com/scores/facts.html. Last Accessed Date: 06/12/2014

[149] Bachu S, Bonijoly D, Bradshaw J, Burruss R, Holloway S, Christensen NP, et al. CO_2 storage capacity estimation: Methodology and gaps. International Journal of Greenhouse Gas Control. 2007;1:430-43.

[150] Bennion B, Bachu S. Drainage and Imbibition Relative Permeability Relationships for Supercritical CO_2/Brine and H_2S/Brine Systems in Intergranular Sandstone, Carbonate, Shale, and Anhydrite Rocks. SPE Reserv Eval Eng. 2008;11:487-96.

[151] Plug WJ, Bruining J. Capillary pressure for the sand–CO_2–water system under various pressure conditions. Application to CO_2 sequestration. Advances in Water Resources. 2007;30:2339-53.

[152] Tokunaga TK, Wan J, Jung J-W, Kim TW, Kim Y, Dong W. Capillary pressure and saturation relations for supercritical CO_2 and brine in sand: High-pressure Pc(Sw) controller/meter measurements and capillary scaling predictions. Water Resources Research. 2013;49:4566-79.

[153] Shi J-Q, Xue Z, Durucan S. Supercritical CO_2 core flooding and imbibition in Tako sandstone—Influence of sub-core scale heterogeneity. International Journal of Greenhouse Gas Control. 2011;5:75-87.

[154] Perrin J-C, Benson S. An Experimental Study on the Influence of Sub-Core Scale Heterogeneities on CO_2 Distribution in Reservoir Rocks. Transp Porous

Med. 2010;82:93-109.

[155] Pini R, Krevor SCM, Benson SM. Capillary pressure and heterogeneity for the CO_2/water system in sandstone rocks at reservoir conditions. Advances in Water Resources. 2012;38:48-59.

[156] Zhang C, Oostrom M, Grate JW, Wietsma TW, Warner MG. Liquid CO_2 Displacement of Water in a Dual-Permeability Pore Network Micromodel. Environ Sci Technol. 2011;45:7581-8.

[157] Song Y, Jiang L, Liu Y, Yang M, Zhao Y, Zhu N, et al. An experimental study on CO_2/water displacement in porous media using high-resolution Magnetic Resonance Imaging. International Journal of Greenhouse Gas Control. 2012;10:501-9.

[158] Brooks RH, Corey AT. Hydraulic properties of porous media. Hydrology Paper No 3, Colorado State University. 1964;3:1-27.

[159] van Genuchten MT. A Closed-form Equation for Predicting the Hydraulic Conductivity of Unsaturated Soils1. Soil Sci Soc Am J. 1980;44:892-8.

[160] Falta RW, Benson SM, Murdoch L, Lawrence C. Understanding and Managing Risks Posed by Brines Containing Dissolved Carbon Dioxide. Stanford University Clemson University; 2010.

Chapter 3: Methods and Materials

3.1 Experimental Methodologies

3.1.1 Pendant Drop Method for Surface Tension Measurements

Interfacial tension is one of the most important factors in multiphase flow transport in porous media. In this study, the surface tension of liquids was determined using the pendant drop method, which is one of the most convenient and reliable methods to measure liquid surface tension (Figure 3.1(a)). Prior to measurement, the syringe's internal diameter must be entered into the FTA 32 (First Ten Angstroms) software, so that the apparatus can be calibrated. The liquid was loaded in the cuvet (or syringe), and was then manually dropped out from the syringe to form the pendant drop. To form a nicely shaped pendant drop, the magnification must be adjusted so that the drop occupies about at least 3/4 of the vertical height of the image (Figure 3.1 (b) and (c)). This is important, since a drop which is too small cannot provide sufficient pixels for good accuracy. The liquid hanging drop should reach the equilibrium state where the liquid gravity force is balanced by the interfacial tension force. By analyzing the shape of the pendant drop using FTA 32, the surface tension (liquid-vapor interfacial tension) can be calculated using the following equation (3.1)[1]:

$$\gamma_{LV} = \frac{\Delta\rho g d_e^2}{H} \tag{3.1}$$

where γ_{LV} is the liquid-vapor interfacial tension (mN/m), g is gravity acceleration (m/s^2), $\Delta\rho$ (kg/m^3) is the density difference between the liquid drop and the surrounding fluid. Since the liquid surface tension was measured in air in this study and the density of air can be negligible here, $\Delta\rho$ is the density of the liquid. H is a drop-shaped correction parameter ($1/H=d_s/d_e$), and d_s is the diameter measured at the length of d_e from the drop's bottom line.

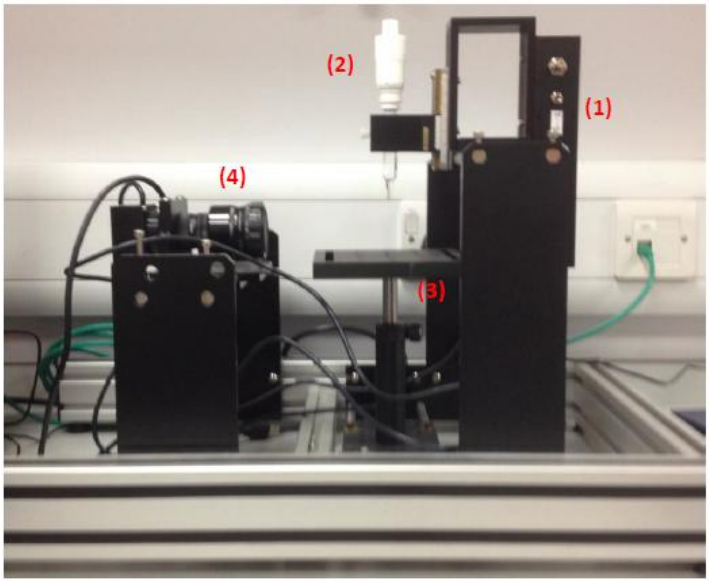

(a)

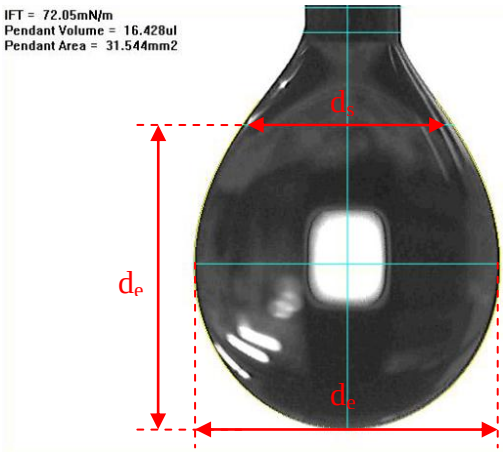

(b)

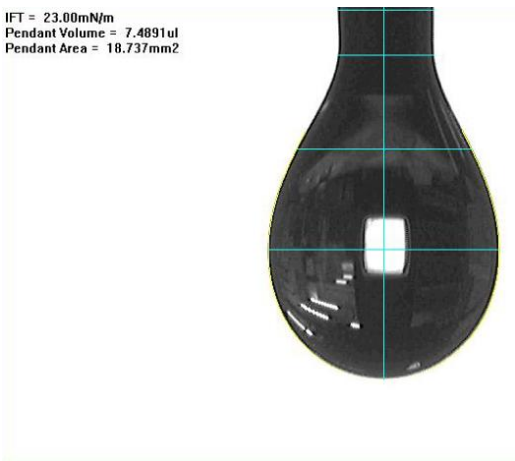

(c)

Figure 3.1 (a) Experimental set-up (FTA 32, First Ten Angstroms) for investigation of surface tension and contact angle measurement on a flat substrate. (1) light source, (2) syringe, (3) substrate holder, (4) camera; Pendant drop methods for surface tension measurements of water (b) and n-decane (c).

3.1.2 Sessile Drop Method for Contact Angle Measurement on a Flat Surface

The contact angle of liquid on a flat solid substrate can be determined from the profile of a sessile drop. The sessile drop image was analyzed using FTA 32 to obtain the contact angle (Figure 3.2). The substrate sample was first mounted on a holder and the test fluid loaded into the syringe (Figure 3.1). The liquid (~1.0 μL) was then dropped onto the substrate, and focused. The sessile drop images were captured by the FTA 32 programme. The contact angle of the drop was analyzed by using the non-spherical fitting option provided by FTA 32. Due to the relatively high vapor pressure of some organics, such as alcohol, alkane and crude oil, the contact angles on a flat surface of these liquids were measured as quickly as possible after dropping the liquid onto the substrate, in order to avoid the effect of evaporation which could distort the original drop shape and thereby affect the contact angle measurements [2].

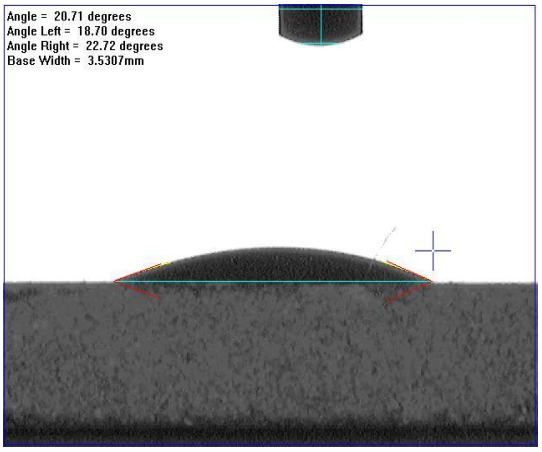

Figure 3.2 Sessile drop method for contact angle measurement on a flat surface; sessile drop image of water on a flat glass surface.

3.1.3 Microscopic Imaging Technique for Contact Angle Measurement in a Micron-sized Pore

A novel method [3, 4] was developed in this study to directly measure the contact angles of a wide range of fluids and CO_2 in a small pore, by considering the effects of a liquid's physical properties (interfacial tension and viscosity), its chemical structure, and the CO_2 phase. The experimental data produced using this technique may contribute to representing the pore wetting more properly than when using the traditional methods.

3.1.3.1 Contact Angle Measurements in a Pore at Ambient Conditions

The pore contact angle measurement apparatus developed in this study is shown in Figure 3.3. An optical microscope (Olympus, BHW) with a 10X objective lens (M PLAN 10X (025)) equipped with a digital camera (AM7023, Dino-Eye) was used to image the vapor-liquid interface in a capillary, as shown in Figure 3.3 (a). As a cylindrical capillary is used, the meniscus image of a small amount of liquid in a pore might be distorted. Cheong et al. stressed that the quality of the interface image of a small volume of liquid in a capillary strongly relies on the measurement method and illumination used [5]. Here, a LED white light source was used, which was located under the glass capillary. The illumination travels from the liquid end upwards to light up the meniscus. This method can overcome the degree of image distortion, and thus improve and facilitate the contact angle measurements in a small pore [5]. The principle of this method is close to those used for the measurement of micron ice crystal size in aqueous solution [6], micron air-bubble size [7] and the

size of a microcapsule or plant cell under a microscope [8]. The outermost two-phase interface boundary was well-lit and focused to produce a clear two-phase interfacial line [9, 10].

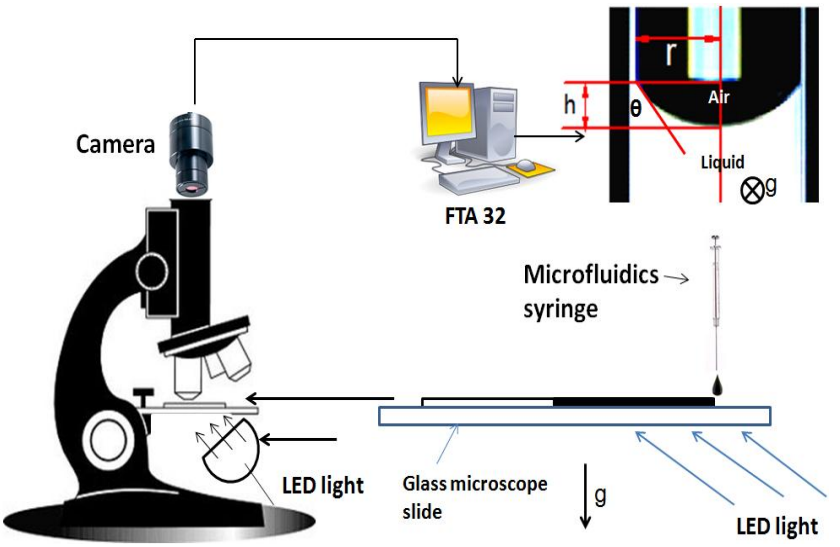

(a)

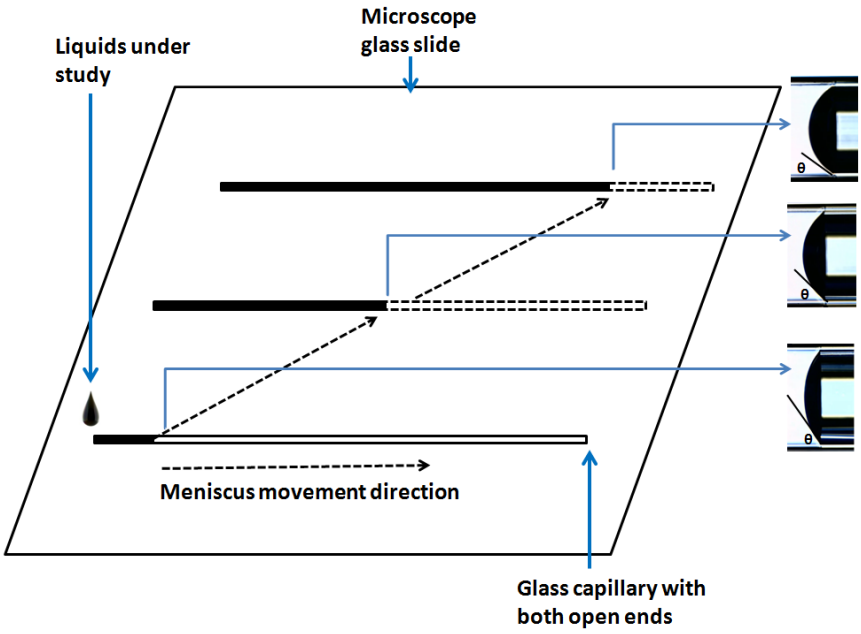

(b)

Figure 3.3 Experimental setup for the study of dynamic contact angles in a capillary: (a) microscopic imaging of contact angle of liquid in a pore (the vector $\bar{g}$ shows the direction of gravity); (b) dynamic contact angles (meniscus movements) under a microscope equipped with a camera

First, a cleaned single glass capillary with open ends was fixed on a transparent slide support, and lighted and focused by the microscope before conducting measurements (Figure 3.3 (a)). A small volume of test liquid (~0.5 μL) was dropped onto one end of the glass capillary using a microfluidics syringe (Hamilton, 701ASN 10 μL). The capillary effect will cause the liquid to spontaneously imbibe into the capillary. During the liquid imbibition invasion, the dynamic advancing liquid menisci can be recorded by the camera tracking for various imbibition rates (interface velocity, m/s), as shown in Figure 3.3(b). The images extracted from the recorded video by video were analyzed using editing software (Adobe Premiere Pro 2.0), and the interface velocity (v=dL/dt) can be calculated by measuring the imbibition length interval (dL) for a time interval (dt). When the imbibition process was entirely completed and there was no more liquid movement, the contact angle at this state was the equilibrium or static pore contact angle of the liquid in a capillary. For this study, the confined liquid in a small pore involves a much less significant effect of evaporation on the contact angle than that measured on a flat surface in an open space. For each measurement, a new fresh clean capillary was used to avoid prewetting of the capillary interior.

To determine the contact angle of liquid in a small capillary, the microscopic images were analyzed using both commercial software (FTA 32) and the method recently proposed by Cheong et al [5]. Cheong et al. developed a simple and robust method for estimating the contact angle of small volumes, by only using the capillary radius (r) and meniscus height (h) (Figure 3.3 (a)) from the microscopic capillary meniscus image [5] (Equation 3.2). This equation is valid based on the assumptions of the small liquid volume applied and a negligible gravity effect [5, 11]. Since the effect of image distortion on meniscus height (h) is not significant, the effect of image distortion on contact angle estimation of a liquid in a small pore can be minimized [5]:

$$\theta = \tan^{-1}\left(\frac{r^2-h^2}{2rh}\right) \tag{3.2}$$

where θ is the contact angle in a pore, r is the radius of the capillary (mm) and h is the height of the capillary meniscus (mm).

In order to estimate the measurement error, Equation (3.2) can be rearranged and differentiated into Equation 3.3 [5]:

$$\delta\theta = \left(-\frac{r^2+h^2}{2rh^2(1+\tan\theta)}\right)\delta h \tag{3.3}$$

From this relationship, it is clear that a small radius gives a large error, and a large radius improves the accuracy of the measurement of the contact angle.

3.1.3.2 Contact Angle Measurements in a Pore at High Pressure

In order to measure the CO_2-fluid contact angle in a small pore under high pressure, the pore contact angle measurement apparatus was modified and developed by being equipped with high pressure pumps. The experimental apparatus shown in Figure 3.4 was designed to measure CO_2-fluid contact angles in a single capillary. The fluids used included CO_2, distilled water, brine and n-decane. The set-up can handle pressures up to 100 bar using the high-pressure CO_2 pump (ISCO syringe pump, 100DM). A hot water bath was used to elevate the temperature of the CO_2/water, CO_2/brine or CO_2/decane interface. The critical temperature of CO_2 is 31 ^{0}C. In order to involve both liquid CO_2 and supercritical CO_2 in this study, two temperatures

applied in this study were 20 ^{0}C (ambient temperature) and 40 ^{0}C. The whole system is first flushed with CO_2 to remove air. Then, valve 3 is closed and water, brine or n-decane injected into the capillary by (d) to ensure that the capillary is full of liquid, and then valve 6 is closed. When the operating pressure is set by the constant-pressure mode of the ISCO CO_2 pump, valve 3 is open and needle valve 6 is slightly released to let CO_2 displace the liquid in the capillary at a constant pressure. When the CO_2/fluid interface entered the measurement zone under the microscope, valve 5 was quickly switched off. There will now be no flow in the system and the pump stops pumping. When any dynamic movement of CO_2/fluid interface was completely ceased, the equilibrium CO_2-liquid contact angle can be achieved and then analyzed. For instance, an image of liquid CO_2-water contact angle is shown in Figure 3.4 (j). The image was analyzed using Equation 3.2 in order to obtain the CO_2-fluid contact angle in a pore.

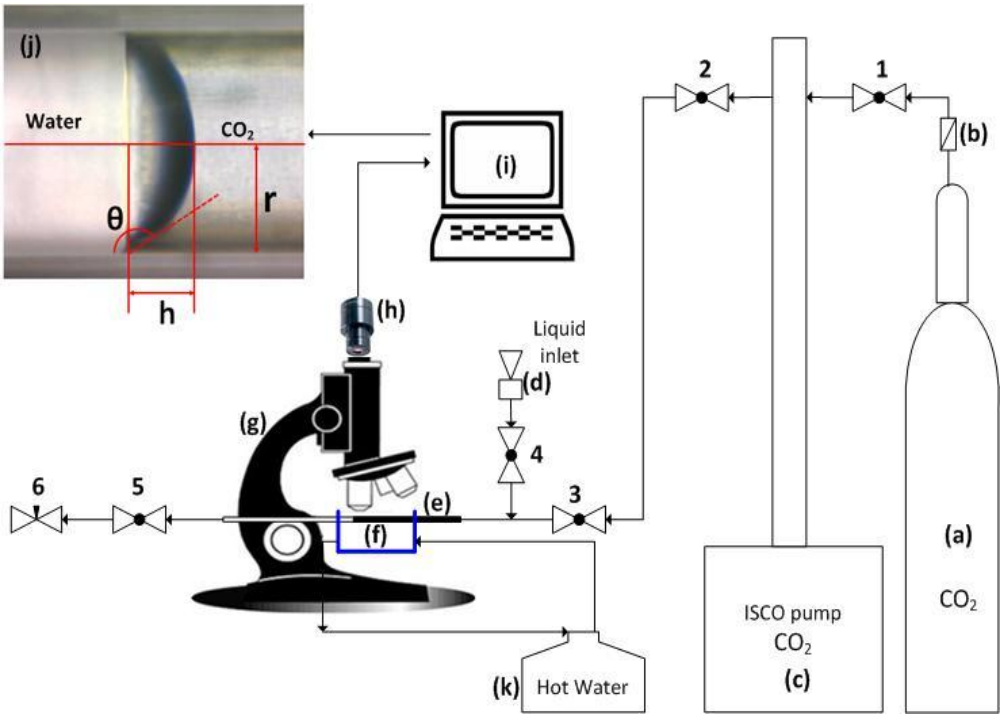

Figure 3.4 Experimental setup for CO_2- fluids pore contact angle measurements: (a) CO_2 cylinder; (b) CO_2 filter; (c) ISCO CO_2 pump; (d) fluid injector; (e) capillary tube; (f) hot water bath chamber; (g) optical microscope (Olympus, BHW) with a 10X objective; (h) digital camera (AM7023, Dino- Eye); (i) data acquisition computer; (j) CO_2-water pore contact angle image; 1~5: ball valve, 6: needle valve

3.1.4 CO_2 Core Flooding Experimental Set-up

A horizontal core flooding experimental apparatus was designed and used for CO_2-water displacement in a sandstone core sample, and is shown in Figure 3.5. The sandstone rock sample was wrapped in a shrinkable Teflon sleeve (Figure 3.6 (a)) and placed in a stainless steel core holder (Figure 3.6 (b)). An overburden-pressure water pump (Milton Roy, CM4000) injected water around the core sleeve to build the overburden pressure (Figure 3.6 (b) and (c)). Two syringe pumps (ISCO syringe pump, 100DM) were connected to the inlet and outlet of the core holder and these can be set to a constant injection flowrate mode (accuracy ±0.00001 ml/min) or a constant pressure mode (±0.1 bar). The CO_2 was injected into the right-hand side of the core holder and the water was injected or collected on the left. A hydrophilic membrane (Nuclepore, Whatman, pore size~2 μm) is located on the left-hand side of the core sample (the water production side) for the drainage experiment. Any leakage is the major concern in this system. The system was tested over the whole pressure range prior to the experiment.

The core sample was initially filled with water. The ISCO water pump was used to apply a pressure of 1 bar, pumping water into the sandstone core sample and removing all possible air. When the sandstone became fully water saturated, valve 4 was closed as shown in Figure 3.5. The ISCO water pump was set to the system pressures applied during the CO_2-water drainage measurements, such as 10, 30, 75 bar with valves 6 and 5 open, and valve 7 and 4 closed. Meanwhile, the ISCO CO_2 pump was filled with CO_2, and set to the same system pressure (valve 2 open, valves 1, 3 and 4 closed). Once the pressures of the two pumps reached exactly the same level and a steady state, valve 4 was opened. The ISCO CO_2 pump was switched to constant-flowrate mode from constant-pressure mode, applying a constant CO_2

injection rate of 0.1, 0.2, 0.4 or 0.6 ml/min. Meanwhile, the ISCO water pump remained at the constant-pressure mode. For supercritical CO_2-water displacement, a hot water bath (Grant, GD 100) was used to elevate the CO_2-water-sandstone system temperature. The temperature was kept at 40 ^{0}C during the experiment, in order to make sure that the CO_2 would be at supercritical state in the core.

The water saturation ($S_w(t)$) was obtained from the cumulative volume V(t) of the ISCO water pump. At the end of the experiment, the integral mass balance can be checked by the initial dried sandstone, wet sandstone after drainage and displaced water collected in the water pump. Thus, the final water saturation (residual water saturation) in the core sample can be readily calculated. The differential pressure during the drainage was measured using two pressure transmitters (RS, 100 bar gauge, ±0.01 bar accuracy) placed on the CO_2 inlet and water outlet of the core holder.

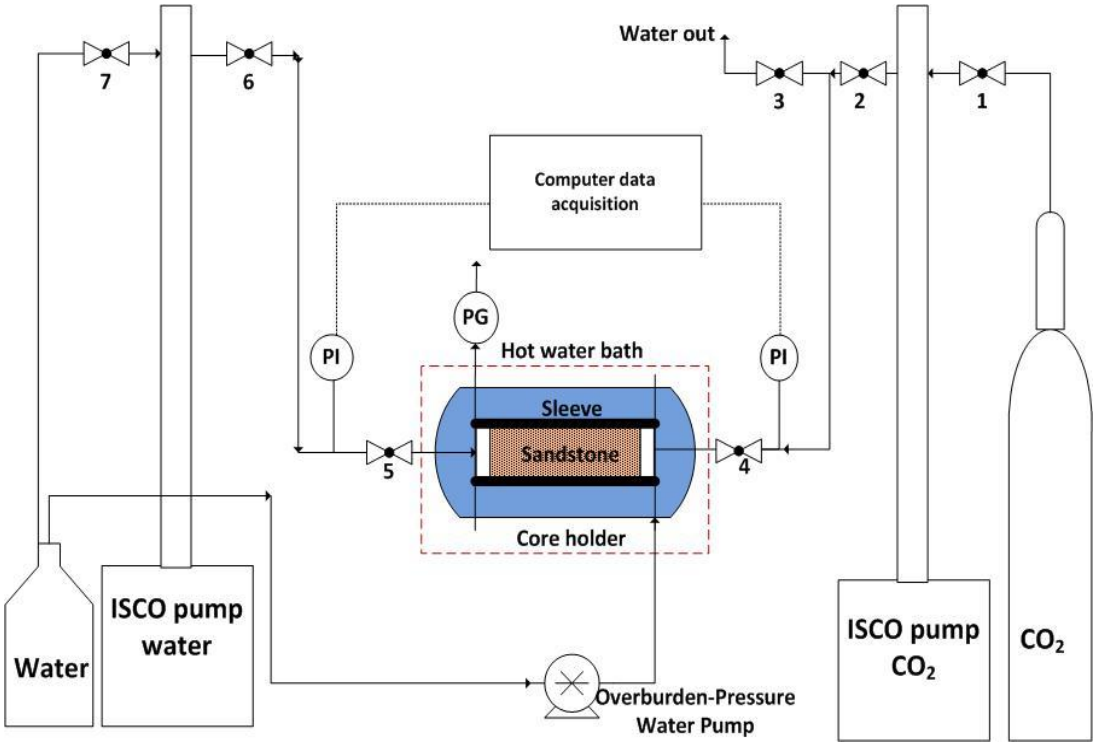

Figure 3.5 Experimental set-up developed for CO_2-water core flooding experiments

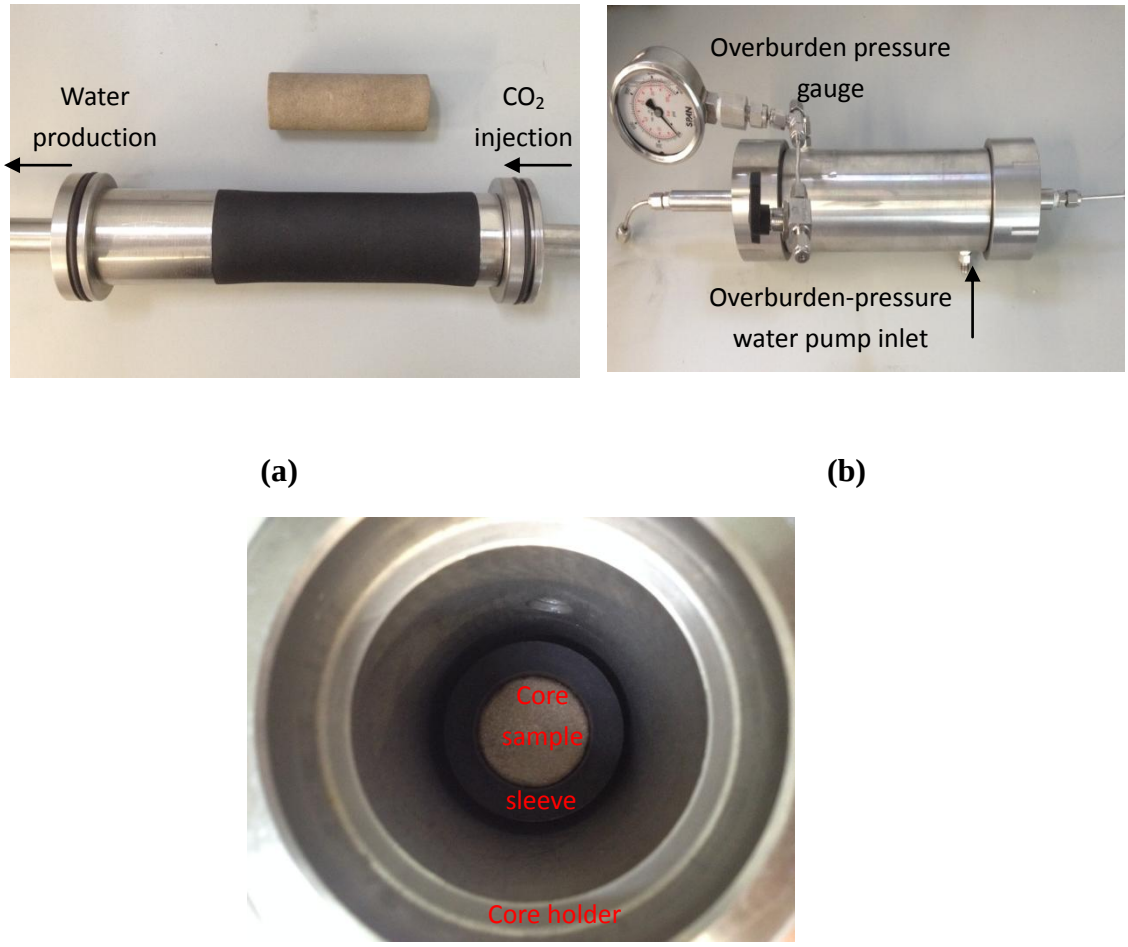

(a) **(b)**

(c)

Figure 3.6 (a) shrinkable Teflon sleeve; (b) stainless steel core holder; (c) cross-section view of core holder

3.2 Materials

3.2.1 Liquids

3.2.1.1 Basic Reservoir Fluids

Deionized water, brine, n-decane and crude oil were used in this study to represent the common fluids in oil reservoirs or saline aquifers. The deionized water was obtained from a Barnstead NANOpure Diamond^{TM} Analytical ultrapure water system. Brine (~200 g(NaCl)/kg(water)) was prepared by mixing water with sodium chloride (NaCl) (ACS reagent, ≥99.0%). n-decane was purchased from Acros Organics (analytic grade, 99+% pure). The crude oil was from MAPLLC Petroleum Crude Oil (density: 659~818 kg/m^3; surface tension: 20.0 mN/m; viscosity: 6.14×10^{-3} Pa s).

3.2.1.2 Liquids with Various Surface Tensions and Viscosities

The viscosity and surface tension of liquids are the crucial properties for studying dynamic wetting behavior in a capillary, since the dynamic contact angle is highly related to the capillary number ($Ca = v\,\eta/\gamma$) and the static contact angle (θ_s), which has been introduced and discussed in Chapter 2 [12-14]. The effect of surface tension on the dynamic pore contact angle was studied by using various concentrations of alcohol aqueous solutions. The surface tensions of water, 1-propanol and aqueous solutions of 1-propanol significantly vary in a range from 24.4 mN/m (1-propanol) to 72.0 mN/m (water), as shown in Table 3.1, but their viscosities are close, ranging from 1.94×10^{-3} to 8.94×10^{-4} Pa s. In order to investigate the effect of liquid viscosity on dynamic pore contact angle, silicone oils with very different viscosities of 9.30×10^{-3} Pa s, 4.80×10^{-2} Pa s, 9.60×10^{-2} Pa s, 4.85×10^{-1} Pa s and 9.70×10^{-1} Pa s

were used in this study.

Table 3.1 The physical properties of liquids for dynamic pore contact angle measurements

Liquids	*Density* [a] *(kg/m^3)*	*Surface tension* [b] *(mN/m)*	*Viscosity* [a] *(Pa s)*
DI water	998.2	72.0	8.94×10^{-4}
1-propanol	803.4	23.7	1.94×10^{-3}
5wt% 1-propanol	987.9	46.2	1.10×10^{-3}
10wt% 1-propanol	976.1	37.3	1.34×10^{-3}
20wt% 1-propanol	953.3	30.3	1.84×10^{-3}
40wt% 1-propanol	910.8	27.8	2.44×10^{-3}
60wt% 1-propanol	872.0	27.2	2.67×10^{-3}
80wt% 1-propanol	836.3	26.3	2.41×10^{-3}
90wt% 1-propanol	819.5	25.0	2.17×10^{-3}
n-decane	730.0	23.8	9.20×10^{-4}
Crude oil	659~818	20.0	6.14×10^{-3}
Silicone oil (10cst)	930.0	19.4	9.30×10^{-3}
Silicone oil (50cst)	960.0	20.8	4.80×10^{-2}
Silicone oil (100cst)	960.0	20.9	9.60×10^{-2}
Silicone oil (500cst)	970.0	21.2	4.85×10^{-1}
Silicone oil (1000cst)	970.0	21.2	9.70×10^{-1}

[a] The fundamental physical properties of the liquids (density and viscosity) were taken from the NIST Chemistry WebBook [15] and the product property specifications were from the manufacturer. The viscosities of 1-propanol aqueous solutions were from data in the literature [16].

[b] The surface tensions of liquids were determined by pendant drop experiments (First Ten Angstroms).

The surface tensions of five kinds of amphiphile aqueous solutions with the amphiphile concentrations from 0 to 1 are shown in Table 3.2.

Table 3.2 Surface tensions of amphiphile aqueous solutions

Amphiphile mass fraction	***Surface tension of amphiphile aqueous solution (mN/m)***				
	Methanol	***Ethanol***	***1-propanol***	***Propylamine***	***Propionic acid***
0	72.75	72.75	72.75	72.75	72.75
0.05	63.46	56.41	42.51	49.15	51.70
0.1	56.87	48.14	34.86	42.18	45.80
0.2	47.86	38.56	28.31	35.51	38.56
0.3	41.09	33.53	26.41	32.52	35.32
0.4	37.02	30.69	25.68	30.60	33.23
0.5	33.37	28.51	25.18	29.43	31.96
0.6	30.32	26.72	24.89	28.52	30.97
0.7	27.91	25.48	24.47	27.66	30.03
0.8	25.98	24.32	24.23	26.79	29.10
0.9	24.37	23.23	23.98	25.80	28.02
1.0	22.95	22.31	23.69	23.11	25.51

3.2.1.3 Organic Liquids with Various Chemical Structures

In order to investigate the effect of the chemical structure of organic compounds on pore wettability, a variety of organics were used to examine the effects of functional group and alkyl chain on pore wetting, such as the non-polar saturated alkanes (Pentane, Hexane, Octane and Decane), and amphiphilic organic compounds, tailed with straight-chain hydrophobic alkyl groups of different chain length ($(CH_3)_n$-),n=1,2,3,4,6,8,10) and headed with hydrophilic functional groups (-OH, $-NH_2$ and -COOH). The structural isomers of 1-propanol and 1-butanol, namely, 2-propanol, tert-butanol, 2-butanol and 2-methyl-1-propanol, were used to investigate the effect of alkyl chain structure on pore wetting. In addition to the alkanols with only one hydroxyl group, ethylene glycol and glycerol with two and three hydroxyl groups were also used to explore the effect of multiple hydroxyls on the alkyl backbone chain on pore wetting.

The physical properties and structural features of all the organic compounds used in this study are shown in Table 3.3. The surface tensions of liquids were determined by pendant drop experiments (First Ten Angstroms).

Table 3.3 Physical and structural properties of organic liquids with various chemical structures

Liquids	*Density (kg/m^3)*	*Surface tension (mN/m)*	*Vapor[a] pressure (kPa)*	*Molecular weight (g/mol)*	*Chemical formula*	*Molecular structure*
Pentane	626.0	18.0	56.5	72.2	C_5H_{12}	
Hexane	654.8	19.0	16.2	86.2	C_6H_{14}	
Octane	703.0	22.0	1.3	114.2	C_8H_{18}	
Decane	730.0	23.2	9.5×10^{-2}	142.3	$C_{10}H_{22}$	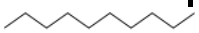
Propionic acid	990.0	25.5	0.4	74.1	$C_3H_6O_2$	
Butyric acid	959.5	25.9	0.1	88.1	$C_4H_8O_2$	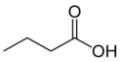
Pentanoic acid	930.0	26.1	8.5×10^{-3}	102.1	$C_5H_{10}O_2$	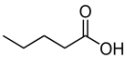
Heptanoic acid	918.1	27.8	2.8×10^{-4}	130.2	$C_7H_{14}O_2$	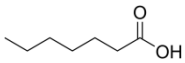
Propylamine	719.0	23.1	33.8	59.1	C_3H_9N	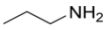
Butylamine	740.0	23.8	9.1	73.1	$C_4H_{11}N$	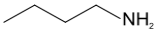
Hexylamine	766.0	25.4	0.9	101.2	$C_6H_{15}N$	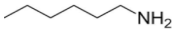
Methanol	791.8	24.5	13.0	32.0	CH_4O	
Ethanol	789.0	23.1	5.9	46.1	C_2H_6O	
1-propanol	803.4	24.4	2.0	60.1	C_3H_8O	
2-propanol	786.0	21.3	4.2	60.1	C_3H_8O	
1-butanol	810.0	24.3	0.6	74.1	$C_4H_{10}O$	

Table 3.4 (Continued) Physical and structural properties of organic liquids with various chemical structures

Liquids	*Density (kg/m^3)*	*Surface tension (mN/m)*	*Vapor[a] pressure (kPa)*	*Molecular weight (g/mol)*	*Chemical formula*	*Molecular structure*
2-Methyl-1-propanol	802.0	22.5	0.9	74.1	$C_4H_{10}O$	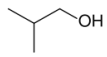
2-butanol	806.3	23.9	1.5	74.1	$C_4H_{10}O$	
tert-butanol	780.9	20.6	4.0	74.1	$C_4H_{10}O$	
1-Hexanol	814.0	25.3	5.6×10^{-2}	102.2	$C_6H_{14}O$	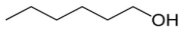
1-Octanol	827.0	27.5	6.6×10^{-3}	130.2	$C_8H_{18}O$	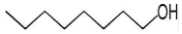
1-Decanol	829.0	27.7	5.5×10^{-4}	158.3	$C_{10}H_{22}O$	
Ethylene Glycol	1110.0	47.9	1.1×10^{-2}	62.1	$C_2H_6O_2$	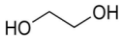
Glycerol	1260.0	63.1	1.3×10^{-4}	92.1	$C_3H_8O_3$	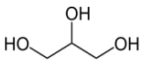

[a] The vapor pressures were calculated using the Antoine equation ($\log_{10}(P) = A - (B / (T + C))$) at 20 ℃. A, B and C are Antoine equation parameters taken from the NIST Chemistry WebBook [15].

3.2.2 CO_2

Carbon dioxide usually behaves as a gas in air at standard temperature and pressure (STP), or as liquid at low temperature and high pressure, or as a solid called dry ice when frozen. The phase of CO_2 varies with the applied pressure and temperature, as

shown in Figure 3.7. At ambient temperature (20 ^{0}C) CO_2 turns from the gas phase into liquid phase at approximately 60 bar. If both temperature and pressure increase to levels at or above the critical point (31 ^{0}C and 73 bar), the CO_2 would be in the supercritical state. Supercritical CO_2 is a fluid state of carbon dioxide where it is held at or above its critical temperature and critical pressure. It can adopt properties midway between a gas and a liquid. Supercritical CO_2 exhibits unique behaviour. It behaves like a gas but with a density like that of a liquid. It can diffuse through solids like a gas, and dissolve materials like a liquid. The density of supercritical CO_2 can be readily changed given minor changes in temperature or pressure. The density of supercritical CO_2 is higher than gas CO_2 and thus it occupies less volume [17]. However, the density of supercritical CO_2 density is lower than those of some geo-fluids such as water and brine. This leads to the upward migration of CO_2. The CO_2 used in this project was supplied by BOC with a mole fraction purity of ≥ 0.99 in a liquid withdrawal cylinder.

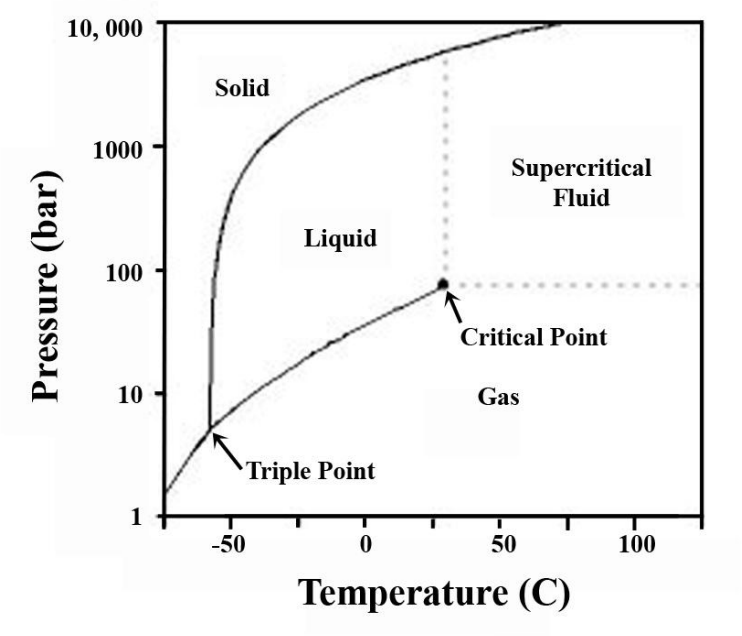

Figure 3.7 CO_2 phase diagram [18]

3.2.3 Capillaries

3.2.3.1 Manufacturing and Cleaning Capillary Tubes

Glass capillaries with inner diameters of 100-1000 μm were used in the measurements. They are made from clean glass tubes (ThermoFisherScientific UK, TWL-611-010M; Bilbate, CAP-100-10). Before the pore contact angle measurements, general cleaning methods were adopted to clean the capillaries [3, 19-25]. The glass tubes were washed using sodium hydroxide solution (Fisher Scientific, 10M concentrate), nitric acid solution (Fisher Scientific, 10M concentrate), and acetone (Fisher Scientific, A/0600/15), and were then rinsed thoroughly with deionized water [21, 24]. The glass tubes were then heated up to 550 ^{0}C on a flame to remove any residue of organic contamination and were kept in an ash-proof enclosure [21]. Single capillaries of various sizes were obtained by melting the middle section of dry and cleaned glass tubes on a butane flame (Butane Battery, D2-BS 0167) and drawing the tube to give glass capillaries of various sizes. The glass is strongly hydrophilic, and therefore the glass capillaries present water-wet pores in this study.

3.2.3.2 Polymeric Capillary

FEP (Fluorinated Ethylene Propylene) and PMMA ((Poly(methyl methacrylate)) are polymeric materials, and are thus hydrophobic. The FEP capillary (VICI Valco Tubing, VITFEP110, ID/OD: 250 μm/1.6 mm) and PMMA capillary (Paradigm, CT250-360-5, ID/OD: 250 μm/360 μm) were used to represent an oil-wet pore in this project.

Both the FEP and PMMA capillaries used are highly transparent. Thus, the pore contact angle can be readily measured. The FEP capillary has a stronger tensile strength, and was therefore used for contact angle measurements under high pressure. The tube can withstand temperatures up to 100 ℃ and can be used to up to 206 bar for a limited time. The FEP capillary could swell significantly or even break when applied pressure is over 100 bar for more than around 15 minutes. Thus, all the measurements must be performed under 100 bar and completed within 15 minutes. The size of a swollen capillary was within 1.5%×250 μm under 100 bar.

For the CO_2-fluid contact angle measurements in a glass capillary under high pressure, since the glass capillary cannot stand high pressure, it was coated with the FEP tube with an inner diameter (ID) of 0.5 mm and outer diameter (OD) of 1.6 mm, as shown in Figure 3.8. For the contact angle measured within a capillary coated by another tube, the meniscus image produced would have a higher degree of distortion. Cheong et al.'s method [5] can minimize the distortion effect, but the contact angle measurement error would be slightly larger than that measured in a single capillary.

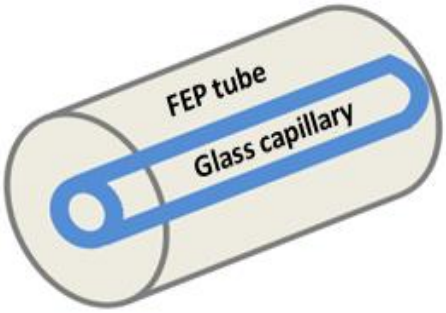

Figure 3.8 A glass capillary coated with a FEP tube for CO_2-fluid contact angle measurements in a glass capillary under high pressure

3.2.4 Sandstone

A sandstone core sample (Berea sandstone) was used for the CO_2-water flooding experiment (Figure 3.9). The diameter and length of the sandstone core are 2.5 cm and 7.5 cm respectively. The absolute horizontal permeability of the sandstone can be estimated using Darcy's law ($q = -k\Delta P/\mu L$) based on flow velocity (q), pressure drop across the bed (ΔP), fluid viscosity (μ) and bed length (L). The absolute permeability (k) is roughly around 6.3×10^{-13} m^2 or 63000 mD.

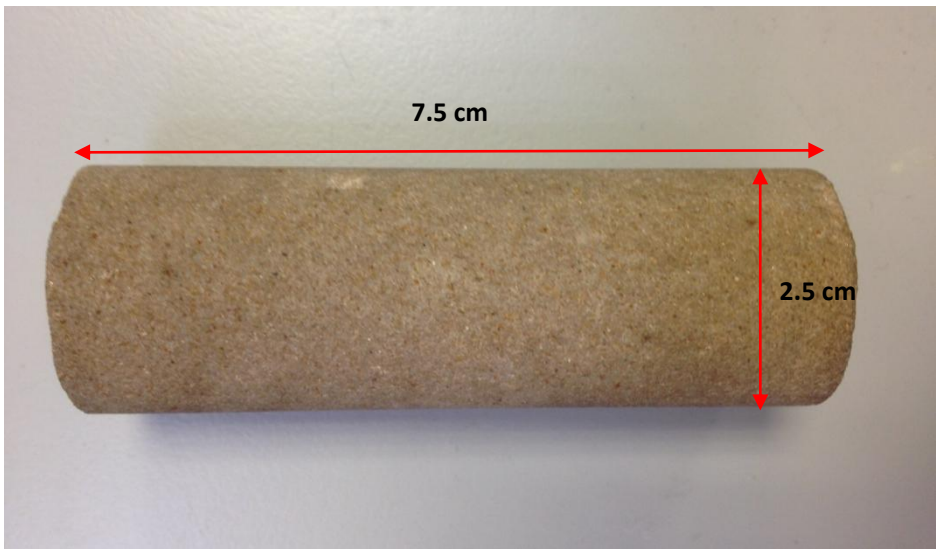

Figure 3.9 Sandstone rock core sample

3.3 References

[1] Adamson AW, Gast AP. Physical Chemistry of Surfaces. Inc, New York: John Wiley and Sons; 1997.

[2] Horng P, Brindza MR, Walker RA, Fourkas JT. Behavior of Organic Liquids at Bare and Modified Silica Interfaces. J Phys Chem C. 2010;114:394-402.

[3] Li X, Fan X, Askounis A, Wu K, Sefiane K, Koutsos V. An Experimental Study on Dynamic Pore Wettability. Chem Eng Sci. 2013;104:988-97.

[4] Li X, Fan X, Brandani S. Difference in pore contact angle and the contact angle measured on a flat surface and in an open space. Chem Eng Sci. 2014;117:137-45.

[5] Cheong BH-P, Ng TW, Yu Y, Liew OW. Using the Meniscus in a Capillary for Small Volume Contact Angle Measurement in Biochemical Applications. Langmuir. 2011;27:11925-9.

[6] Fan X, Ten P, Clarke C, Bramley A, Zhang Z. Direct Measurement of the Adhesive Force Between Ice Particles by Micromanipulation. Powder Technol. 2003;131:105-10.

[7] Fan X, Zhang Z, Li G, Rowson NA. Attachment of Solid Particles to Air Bubbles in Surfactant-free Aqueous Solutions. Chem Eng Sci. 2004;59:2639-45.

[8] Rosiński S, Grigorescu G, Lewińska D, Ritzén LG, Viernstein H, Teunou E, et al. Characterization of Microcapsules: Recommended Methods Based on Round-robin Testing. J Microencapsulation. 2002;19:641-59.

[9] Danisman MF, Calkins JA, Sazio PJA, Allara DL, Badding JV. Organosilane Self-Assembled Monolayer Growth from Supercritical Carbon Dioxide in Microstructured Optical Fiber Capillary Arrays. Langmuir. 2008;24:3636-44.

[10] Kohonen MM. Engineered Wettability in Tree Capillaries. Langmuir. 2006;22:3148-53.

[11] Zheng QS, Yu Y, Zhao ZH. Effects of Hydraulic Pressure on the Stability and

Transition of Wetting Modes of Superhydrophobic Surfaces. Langmuir. 2005;21:12207-12.

[12] Hoffman RL. A study of the advancing interface. I. Interface shape in liquid-gas systems. J Colloid Interface Sci. 1975;50:228-35.

[13] Jiang TS, Oh SG, Slattery JC. Correlation for dynamic contact angle. J Colloid Interface Sci. 1979;69:74-7.

[14] Meiron TS, Marmur A, Saguy IS. Contact angle measurement on rough surfaces. J Colloid Interface Sci. 2004;274:637-44.

[15] NIST. NIST Chemistry WebBook, NIST Standard Reference Database Number 69: National Institute of Standards and Technology; 2005.

[16] Fong-Meng P, Chye-Eng S, Tjoon-Tow T, Ibrahim MH. Densities and viscosities of aqueous solutions of 1-propanol and 2-propanol at temperatures from 293.15 K to 333.15 K. J Mol Liq 2007;136:71-8.

[17] Law DHS, Bachu S. Hydrogeological and numerical analysis of CO_2 disposal in deep aquifers in the Alberta sedimentary basin. Energy Conversion and Management. 1996;37:1167-74.

[18] Carbon Dioxide 2010 OpenStax-CNX Web site. http://cnx.org/content/m32935/1.2/. Last Accessed Date: 06/12/2014

[19] Chiquet P, Broseta D, Thibeau S. Wettability alteration of caprock minerals by carbon dioxide. Geofluids. 2007;7:112-22.

[20] Farokhpoor R, Bjørkvik BJA, Lindeberg E, Torsæter O. Wettability behaviour of CO_2 at storage conditions. International Journal of Greenhouse Gas Control. 2013;12:18-25.

[21] Fisher LR, Lark PD. An Experimental Study of the Washburn Equation for Liquid Flow in Very Fine Capillaries. J Colloid Interface Sci. 1979;69:486-92.

[22] Saraji S, Goual L, Piri M, Plancher H. Wettability of Supercritical Carbon Dioxide/Water/Quartz Systems: Simultaneous Measurement of Contact Angle and Interfacial Tension at Reservoir Conditions. Langmuir. 2013;29:6856-66.

[23] Wang S, Edwards IM, Clarens AF. Wettability Phenomena at the CO_2–Brine–Mineral Interface: Implications for Geologic Carbon Sequestration. Environ Sci Technol. 2012;47:234-41.

[24] Xue HT, Fang ZN, Yang Y, Huang JP, Zhou LW. Contact Angle Determined by Spontaneous Dynamic Capillary Rises with Hydrostatic Effects: Experiment and Theory. Chem Phy Lett. 2006;432:326-30.

[25] Yang D, Gu Y, Tontiwachwuthikul P. Wettability Determination of the Reservoir Brine−Reservoir Rock System with Dissolution of CO_2 at High Pressures and Elevated Temperatures. Energy & Fuels. 2007;22:504-9.

Chapter 4: Static Pore Wetting[1]

4.1 Introduction

It is commonly assumed that the wetting of a liquid measured on external planar substrates could represent the wetting of the confined liquid in a small pore [1]. Because of the lack of a technique for contact angle measurements in small pores, the contact angle in a pore has often been approximated from the contact angle measured in a sessile drop experiment on a flat surface in an open space [2-5], or theoretically calculated by the Lucas-Washburn or Young-Laplace equations [6-11]. Moreover, many studies also merely oversimplify the contact angle in a small pore as zero, by assuming the liquid to be a perfectly wetting liquid [12, 13]. Most of these previous studies, assumptions and simplifications for the estimation of the wetting in porous media might be true in some cases. However, they still need to be assessed and confirmed [8]. Thus, it is worth while studying the contact angle in small pores experimentally to appropriately indicate pore wetting and avoid using incorrect contact angles for cases of porous surfaces. In this chapter, the equilibrium contact angles of various liquids in single glass capillaries are measured, by using a pore contact angle measurement technique [14]. The effects of glass pore size and the surface tension and chemical structure of a liquid on the contact angle in a glass capillary are considered. The results demonstrate the difference between contact angles measured in a glass pore and on a flat glass surface in an open space. The information presented in this chapter also lays the foundation and has various implications for the next two chapters, concerning dynamic pore contact angle and the effect of chemical structure on pore contact angle.

[1] This chapter has been published in Chemical Engineering Science 2014;117:137-45

4.2 Equilibrium Contact Angle in a Single Glass Capillary

Liquid imbibition in a single capillary by capillary pressure can be numerically described using the Lucas-Washburn equation ($l^2 = \gamma r t \cos\theta / 2\eta$). The Lucas-Washburn equation shows a proportional correlation between the square of the imbibition length (l^2) and time (t) if the contact angle (θ) and capillary size (r) are given. Fisher and Lark conducted water imbibition experiments in single micron-size glass capillaries, and compared their experimental data with the correlation between l^2/t and r by simply assuming $\theta=0^0$. They confirmed that their experimental data were significantly different from the Lucas-Washburn correlation plotted by assuming $\theta=0^0$ (Figure 4.1). This may imply that the contact angle of water in a glass capillary cannot be treated as $\theta=0^0$ [15]. However, few studies have experimentally proved this so far. Many studies still use $\theta=0^0$ in modeling, simulations or calculations of multiphase capillary flows in complex porous media [12, 13]. The water contact angles in glass capillaries with pore sizes from 100 to 250 μm are measured in this study. The results in Figure 4.2 show that the pore contact angles stay roughly around 30^0 and differ greatly from the theoretical assumption using $\theta=0^0$. Using our measured water contact angle of 30^0 in a glass capillary, Fisher and Lark's experimental data give better agreement with predictions from the Lucas-Washburn correlation (Figure 4.1).

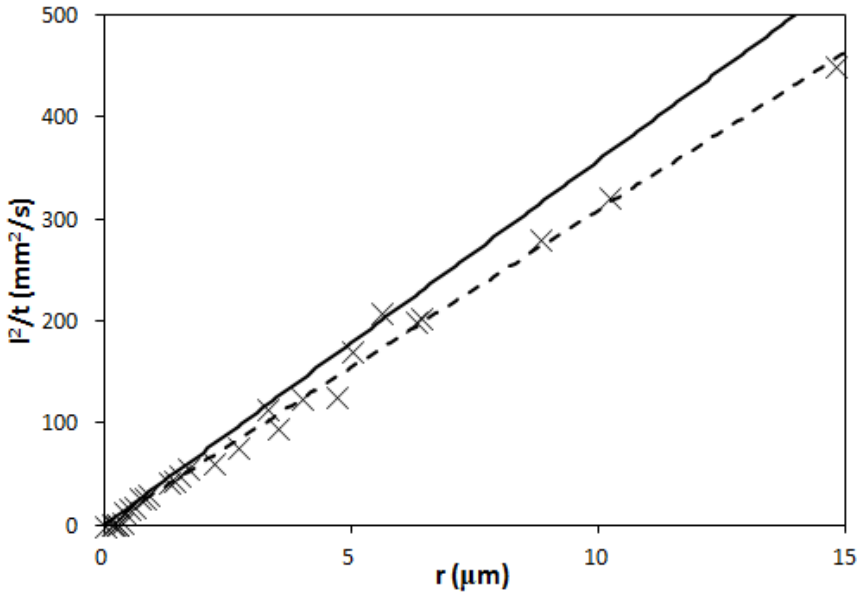

Figure 4.1 l^2/t vs r for water capillary imbibition. (×) Experimental points [15]; (—) theoretical line from Lucas-Washburn equation by assuming $\theta=0^0$; (---) Lucas-Washburn equation with our measured air-water pore contact angle $\theta=30^0$

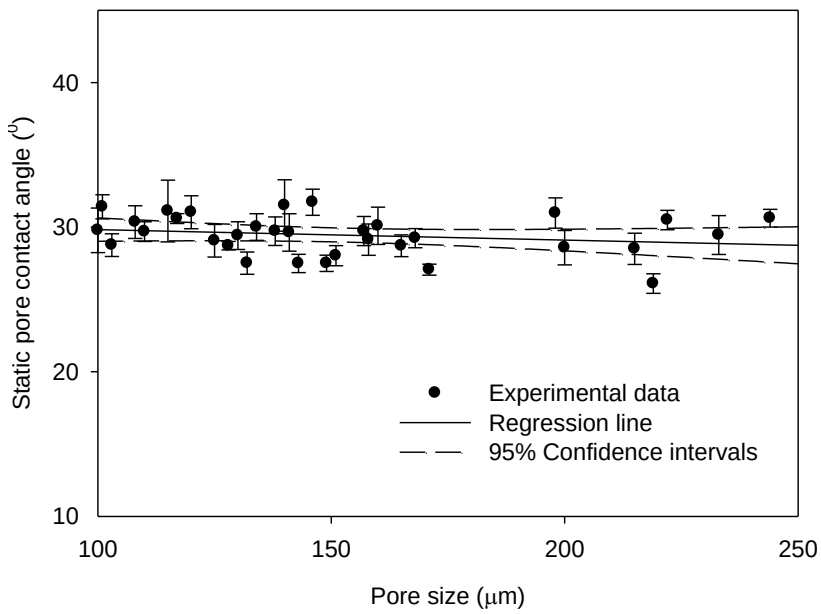

Figure 4.2 Static water contact angles in glass capillaries with a pore size from 100 to 250 μm.

According to the Young-Laplace equation ($P_c=2\gamma\cos\theta/r$), the capillary pressure (P_c) can be described based on both the pore contact angle (θ) and capillary radius (r). These two parameters are of significance for multiphase flows in porous media. Thus,

it was decided to study the relationship between the contact angle in a glass pore and glass pore size in the present research. The static pore contact angles in a range of glass capillary size from 100 to 1000 μm were measured for four different kinds of liquids as shown in Figure 4.3.

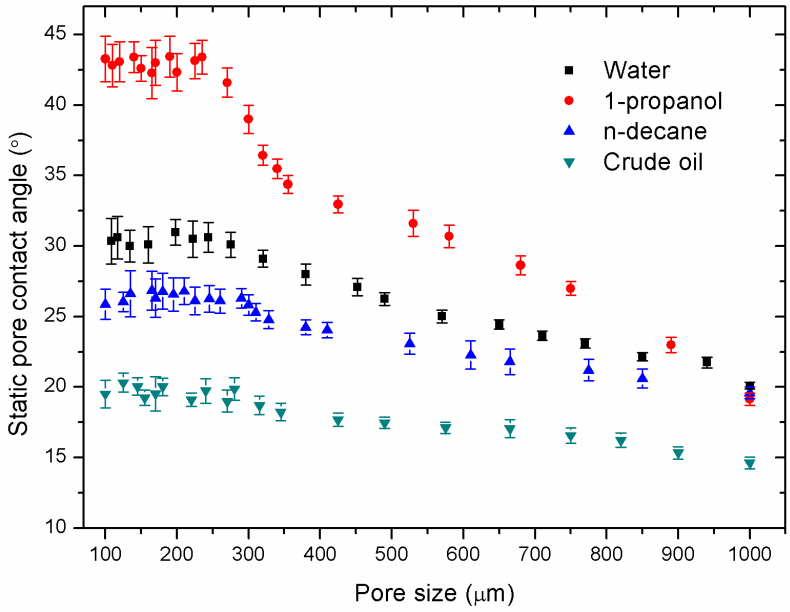

Figure 4.3 Static pore contact angles for DI water, 1-propanol, n-decane and crude oil in glass capillaries with a pore size ranging from 100 to 1000 μm.

Figure 4.3 shows that the static contact angle of liquid in a glass capillary varies with glass capillary size. For instance, when the glass pore size decreases from 1000 to around 300 μm, the static water contact angle increases from around 20^0 to 30^0. This variation in contact angle with pore size is less significant when the pore size is roughly between 300 and 100 μm. The relationships between static contact angle and pore size for 1-propanol, n-decane and crude oil were also studied and the results are shown in Figure 4.3. It can be seen that these three liquids give similar trends for contact angle-pore size. Crude oil and 1-propanol have the smallest and largest changes respectively in static contact angles.

At a pore size of 1000 μm, the contact angles of water, 1-propanol and n-decane are around 20^0, while the crude oil has a lower static pore contact angle, which is approximately 15^0. However, when the pore size decreases to around 300 μm, the static pore contact angle increase for 1-propanol, DI water, n-decane and crude oil becomes less significant. The average static pore contact angles of 1-propanol, water, n-decane and crude oil are 42^0, 30^0, 26^0 and 20^0 respectively, in the pore size range from 100 to 300 μm, Figure 4.3 also shows that the pore contact angles of water and 1-propanol are always larger than those from crude oil and n-decane.

Many experimental studies have reported the dependence of contact angle on the three-phase contact line. Good and Koo proposed that contact angle might depend on the three-phase line curvature according to their observations from sessile droplet experiments [16]. However, the mechanism of the dependence of contact angle on line curvature is not yet well understood [17, 18]. Ward and Sefiane, and Ward and Wu reported that the contact angle was a function of three-phase line curvature after conducting water-cylinder experiments [19, 20]. They explained these observations by the contribution of adsorption at the solid-liquid interface [19, 20]. Mason and Morrow proposed that the curvature of an interface in a pore could be related to pore shape and size [21, 22]. Brovchemko and Oleinikova stressed the effect of pore size on capillary wetting phenomenon of confined water [23]. Tolman, Gleb and Gubbins concluded that the surface tension of a small meniscus could be affected by the capillary radius [24, 25]. The dependence of the contact angle on the size of a liquid droplet on a solid surface has been reported in numerous simulations and experiments [26-28]. Neumann et al. proposed that the dependence of the contact angle on system size is a result of the effect of the three-phase line tension [26, 29-34]. This might be one of the important reasons for the dependence of contact angle on capillary size.

The dependence of contact angle on glass capillary size within the size range from 300 to 1000 μm might be caused by the effects of the curvature of the three-phase line and line tension. However, these factors may not be able to explain the results for the contact angles for the glass pore size ranging from 100 to 300 μm in this study. Less significant inconsistency regarding the dependence of contact angle on glass pore size can be observed with a size range from 100 to 300 μm. A recent study by Kaveh et al. proposed an apparent dependence of CO_2-water static contact angle on the contact radius, and they also observed that the effect of contact radius on contact angle became insignificant at small values of contact radius [35].

Because of the limitations of optical microscopy and the small cylindrical capillaries used in this study, the contact angle measurement errors are larger for capillaries with smaller sizes. A clear liquid meniscus image is difficult to obtain for the liquid for a pore with a size less than 100 μm. Thus, the pore contact angles for capillary sizes less than 100 μm are not included. The possible reasons for and mechanisms of the dependence of contact angle dependence on glass pore size may be complex. It might be jointly affected by three-phase line curvature, vapor saturation conditions, and liquid-vapor-solid line tension. Hence, the mechanisms involved cannot be confirmed at this stage. They will be further investigated and clarified in future work.

Lam et al. found that different contact angles were formed by various kinds of liquids on an identical smooth surface. This difference might not only be caused by their surface tensions based on Young's equation, but also by their different chemical molecular structures [36]. The surface tension might not be the only dominant parameter affecting contact angle. Young's equation cannot effectively predict a liquid spreading on a solid surface until several assumptions underlying the equation are considered [36, 37]. In order to eliminate the effect of surface tension on the contact angle in a glass pore, the static pore contact angle at unit surface tension (θ/γ)

for each liquid is shown in Figure 4.4. The results indicate that the contribution of unit surface tension of 1-propanol (θ/γ) to its contact angle is the highest, while the contribution of unit surface tension of water (θ/γ) is the lowest among these four liquids. In terms of the chemical structure of the four liquids used in this study, 1-propanol is a polar amphiphilic organic compound, having two completely different parts in a molecule, headed with a strong hydrophilic hydroxyl (-OH) function group and ended by a straight alkyl chain which is hydrophobic. These two extreme ends of the amphiphile may lead to the highest contribution to the contact angle in a glass capillary. On the other hand, the n-decane and crude oil are non-polar organics with no -OH group in the carbon chains. This may cause the lower (θ/γ) than that from 1-propanol. Thus, the chemical structure of a liquid might significantly affect its contact angle in a glass pore. Detailed studies of the effect of the chemical structure of amphiphilic organic compounds on pore wetting are presented in chapter 6.

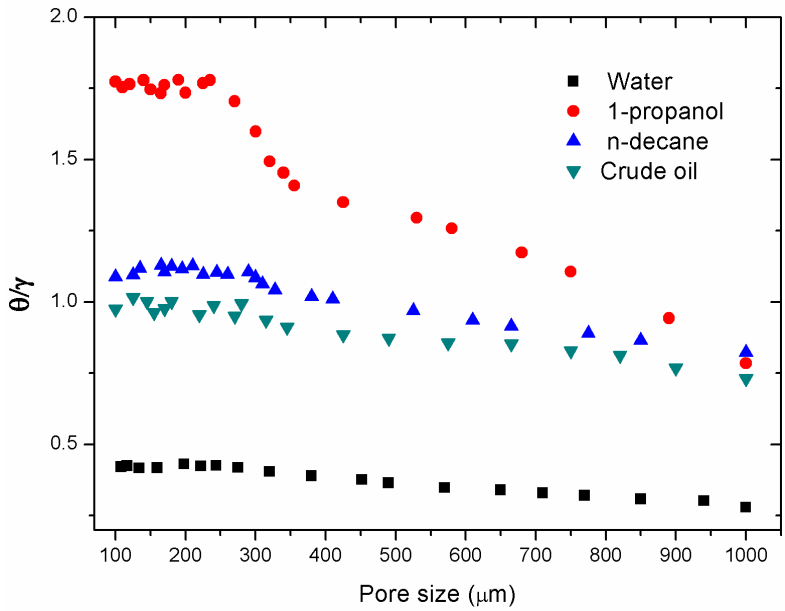

Figure 4.4 Static pore contact angles at unit surface tension (θ/γ) for water, 1-propanol, n-decane and crude oil

4.3 Comparison of Pore Contact Angle with the Contact Angle Measured on a Flat Surface and in an Open Space

Table 4.1 presents the contact angles for water, 1-propanol, n-decane and crude oil measured on a planar glass substrate in an open space and the relevant data available in the literature. The contact angles of 1-propanol, n-decane and crude oil are much smaller than those of water on a flat glass surface, and this is in very good agreement with data reported in the literature [38-42]. Horng et al. explained that this could be caused by very high surface energy (72mN/m) and the considerable self-affinity of water in air [39]. On the other hand, 1-propanol, n-decane and crude oil give very small contact angles on a flat glass surface in an open space. This is due to their weak self-affinities, small surface tensions and the significant effect of evaporation in an open space. In other words, they have stronger affinities and dispersive interactions to the glass surface than to themselves in air [39].

Table 4.1 Static contact angles on flat glass surface for water, 1-propanol, n-decane and crude oil

Liquids	***Static contact angle on a flat glass surface***	
	Measured contact angle (^{0})	***Literature values (^{0})***
Water	20.7±0.7	≈ 19~24 [41, 42, 45]
1-propanol	5.1±0.9	≈0 [38, 40]
n-decane	3.2±0.5	<5 [39]
Crude oil	8.3±0.6	<10 [46]

Figure 4.5 compares contact angles measured in a glass capillary and on a planar glass substrate. The results indicate that the static contact angles in a small pore are larger than those measured on flat glass surfaces in an open space for these four types of liquids. The difference between contact angles on a flat glass substrate and in

capillaries decreases with increasing pore size. The magnitude of the difference varies among the liquids. The most significant difference is in 1-propanol, which is around 40^0. We could observe that the contact angle in a pore tends to approach the value measured on a planar substrate once the pore size is large enough.

Overall, the results show that the contact angle of a confined liquid in a glass capillary differs from that measured on a planar glass surface in an open space. This finding cannot be explained using Young's equation ($\gamma_{lv}\cos\theta=\gamma_{sv}-\gamma_{ls}$). According to Young's equation, the contact angle depends solely on the surface energies (solid-vapor interfacial tension (γ_{sv}), liquid-solid interfacial tension (γ_{ls}) and liquid-vapor interfacial tension (γ_{lv})), rather than the geometry of the surface. However, it is essential to note that Young's equation is only valid when the surface is physically and chemically inert to the liquid and sufficiently hydrophobic to form an apparent contact angle [43, 44]. In this study, the surface used is strongly hydrophilic glass, which has a very high surface energy. Most liquids could readily or even completely spread on the glass substrate. Therefore, Young's equation might be applicable in this study. The effect of curved geometry or confinement in a glass capillary might be one of the reasons which cause the difference. This phenomenon does not exist with the contact angle of liquids on a flat glass substrate in an open space. In addition, the effect of the vapor saturation of the liquids used in this study could also cause the difference. The contact angle measurement on a flat surface in an open space or a large-size pore is performed in a solid-liquid-unsaturated vapor system. On the other hand, the pore contact angle in a small-size capillary is measured under solid-liquid-saturated vapor conditions. As shown in Figure 4.5, the difference between the contact angles measured in a pore and on a flat surface is higher for the more volatile liquids. The differences for water, crude oil, n-decane and 1-propanol are in the order of $0\sim10^0$, $7\sim12^0$, $17\sim22^0$, and $15\sim37^0$ respectively.

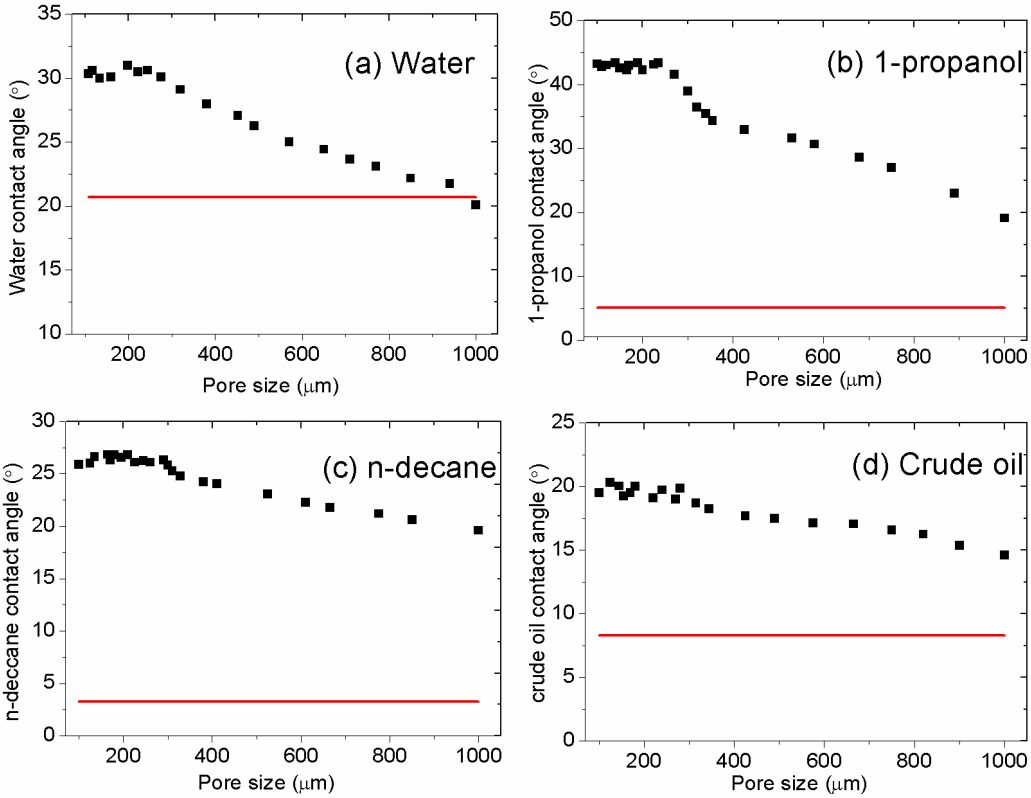

Figure 4.5 Comparison of pore contact angles with contact angles on a flat surface. (a) water; (b) 1-propanol; (c) n-decane; (d) crude oil

■ Pore contact angle; — Contact angle on a flat surface

4.4 Summary

In this chapter, the contact angles of various liquids are directly measured in single glass capillaries and compared with the contact angles measured on a flat glass surface in an open space [14]. The results indicate the following:

(1) The static contact angle of a liquid in a glass capillary varies with the glass pore size. When glass pore size decreases from 1000 to around 300 μm, the contact angles for water, 1-propanol, n-decane and crude oil respectively increase from 20^0 to 30^0, from 19^0 to 39^0, from 20^0 to 26^0 and from 15^0 to 20^0. The contact angle increase becomes less significant when the glass pore size ranges between 100 to 300 μm. None of the contact angles measured in a pore are zero, which is the value commonly applied in most of the previous studies in the literature.

(2) Contact angles in a glass capillary not only vary with liquid surface tension, but also depend on the liquid's chemical structure. The polar amphiphilic organic compound headed with a strong hydrophilic functional group and ended a straight hydrophobic alkyl chain contributes most to the glass pore contact angle. The effects of functional group and carbon chain length of amphiphilic organic compounds on contact angle in glass pores is discussed in detail in chapter 6.

(3) The contact angle of a confined liquid in a single glass capillary differs from that measured on a flat glass surface in an open space. The pore contact angle tends to draw close to that on a planar substrate if the pore size is large enough. The difference might result from the effects of the curved geometry or confinement, three-phase line tension, and the different vapour saturation conditions in a small pore and on a flat surface in an open space.

4.5 References

[1] Patro D, Bhattacharyya S, Jayaram V. Flow Kinetics in Porous Ceramics: Understanding with Non-Uniform Capillary Models. J Am Ceram Soc. 2007;90:3040-6.

[2] Anderson WG. Wettability Literature Survey. Part 2: Wettability Measurement. JPT (Nov 1986). 1986;38:1246-62.

[3] Buckley JS, Bousseau C, Liu Y. Wetting Alteration by Brine and CrudeOil: From Contact Angles to Cores. SPE Annual Tech. 1996:341.

[4] Kwok DY, Lin R, Mui M, Neumann AW. Low-rate Dynamic and Static Contact Angles and the Determination of Solid Surface Tensions. Colloids and Surf A: Physicochem Eng Asp. 1996;116:63-77.

[5] Morrow NR. Wettability and Its Effect on Oil Recovery. J Pet Technol. 1990;42:1476-84.

[6] Chibowski E, Hoysz L. On the use of Washburn's equation for contact angle determination. J Adhesion Sci Technol. 1997;11:1289-301.

[7] Galet L, Patry S, Dodds J. Determination of the wettability of powders by the Washburn capillary rise method with bed preparation by a centrifugal packing technique. J Colloid Interface Sci. 2010;346:470-5.

[8] Gomez F, Denoyel R, Rouquerol J. Determining the Contact Angle of a Nonwetting Liquid in Pores by Liquid Intrusion Calorimetry. Langmuir. 2000;16:4374-9.

[9] Kwok DY, Budziak CJ, Neumann AW. Measurements of Static and Low Rate Dynamic Contact Angles by Means of an Automated Capillary Rise Technique. J Colloid Interface Sci. 1995;173:143-50.

[10] Labajos-Broncano L, Gonzalez-Martin ML, Bruque JM, Gonzalez-Garcia CM. Comparison of the use of Washburn's equation in the distance-time and weight-time imbibition techniques. J Colloid Interface Sci. 2001;233:356-60.

[11] Xue HT, Fang ZN, Yang Y, Huang JP, Zhou LW. Contact Angle Determined

by Spontaneous Dynamic Capillary Rises with Hydrostatic Effects: Experiment and Theory. Chem Phy Lett. 2006;432:326-30.

[12] Popescu MN, Ralston J, Sedev R. Capillary Rise with Velocity-Dependent Dynamic Contact Angle. Langmuir. 2008;24:12710-6.

[13] Siebold A, Nardin M, Schultz J, Walliser A, Oppliger M. Effect of dynamic contact angle on capillary rise phenomena. Colloids Surf A: Physicochemical and Engineering Asp. 2000;161:81-7.

[14] Li X, Fan X, Brandani S. Difference in pore contact angle and the contact angle measured on a flat surface and in an open space. Chem Eng Sci. 2014;117:137-45.

[15] Fisher LR, Lark PD. An Experimental Study of the Washburn Equation for Liquid Flow in Very Fine Capillaries. J Colloid Interface Sci. 1979;69:486-92.

[16] Good RJ, Koo MN. The effect of drop size on contact angle. J Colloid Interface Sci. 1979;71:283-92.

[17] de Gennes PG, Brochard-Wyart F, Quéré D. Capillarity and wetting phenomena. New York: Springer; 2004 .p.15

[18] Vafaei S, Podowski MZ. Theoretical analysis on the effect of liquid droplet geometry on contact angle. Nucl Eng Des. 2005;235:1293-301.

[19] Ward CA, Sefiane K. Adsorption at the solid–liquid interface as the source of contact angle dependence on the curvature of the three-phase line. Adv Colloid Interface Sci. 2010;161:171-80.

[20] Ward CA, Wu J. Effect of Contact Line Curvature on Solid-Fluid Surface Tensions Without Line Tension. Phys Rev Lett. 2008;100:256103.

[21] Mason G, Morrow NR. Effect of Contact Angle on Capillary Displacement Curvatures in Pore Throats Formed by Spheres. Journal of Colloid and Interface Science. 1994;168:130-41.

[22] Mason G, Morrow N. Meniscus displacement curvatures of a perfectly wetting liquid in capillary pore throats formed by spheres. Journal of Colloid

and Interface Science. 1986;109:46-56.

[23] Brovchenko I, Oleinikova A. Effect of Pore Size on the Condensation/Evaporation Transition of Confined Water in Equilibrium with Saturated Bulk Water. J Phys Chem B. 2011;115:9990-10000.

[24] Tolman RC. The Effect of Droplet Size on Surface Tension. The Journal of Chemical Physics. 1949;17:333-7.

[25] D. GL, E. GK. Characterization of porous glasses by adsorption: models, simulations and data inversion. 6th Fundam of Adsorption Conference. Giens, France1998. p. 551-6.

[26] Amirfazli A, Neumann AW. Status of the three-phase line tension: a review. Advances in Colloid and Interface Science. 2004;110:121-41.

[27] Dutta RC, Khan S, Singh JK. Wetting transition of water on graphite and boron-nitride surfaces: A molecular dynamics study. Fluid Phase Equilibria. 2011;302:310-5.

[28] Werder T, Walther JH, Jaffe RL, Halicioglu T, Koumoutsakos P. On the Water−Carbon Interaction for Use in Molecular Dynamics Simulations of Graphite and Carbon Nanotubes. The Journal of Physical Chemistry B. 2003;107:1345-52.

[29] Amirfazli A, Chatain D, Neumann AW. Drop size dependence of contact angles for liquid tin on silica surface: line tension and its correlation with solid–liquid interfacial tension. Colloids and Surfaces A: Physicochemical and Engineering Aspects. 1998;142:183-8.

[30] Amirfazli A, Keshavarz A, Zhang L, Neumann AW. Determination of line tension for systems near wetting. Journal of Colloid and Interface Science. 2003;265:152-60.

[31] Amirfazli A, Kwok DY, Gaydos J, Neumann AW. Line Tension Measurements through Drop Size Dependence of Contact Angle. Journal of Colloid and Interface Science. 1998;205:1-11.

[32] David R, Park MK, Kalantarian A, Neumann AW. Drop size dependence of contact angle on two fluoropolymers. Colloid Polym Sci. 2009;287:1167-73.

[33] Duncan D, Li D, Gaydos J, Neumann AW. Correlation of Line Tension and Solid-Liquid Interfacial Tension from the Measurement of Drop Size Dependence of Contact Angles. Journal of Colloid and Interface Science. 1995;169:256-61.

[34] Gaydos J, Neumann AW. The dependence of contact angles on drop size and line tension. Journal of Colloid and Interface Science. 1987;120:76-86.

[35] Kaveh NS, Rudolph ESJ, van Hemert P, Rossen WR, Wolf KH. Wettability Evaluation of a CO2/Water/Bentheimer Sandstone System: Contact Angle, Dissolution, and Bubble Size. Energy & Fuels. 2014;28:4002-20.

[36] Lam CNC, Kim N, Hui D, Kwok DY, Hair ML, Neumann AW. The effect of liquid properties to contact angle hysteresis. Colloids and Surf A: Physicochem Eng Asp. 2001;189:265-78.

[37] Spelt JK, Li D. The equation of state approach to interfacial tensions. Applied Surface Thermodynamics. New York: Marcel Dekker; 1996. p. 239-92.

[38] Busscher HJ, Kip GAM, Van Silfhout A, Arends J. Spreading pressures of water and n-propanol on polymer surfaces. J Colloid Interface Sci. 1986;114:307-13.

[39] Horng P, Brindza MR, Walker RA, Fourkas JT. Behavior of Organic Liquids at Bare and Modified Silica Interfaces. J Phys Chem C. 2010;114:394-402.

[40] ikalo S, Marengo M, Tropea C, Ganic EN. Analysis of impact of droplets on horizontal surfaces. Exp Therm Fluid Sci. 2002;25:503-10.

[41] Li X. Asphaltene Precipitation from Crude Oil by Filtration and AFM studies on Surface Characteristics of Asphaltenes (dissertation) [Msc thesis]. London: Imperial College London; 2011. p.102

[42] Orejon D, Sefiane K, Shanahan MER. Stick–Slip of Evaporating Droplets:

Substrate Hydrophobicity and Nanoparticle Concentration. Langmuir. 2011;27:12834-43.

[43] Kwok DY, Neumann AW. Contact Angle Interpretation in terms of Solid Surface Tension. Colloids and Surf A: Physicochem Eng Asp. 2000;161:31-48.

[44] Spelt JK, Li D, Neumann AW. The Equation of State Approach to Interfacial Tensions. In: Schrader M, Loeb G, editors. Modern Approaches to Wettability: Springer US; 1992. p. 101-42.

[45] Sghaier N, Prat M, Ben Nasrallah S. On the influence of sodium chloride concentration on equilibrium contact angle. Chemical Engineering Journal. 2006;122:47-53.

[46] Khan MI, Nasef MM. Spreading behaviour of silicone oil and glycerol drops on coated papers. Leonardo Journal of Sciences. 2009:18-30.

Chapter 5: Dynamic Pore Wetting[2]

5.1 Introduction

Dynamic pore wetting is significant for the understanding of fluid behaviour and adsorption in porous media for fuel cells, enhanced oil recovery, groundwater movements, nanofluidics and nanolubrication. However, few studies have been conducted which measure the dynamic contact angle in a small pore. Most experimental and theoretical work on dynamic wettability have considered a planar solid substrate rather than pores [1]. It is generally accepted that an ensemble of single capillaries with simplified geometries could represent a porous system [2]. In this chapter, in order to investigate the dynamic pore wetting phenomenon in porous media, the dynamic contact angles of various liquids imbibed into single glass capillaries are measured as a function of interfacial velocity during imbibition experiment [3]. The dependence of the dynamic pore contact angle on the interfacial velocity of the invading liquid is studied. The results reveal the effects of surface tension and viscosity of liquids on the dynamic contact angle of liquids in pores.

The dynamic wetting of liquids can be described by Blake's molecular-kinetic theory [4] and a number of empirical correlations [1, 5, 6]. In this study, a new empirical correlation is developed to describe the dynamic wetting in a pore in a low capillary number regime. Blake's molecular-kinetic theory is also used to explain our experimental the dynamic pore contact angle results.

[2] Some of the content of this chapter has been published in Chemical Engineering Science 2013;104:988-97

5.2 Dynamic Contact Angles in Glass Capillaries

The dynamic contact angles of a number of liquids with various surface tensions and viscosities were measured as a function of interfacial velocity in single glass capillaries in this study. For example, the dynamic contact angles of silicone oil with a viscosity of 9.30×10^{-3} Pa s in a micron-sized glass capillary for the interfacial velocity range from 0 to 0.0012 m/s are shown in Figure 5.1. The results indicate that the dynamic contact angle depends on the imbibition rate (interfacial velocity) and monotonically increases with imbibition rate. The contact angle of silicone oil at the interface velocity of zero corresponds to the static contact angle, which is around 23°. The dynamic contact angle of silicone oil significantly increases by roughly 15° when the velocity increases from 0 to 0.0004 m/s. This increase is less significant as the imbibition rate increases from 0.0004 to 0.0012 m/s. Within this range, the contact angle increases from around 38° to 48°. The measurement errors become larger at higher interfacial velocities.

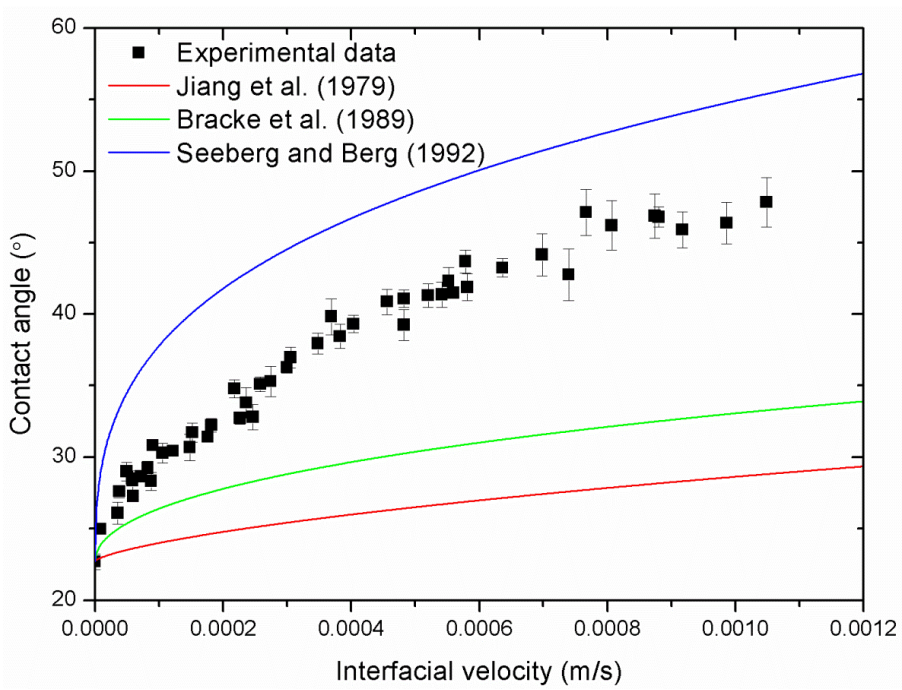

Figure 5.1 Experimental data of dynamic contact angles of silicone oil ($\eta=9.30\times10^{-3}$ Pa s) in glass capillaries, and data calculated using empirical correlations [1, 5, 6]

In Figure 5.1, the experimental contact angle data of silicone oil is compared with results predicted by empirical correlations [1, 5, 6] in the literature. In general, the dynamic contact angles calculated using empirical correlations increase monotonically with imbibition rate from 0 to 0.0012 m/s, but their profiles are very different. The dynamic pore contact angles calculated from the correlation proposed by Seeberg and Berg [1] is much higher than the present experimental data and those from other correlations. The dynamic contact angles measured in this study are closer to the predictions of Jiang et al.'s [5] and Bracke et al.'s [6] empirical correlations, but there are still significant deviations. The comparison might imply that these three empirical correlations in literature do not accurately describe the dynamic wetting behaviour of liquids in a small pore found in this study.

The dynamic pore contact angles of water, 1-propanol, n-decane, crude oil and silicone oil are shown in Figure 5.2, for imbibition rates ranging from 0 to 0.0012 m/s. When the interfacial velocity increases from 0 to 0.0012 m/s, the dynamic contact angle of silicone oil significantly increases with the interfacial velocity, from 22° to 50°, and the contact angle of crude oil increases by approximately 40°. On the other hand, the dynamic contact angles of water, 1-propanol and n-decane vary only by 3.0-5.2^{o}. Thus, the results could indicate that the dynamic contact angles of crude oil and silicone oil, which have greater viscosities, are highly velocity-dependent, while the dynamic contact angles of water, 1-propanol and n-decane are less velocity-dependent. These five liquids have various physical and chemical properties. The velocity-dependent dynamic pore wetting behaviour might be jointly affected by viscosity and surface tension of the liquid. Thus, these two important properties of liquids are studied separately in the following section to reveal the effects of the surface tension and viscosity of liquids on their dynamic contact angles in a capillary.

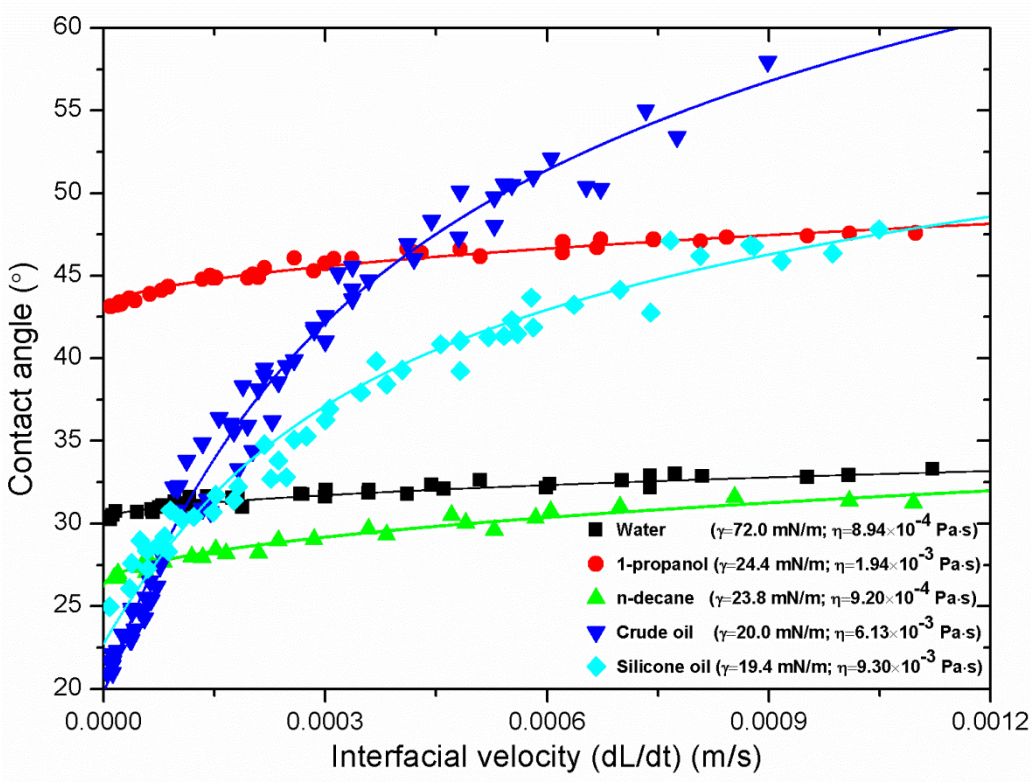

Figure 5.2 Dynamic contact angles of DI water, 1-propanol, n-decane, crude oil and silicone oil (η=9.30×10^{-3} Pa s) in a pore

5.3 Effects of Surface Tension and Viscosity on the Dynamic Contact Angle in a Pore

5.3.1 Effect of Surface Tension

The effect of the surface tension of a liquid on its dynamic contact angle in a pore is illustrated in Figure 5.3. To investigate the effect of surface tension on dynamic pore wetting, the effect of liquid viscosity should be minimized. Here, water, and 1-propanol and its aqueous solutions are used. The surface tensions of water, 1-propanol aqueous solutions and 1-propanol vary significantly from 24.4 to 72.0 mN/m, but their viscosities are small and close together, ranging from 8.94×10^{-4} to 1.94×10^{-3} Pa s. Figure 5.3(a) indicates that these four liquids have similar dynamic contact angle trends. However, they differ in the magnitude of contact angle variation (Figure 5.3(b)).

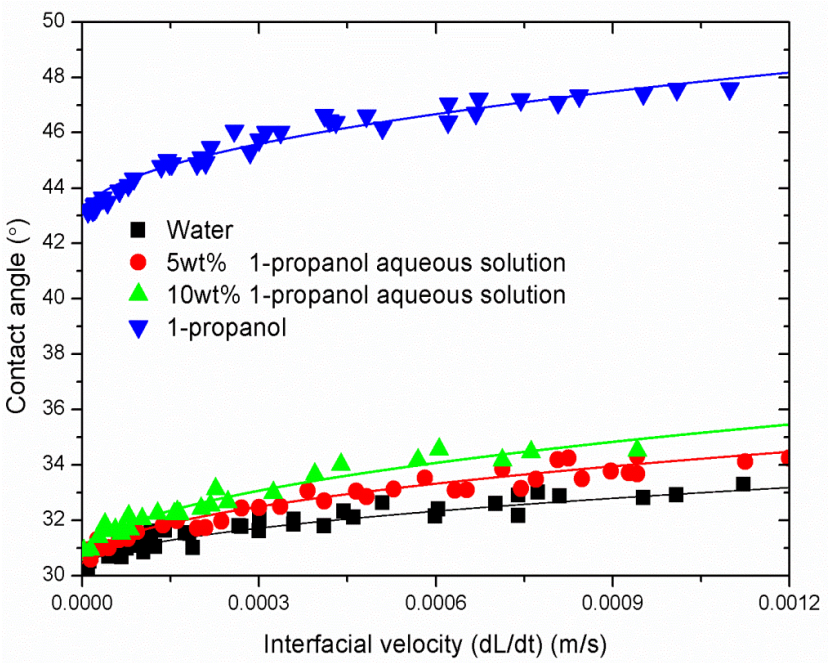

(a)

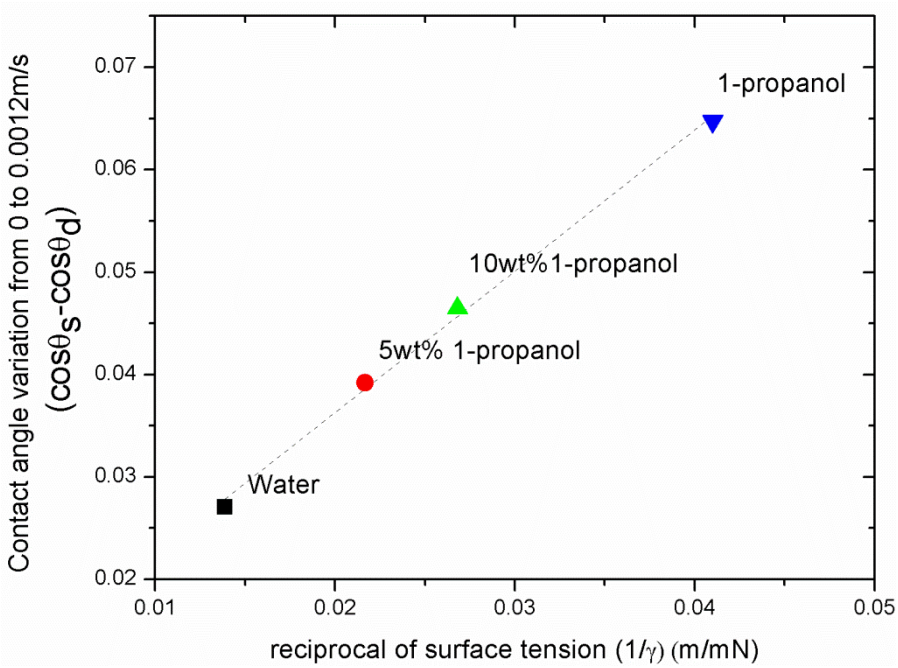

(b)

Figure 5.3 (a) Dynamic contact angle; and (b) contact angle variation from 0 to 0.0012 m/s of water (γ=72.0 mN/m; η=8.94×10^{-4} Pa s), 1-propanol (γ=24.4 mN/m; η=1.94×10^{-3} Pa s), 5wt% 1-propanol aqueous solution (γ=46.2 mN/m; η=1.10×10^{-3} Pa s) and 10wt% 1-propanol aqueous solution (γ=37.3 mN/m; η=1.34×10^{-3} Pa s)

Figure 5.3(b) indicates that the variation between the cosine of the equilibrium contact angle and the dynamic contact angle at an interfacial velocity of 0.0012 m/s ($\cos\theta_s$-$\cos\theta_d$) increases positively and linearly with the reciprocal of surface tension ($1/\gamma$). Water has the highest surface tension (72.0 mN/m), while its dynamic contact angle increases insignificantly at an interfacial velocity of 0 to 0.0012 m/s, only by 3°. The 5 wt% and 10 wt% 1-propanol aqueous solutions have lower and close surface tensions of 37.3 mN/m and 46.2 mN/m. Their dynamic contact angles vary by approximately 4.8° and 4.2° respectively. 1-propanol has the lowest surface tension (24.4 mN/m), while the variation of dynamic contact angle with interfacial velocity is more significant at around by 5.2°. Therefore, it can be concluded that the velocity-dependent dynamic pore contact angle can be affected by the surface tension of liquid, and this effect is more significant for liquids with lower surface tension.

It can also be seen from Figure 5.3(a) that the static contact angles of water and 1-propanol aqueous solutions are significantly different from those of 1-propanol at the interfacial velocity of zero. Water and 1-propanol aqueous solutions have similar equilibrium contact angles of around 30°, but the static contact angle of 1-propanol is much higher by 10°. This is due to the effect of the concentration of the amphiphile in an amphiphile-water mixture on the glass pore contact angle, which is discussed in detail in Chapter 6.

5.3.2 Effect of Viscosity

Five silicone oils were used in this study to investigate the effect of the viscosity of a liquid on its dynamic pore contact angle. The viscosities of these five silicone oils are significantly different, ranging from 9.30×10^{-3} Pa s to 9.70×10^{-1} Pa s, but they have very similar surface tensions of around 20 mN/m. The effect of liquid viscosity on

the dynamic contact angle in a pore is shown in Figure 5.4. Figure 5.4 (a) indicates that these five silicone oils have similar dynamic contact angle trends. The contact angle monotonically increases with interfacial velocity. However, they give different magnitudes of contact angle variation (Figure 5.4(b)). The results show that viscosity significantly affects the dynamic contact angle but not the static contact angle (Figure 5.4 (a)). The static contact angles of all the silicone oils stay at around 23°. However, the dynamic contact angles of the more viscous silicone oils are always higher than those from less viscous silicone oils at the same interfacial velocity. Figure 5.4(b) indicates that the difference between the cosine of the equilibrium contact angle ($\cos\theta_s$) and dynamic contact angle ($\cos\theta_d$) at an interfacial velocity of 0.001 m/s increases with the logarithm of viscosity ($\log \eta$) in a linear fashion.

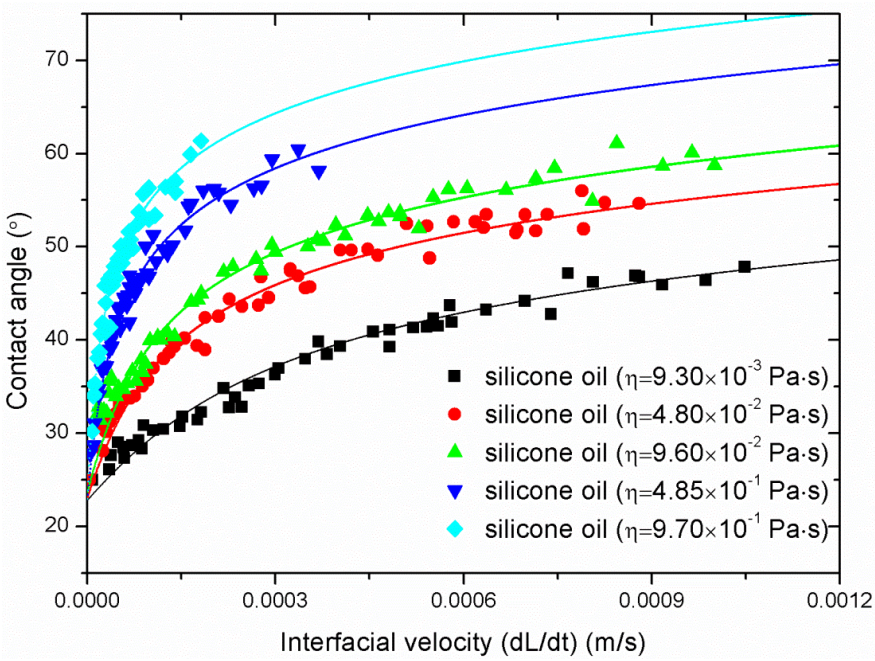

(a)

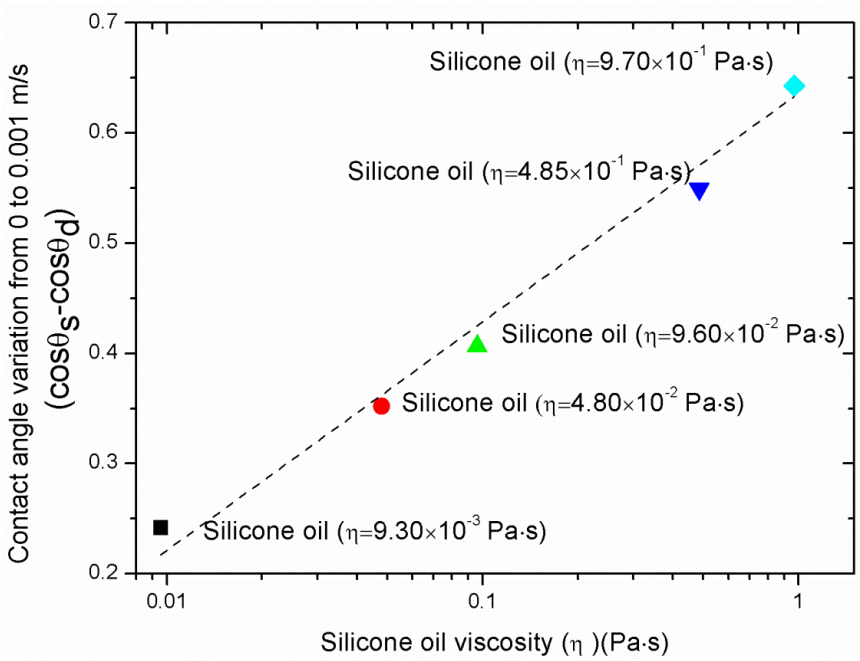

(b)

Figure 5.4 (a) Dynamic contact angle; and (b) contact angle variation ($\cos\theta_s$-$\cos\theta_d$) from 0 to 0.0012 m/s of silicone oils with different viscosities of 9.30×10^{-3} Pa s, 4.80×10^{-2} Pa s, 9.60×10^{-2} Pa s, 4.85×10^{-1} Pa s and 9.70×10^{-1} Pa s and similar surface tensions of 19.4 mN/m, 20.8 mN/m, 20.9 mN/m, 21.2 mN/m and 21.2 mN/m respectively. The scale in the x-axis (the viscosity of silicone oil) of (b) is logarithmic with base 10.

Thus, we can conclude that the dependence of the contact angle on interfacial velocity is more significant for liquids with lower liquid-gas surface tension and higher viscosity in porous materials. For example, Friedman proposed that the dynamic contact angle depends on the velocity more markedly for NAPLs than for water [2], due to the fact that water has a very large surface tension but low viscosity.

5.4 A New Empirical Correlation for Dynamic Pore Contact Angle

Dynamic wetting could be expressed by the empirical correlations proposed by Jiang et al. [5], Bracke et al. [6] and Seebergh et al. [1]. All these empirical correlations describe the dynamic contact angle as a function of the capillary number (Ca) and the static contact angle (θ_s):

$$\theta_d = f\,(Ca, \theta_s) \tag{5.1}$$

where Ca is the capillary number defined as the ratio of viscous forces to interfacial forces: $Ca = v\,\eta/\gamma$.

All three of these empirical correlations can be unified into a "universal function" [1] as:

$$H = \frac{\cos\theta_s - \cos\theta_d}{\cos\theta_s + 1} = ACa^B \tag{5.2}$$

$$\log_{10}(H) = B\log_{10}(Ca) + \log_{10}(A) \tag{5.3}$$

where H is the dimensionless function for dynamic contact angle, and A and B are correlation constants. Although the correlations can follow a linear relationship between $\log_{10}(H)$ and $\log_{10}(Ca)$, different constants (A,B) are required to fit the data [1].

Table 5.1 Empirical correlations and fitting parameters for dynamic contact angle in the literature

Author	***Empirical correlation***	***Correlation constants in Equations 5.2,5.3***	
		A	***B***
Jiang et al. [5]	$H = \frac{\cos\theta_s - \cos\theta_d}{\cos\theta_s + 1} = 4.96Ca^{0.702}$ $\log_{10}(H) = 0.702 \log_{10}(Ca) + 0.70$	4.96	0.702
Bracke et al. [6]	$H = \frac{\cos\theta_s - \cos\theta_d}{\cos\theta_s + 1} = 2Ca^{0.5}$ $\log_{10}(H) = 0.5 \log_{10}(Ca) + 0.30$	2	0.5
Seebergh and Berg [1]	$H = \frac{\cos\theta_s - \cos\theta_d}{\cos\theta_s + 1} = 4.47Ca^{0.42}$ $\log_{10}(H) = 0.42 \log_{10}(Ca) + 0.65$	4.47	0.42

The dynamic wetting empirical correlations proposed by Jiang et al. [5], Bracke et al. [6] and Seebergh et al. [1] are presented in Table 5.1. The correlations proposed by Jiang et al. and Bracke et al. are preferred to describe dynamic wetting for a high capillary number regime, such as when the capillary number is over 0.001 [5, 6]. Seebergh and Berg noticed that the contact angles predicted by Jiang et al. and Bracke et al. had weak consistency with experimental contact angle data for low capillary numbers ($10^{-3} < Ca < 10^{-7}$) [1]. Thus, Seebergh and Berg extended the dynamic contact angle measurements to a low capillary number region. They

proposed an empirical correlation to describe dynamic wetting behaviour at low capillary numbers and considered the effect of the stick-slip phenomenon [1].

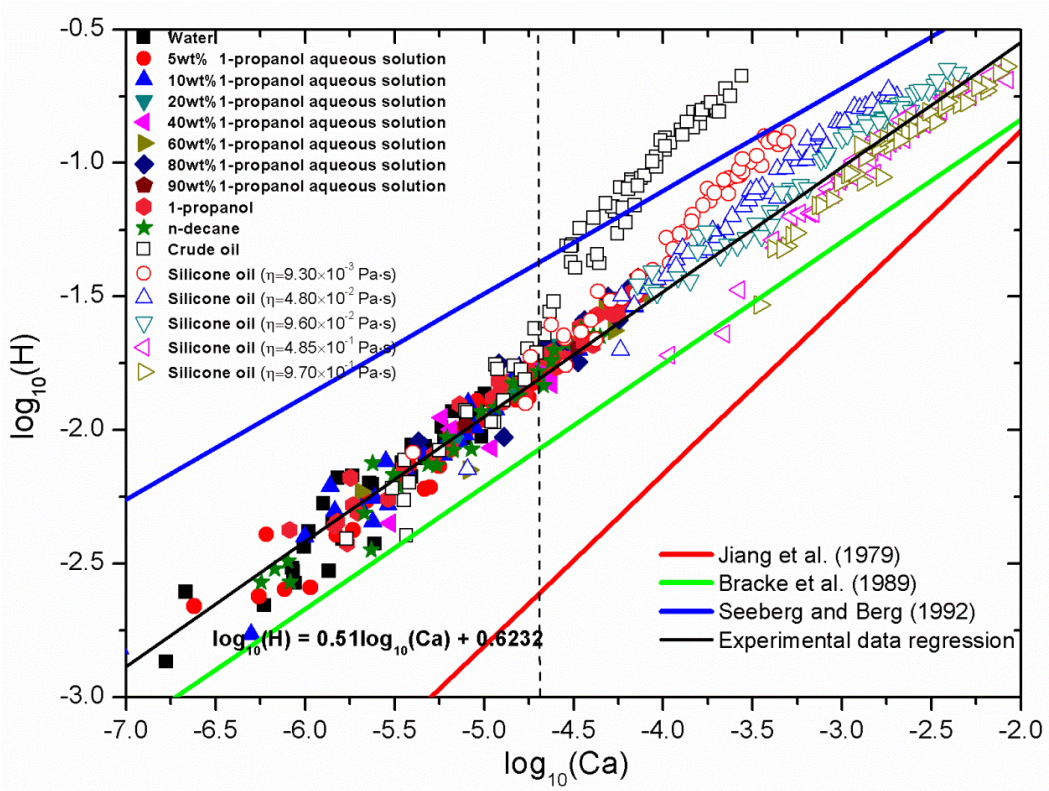

Figure 5.5 Comparison of empirical correlations (Table 5.1) with the experimental data in the present study in a low capillary number (Ca) range

As discussed, a few empirical correlations have been developed to describe dynamic wetting behaviour [1, 5, 6]. However, these correlations have not been developed to describe the dynamic contact angle in a micron-sized pore. In Figure 5.5, our experimental dynamic pore contact angle data is compared with the results calculated by these previous empirical correlations. Based on Equation 5.3, all the data is plotted using $\log_{10}(\mathrm{H})$ against $\log_{10}(\mathrm{Ca})$. The comparison shows that our experimental results are different from predictions based on the empirical correlations proposed by Jiang et al. [5], Bracke et al. [6], and Seeberg and Berg [1]. Our experimental values are larger than the data calculated from the correlations developed by Jiang et al. [5] and Bracke et al. [6]. The dynamic pore contact angles

calculated using Seeberg and Berg's [1] correlation differ from and are greater than our experimental results, even though a similar capillary regime was investigated in Seeberg and Berg's work [1] and this study. The Seebergh and Berg [1] correlation concerns the stick-slip effect on the dynamic contact angle. For their systems, the stick-slip effect might produce a large degree of scatter. Thus, this might be one of the reasons why Seebergh and Berg's [1] correlation gives the highest estimation of dynamic contact angles. Stick-slip behaviour mainly results from the effect of rough surfaces. However, smooth capillary interiors were used in this study, and thus the stick-slip effect will have been negligible.

The contact angle trends in Figure 5.5 show that our measured $\log_{10}(\mathrm{H})$ for all the liquids are very close and increase with $\log_{10}(\mathrm{Ca})$ in a linear fashion when the capillary number ($\log_{10}(\mathrm{Ca})$) is less than -4.75. The measured $\log_{10}(\mathrm{H})$ varies with the liquids used when the capillary number ($\log_{10}(\mathrm{Ca})$) is greater than -4.75. The highest $\log_{10}(\mathrm{H})$ can be observed for crude oil, even though its surface tension and viscosity are similar to those of silicone oil ($\eta = 9.30 \times 10^{-3}$ Pa s). This most significant difference in crude oil's dynamic contact angle might be attributed to the dewetting behaviour caused by the effect of the amphiphilic surfactants in the crude oil on the invading interface on a high-energy glass surface [7-10]. The effect of amphiphile organic compounds on glass pore wetting is discussed in detail in the following chapter.

A linear least-square fit of the experimental data yields Equation 5.4, based on a good linear relationship between $\log_{10}(\mathrm{H})$ and $\log_{10}(\mathrm{Ca})$ for capillary number $\log_{10}(\mathrm{Ca})$ ranging from -7.0 to -4.75. This adopts the same format as the empirical correlation in Equation 5.3 in which $\log_{10}(\mathrm{H})$ increases linearly with $\log_{10}(\mathrm{Ca})$ (Figure 5.5):

$$H = 4.2\ Ca^{0.51} \tag{5.4}$$

Equation 5.4 is a regression of the dynamic contact angles in a pore based on our experimental data. The dynamic contact angle predicted by our correlation is greater than those of Jiang et al.'s [5] and Bracke et al.'s [6] correlations, but smaller than Seeberg and Berg correlation [1]. The constants A and B in Equation 5.4 differ from those in Jiang et al. [5], Bracke et al. [6] and Seeberg and Berg [1] (Table 5.1). This new empirical correlation developed here can be used to predict the dynamic contact angle in a small pore for liquids with a capillary number ($\log_{10}(Ca)$) less than -4.75 in a low capillary number range ($1.0\times10^{-7} < Ca < 1.8\times10^{-5}$).

5.5 Prediction of Dynamic Pore Wetting by Molecular-kinetic Theory

Blake developed a molecular-kinetic theory of a three-phase moving line [11, 12] based on an adsorption/desorption model. The imbibition rate (penetration/interfacial velocity) is given by:

$$v = \frac{dL}{dt} = 2K_0\lambda\sinh\left[\frac{\gamma(\cos\theta_s - \cos\theta_d)}{2nk_BT}\right] \tag{5.5}$$

For small values of $\sinh(\frac{w}{2nk_BT})$ in Eq (5.5), the Eq (5.5) can be linearized to [13]

$$v = \frac{dL}{dt} = \frac{\kappa_0\lambda^3}{K_BT}[\gamma(\cos\theta_s - \cos\theta_d)] \tag{5.6}$$

or

$$\cos\theta_d = \cos\theta_s - \frac{\xi}{\gamma}\frac{dL}{dt} \tag{5.7}$$

where $\xi = \frac{K_BT}{\kappa_0\lambda^3}$ is a coefficient of so-called 'wetting line friction'[14].

where κ_0 is the frequency of molecular displacement (s^{-1}), n denotes the number of adsorption sites per unit area ($n^{-1}=\lambda^2$) (m^{-2}), λ is the average length of each molecular displacement (m), T is temperature (K) and k_B denotes the Boltzmann constant (k_B = 1.381×10^{-23} J K^{-1}). The term $\gamma(\cos\theta_s - \cos\theta_d)$ can be regarded as the nonequilibrated surface tension force needed to drive the motion of the wetting line.

Because our empirical correlation cannot adequately describe the dynamic pore contact angles in a large capillary number regime (Ca>1.8×10^{-5},$\log_{10}$(Ca)>4.75),

Blake's molecular-kinetic theory (Equation 5.5) can be used to describe the dynamic pore contact angle of a liquid with a higher viscosity or larger capillary number by fitting two important parameters of liquids, the frequency of molecular displacement (κ_0) and the average length of displacement (λ) in Equation 5.6 (Table 5.2). Bertrand et al. defined a coefficient based on molecular-kinetic theory called the wetting line friction ($\zeta=k_BT/\kappa_0\lambda^3$ in Equations 5.6 and 5.7)) involving frequency of molecular displacement (κ_0) and average length of displacement (λ) [14]. This wetting line friction coefficient depends on both fluid viscosity and liquid-solid interaction [14]. The wetting line friction coefficients for the dynamic pore wetting of our measured liquids are calculated and shown in Figure 5.6, showing a similar trend as for liquid viscosity. The wetting line friction coefficient increases from the less viscous liquids to NAPLs (non-aqueous phase liquids) with higher viscosities. If this coefficient could be estimated, the dynamic pore contact angle can be readily determined based on Equation 5.7. Thus, all the dynamic pore wetting phenomena can be well described. In this study, the wetting line friction coefficients of water, n-decane, 1-propanol, crude oil and silicone oils in glass pores were evaluated. Because of the importance of this coefficient, the wetting line friction coefficients for other liquids in pores with different materials will be estimated in future work.

Table 5.2 The fitting parameters (κ_0, λ) in molecular-kinetic theory for various liquids

Liquids	*Fitting parameters*	
	λ (molecular displacement length)	*κ_0 (molecular displacement frequency)*
n-decane	4.5	1.60×10^4
1-propanol	3.95	1.70×10^4
Water	3.5	2.00×10^4
Silicone oil (10cst)	2	5.00×10^4
Crude oil	1.43	8.80×10^4
Silicone oil (50cst)	1.9	2.00×10^4
Silicone oil (100cst)	1.8	1.85×10^4
Silicone oil (500cst)	1.74	7.40×10^3
Silicone oil (1000cst)	1.72	4.00×10^3

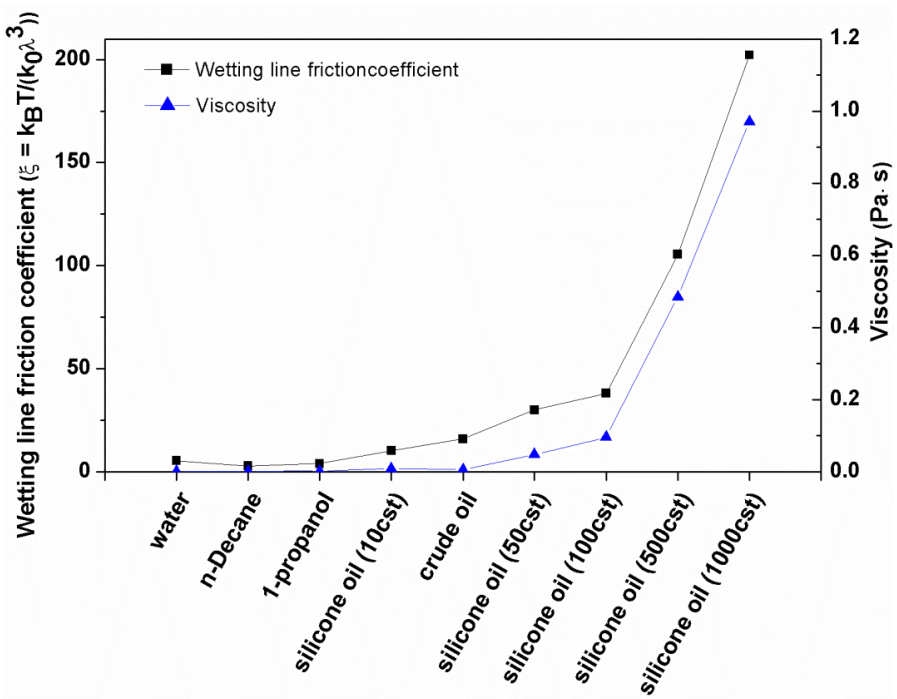

Figure 5.6 Wetting line friction coefficients of various liquids

5.6 Summary

This chapter mainly focuses on the direct measurements of the dynamic contact angles of various liquids in a single glass pore by conducting spontaneous imbibition experiments, and determine the effects of surface tension and the viscosity of liquids on the dynamic pore contact angle [3]. A new empirical correlation is developed to describe the dynamic wetting in a small pore at a low capillary regime. The results indicate that:

(1) The dynamic contact angle of a liquid in a pore varies and increases monotonically with interfacial velocity.

(2) The dynamic pore contact angle is significantly affected by the surface tension and viscosity of liquids. A liquid with higher viscosity or lower surface tension tends to have greater variation in dynamic contact angle with changing interfacial velocity.

(3) A new empirical correlation (Equation 5.4) developed based on our experimental data can describe the dynamic wetting of liquids in a small pore at a low capillary number regime ($1.0\times10^{-7} < Ca < 1.8\times10^{-5}$).

(4) The dynamic pore contact angles of highly viscous liquids (crude oil, silicone oils) with larger capillary numbers ($1.80\times10^{-5} < Ca < 6.74\times10^{-3}$) could be effectively described by Blake's (1998) molecular-kinetic theory by estimating the wetting line friction coefficients of the movement of liquids against solid surfaces.

5.7 References

[1] Seebergh JE, Berg JC. Dynamic Wetting in the Low Capillary Number Regime. Chem Eng Sci 1992;47:4455-64.

[2] Friedman SP. Dynamic contact angle explanation of flow rate-dependent saturation-pressure relationships during transient liquid flow in unsaturated porous media. J Adhes Sci Technol. 1999;13:1495-518.

[3] Li X, Fan X, Askounis A, Wu K, Sefiane K, Koutsos V. An Experimental Study on Dynamic Pore Wettability. Chem Eng Sci. 2013;104:988-97.

[4] Martic G, Gentner F, Seveno D, Coulon D, De Coninck J, Blake TD. A Molecular Dynamics Simulation of Capillary Imbibition. Langmuir. 2002;18:7971-6.

[5] Jiang TS, Oh SG, Slattery JC. Correlation for dynamic contact angle. J Colloid Interface Sci. 1979;69:74-7.

[6] Bracke M, De Voeght F, Joos P. The kinetics of wetting: the dynamic contact angle. Prog Colloid Polym Sci. 1989;79:142-9.

[7] Afsar-Siddiqui AB, Luckham PF, Matar OK. Unstable Spreading of Aqueous Anionic Surfactant Solutions on Liquid Films. Part 1. Sparingly Soluble Surfactant. Langmuir. 2003;19:696-702.

[8] Afsar-Siddiqui AB, Luckham PF, Matar OK. Unstable Spreading of Aqueous Anionic Surfactant Solutions on Liquid Films. 2. Highly Soluble Surfactant. Langmuir. 2003;19:703-8.

[9] Afsar-Siddiqui AB, Luckham PF, Matar OK. Dewetting Behavior of Aqueous Cationic Surfactant Solutions on Liquid Films. Langmuir. 2004;20:7575-82.

[10] Craster RV, Matar OK. On Autophobing in Surfactant-Driven Thin Films. Langmuir. 2007;23:2588-601.

[11] Blake TD. Dynamic contact angles and wetting kinetics. in Wettability. 1993:251-309.

[12] Glasstone S, Laidler KJ, Eyring HJ. The theory of rate processes. 1941.

[13] Stukan MR, Ligneul P, Crawshaw JP, Boek ES. Spontaneous Imbibition in Nanopores of Different Roughness and Wettability. Langmuir. 2010;26:13342-52.

[14] Bertrand E, Blake TD, De Coninck J. Influence of solid-liquid interactions on dynamic wetting: a molecular dynamics study. J Phys: Condens Matter. 2009;21:464124.

Chapter 6: Effect of Chemical Structure of Organics on Pore Wetting

6.1 Introduction

Young's equation can describe the extent of wetting in terms of the contact angle (θ) and surface tension (γ). An important conclusion of this equation is that a liquid with low surface tension is expected to give a small contact angle or to completely spread on a solid surface with high energy, such as glasses, metals and oxides [1]. However, some pure organics with low values of surface tension form a large contact angle on mica or glass surfaces instead of completely spreading [2, 3]. Zisman and co-workers noted that some amphiphilic organic compounds with low surface tensions did not completely spread on high-energy solid surfaces [4, 5]. An oriented monolayer of amphiphilic molecules forms on the high-energy solid surface because of the sufficiently strong surface interaction between the solid surface and the liquid molecules. This leads to the incomplete spreading of the amphiphlic liquid on its own monolayers, which is called autophobing [5, 6]. Some studies have reported the incomplete spreading of pure amphiphiles and amphiphile aqueous solutions on a high-energy hydrophilic flat substrate [7-12], but few such studies have been conducted in a small pore.

Most amphiphilic organics are fundamental components of nonionic surfactants, which are tailed with hydrophobic groups (apolar fatty alkyl chains) but headed with hydrophilic functional groups such as –OH, -NH_2 and -COOH. However, the effects of the functional and alkyl groups of these amphiphilic organic compounds on the

pore wetting of high-energy hydrophilic surfaces have not been systematically investigated. This chapter examines the effects of functional group (-OH, $-NH_2$, -COOH) and the length and structure of alkyl chains of pure amphiphilic organic compounds on their contact angles in glass and polymeric capillaries. As is well known, pore wetting is a crucial factor for the estimation of the displacement of oil by water and oil-water migration in the enhanced oil recovery process. The information presented in this chapter can give some indications as to how chemical structure affects pore wetting, and further influences the displacement and migration of pore fluids, and consequently the selection of chemicals in surfactant flooding.

6.2 Pore Contact Angle of Pure Amphiphile

The contact angles in a glass pore and on a flat glass surface for the organics used in this study are shown in Figure 6.1. The results indicate that contact angle varies with the functional group, the length of the carbon chain, and the arrangement of carbons in the alkyl chain of organics, even though their surface tensions are very similar (~20 mN/m). The change in contact angle is not proportional to the change in liquid surface tension. Alkanols, alkylamines and alkyl carboxyl acids have similar surface tensions, but some of them give very different contact angles. For instance, heptanoic acid, 1-octanol and 1-decanol have similar surface tensions to those of all of the other organics (~20 mN/m), but give a contact angle of around 20° which is much larger than the contact angles from other organics on a flat glass surface by more than 10°, as shown in Figure 6.1. The long-chain alkyl acids, amines and alcohols have low surface tensions, but give large contact angles of up to 20° and 65° on a flat surface and in a pore respectively.

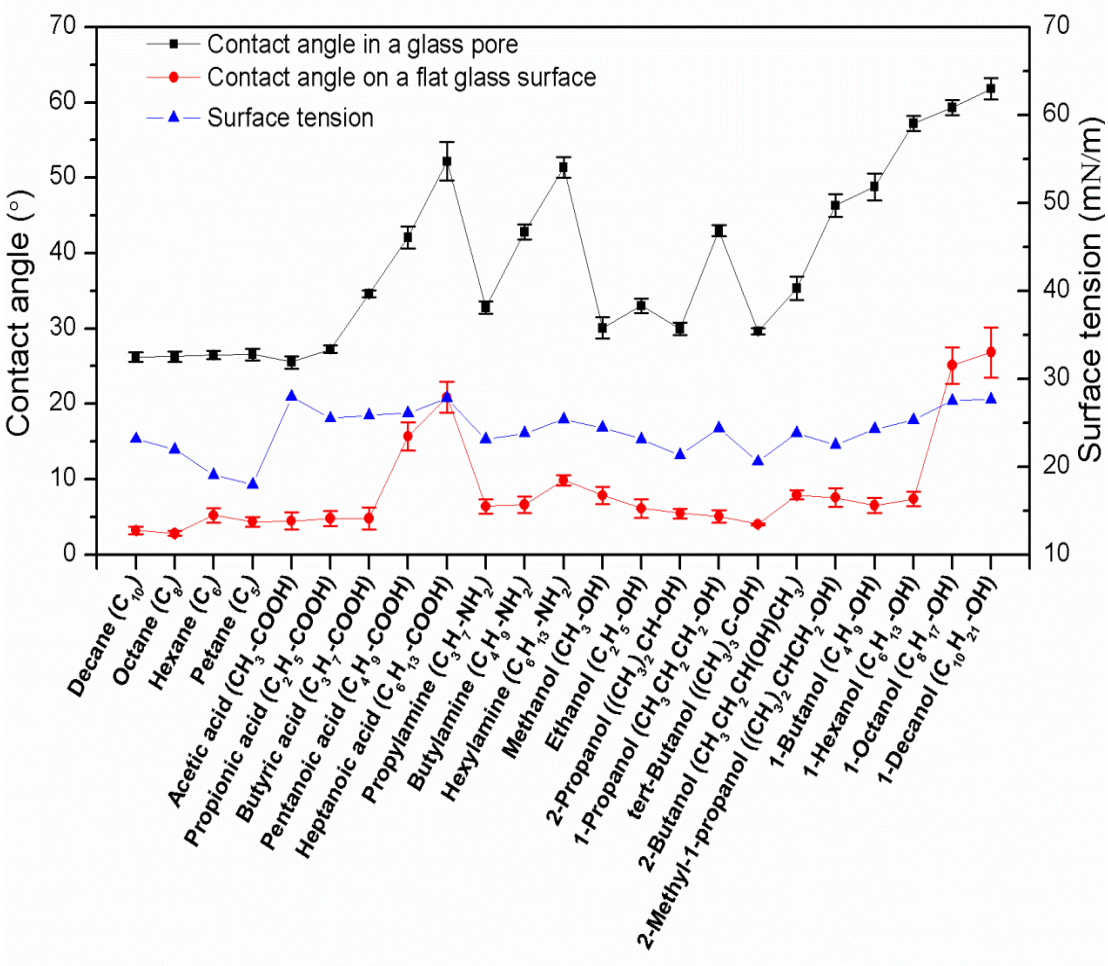

Figure 6.1 Contact angles in a glass pore and on a flat glass surface and the surface tensions for the organics used in this study

The contact angles of most organics on a flat glass surface are always smaller than those in a glass pore (Figure 6.1). This difference has been discussed and explained in chapter 4. The difference in the contact angles measured in a small pore and on a flat surface in an open space might also mainly result from the effects of curved geometry or confinement and the three-phase line curvature in a capillary, as well as the different vapor saturation conditions on a flat surface and in a small pore [13].

The alkanols, alkyl amines and alkyl carboxyl acids with an alkyl chain over 4 carbon atoms gave contact angles over 40 ° and 20 ° in a glass pore and on a flat glass surface respectively. The large contact angles of long-chain amphiphilic organic

compounds in a glass pore and on a flat glass surface might be caused by the adsorption of oriented amphiphile layers on the high-energy surface, which is called autophobing [7-12, 14-17]. It has been reported that several organics with low surface tensions cannot spread completely on high energy solid surfaces under their own saturated vapor [4-6]. The adsorbed amphiphile molecules lead the solid-vapor interfacial tension (γ_{SV}) to be lower than the solid-vacuum interfacial tension (γ_S), and thus result in incomplete spreading and the higher contact angle of the drop [16-18].

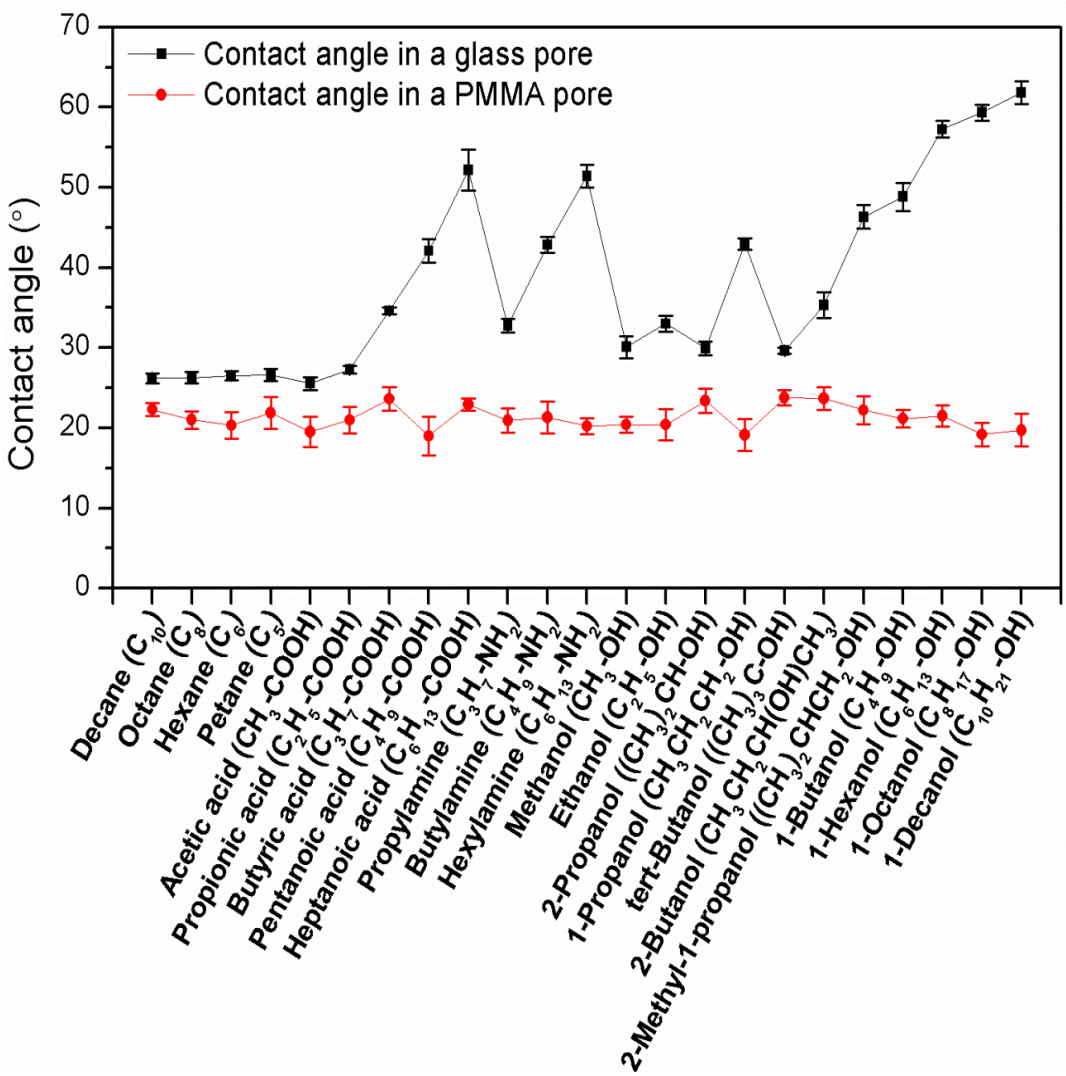

Figure 6.2 Comparison of contact angles measured in a glass pore and a PMMA pore

In addition, the pore contact angles of the amphiphiles used in this study were also

measured in a PMMA (polymethyl methacrylate) capillary, and compared with those in a glass capillary as shown in Figure 6.2. PMMA is hydrophobic, oil-wet and has low surface energy ($\gamma_s \approx 38$ mN/m) [18]. The results indicate that all the organics give similar and small pore contact angles of 20°. The wetting behaviour of amphiphilic organic compounds in an oil-wet pore is not significantly related to the molecular structure of the amphiphile.

Novotny and Marmur demonstrated that the amphiphile vapor film formation mechanism involved evaporation followed by adsorption rather than surface diffusion [17]. As the amphiphile layer is formed by evaporation, its vapor pressure must be considered as one of the important factors in this study. However, the results shown in Figure 6.3 indicate that the contact angles of alkanols, alkylamines and alkyl carboxyl acids do not clearly relate to their vapor pressures. Novotny and Marmur suggested that the adsorbed vapor film could be mainly controlled by the adsorption characteristics of the amphiphile molecules rather than vapor pressure [17]. In Figures 6.2 and 6.3, the contact angle of pure amphiphile in a glass pore varies greatly with molecular structure and molecular weight. The effect of molecular structure on contact angle is likely to be complex. In the following sections of this chapter, the effects of functional group and the alkyl chains of amphiphiles on the pore contact angle in a glass pore are discussed separately.

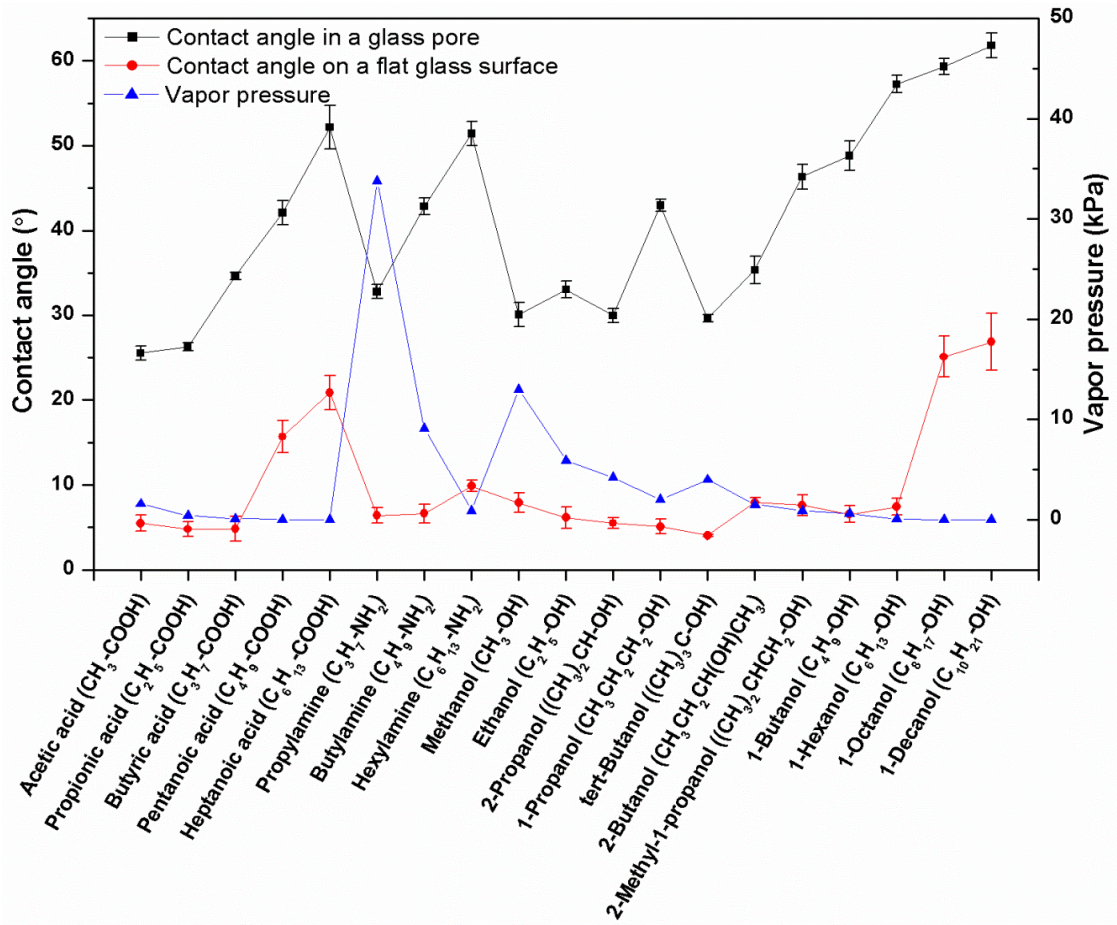

Figure 6.3 Contact angles in a pore and on a flat surface and vapor pressures at 20 ℃ for all amphiphiles used in this study

6.3 Effects of Functional Group and Alkyl Chain of Amphiphile on Pore Wetting

Three amphiphilic organic compounds were used to investigate the effect of functional group on glass pore wetting. They have the same alkyl chain length with three carbon atoms but with different hydrophilic functional groups, namely carboxyl acid (-COOH), amino ($-NH_2$), and hydroxyl (-OH) groups. The results in Figure 6.4 indicate that the effect of functional group on contact angle in a glass pore is in the order of $\theta_{-OH} > \theta_{-COOH} \approx \theta_{-NH_2}$, but their surface tensions are similar and at around 20 mN/m. Pentane and 1-propanol have the lowest and largest pore contact angles, which are 26.6° and 42.0° respectively. Similar pore contact angles are given by propylamine and butyric acid at around 34°. The amphiphilic organics with functional groups have larger pore contact angles than that of the nonpolar alkane.

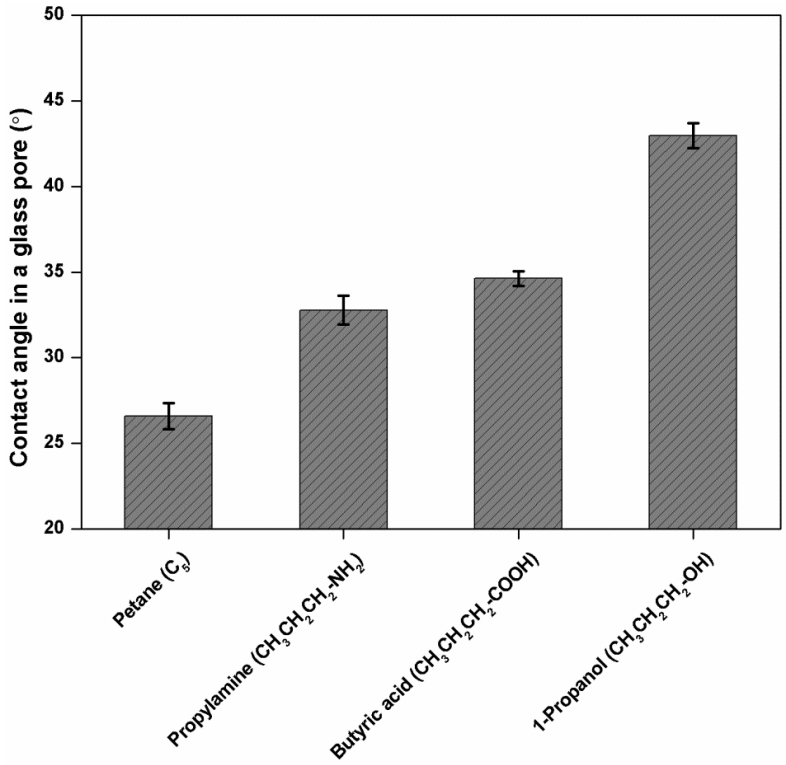

Figure 6.4 Contact angles of pentane, propionic acid, propylamine and 1-propanol in a glass pore

The results in Figure 6.5 further demonstrate the effect of functional group and also indicate the effect of the length of the straight alkyl chain on glass pore contact angle. It is clearly shown that the contribution of the functional groups studied on glass pore wetting is in the order: alkanol > alkyl amines ≈ alkyl carboxyl acid. For the saturated alkanes, the pore contact angle does not vary with the length of the alkyl chain. The pore contact angles of pentane, hexane, octane and decane remain at around 26°. However, once a polar functional group is introduced to the molecule, the pore contact angle increases significantly with alkyl chain length. For instance, the pore contact angle of ethanol is larger than that of methanol by 3°. The effect of alkyl chain length becomes more significant when the number of carbon atoms in the straight alkyl chain increases from 3 to 6. The pore contact angle of 1-hexanol ($C_6H_{13}OH$) is larger than that of 1-propanol (C_3H_7OH) by 14°. The contact angles of alkylamines and alkyl carboxyl acids are similar at the same alkyl chain length. They are smaller than the contact angles of alkanol by 6~10°. However, the dependence of glass pore contact angle on alkyl chain length for alkylamines and alkyl carboxyl acids is consistent with that for alkanols in the range of alkyl chain length from 1 to 6. When the number of carbon atoms in the alkyl chain is more than 6, the pore contact angle of alkanols increases with alkyl chain length less significantly. The difference between the pore contact angles of 1-decanol ($C_{10}H_{21}OH$) and 1-hexanol ($C_6H_{13}OH$) is only 5°. Alkyl amines and alkyl carboxyl acid with more than 6 carbons are solids. Methylamine and ethylamine are gases at ambient conditions. Thus, they were not considered in this study.

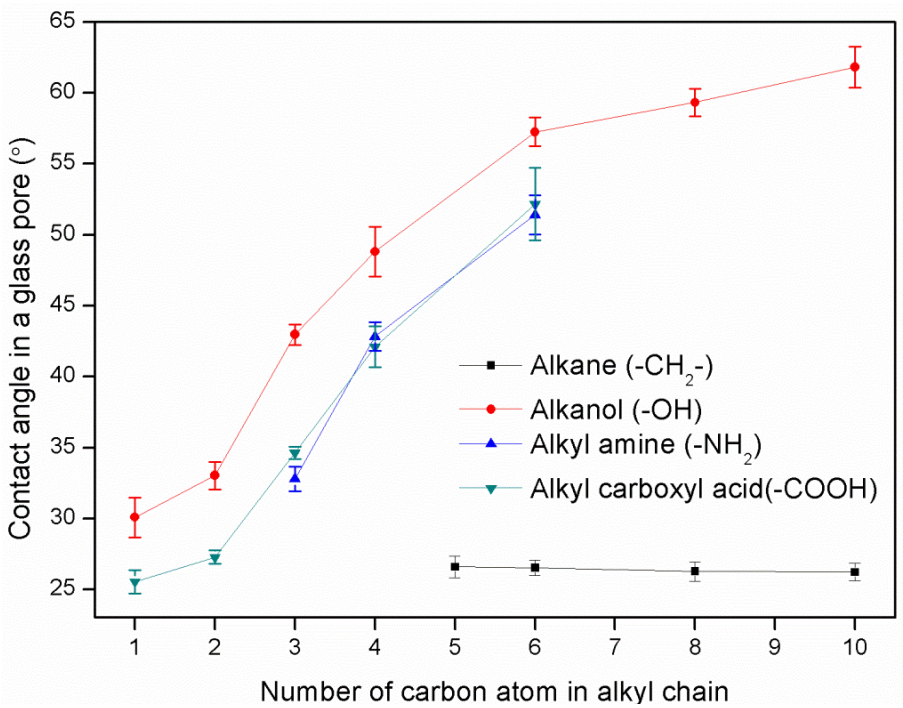

Figure 6.5 Pore contact angles of alkanes, alkanols, alkylamines and alkyl carboxyl acid with different straight alkyl chain lengths

6.4 Effects of Structural Isomer and Symmetrical Structure on Pore Wetting

To investigate the effect of the alkyl chain structure of amphiphilic organic compounds on pore contact angle, the structural isomers of 1-propanol and 1-butanol were used in this study. 2-propanol is the only structural isomer of 1-propanol. Its alcohol carbon is attached to two other carbons (

). 1-butanol has three structural isomers, which are 2-butanol, 2-methyl-1-propanol and tert-butanol. 2-butanol is a straight chain isomer with the hydroxyl at an internal carbon (

), 2-methyl-1-propanol is a branched isomer with the hydroxyl at a terminal carbon (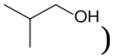

) and tert-butanol is a branched isomer with the hydroxyl at the internal carbon (

). As shown in Figure 6.6, the difference in pore contact angle between 1-propanol and 2-propanol is 12 °. This is caused by their different propyl chains. The straight n-propyl chain of 1-propanol gives a larger pore contact angle than that given by the isopropyl of 2-propanol, by 12 °. Similarly, the structural isomers of 1-butanol also give various pore contact angles. The straight n-butyl chain of 1-butanol gives the largest pore contact angle of 49 °. The pore contact angles of 2-methyl-1-propanol and 2-butanol are smaller, which are 46 ° and 35 ° respectively. This is caused by the effects of the isobutyl group of 2-methyl-1-propanol and the sec-butyl group of 2-butanol. The difference between isobutyl and sec-butyl group is in the location of the methyl side chain. The methyl side chain on the alcohol carbon tends to reduce the pore contact angle more significantly than the methyl side chain on the internal carbon. The pore contact angle of tert-butanol is the smallest, which is only around 29 °. This is due to the two methyl side chains on the alcohol carbon and the shortest carbon backbone chain. Overall, it can be concluded that the structure of the alkyl chain of an amphiphilic organic compound has a significant effect on glass pore wetting. The straight alkyl chain favours the pore contact angle most and the side

chain on the carbon of the backbone tends to reduce the pore contact angle, and the side chain on the alcohol carbon decreases the pore contact angle most significantly.

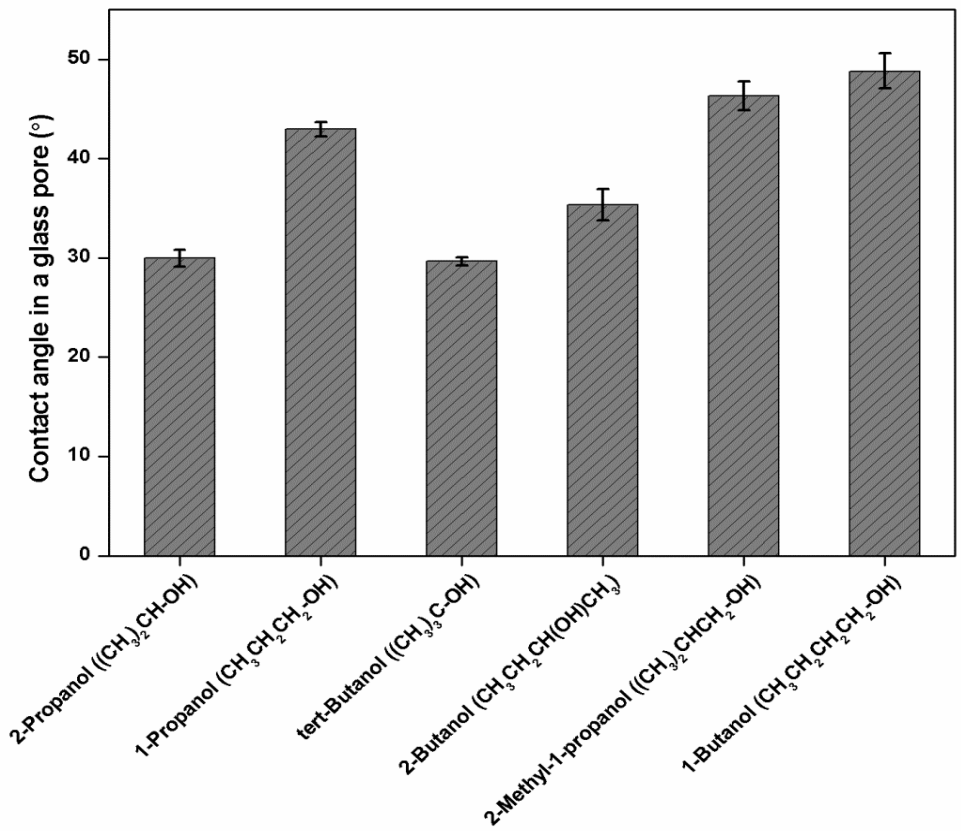

Figure 6.6 Contact angles of structural isomers of 1-propanol and 1-butanol in a glass pore

The effect of the hydroxyl group on the pore contact angle as shown in Figures 6.5 and 6.6 was investigated by using the alkanols with only one hydroxyl located on the terminal carbon, such as in ethanol and 1-propanol. An alkanol with a single hydroxyl has a larger pore contact angle than the alkane with the same chain length. To investigate the effect of multiple hydroxyls on the pore wetting of alkanols, ethylene glycol and glycerol were used. They have the same number of carbons as ethanol and 1-propanol but have two and three hydroxyls respectively on all carbons of their backbone chains. As shown in Figure 6.7, the pore contact angles of ethylene glycol and glycerol are smaller than those of ethanol and 1-propanol by 4.5 ° and 17 °

respectively. The pore contact angle is not increased by increasing the number of hydroxyls in the alkanols. Instead, the pore contact angle is significantly reduced due to the symmetrical molecular structure formed by introducing more hydroxyl functional groups on the backbone chain carbons.

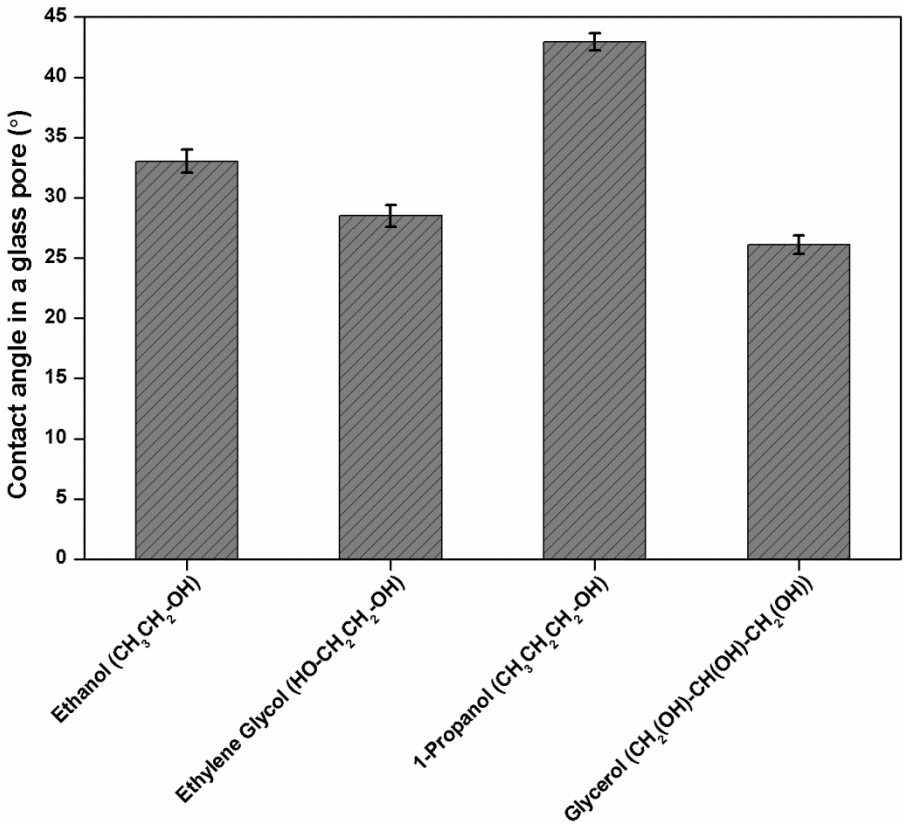

Figure 6.7 Pore contact angles of ethanol, ethylene glycol, 1-propanol and glycerol

6.5 Contact Angle of Amphiphile Aqueous Solution

The contact angles of aqueous solutions of amphiphilic organic compounds were also studied in hydrophilic glass pores and hydrophobic PMMA pores. The amphiphiles include methanol (CH_3-OH), ethanol (CH_3-CH_2-OH), 1-propanol (CH_3-CH_2-CH_2-OH), propylamine (CH_3-CH_2-CH_2-NH_2) and propionic acid (CH_3-CH_2-COOH). The mass fractions of amphiphiles in the amphiphile aqueous solutions range from 0 to 1.

Figure 6.8 (a) and (b) indicate the contact angles of methanol, ethanol and 1-propanol aqueous solutions in a PMMA pore and glass pore respectively. The surface tensions of these alcohol aqueous solutions are also shown in Figure 6.8. From the surface tension curves of the alcohol aqueous solutions, it is clear that the surface tension of alcohol aqueous solution changes markedly with alcohol concentration before reaching the CMC (Critical Micelle Concentration). After reaching the CMC, the surface tension remains relatively constant or changes with a lower slope.

In a PMMA pore (Figure 6.8 (a)), the contact angle trends of alcohol aqueous solutions are similar to their surface tension trends. The contact angle decreases with increasing alcohol concentration before it reaches its CMC. Beyond the CMC, the contact angle stops decreasing and remains at around 20°. The three alcohols have different CMCs, where 1-propanol has the lowest at 0.4 and methanol has the highest at 0.9. The contact angle of 1-propanol aqueous solution decreases with alcohol concentration most significantly and approaches a constant at its CMC of 0.4 in a PMMA pore. In comparison, the contact angles of ethanol and methanol aqueous solutions vary with alcohol mass fraction less significantly. They reach constant values at their CMCs of 0.6 and 0.9 respectively in PMMA pores.

However, in a glass pore (Figure 6.8 (b)), the effect of the concentration of amphiphile on the pore contact angle is significantly different from that in a PMMA pore. The contact angles of the three alcohol aqueous solutions do not change significantly with alcohol concentration or surface tension when the alcohol mass fraction ranges from 0 to 0.6 (Figure 6.8 (b)). When the mass fraction exceeds 0.6, the alcohol concentration does start to affect the pore contact angles of ethanol and 1-propanol aqueous solutions. Their contact angles increase with alcohol concentration. This increase is more significant for the contact angle of 1-propanol aqueous solution than that of ethanol aqueous solution. The contact angle of methanol aqueous solution does not vary significantly with methanol concentration in a glass pore. The surface tension and CMC do not significantly affect the contact angle trends.

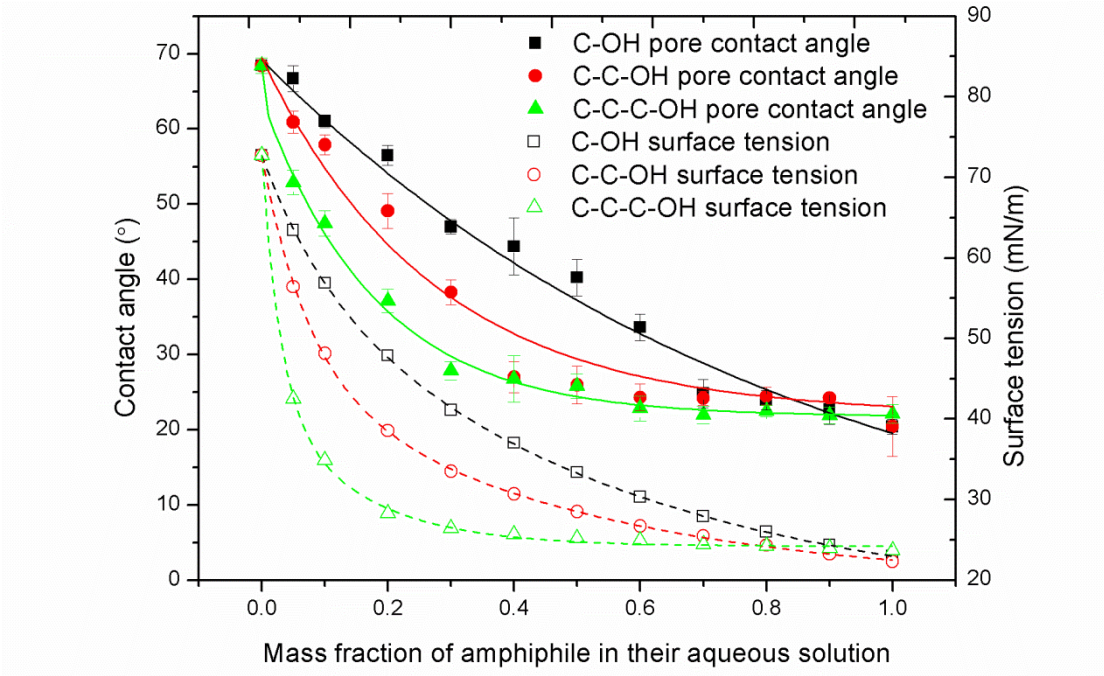

(a)

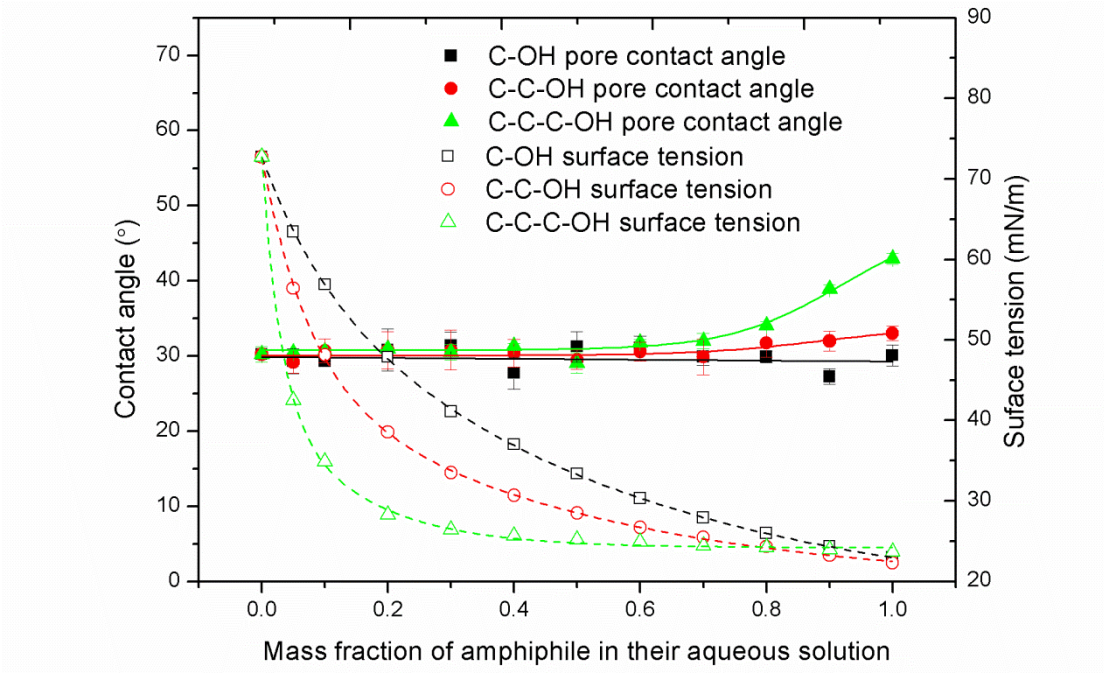

(b)

Figure 6.8 Contact angles of methanol, ethanol and 1-propanol aqueous solutions in a (a) PMMA pore and (b) glass pore

Figure 6.9 (a) and (b) show the contact angles of 1-propanol, propylamine and propionic acid aqueous solutions in a PMMA pore and a glass pore respectively. The results further prove the findings in Figure 6.8. In a PMMA pore (Figure 6.9 (a)), the contact angle trend follows the surface tension trend. Increasing amphiphile concentration before the CMC in the amphiphile aqueous solutions leads to dramatic decreases in contact angles. The contact angle does not markedly vary with amphiphile concentration beyond the CMC. 1-propanol aqueous solution has the lowest CMC, giving the most significant contact angle decrease. By contrast, the contact angles of propylamine and propionic acid aqueous solutions vary with their concentrations less significantly in PMMA pores.

In a glass pore (Figure 6.9 (b)), the contact angles of aqueous solutions of amphiphiles do not change with their concentration or surface tension until the mass fraction reaches around 0.6. When their mass fractions are over 0.6, the contact angles of 1-propanol and propionic acid aqueous solutions vary with their concentrations but showing different trends. The contact angle of 1-propanol aqueous solution increases with its concentration. However, increasing concentrations of propionic acid aqueous solution decrease its contact angle. The concentration of propylamine aqueous solution has no significant effect on its contact angle in a glass pore.

Thus, it can be concluded that the contact angles of amphiphile aqueous solutions in a PMMA pore significantly differ from those in a glass pore. In a PMMA pore, the contact angle changes with the surface tension or concentration of the amphiphilic aqueous solution. The contact angle decreases with surface tension before the alcohol concentration reaches its CMC. Beyond the CMC, the contact angle remains constant. The surface tension does significantly affect the contact angle. However, in a glass pore, the contact angle does not significantly vary with surface tension or amphiphile

concentration. When the amphiphile mass fraction is over around 0.6, the chemical structure of the amphiphile affects the contact angle. Long-chain alcohol aqueous solutions always give the largest contact angles.

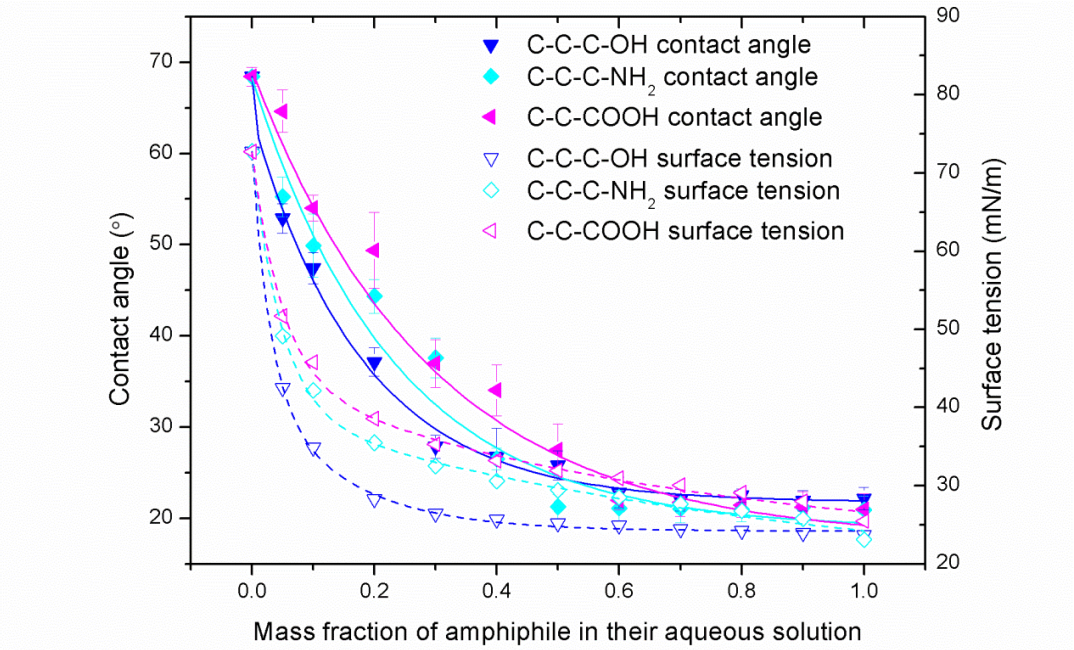

(a)

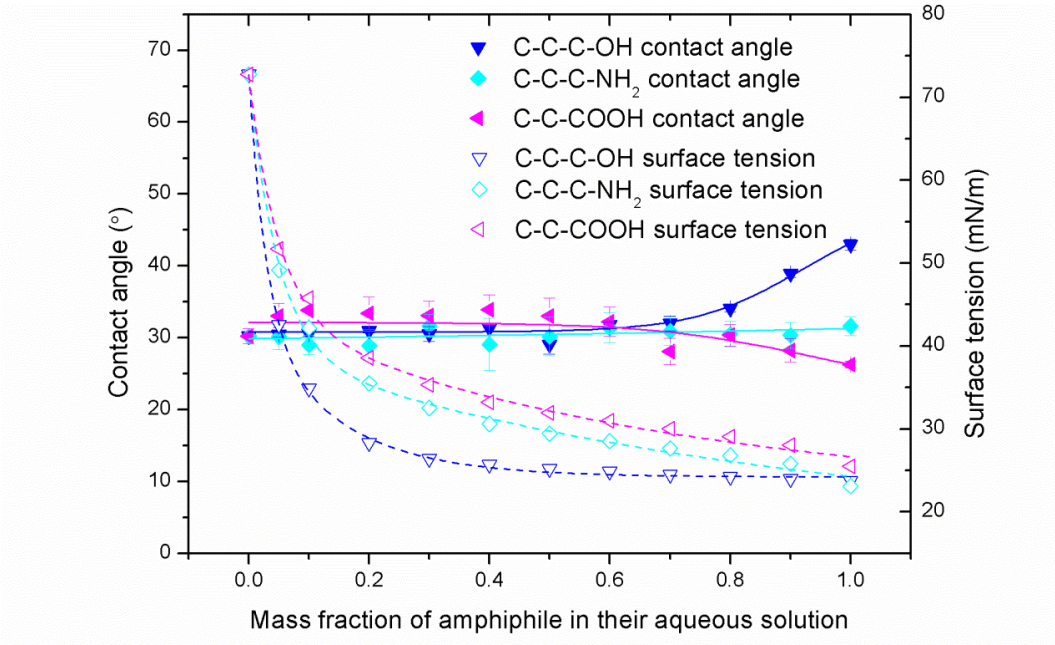

(b)

Figure 6.9 Contact angles of 1-propanol, propylamine and propionic acid aqueous solutions in a (a) PMMA pore and (b) glass pore

6.6 Summary

In this chapter, the contact angles of a range of pure amphiphilies and amphiphilie aqueous solutions in a glass pore and a PMMA pore are measured, in order to reveal the effect of the chemical structure of organics on pore wetting in terms of functional group, alkyl chain length and chain structural isomer. The main results indicate that:

(1) Contact angles of organics in a glass pore and on a flat glass surface depend on their chemical molecular structure. Some organics have very similar surface tensions, but their contact angles are very different in a glass pore due to the contributions from the effects of functional groups, alkyl chain length and alkyl chain structure. These effects on the contact angle are more significant in a glass pore than on a flat glass substrate. However, the chemical structure of the amphiphile only affects the contact angle in a hydrophilic glass pore. The findings cannot be applied to the hydrophobic oil-wet PMMA surface.

(2) The amphiphilic organics with functional groups of hydroxyl, amino and carboxyl acid have larger pore contact angles than non-polar organics, of the order of $\theta_{-OH} > \theta_{-NH2} \approx \theta_{-COOH}$. The pore contact angles of polar amphiphiles increase with the length of the straight alkyl chain. However, the pore contact angles of non-polar organics do not depend on alkyl chain length. The structure of the alkyl chain of amphiphilic compounds also has an effect on glass pore wetting. The straight alkyl chain contributes most to pore contact angle and the side chain on the carbon of backbone tends to reduce pore contact angle. The symmetrical molecular structure of organics gives the smallest contribution to pore wetting. However, even though the effect of chemical structure of amphiphile on glass pore wetting has been addressed, the true mechanism behind this may be complicated and cannot be confirmed in this study. This needs to further investigation.

(3) The contact angles of amphiphile aqueous solutions in an oil-wet pore are significantly different from those in a water-wet pore. In an oil-wet pore, the amphiphile concentration or surface tension does affect the contact angle. The contact angle data follows the surface tension trend. However, in a glass pore, the contact angle does not vary significantly with surface tension or amphiphile concentration. When the mass fraction is over around 0.6, the chemical structure of the amphiphile may significantly affect the contact angle.

6.7 References

[1] Adamson AW. Physical Chemistry of Surfaces. 4th ed. New York: Wiley-Interscience; 1982.

[2] Bangham DH, Saweris Z. The Behaviour of Liquid Drops and Adsorbed Films at Cleavage Surfaces of Mica. Transactions of the Faraday Society. 1938;34:554-70.

[3] Hardy WB. The Spreading of Fluids on Glass. Philos Mag. 1919;38:49-55.

[4] Fox HW, Hare EF, Zisman WA. Wetting Properties of Organic Liquids on High Energy Surfaces. JPhysChem. 1955;59:1097-106.

[5] Hare EF, Zisman WA. Autophobic Liquids and the Properties of Their Adsorbed Films. J Phys Chem. 1955;59:335-40.

[6] Zisman WA. Relation of the Equilibrium Contact Angle to Liquid and Solid Constitution. Contact Angle, Wettability, and Adhesion: American Chemical Society; 1964. p. 1-51.

[7] Afsar-Siddiqui AB, Luckham PF, Matar OK. Unstable Spreading of Aqueous Anionic Surfactant Solutions on Liquid Films. Part 1. Sparingly Soluble Surfactant. Langmuir. 2003;19:696-702.

[8] Afsar-Siddiqui AB, Luckham PF, Matar OK. Unstable Spreading of Aqueous Anionic Surfactant Solutions on Liquid Films. 2. Highly Soluble Surfactant. Langmuir. 2003;19:703-8.

[9] Afsar-Siddiqui AB, Luckham PF, Matar OK. Dewetting Behavior of Aqueous Cationic Surfactant Solutions on Liquid Films. Langmuir. 2004;20:7575-82.

[10] Craster RV, Matar OK. On Autophobing in Surfactant-Driven Thin Films. Langmuir. 2007;23:2588-601.

[11] Kumar N, Varanasi K, Tilton RD, Garoff S. Surfactant Self-Assembly ahead of the Contact Line on a Hydrophobic Surface and Its Implications for Wetting. Langmuir. 2003;19:5366-73.

[12] Sharma R, Kalita R, Swanson ER, Corcoran TE, Garoff S, Przybycien TM, et

al. Autophobing on Liquid Subphases Driven by the Interfacial Transport of Amphiphilic Molecules. Langmuir. 2012;28:15212-21.

[13] Li X, Fan X, Brandani S. Difference in pore contact angle and the contact angle measured on a flat surface and in an open space. Chem Eng Sci. 2014;117:137-45.

[14] Frank B, Garoff S. Surfactant Self-assembly Near Contact Lines: Control of Advancing Surfactant Solutions. Colloids and Surf A: Physicochem Eng Asp. 1996;116:31-42.

[15] Qu D, Suter R, Garoff S. Surfactant Self-Assemblies Controlling Spontaneous Dewetting. Langmuir. 2002;18:1649-54.

[16] Frank B, Garoff S. Temporal and Spatial Development of Surfactant Self-Assemblies Controlling Spreading of Surfactant Solutions. Langmuir. 1995;11:4333-40.

[17] Novotny VJ, Marmur A. Wetting Autophobicity. J Colloid Interface Sci. 1991;145:355-61.

[18] Kwok DY, Neumann AW. Contact Angle Interpretation in terms of Solid Surface Tension. Colloids and Surf A: Physicochem Eng Asp. 2000;161:31-48.

Chapter 7: Gas/Liquid/Supercritical CO_2-fluids Contact Angles in Oil-wet and Water-wet Pores[3]

7.1 Introduction

The pore wetting of deep saline aquifers and oil reservoirs is a principal factor in the control of CO_2 trapping, mobility, storage capacity and in the performance of CO_2 storage and CO_2-enhanced oil recovery. However, CO_2-fluid contact angle measurements on non-flat substrates still remain a challenge; few measurements have been directly carried out in micro-size pores to characterize CO_2 pore wetting. In addition, the contact angle of the CO_2-water/brine-mineral surface system has been regarded as a subject of controversy [1]. Some studies have reported that the contact angle does not depend on the CO_2 phase or pressure [2-5]. For instance, Espinoza and Santamarina concluded that the CO_2-water/brine contact angle was independent of pressure and CO_2 phases from their sessile drop experiments on calcite and quartz surfaces [4]. Bikkina did not see any clear variation in the CO_2-water contact angle with changes in pressure or CO_2 phase [2]. However, other researchers have insisted that the CO_2 phase or pressure does affect the contact angle [1, 4, 6-12]. For example, Saraji et al. proposed that change in the CO_2-water contact angle occurred mostly in the CO_2 phase transition zone and then remained unchanged [1]. Sutjiadi-Sia et al. observed that the CO_2-water contact angle on PTFE, stainless steel and glass surfaces increased gradually with pressure increase [6]. Due to these discrepancies in the previous studies and the unclear underlying mechanism,

[3] This chapter has been published in International Journal of Greenhouse Gas Control 36 (2015) 106-113.

it is necessary to work on this further.

In this chapter, the CO_2-fluid contact angles in a single capillary are directly measured, taking into consideration of the effect of CO_2 phase (gas, liquid and supercritical). The fluids used in this study were deionized water, n-decane and brine with a salinity of 3 M NaCl. A hydrophobic FEP (fluorinated ethylene propylene) capillary and a hydrophilic glass capillary were used, representing the oil-wet and water-wet pores in reservoirs respectively. The pore contact angle measurements in this study should advance the understanding of CO_2-fluid pore wetting in aquifers and oil and gas reservoirs.

7.2 CO_2-fluid Contact Angles in an Oil-wet Pore

The equilibrium CO_2-water contact angles in a FEP pore in a pressure range from 0 to 100 bar at 20 ℃ are shown in Figure 7.1. The FEP capillary is used to represent an oil-wet pore. The results show that the gas CO_2-water pore contact angle remains almost constant around 115 °when the pressure is less than 50 bar. At 20 ℃, CO_2 turns from the gas phase to the liquid phase at a boundary pressure approximately between 50 and 60 bar. When the pressure increases over the CO_2 vapor-liquid boundary pressure, the contact angle suddenly increases to approximately 150 °(Figure 7.1). The liquid CO_2-water contact angle does not depend on pressure significantly when the pressure further increases from 60 to 100 bar. The results clearly indicate that the CO_2-water contact angle in a FEP pore can be significantly altered when the CO_2 phase changes from gas to liquid. The effect of pressure on the CO_2-water contact angle is insignificant if there is no CO_2 phase change. Detailed results for the CO_2-water pore contact angle under a pressure range from 50 to 60 bar are presented in the small diagram in Figure 7.1. The sudden change in contact angle actually occurs at 57 bar at 20 ℃, which corresponds to the CO_2 phase change.

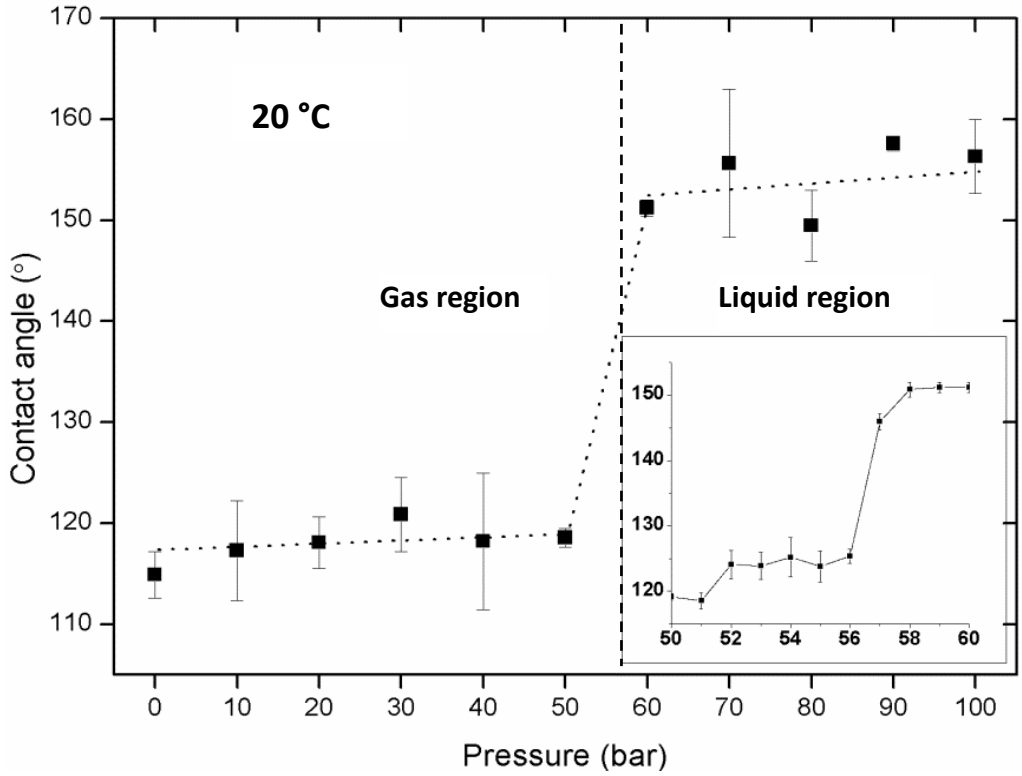

Figure 7.1 CO_2-water contact angle in a FEP pore versus pressure at 20 ℃ (small diagram: contact angle data from 50 to 60 bar)

Since brine and oil are common reservoir fluids in oil reservoirs and saline aquifers, brine and n-decane were also used to study CO_2-brine and CO_2-decane contact angles in a micron-sized pore. The brine used in this study is NaCl aqueous solution with a NaCl concentration of 3 M (~200 g(NaCl)/kg(water)). Figure 7.2 (a) presents the water-CO_2, brine-CO_2 and decane-CO_2 contact angles in a FEP pore under a pressure range from 0 to 100 bar at 20 ℃. It can be seen that the effect of salinity on the CO_2-water/brine contact angle in a FEP pore is not significant. The CO_2-brine contact angle shows a very similar trend to the one for the CO_2-water contact angle. The gas CO_2-water and gas CO_2-brine contact angles remain around 115 ~118 ° in the pressure range from 0 to 50 bar. When the pressure exceeds the CO_2 vapor-liquid boundary pressure, both CO_2-water and CO_2-brine contact angles increase to around 150 ° and remain unchanged. The CO_2-decane contact angles are much smaller than those from CO_2-water and CO_2-brine systems, by approximately 85 °. The gas

CO_2-decane contact angle is around 28° for the pressure range from 0 to 50 bar at 20 ℃. It is difficult to obtain the CO_2-decane interface when the pressure is over 50 bar at 20 ℃, since the CO_2-decane minimum miscibility pressure (MMP) is around 52~55 bar at 20 ℃ [13]. It was noted that the gas CO_2 started to dissolve into the n-decane upon pressurization at around 53 bar during the experiment. The CO_2-decane immiscible flows start to be miscible beyond the MMP, so that the CO_2-decane interface cannot be observed in the capillary measurement zone under the microscope. Thus, the contact angles between liquid CO_2 and n-decane in a capillary at 20 ℃ are not considered in this study as shown in Figure 7.2 (a).

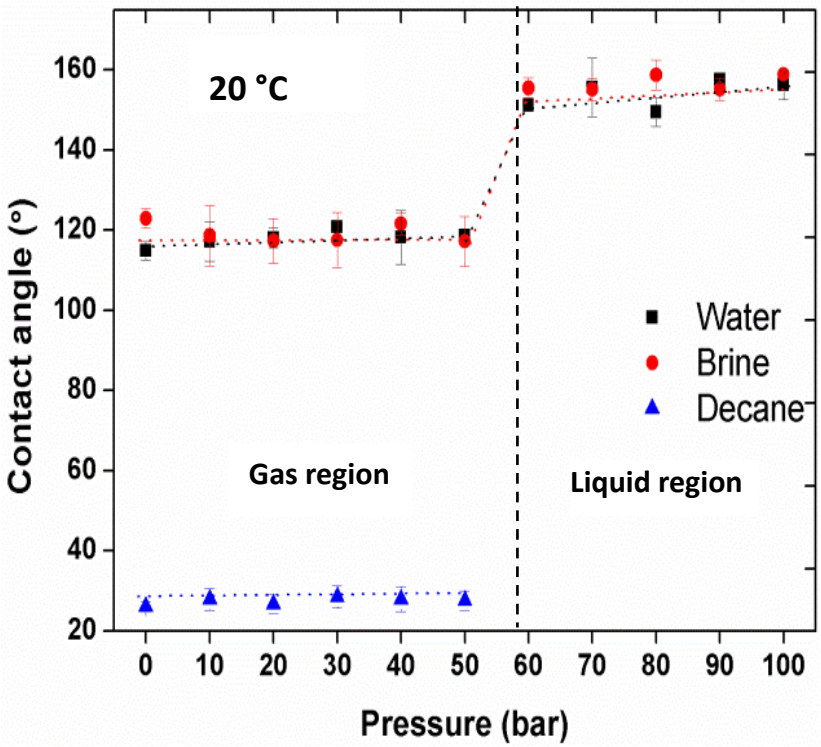

(a)

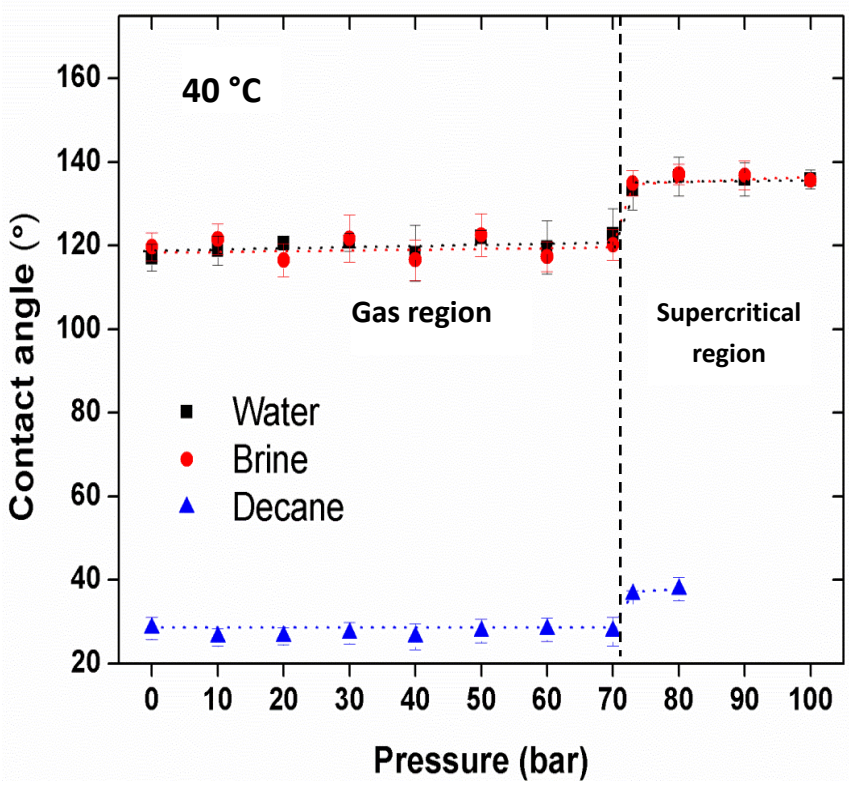

(b)

Figure 7.2 Contact angles for water-CO_2, brine-CO_2 and decane-CO_2 in a FEP pore at 20 ℃ (a) and 40 ℃ (b)

To investigate the supercritical CO_2-fluid contact angles, the CO_2-water, CO_2-brine and CO_2-decane contact angles were measured in a FEP in a pressure range from 0 to 100 bar at an elevated temperature of 40 ℃ (Figure 7.2 (b)). As shown in Figure 7.2 (a), no significant contact angle deviations can be observed in CO_2-water and CO_2-brine systems at 20 ℃. Similarly, contact angles from the CO_2-water interfaces and CO_2-brine interfaces in a FEP pore are also close at 40 ℃. When the pressure is in the range from 0 to 70 bar, the gas CO_2-water and gas CO_2-brine contact angles in a FEP pore remain at around 118°, and the gas CO_2-decane contact angles are around 28° at 40 ℃.

At 40 ℃, CO_2 changes from the gas phase to the supercritical phase when the applied pressure increases over the critical pressure (around 73 bar). As shown in Figure 7.2 (b), when the pressure increases over 73 bar, the CO_2-water and CO_2-brine contact angles suddenly rise from 118° to 135°. When the pressure is further increased from 73 to 100 bar, the supercritical CO_2-water and supercritical CO_2-brine contact angles remain at around 135°. The MMP of the CO_2-decane system depends on the temperature applied. Elevated temperature induces an increase in MMP. At 40 ℃, the estimated CO_2-decane MMP is approximately around 81~82 bar [13], which exceeds the CO_2 critical pressure of 73 bar. Thus, the interface between supercritical CO_2 and n-decane in a pore could be established in this study. The CO_2-decane pore contact angle increases from 28° to around 38° when the CO_2 turns from the gas to the supercritical phase at 73 bar. The contact angle data at 40 ℃ indicates that the supercritical CO_2 behaves as more oil-wet than gas CO_2 in a FEP pore. The change in contact angle mainly occurs on the gas-supercritical CO_2 phase transition boundary. Beyond the phase transition boundary, the contact angles remain unchanged. By comparing Figure 7.2 (a) and (b), it is worth noting that the supercritical CO_2-water and supercritical CO_2-brine contact angles are smaller than those for liquid CO_2-water

and liquid CO_2-brine by approximately 15°. It can be concluded that the CO_2-fluid contact angles in a FEP pore (oil-wet) are significantly altered when the CO_2 phase changes. The contact angles of CO_2-water, CO_2-brine and CO_2-decane systems are in the order of $\theta_{gasCO2}<\theta_{supercritical\ CO2}<\theta_{liquidCO2}$, and the CO_2-water and CO_2-brine contact angles are similar ($\theta_{brine} \approx \theta_{water}$) in an oil-wet pore.

7.3 CO_2-fluid Contact Angles in a Water-wet Pore

The CO_2-fluid wetting phenomena in an oil-wet pore have been discussed by investigating the CO_2-fluids contact angles in a FEP capillary. In this section, a glass capillary is used to study the CO_2-fluid contact angle in a water-wet pore. Figure 7.3 shows that the water-CO_2, brine-CO_2 and decane-CO_2 contact angles remain at around 30°, 40° and 26° respectively, under a pressure range from 0 to 100 bar and at temperatures of 20℃ and 40℃. The CO_2 phase has insignificant effect on contact angles in a glass pore.

Comparing the contact angles of water, brine and n-decane in a FEP pore and in a glass pore (Figure 7.2 and 7.3), it is clear that the CO_2-water and CO_2-brine contact angles in a glass pore are much smaller than those in a FEP pore by approximately 85°~120°. The sudden contact angle swings in a FEP pore in the CO_2 gas-liquid transition zone and in the CO_2 gas-supercritical phase transition zone cannot be observed in a glass pore. It is worth noting that the brine-CO_2 contact angle is significantly different from and larger by 10° than that of water-CO_2 in a glass pore, but this difference cannot be observed in the FEP pore (Figure 7.2). Here it could be concluded that the contact angles of CO_2-water, CO_2-brine and CO_2-decane systems are in the order of $\theta_{gasCO2} \approx \theta_{supercritical\ CO2} \approx \theta_{liquidCO2}$ and $\theta_{brine} > \theta_{water}$ in a hydrophilic pore.

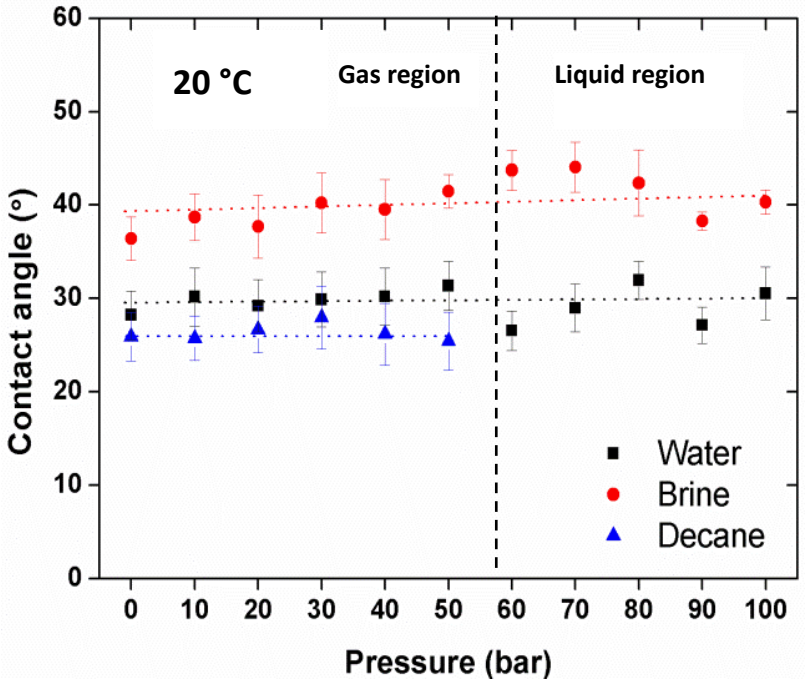

(a)

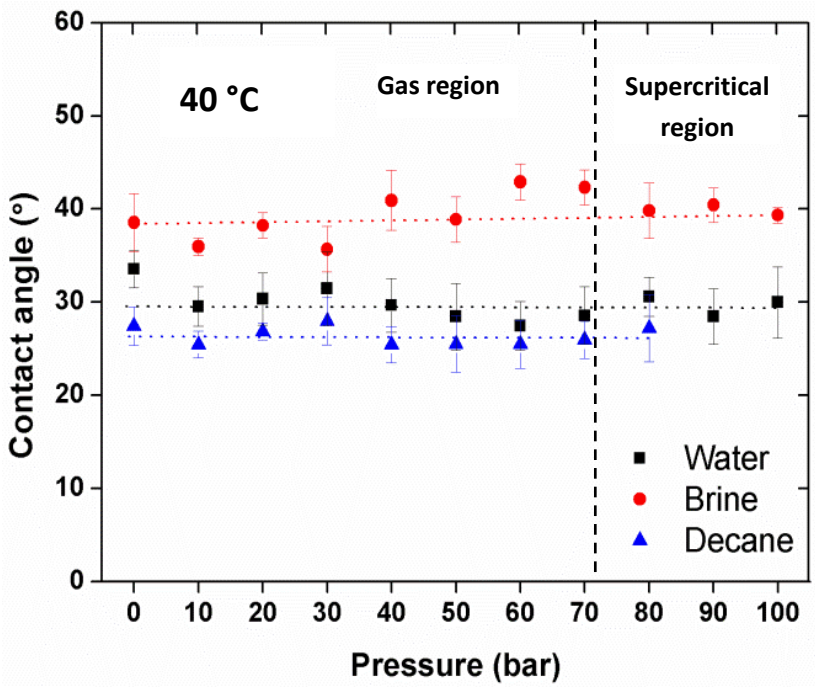

(b)

Figure 7.3 Contact angles for water-CO_2, brine-CO_2 and decane-CO_2 in a glass pore at two different temperatures: (a) 20 ℃; (b) 40 ℃

7.4 Discussion

The CO_2-water/brine contact angle on a mineral surface has recently become a controversial issue, with reported results being inconsistent. Some studies report no effect of CO_2 phase or pressure on the CO_2-water/brine contact angle on a mineral surface [2-5]. On the other hand, others have observed a gradual or sudden significant alteration in CO_2-water/brine contact angle on a mineral surface as pressure increases or the CO_2 phase changes [6, 7, 9, 12, 14-17]. Saraji et al. explained that the discrepancies observed in these recent studies might result from the various cleaning methods, equilibration states of CO_2 phases, and measurement conditions [1]. However, these might be complex and need to be assessed and confirmed further. This section reviews and discusses five recent studies by Espinoza and Santanmarina [4], Sutjiadi-Sia et al. [6], Jung and Wan [7], Saraji et al. [1] and Kaveh et al. [5]. The surface materials and geometries used, working liquids investigated and operating condition applied in their and our studies are summarized in Table 7.1.

Table 7.1 Summary of materials and operating conditions in the studies on CO_2-liquid-mineral system from literatures

Author	*Substrate material/geometry*		*Working fluids*	*Temperature (℃)*
	Hydrophobic	*Hydrophilic*		
Our study	FEP (fluorinated ethylene propylene) capillary	Glass capillary	DI water, brine (3M), CO_2(g), CO_2(l), CO_2(sc)	20 ℃, 40 ℃
Espinoza and Santamarina[4]	PTFE (Poly tetra fluoro ethylene) flat substrate	Quartz flat substrate	DI water, brine (3M), CO_2(g), CO_2(l)	20 ℃
Sutjiadi-Sia et al.[6]	PTFE flat substrate	Glass flat substrate	DI water, CO_2(g), CO_2(sc)	40 ℃
Jung and Wan[7]	_____	Silica plate	DI water, brine (3M), CO_2(g),CO_2(sc)	45 ℃
Saraji et al.[1]	_____	Quartz flat substrate	DI water, CO_2(g),CO_2(sc)	35 ℃
Kaveh et al.[5]	_____	Sandstone	DI water, CO_2(g),CO_2(sc)	45 ℃

It is known that the contact angles measured in a pore could represent the porous wetting phenomena better than those measured on flat substrates [18, 19]. Thus, the contact angles of a CO_2-fluid-mineral system were measured in single micron-sized capillaries in this study. The FEP and glass capillaries were used to represent the oil-wet and water-wet pores respectively. In the studies by Espinoza and Santanmarina

[4], Sutjiadi-Sia et al. [6], Jung and Wan [7], Saraji et al. [1] and Kaveh et al. [5], the flat PTFE (poly tetra fluoro ethylene) substrates were used to present hydrophobic minerals, while flat glass, quartz, silica plates and planar sandstone substrate were used to represent hydrophilic minerals. All these studies mainly focused on the CO_2-water contact angle measurements on mineral surfaces. In addition, Espinoza and Santamarina [4] and Jung and Wan [7] investigated the wetting of CO_2-brine-mineral systems. The temperatures applied in these five previous studies ranged from 20 to 45 ℃. Since the critical temperature of CO_2 is 31 ℃, Espinoza and Santamarina [4] considered the CO_2 in the gas and liquid phases, while Sutjiadi-Sia et al. [6], Jung and Wan [7], Saraji et al. [1] and Kaveh et al. [5] studied the CO_2 in the gas and supercritical states. The hydrophobic and hydrophilic materials, operating temperatures, and experimental methods used in this work in fact differ from those used in previous studies, and thus might lead to a perfect comparison. However, it is still possible to indicate the effects of pressure and CO_2 phase on CO_2-fluid-mineral surface wetting.

7.4.1 Hydrophobic Surface

Figure 7.4 compares the experimental results in this study measured in a FEP pore with the experimental data from Espinoza and Santamarina [4] and Sutjiadi-Sia et al.[6]. It can be seen that the trends in our experimental data match those of Espinoza and Santamarina [4] very well. Espinoza and Santamarina also reported that the CO_2-water-PTFE contact angle suddenly increased when the CO_2 phase changed from gas to liquid, and the pressure did not affect the CO_2-water-PTFE contact angle significantly if there was no phase change [4]. Our contact angles are larger than those of Espinoza and Santamarina [4], by 7° to 15°. This might be due to the different hydrophobic polymeric materials used. The minor effect of salinity on CO_2-brine contact angle on a hydrophobic surface can also be observed in the experimental data

from Espinoza and Santamarina [4]. However, Sutjiadi-Sia et al. proposed that the CO_2-water contact angle is greatly dependent on pressure, and gradually increased with pressure in the range from 0 to 100 bar.

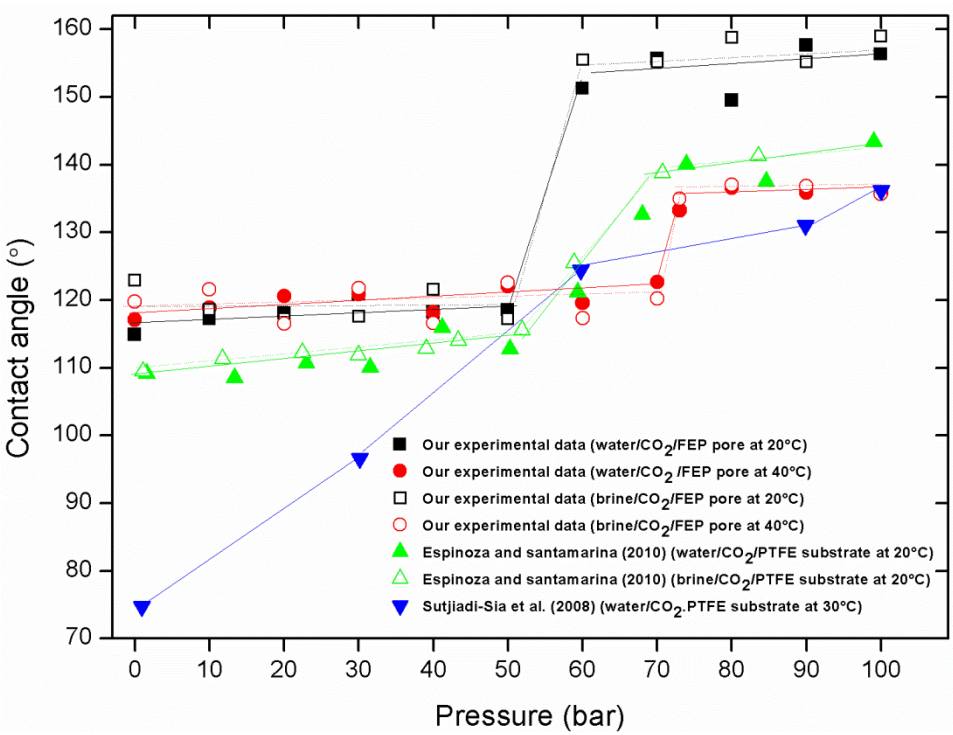

Figure 7.4 Comparison of our experimental contact angles measured in a FEP pore with values recently reported in the literature [4, 6]

7.4.2 Hydrophilic Surface

Figure 7.5 shows the CO_2-water and CO_2-brine contact angles on several hydrophilic surfaces in the present study and the literature. As discussed, the effect of pressure on CO_2-water and CO_2-brine contact angles in glass capillaries is not significant in our study, even in the CO_2 phase transition zone. This agrees with the findings of Espinoza and Santamarina [4], Saraji et al. [1] and Kaveh et al. [5]. However, Jung and Wan [7], and Sutjiadi-Sia et al. [6] reported that the contact angles measured for CO_2-water and CO_2-brine system on a flat surface strongly depended on pressure and

CO_2 phase.

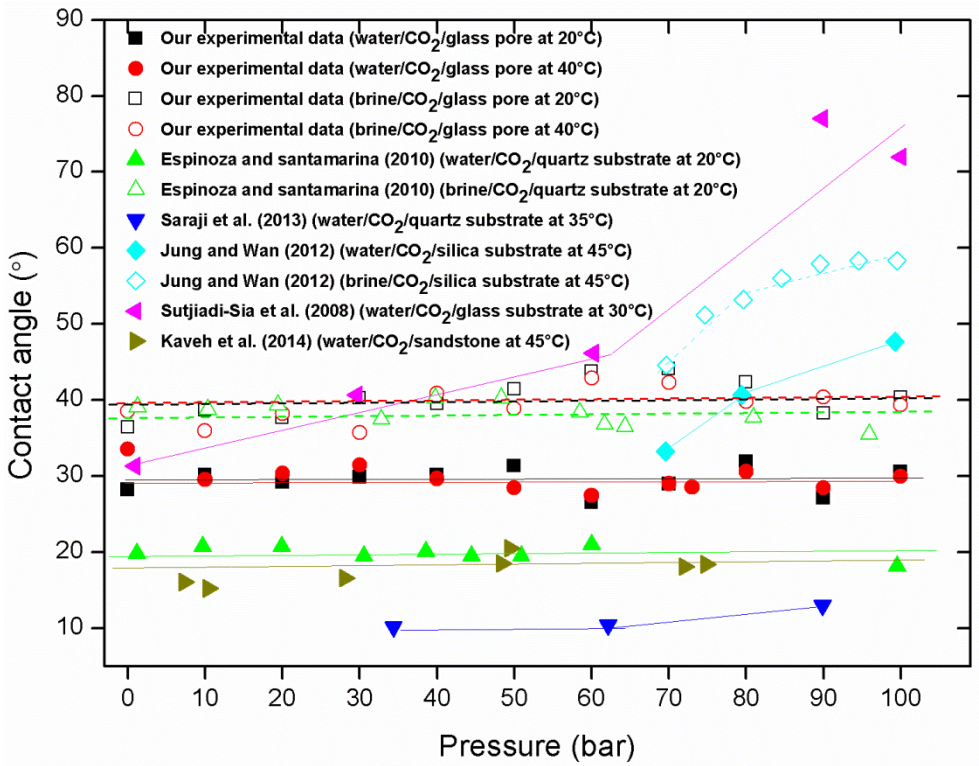

Figure 7.5 Comparison of our experimental contact angles measured in a glass pore with values recently reported in the literature [1, 4, 6, 7]

In this study, the addition of salt (NaCl) (~200 g(NaCl)/kg(water)) in the brine does affect the CO_2-water/brine contact angle in a glass pore. The CO_2-brine contact angle is significantly larger than the CO_2-water contact angle in a glass capillary by 10°. Similar observations were also made by Espinoza and Santamarina [4] and Jung and Wan [7] as shown in Figure 7.5. These phenomena have also been reported in other studies [9, 14, 20, 21]. For instance, Kim et al. and Sghaier et al. noted that the contact angle significantly increased with ionic strength on hydrophilic surfaces, but only very minor variations in contact angle with ionic strength were observed on hydrophobic surfaces [14, 20]. From Figures 7.4 and 7.5, it can be seen that Sutjiadi-Sia et al. may have needed more data to confirm their conclusion, as the gaps between their data points are large.

7.5 Summary

The contact angles of CO_2-water, CO_2-brine and CO_2-decane systems in small single oil-wet and water-wet pores [22] are presented in this chapter. The effect of CO_2 phase on the pore contact angle has been investigated [22]. The results indicate that the CO_2-fluid wetting phenomenon in an oil-wet pore differs from that in a water-wet pore.

(1) In an oil-wet pore, the CO_2-brine contact angles are close to the CO_2-water contact angles; $\theta_{brine} \approx \theta_{water}$ in an oil-wet pore. The effect of salinity on the pore contact angle is not significant in an oil-wet pore. CO_2-water and CO_2-brine contact angles are significantly larger than CO_2-decane contact angles by 92° to 117°. The CO_2 phase change does affect the CO_2-fluid contact angle. The effect of pressure on CO_2-fluids contact angles is not significant when there is no CO_2 phase change. The CO_2-fluid contact angles in an oil-wet pore are in the order of $\theta_{gasCO2} < \theta_{supercritical\ CO2} < \theta_{liquid\ CO2}$.

(2) In a water-wet pore, the CO_2-water, CO_2-brine and CO_2-decane contact angles in a glass capillary are approximately around 30°, 40° and 26° respectively. Salinity has a significant effect on the CO_2-brine/water-glass pore contact angle in a water-wet pore; $\theta_{brine} > \theta_{water}$. CO_2 phase does not affect the CO_2-fluid contact angle significantly in a water-wet pore; $\theta_{gasCO2} \approx \theta_{supercritical\ CO2} \approx \theta_{liquidCO2}$.

The CO_2-water/brine contact angle on mineral surface has become a controversial issue recently. The reported results are inconsistent. Some studies reported no effect of CO_2 phase or pressure on the CO_2-water/brine contact angle on mineral surface [2, 3, 5]. On the other hand, others observed a gradual or sudden significant alteration of CO_2-water/brine contact angles on mineral surface as pressure increase or CO_2 phase change [4, 6, 7, 9, 12, 14-17]. Recent studies explained that the discrepancies observed

from these recent studies might result from the substrate surface characteristics, various cleaning methods, equilibration states of CO_2 phases, salinities of brines and the measurement conditions [5].

The experimental results in this study confirm previous findings from Chalbaud et al. [3], Espinoza and Santamarina [4], and Kaveh et al. [5] which concluded that the CO_2-fluid contact angle could be significantly altered on a hydrophobic surface when CO_2 phase changes, but no clear trend of variation in contact angle with changes in pressure and CO_2 phase can be observed on strong hydrophilic substrates.

7.6 References

[1] Saraji S, Goual L, Piri M, Plancher H. Wettability of Supercritical Carbon Dioxide/Water/Quartz Systems: Simultaneous Measurement of Contact Angle and Interfacial Tension at Reservoir Conditions. Langmuir. 2013;29:6856-66.

[2] Bikkina PK. Contact Angle Measurements of CO_2–water–quartz/calcite systems in the Perspective of Carbon Sequestration. Int J Greenh Gas Con. 2011;5:1259-71.

[3] Chalbaud C, Robin M, Lombard JM, Martin F, Egermann P, Bertin H. Interfacial tension measurements and wettability evaluation for geological CO_2 storage. Adv Water Resour. 2009;32:98-109.

[4] Espinoza DN, Santamarina JC. Water-CO_2-mineral systems: Interfacial tension, contact angle, and diffusion—Implications to CO_2 geological storage. Water Resour Res. 2010;46:W07537.

[5] Kaveh NS, Rudolph ESJ, van Hemert P, Rossen WR, Wolf KH. Wettability Evaluation of a CO2/Water/Bentheimer Sandstone System: Contact Angle, Dissolution, and Bubble Size. Energy & Fuels. 2014;28:4002-20.

[6] Sutjiadi-Sia Y, Jaeger P, Eggers R. Interfacial phenomena of aqueous systems in dense carbon dioxide. The Journal of Supercritical Fluids. 2008;46:272-9.

[7] Jung J-W, Wan J. Supercritical CO_2 and Ionic Strength Effects on Wettability of Silica Surfaces: Equilibrium Contact Angle Measurements. Energy & Fuels. 2012;26:6053-9.

[8] Ameri A, Kaveh NS, Rudolph ESJ, Wolf KH, Farajzadeh R, Bruining J. Investigation on Interfacial Interactions among Crude Oil–Brine–Sandstone Rock–CO_2 by Contact Angle Measurements. Energy & Fuels. 2013;27:1015-25.

[9] Dickson JL, Gupta G, Horozov TS, Binks BP, Johnston KP. Wetting Phenomena at the CO_2/Water/Glass Interface. Langmuir. 2006;22:2161-70.

[10] Li Y, Pham JQ, Johnston KP, Green PF. Contact Angle of Water on

Polystyrene Thin Films: Effects of CO_2 Environment and Film Thickness. Langmuir. 2007;23:9785-93.

[11] Yang D, Gu Y, Tontiwachwuthikul P. Wettability Determination of the Reservoir Brine−Reservoir Rock System with Dissolution of CO_2 at High Pressures and Elevated Temperatures. Energy & Fuels. 2007;22:504-9.

[12] Yang D, Gu Y, Tontiwachwuthikul P. Wettability Determination of the Crude Oil−Reservoir Brine−Reservoir Rock System with Dissolution of CO_2 at High Pressures and Elevated Temperatures. Energy & Fuels. 2008;22:2362-71.

[13] Song YC, Zhu NJ, Liu Y, Zhao JF, Liu WG, Zhang Y, et al. Magnetic Resonance Imaging Study on the Miscibility of a CO_2/n-Decane System. Chinese Physics Letters. 2011;28.

[14] Kim Y, Wan J, Kneafsey TJ, Tokunaga TK. Dewetting of Silica Surfaces upon Reactions with Supercritical CO_2 and Brine: Pore-Scale Studies in Micromodels. Environ Sci Technol. 2012;46:4228-35.

[15] Plug WJ, Bruining J. Capillary pressure for the sand–CO_2–water system under various pressure conditions. Application to CO_2 sequestration. Advances in Water Resources. 2007;30:2339-53.

[16] Plug WJ, Mazumder S, Bruining J. Capillary pressure and wettability behavior of CO_2 sequestration in coal at elevated pressures. SPE J. 2008;13:455-64.

[17] Wang S, Edwards IM, Clarens AF. Wettability Phenomena at the CO_2–Brine–Mineral Interface: Implications for Geologic Carbon Sequestration. Environ Sci Technol. 2012;47:234-41.

[18] Li X, Fan X, Askounis A, Wu K, Sefiane K, Koutsos V. An Experimental Study on Dynamic Pore Wettability. Chem Eng Sci. 2013;104:988-97.

[19] Li X, Fan X, Brandani S. Difference in pore contact angle and the contact angle measured on a flat surface and in an open space. Chem Eng Sci. 2014;117:137-45.

[20] Sghaier N, Prat M, Ben Nasrallah S. On the influence of sodium chloride concentration on equilibrium contact angle. Chemical Engineering Journal. 2006;122:47-53.

[21] Vishnyakov A, Shen Y, Tomassone MS. Interactions of silica nanoparticles in supercritical carbon dioxide. The Journal of Chemical Physics. 2008;129:174704.

[22] Li, X, Fan, X. Effect of CO_2 phase on contact angle in oil-wet and water-wet pores. International Journal of Greenhouse Gas Control. 2015; 36:106-113.

Chapter 8: CO_2-water Displacements in a Sandstone Core Sample

8.1 Introduction

Geological carbon storage has emerged as one of the most promising approaches to mitigate the climate changes caused by global warming. Saline aquifer and depleted oil reservoirs have been regarded as having the largest CO_2 storage capacities. In the context of CO_2 storage, deep geological formations can be seen as capillary systems, in which fluid displacement mechanisms at pore scale mainly govern multiphase flow transport in porous media, especially in CO_2 capillary/residual trapping process [1, 2]. A thorough understanding of CO_2-fluid displacement behaviour is very important for long-term subsurface CO_2 storage. The two-phase displacement behaviour in porous media is closely related to capillary pressure (P_c) and relative permeability (k_r). The dependence of capillary pressure and relative permeability on water saturation (S_w) are the basic constitutive relationships required to predict CO_2 flows and capillary trapping during CO_2 storage [3-5]. In this chapter, CO_2-water displacement in sandstone is investigated by conducting CO_2-water core flooding experiments, and the process is characterized by studying the capillary pressure-saturation curve (P_c-S_w), relative permeabilities ($k_{r,water}$, $k_{r,CO2}$) and water production behaviour. The effects of pressure, CO_2 phase and injection rate are considered.

8.2 Capillary Pressure-Saturation Curve and Water Production Behaviour

- **Capillary Pressure**

The capillary pressure-saturation (P_c-S_w) relationship is of significance for the characterization of two-phase flow transport in porous media. In this study, the displacement of water by CO_2 in a sandstone core sample is investigated by considering the effects of pressure and CO_2 phase (gas, liquid and supercritical). Capillary pressure (P_c) is defined as the pressure difference (ΔP) between gas and water bulk phases for small injection rates [2, 6, 7]. Since the viscous drag effect is negligible for low-velocity fluids with small viscosities, the pressure drop is close to the capillary pressure, as shown in Equation 8.1 [8]. In this study, capillary pressure (P_c) is measured as the pressure difference (ΔP) between the CO_2 inlet ($P_{inlet, CO2}$) and the water outlet ($P_{outlet, water}$), as shown in Figure 8.1.

$$\Delta P = P_{CO_2} - P_{water} = 4\frac{\gamma\cos\theta}{d} + v\frac{32L}{d^2}\left(\frac{l_{CO_2}\mu_{CO_2} + l_{water}\mu_{water}}{L}\right) \quad (8.1)$$

where ΔP is the pressure difference (Pa) between CO_2 and water bulk phases, $4\frac{\gamma\cos\theta}{d}$ is capillary pressure (P_c) based on Young-Laplace's equation (γ is CO_2-water interfacial tension (mN/m), θ is contact angle and d is pore diameter); $v\frac{32L}{d^2}\left(\frac{l_{CO_2}\mu_{CO_2} + l_{water}\mu_{water}}{L}\right)$ is Posiseuille's equation, representing the viscous drag effect from the two fluids (L is the total pore length, l is the length of each fluid, v is the flow velocity and μ is the fluid viscosity. The viscosities (μ) of CO_2 and water are small, ranging from 1.47×10^{-5} Pa s to 8.05×10^{-5} Pa s [9], and the injection velocity (v) is low in this study. Thus, the viscous pressure drop is small and the differential pressure (ΔP) roughly equals the capillary pressure (P_c).

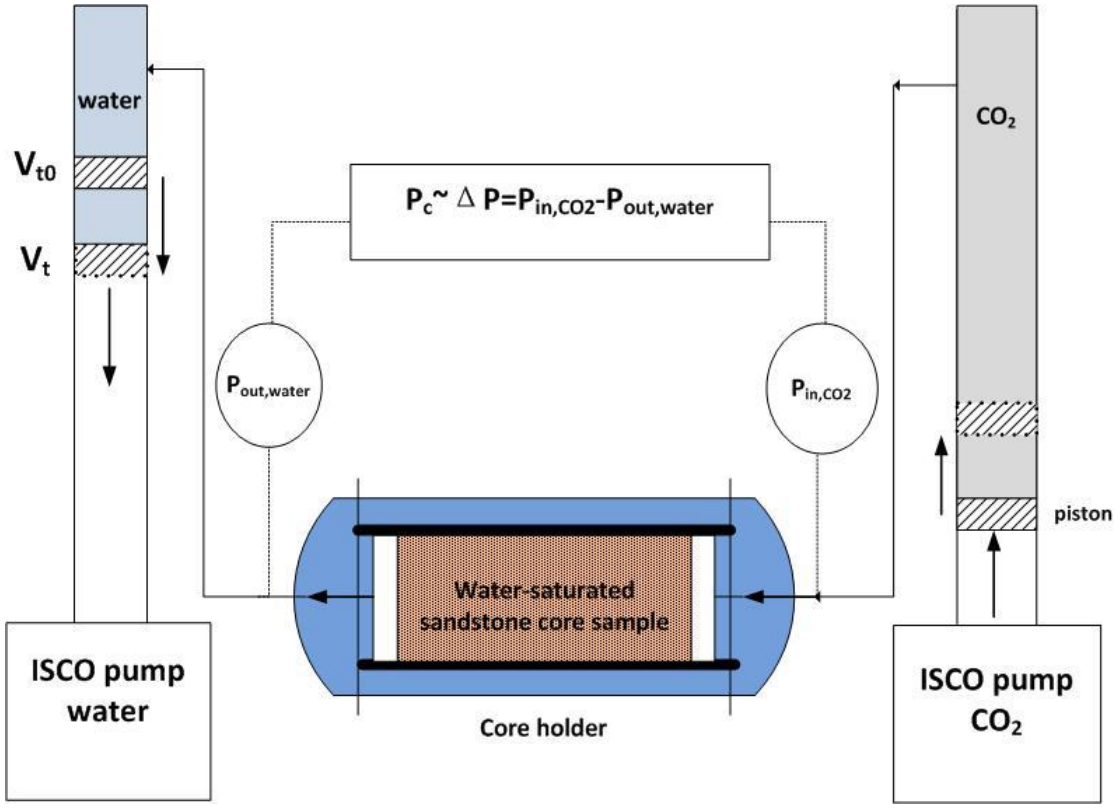

Figure 8.1 CO_2-water core flooding

- **Water Saturation**

Figure 8.1 shows that the water pump collects cumulative water displaced from the core holder during the CO_2-water drainage experiment. The water saturation (S_w) can be obtained from the volume change of water production by the water pump (Equation 8.2), as shown in Figure 8.1.

$$S_w(t) = \frac{V_s - (V_t - V_{t_0})}{V_s} \tag{8.2}$$

where $S_w(t)$ is water saturation as a function of time, V_s is the volume of the water saturated in the sandstone core sample before the displacement (ml), $(V_t - V_{t_0})$ is the volume of water displaced from the sandstone core sample by CO_2, which is

collected by the water pump, as shown in Figure 8.1. The final water saturation can be determined by weighting the sandstone core sample with residual water content at the end of the experiment.

- **Capillary Pressure-Satuation Relationship**

The capillary pressure-saturation curves (P_c-S_w) are obtained on the basis of the following assumptions [6]:

1) The initial water saturation for primary drainage is 1.0.

2) The water is considered as being incompressble under all pressurized conditions.

3) The porosity and wetting condition are assumed to be insignificantly changed during the drainage process.

4) Since the viscous pressure drop over the sample holder is negligible for small injection rates, the capillary pressure is defined as the difference between the CO_2 and water bulk phase pressures.

Here a typical CO_2-water displacement experiment is discussed which was conducted with a constant liquid CO_2 injection rate (0.2 ml/min) at P = 75 bar and T = 20 ℃ (Figures 8.2 and 8.3).

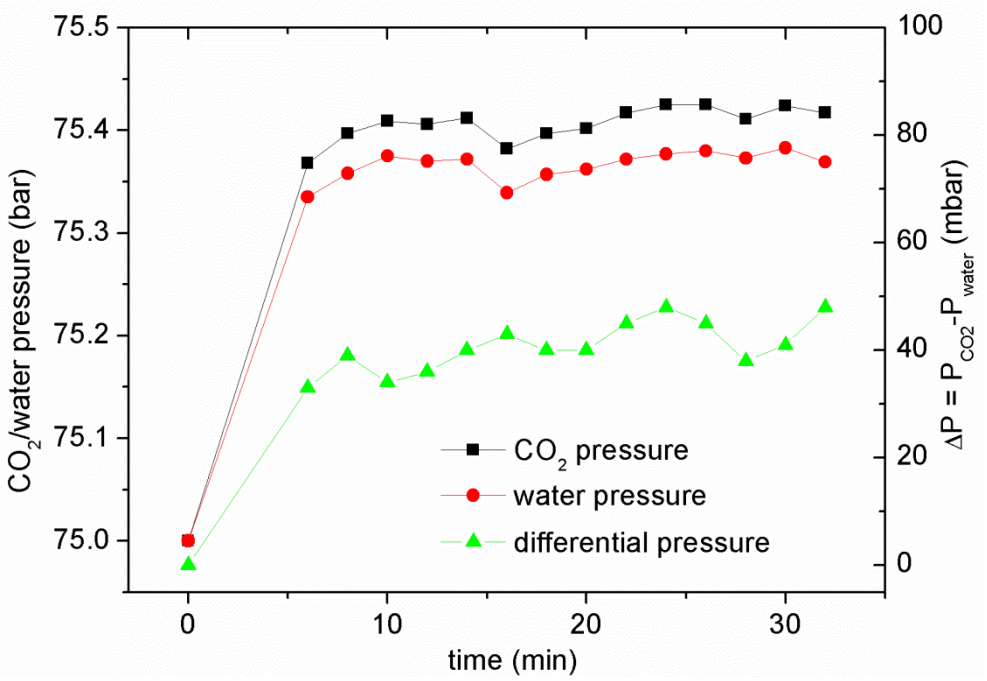

(a)

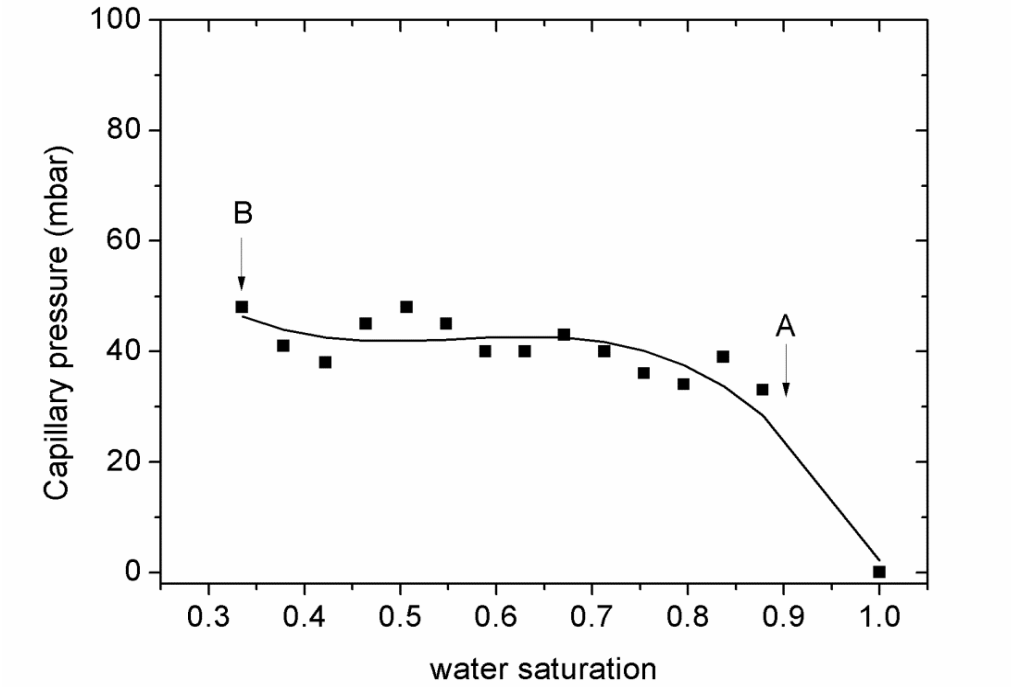

(b)

Figure 8.2 (a) Pressures at the inlet (CO_2) and outlet (water) of the core holder and the differential pressure (capillary pressure) between the two ends of the core as a function of time; (b) Capillary pressure curve as a function of water saturation, at 75 bar and 20 ℃

The pressures of the CO_2 and water bulk phases (P_{CO2}, P_{water}) measured at the inlet and outlet of the core holder are shown in Figure 8.2 (a). The data indicates that both inlet and outlet pressures increased significantly with time at the beginning of the experiment (0~6 min). The CO_2 inlet pressure was always higher than the water outlet pressure. During this period, the pressure difference between inlet and outlet increased significantly with time, from 0 to around 40 mbar. After around 10 min, the CO_2 inlet and water outlet pressures remained at around 75.40 bar and 75.35 bar respectively. The differential pressure also tended to be stable.

The capillary pressure (pressure difference between CO_2 and water) is plotted as a function of water saturation in the sandstone core sample, as shown in Figure 8.2 (b). This indicates that the capillary pressure increases with decreasing water saturation. The pressure at point A is defined as the capillary entry pressure, also called threshold capillary pressure [10], which is around 35 mbar at around the water saturation of 0.9. It is difficult to drain water out of water-saturated porous media until the differential pressure reaches the capillary entry pressure [10]. When the pressure exceeds the capillary entry pressure, a plateau can be obtained. The capillary pressure slightly increases with decreasing water saturation within this plateau region. When the drainage process is completed, the water saturation approaches an irreducible value of residual water saturation (S_{cw}) of around 0.3 (Point B).

- **Water Production Behaviour**

Figure 8.3 shows the cumulative volumes of CO_2 injection and water production as a function of time. The CO_2 was injected at a constant rate of 0.2 ml/min. The cumulative volume of CO_2 injection increases linearly with time. It can be seen that

the cumulative volume of produced water also has a linear relationship with time. However, minor difference can be observed between them. The cumulative volume of water production is slighly smaller than that of CO_2 injection during the displacement. In order to investigate the effects of pressure and the CO_2 phase on the CO_2 core flooding, the dynamic CO_2-water drainage processes are separately discussed in the following sections for gas CO_2-water, liquid CO_2-water and supercritical CO_2-water systems.

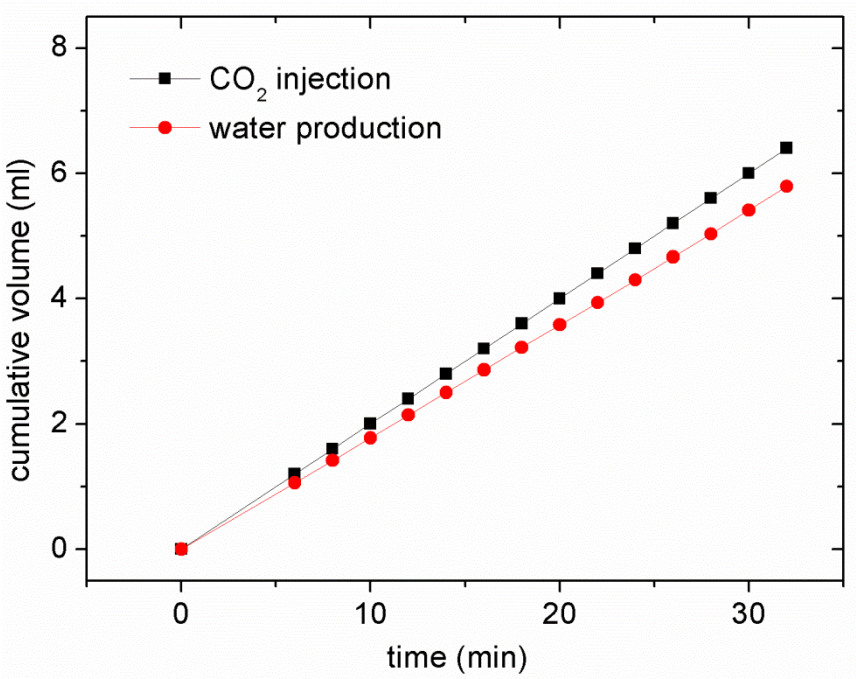

Figure 8.3 Cumulative volumes of liquid CO_2 injection and water production at 75 bar and 20 ℃

8.2.1 Experimental Results on Gas CO_2-water and Liquid CO_2-water Displacements

8.2.1.1 Capillary Pressure-Saturation Curve

The capillary pressure-water saturation (P_c-S_w) curves for gas CO_2 displacing water at 10 bar and 30 bar, and liquid CO_2 displacing water at 75 bar are shown in Figure 8.4. These three capillary pressure-water saturation curves have similar trends. The capillary pressure significantly increases with decreasing water saturation from 1.0 to 0.9. The significant dependence of capillary pressure on water saturation cannot be observed between water saturation values of 0.90 to 0.45. In this range, the capillary pressures remain around 40 mbar, 52 mbar and 60 mbar at 10 bar, 30 bar and 75 bar respectively. The capillary pressure suddenly rises beyond the water saturation of 0.45. The gas CO_2-water displacements are completed at similar connate water saturations at 10 bar and 30 bar, which are approximately around 0.40. The liquid CO_2-water displacement give a lower connate water saturation, which is around 0.30.

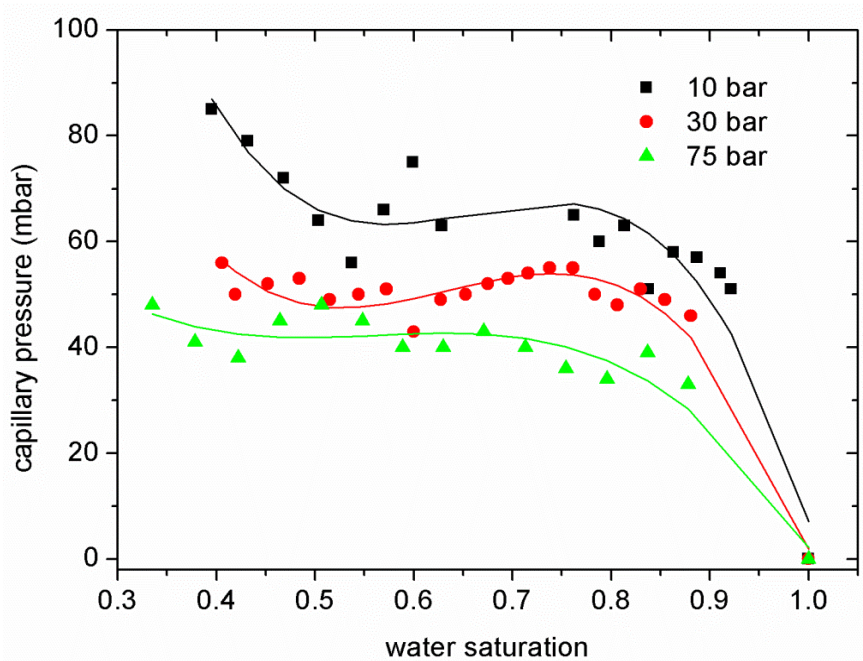

Figure 8.4 Capillary pressure-water saturation curves for gas CO_2-water displacements at 10 bar and 30 bar and liquid CO_2-water displacement at 75 bar

It is obvious that the magnitude of capillary pressure is significantly affected by the pressure applied. This pressure dependence of capillary pressure could be a result of CO_2-water interfacial tension [11]. The CO_2-water interfacial tenions at 10 bar, 30 bar and 75 bar are 65 mN/m, 50 mN/m and 35 mN/m respectively [8]. The capillary pressure curves are normalized according to the interfacial tension, as shown in Figure 8.5. P_c/γ is plotted as a function of water saturation (S_w). Small deviations can be observed here in the normalized pressure curves at these three applied pressures. Thus, it can be concluded that the effect of pressure on CO_2-water drainage capillary pressure is significant, because the capillary pressure is proportional to the interfacial tension based on the Young-Laplace equation.

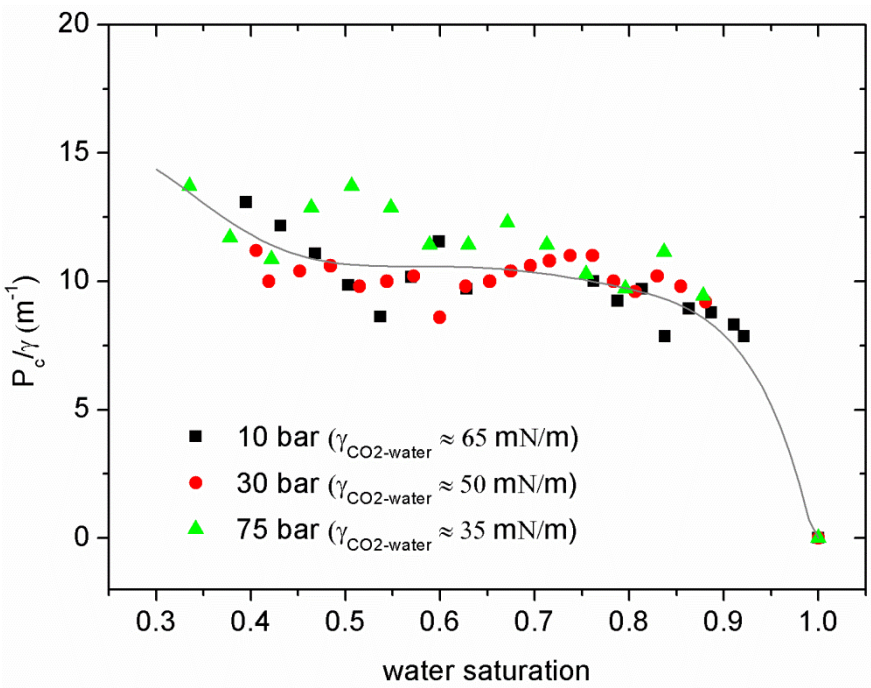

Figure 8.5 Drainage capillary pressures normalized by the interfacial tension (P_c/γ) for different CO_2 pressures

8.2.1.2 Water Production

Figure 8.6 describes the CO_2 injection and water production behaviour of gas CO_2-water displacements at 10 bar and 30 bar, and liquid CO_2-water displacement at 75 bar. The CO_2 was injected into the water-saturated sandstone core sample at a constant injection rate of 0.2 ml/min. For gas CO_2 displacing water, the cumulative volume of produced water is significantly smaller than that of injected CO_2. The difference becomes increasingly significant over time. At the end of the experiment, the cumulative volume of injected CO_2 is more than that of water produced by appoximately 50%. This remarkable disagreement between CO_2 injection and water production for gas CO_2 displacing water can be explained by the significant dissolution of gas CO_2 into water and the high compressibility of gas CO_2. On the other hand, for liquid CO_2-water displacement, the deviation between the cumulative volumes of liquid CO_2 injection and water production is insignificant. The results also indicate that less time is consumed by liquid CO_2 displacing water rather than gas CO_2 displacing water. For the CO_2 injection rate of 0.2 ml/min, the gas CO_2-water displacement and liquid CO_2-water displacement can be completed after 50 min and 30 min respectively, as shown in Figure 8.6. Plug and Bruining studied water production behaviour in CO_2-water displacements in a CO_2-water-sand packing system (Figure 8.7) [6]. They also observed a pronounced gas CO_2 dissolution effect when gas CO_2 drainaged water [6]. Comparing Figures 8.6 and 8.7, good agreement can be found between the present experimental data and Plug and Bruining's results for water production behaviour trends in CO_2-water displacement.

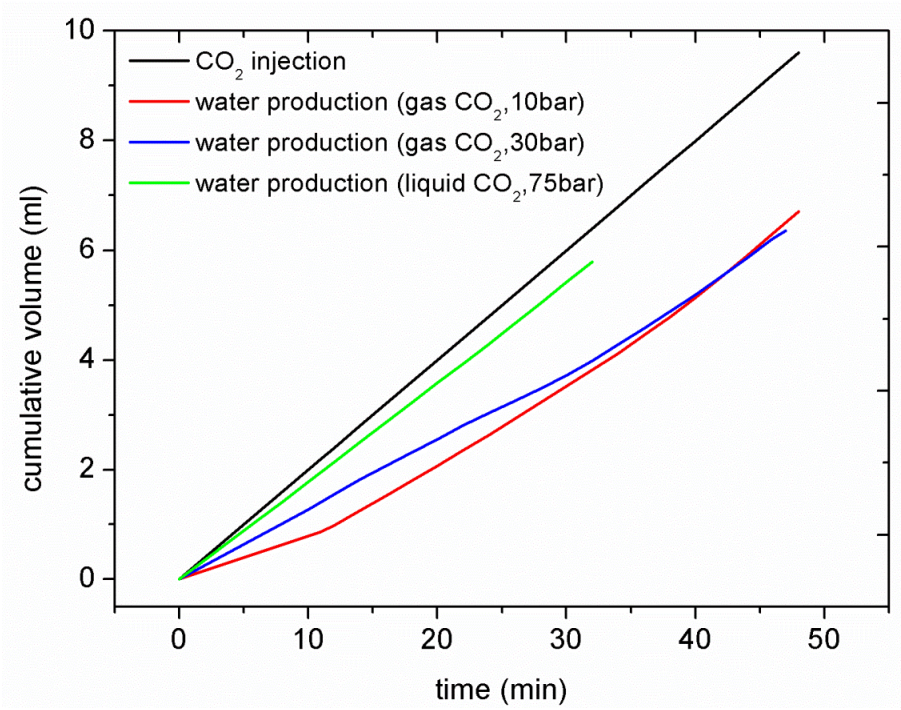

Figure 8.6 Cumulative volumes of CO_2 injection and water production at 10 bar, 30 bar and 75 bar at a CO_2 injection rate of 0.2 ml/min

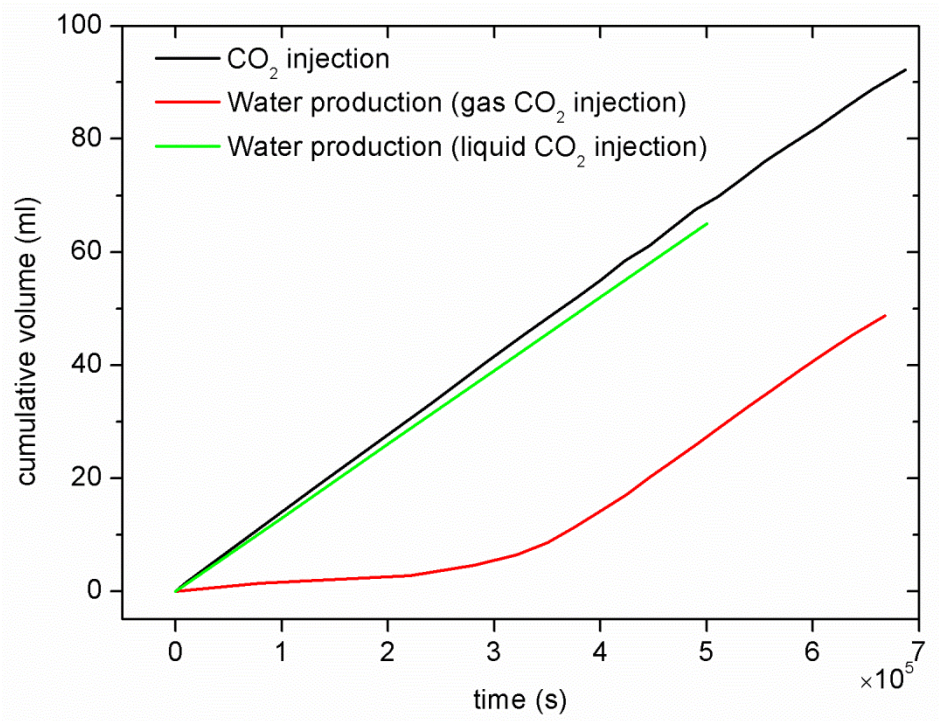

Figure 8.7 Plug and Bruining's experimental data for cumulative volumes of water production for gas CO_2 injection (atmospheric conditions) and liquid CO_2 injection (85 bar), with both gas CO_2 and liquid CO_2 at an injection rate of 0.5ml/h [6]

8.2.2 Experimental Results on Supercritical CO_2-water Displacement

8.2.2.1 Capillary Pressure-Saturation Curve

Supercritical CO_2-water displacement was studied at 75 bar and 40 ℃. Figure 8.8 shows the capillary pressure-water saturation (P_c-S_w) curve for supercritical CO_2 displacing water, which is compared with those from gas CO_2-water and liquid CO_2-water displacement. The results shows significant irregular capillary pressure-water saturation behaviour for supercritical CO_2 displacing water. Marked pressure fluctuations can be observed for the supercritical CO_2-water displacement, whereas steady capillary pressure-water saturation curves for gas and liquid CO_2 conditions are found.

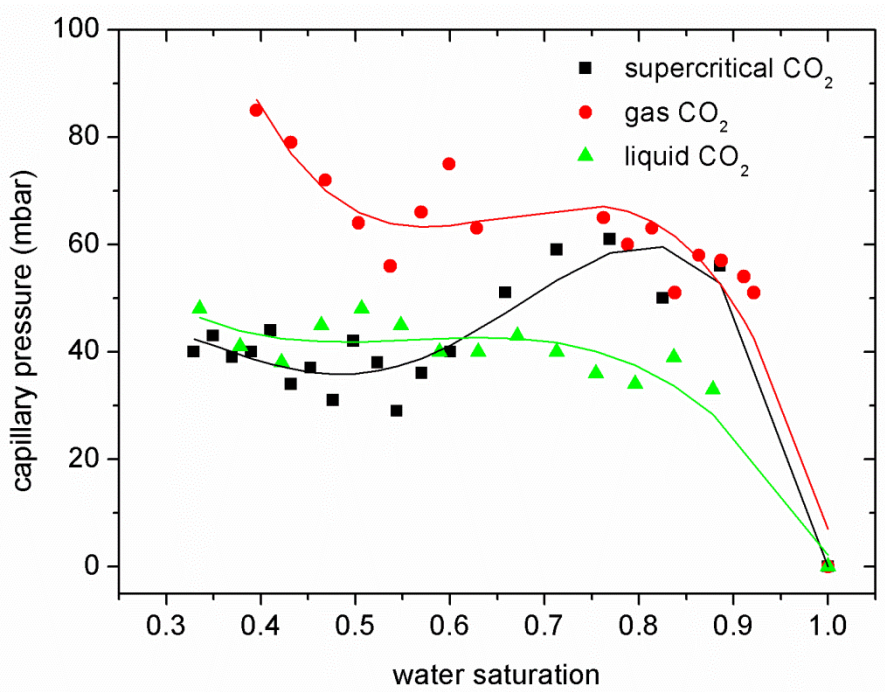

Figure 8.8 Capillary pressure-water saturation curves for supercritical CO_2-water displacement (75 bar, 40 ℃), gas CO_2-water displacement (10 bar, 20 ℃) and liquid CO_2-water displacement (75 bar, 20 ℃)

The supercritical CO_2-water capillary pressure dramatically increases from 0 to 55 mbar as the water saturation decreases from 1.0 to 0.9 at the beginning of the drainage, and reaches a peak pressure value of 55 mbar at water saturation of around 0.8. For this water saturation range (1.0 to 0.8), the capillary pressure trend of supercritical CO_2-water displacement is similar to that from gas CO_2-water displacement. When the water saturation decreases from 0.8 to 0.6, the supercritical CO_2-water capillary pressure significantly drops from 55 to around 45 mbar. As the water saturation decreases further from 0.6 to the connate water saturation of 0.3, the capillary pressure tends to remain stable at around 40 mbar. In this range, the capillary pressure-saturation behaviour is slightly lower than and close to that from liquid CO_2-water displacement. This could be explained by the effect of CO_2-water interfacial tension. The supercritical CO_2-water interfacial tension is much smaller than that for gas CO_2-water but close to that of liquid CO_2-water interfacial tension, which is around 30 mN/m. The supercritical CO_2-water interfacial tension reported recectly in the literature ranges from 27.2 to 35.4 mN/m [12-16]. However, the effect of CO_2-water interfacial tension cannot contribute to the significant capillary pressure fluctuation in the water saturation range from 1.0 to 0.6.

This implies that other mechanisms might influence the capillary pressure at or near the CO_2 critical condition. Plug and Bruining also observed significant capillary presure fluctuations with the CO_2 supercritical condition by studying the sand-CO_2-water system in unconsolidated sand packing with high permeability [6]. They stressed that the complex displacement behaviour observed for the supercritical CO_2-water system could be explained by phase instabilities in the vicinity of the critical point [6]. Other studies have also reported that the complexity of the phase behaviour of CO_2 could also significantly affect the density and viscosity of CO_2, and thus greatly change CO_2-fluid displacement behaviour in pores [17-19]. These

relevant explanations proposed in previous work might contribute to the irregular supercritical CO_2-water displacement behaviour, but the real underlying mechanisms need to be further explored and clarified.

In order to investigate the effect of CO_2 injection rate on CO_2-water capillary pressure, CO_2 injection rates of 0.1~0.6 ml/min were employed in this study. Figure 8.9 shows the capillary pressure-water saturation curves for the supercritical CO_2-water displacements with different CO_2 injection rates. Higher capillary pressures can be measured when higher injection rates are applied. The capillary pressures range from 0 to 45 mbar, 0 to 55 mbar, 0 to 61 mbar and 0 to 70 mbar at the CO_2 injection rates of 0.1, 0.2, 0.4 and 0.6 ml/min respectively. It is worth noting that the results shown in Figure 8.9 can further support the findings shown in Figure 8.8. The significant capillary pressure fluctuations and instabilities can also be observed for supercritical CO_2 displacing water at other CO_2 injection rates.

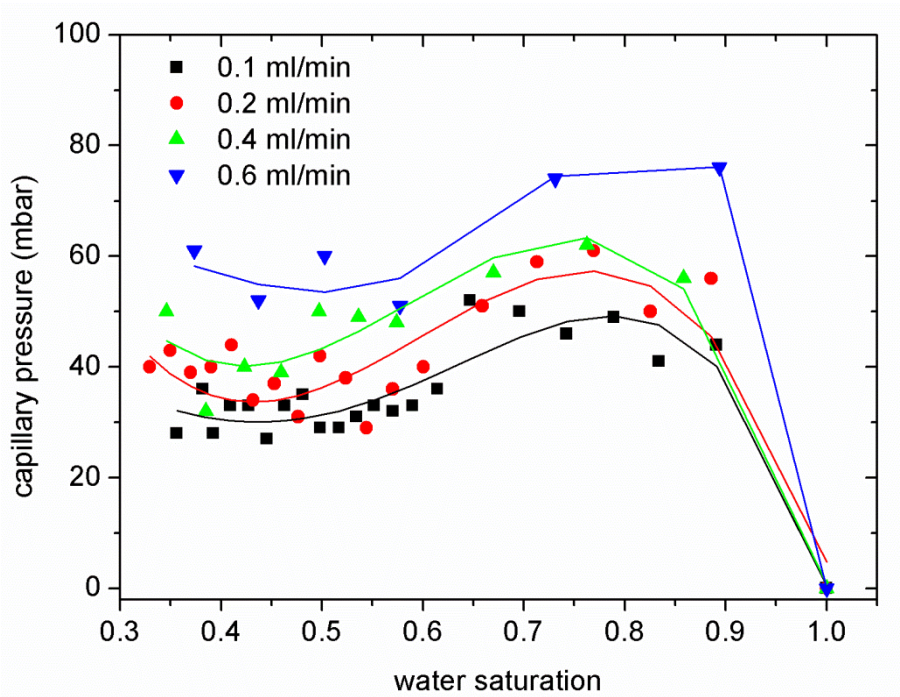

Figure 8.9 Capillary pressure-water saturation curves for a supercritical CO_2-water system at CO_2 injection rates of 0.1, 0.2, 0.4 and 0.6 ml/min

8.2.2.2 Water Production

The water production behaviour from gas CO_2-water and liquid CO_2-water displacement has been shown in Figure 8.6 and discussed in section 8.2.1.2. The liquid CO_2-water displacement shows a linear relationship between the cumulative volume of water production and time. The cumulative volume of water production is almost equal to that from CO_2 injection. Due to the pronounced effect of gas CO_2 dissolution, the amount of water produced is significantly less than the amount of CO_2 injected. Thus, a less linear water production curve and smaller amounts of water are produced from gas CO_2-water displacement. As discussed, the supercritical CO_2-water system exhibits significantly irregular behaviour in terms of capillary pressure. This can be also reflected in its water production behaviour. As shown in Figure 8.10 (a), the water production behaviour for the supercritical CO_2-water system is very different from that for gas CO_2-water and liquid CO_2-water systems. At the beginning of the displacement process, water production dramatically increases. Water production is greater than the CO_2 injection, which leads to a very high water production rate of around 0.48 ml/min. After around 8 minutes, this increase becomes less significant. The water production rate tends to equal the CO_2 injection rate of 0.2 ml/min. From Figure 8.10 (b), it can be seen that the water production rate transition point (8 min) corresponds to the end of the significant fluctuation in capillary pressure. Figure 8.10 (a) also indicates that the time consumed for the completion of CO_2-water displacement for supercritical CO_2 displacing water is the shortest. It can be concluded that the time (t) required for the completion of CO_2-water displacement is in the order of $t_{supercritical\ CO2} < t_{liquidCO2} < t_{gasCO2}$.

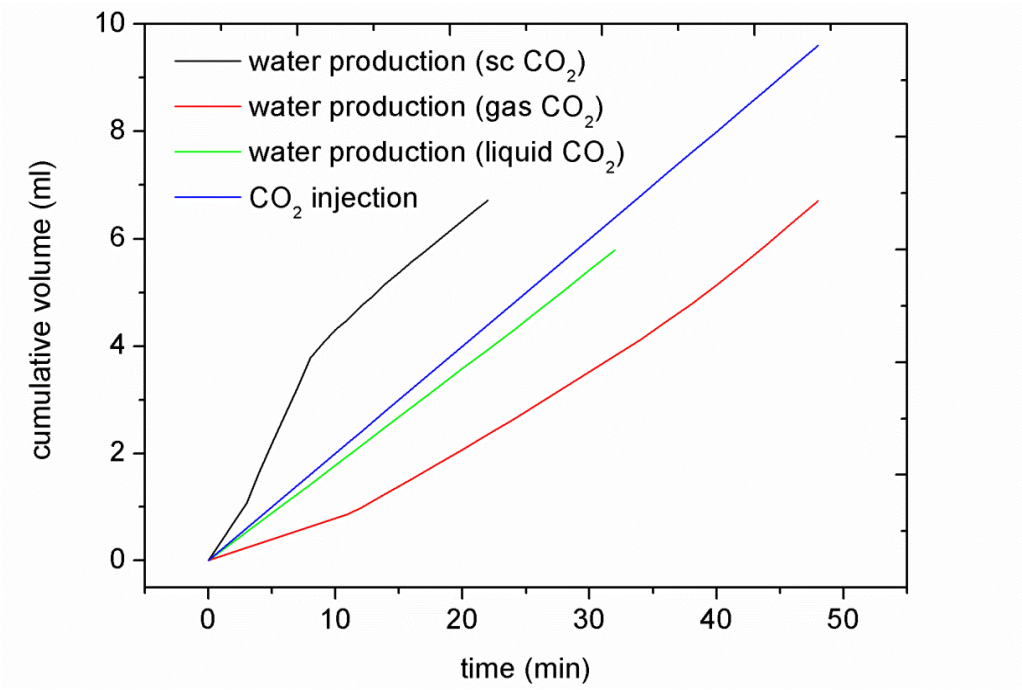

(a)

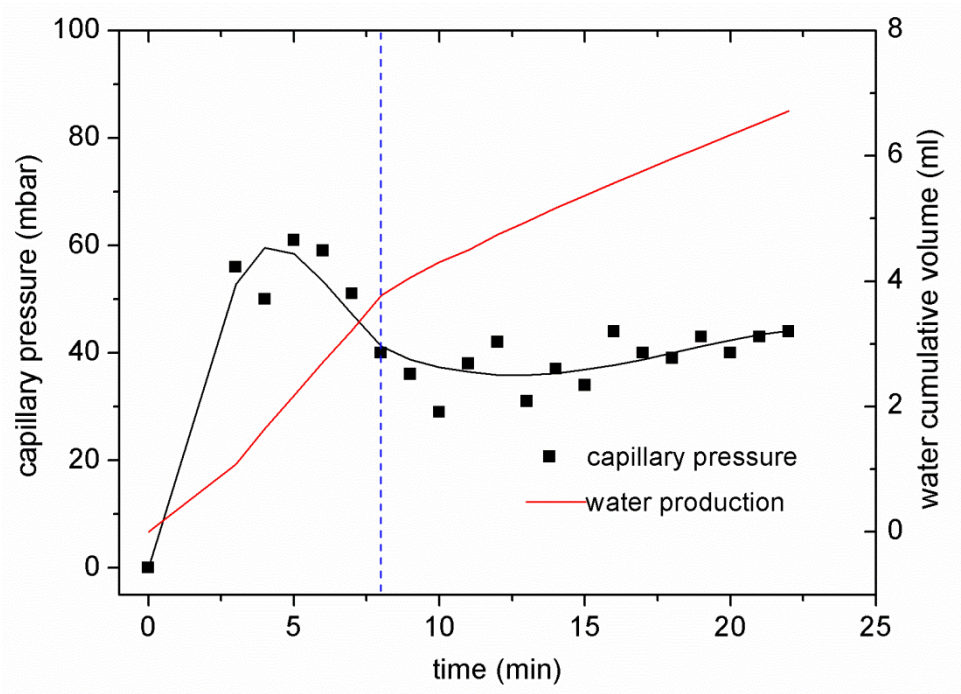

(b)

Figure 8.10 Water production behaviour during supercritical CO_2-water displacement. (a) comparison of water production behaviour of gas CO_2-water, liquid CO_2-water and supercritical CO_2-water systems; (b) water production behaviour and capillary pressure as a function of time for supercritical CO_2-water displacement

From this study, it is believed that the dramatic variation in CO_2 density near the critical point could be one of the possible reasons leading to the significant volume imbalance between water production and CO_2 injection in supercritical CO_2-water displacement. Figure 8.11 shows the significant and sudden CO_2 density swing in the vicinity of the critical point of 31 ℃ at 75 bar. For instance, the densities of CO_2 are 661.10 kg/m^3 at 30 ℃ and 365.93 kg/m^3 and 32 ℃. This small temperature increase of 2 ℃ could cause a significant volume expansion of CO_2 by roughly 200%. Thus, in this study, the higher water production than CO_2 injection in supercritical CO_2-water displacement is a result of the remarkable variation in CO_2 density near the critical point.

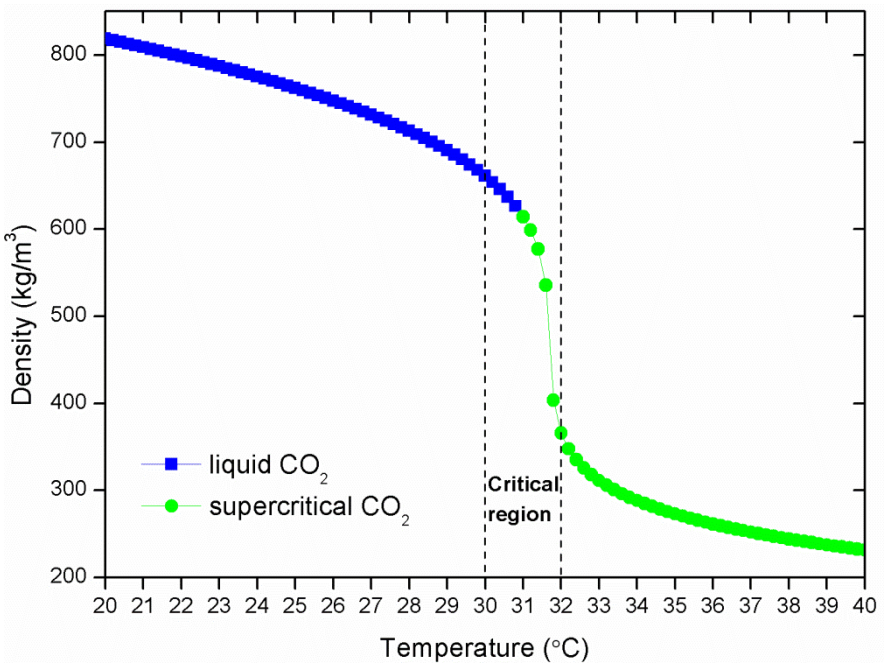

Figure 8.11 Densities of liquid CO_2 and supercritical CO_2 from 20 to 40 ℃ at 75 bar [9]

In order to further confirm this irregular water production behaviour for supercritical CO_2-water displacement, the water production was also studied at other supercritical CO_2 injection rates. Figure 8.12 indicates the behaviour of water production and CO_2

injection for a supercritical CO_2-water system at various supercritical CO_2 injection rates of 0.1, 0.2, 0.4 and 0.6 ml/min. It can be seen that the irregular water production behaviour by supercritical CO_2 injection at an injection rate of 0.2 ml/min can also be observed at other injection rates.

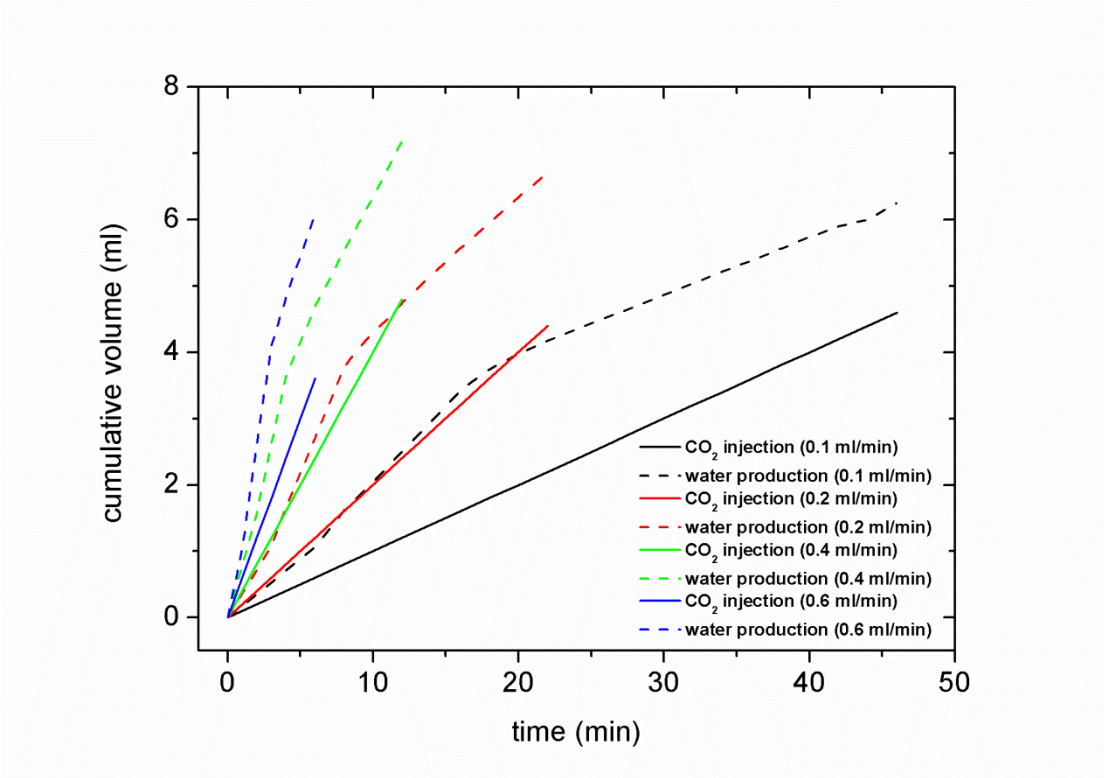

Figure 8.12 Cumulative water production and CO_2 injection for the supercritical CO_2-water system at various supercritical CO_2 injection rates of 0.1, 0.2, 0.4 and 0.6 ml/min

In order to more explicitly show the irregular water production behaviour of the supercritical CO_2-water displacement, the water production rate is normalized by the CO_2 injection rate as a function of water saturation, so that the effect of CO_2 injection rate can be eliminated. The normalized water production rate is defined as the ratio of water production rate to CO_2 injection rate. If the CO_2 can completely effectively displace the water, the normalized water production rate should always remain constant at 1.0 with decreasing water saturation.

In Figure 8.13, the normalized water production rate for supercritical CO_2 injection is

compared with those from gas CO_2 injection and liquid CO_2 injection. The normalized water production rate of liquid CO_2-water system remains at a constant value of approximately 0.95, which is close to 1.0. Due to the significant gas CO_2 dissolution effect, the normalized water production rate of gas CO_2 injection is smaller than those from liquid CO_2 injection by approximately 0.3, and does not vary significantly with water saturation although some minor deviations can be observed. On the other hand, the normalized water production rate of supercritical CO_2 injection gives a very different trend, which is larger than 1.0. It gives a non-linear correlation with water saturation. The significant non-linear behaviour ranges from values of water saturation from 1.0 to 0.6.

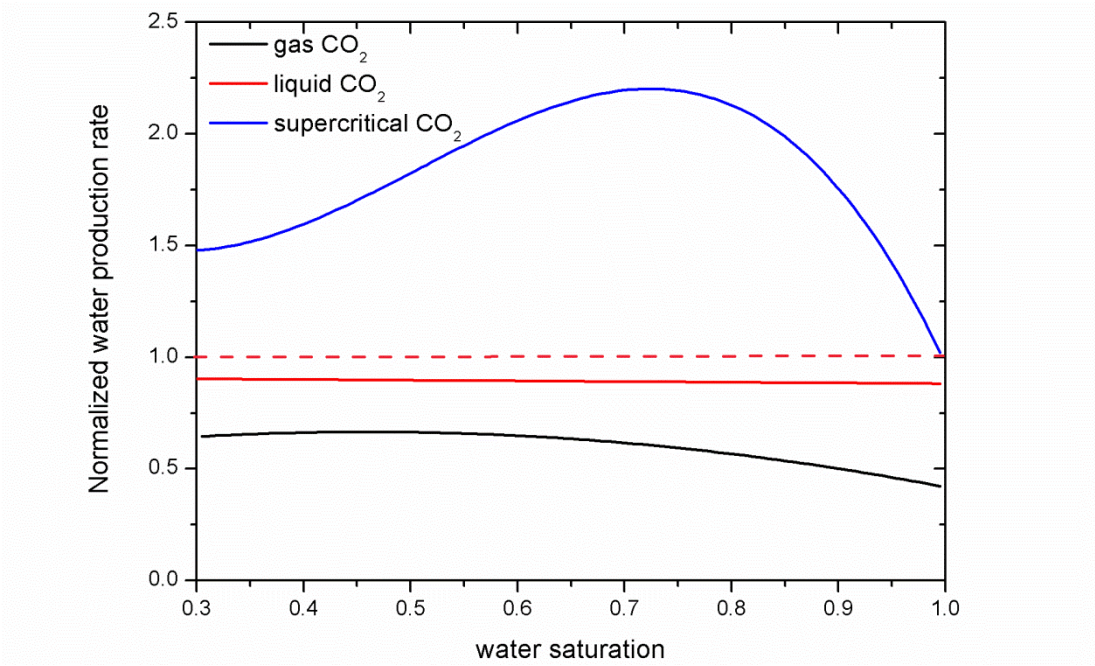

Figure 8.13 Normalized water production rates of gas CO_2-water, liquid CO_2-water and supercritical CO_2-water systems against water saturation

8.3 CO_2-water Relative Permeability Curves

The effective permeability of flow through porous media varies insignificantly in a single-phase system because there is no change in fluid saturation. However, in a multiphase flow system, the effective permeability of each phase will vary with its corresponding saturation in the porous medium. Relative permeability is a measure of the conductance of a porous medium for one fluid when the medium is saturated with more than one fluid. It can be used to define the effective permeability of each phase as a dimensionless function of wetting fluid saturation ranging from 0 to 1. Relative permeability data can be applied to characterize the multiphase flow transport behaviour in reservoir rock and to model a particular process; for example, fractional flow and fluid distribution for complex multiphase flows in porous systems for enhanced oil recovery and carbon storage purposes.

The equations of van Genuchten (VG) [20], commonly applied to two-phase systems in the petroleum industry, are used to describe the capillary pressure, wetting-phase and non-wetting-phase relative permeabilities, by fitting a set of parameters (P_0, m). The equations are:

$$P_c = P_0({S_w^*}^{-m} - 1)^{1-1/m} \tag{8.3}$$

$$k_{r,w} = (S_w^*)^2 \left\{1 - [1 - (S_w^*)^m]^{\frac{1}{m}}\right\} \tag{8.4}$$

$$k_{r,nw} = (1 - S_w^*)^2 [1 - (S_w^*)^m]^{\frac{1}{m}} \tag{8.5}$$

where P_c is capillary pressure, $k_{r,w}$ and $k_{r,nw}$ are the relative permeabilities of the wetting phase and non-wetting phase respectively, the effective water saturation

$S_w^* = \frac{S_w - S_{w,ir}}{1 - S_{w,ir}}$, S_w is water saturation, $S_{w,ir}$ is the irreducible saturation (connate water saturation), P_0 is capillary entry pressure and m is a fitting parameter.

Equation 8.3 is used in this study to describe the capillary pressure-water saturation data (P_c-S_w), by fitting the parameters (P_0,m) in the VG model. Once the fitting parameter (m) is obtained from Equation 8.3, Equations 8.4 and 8.5 can be used to predict the CO_2-water relative permeability curves for gas CO_2-water, liquid CO_2-water and supercritical CO_2-water displacements. The curve fitting results for the experimental data using Equations 8.3 are presented in Figure 8.14 and the fitted parameters are summarized in Table 8.1.

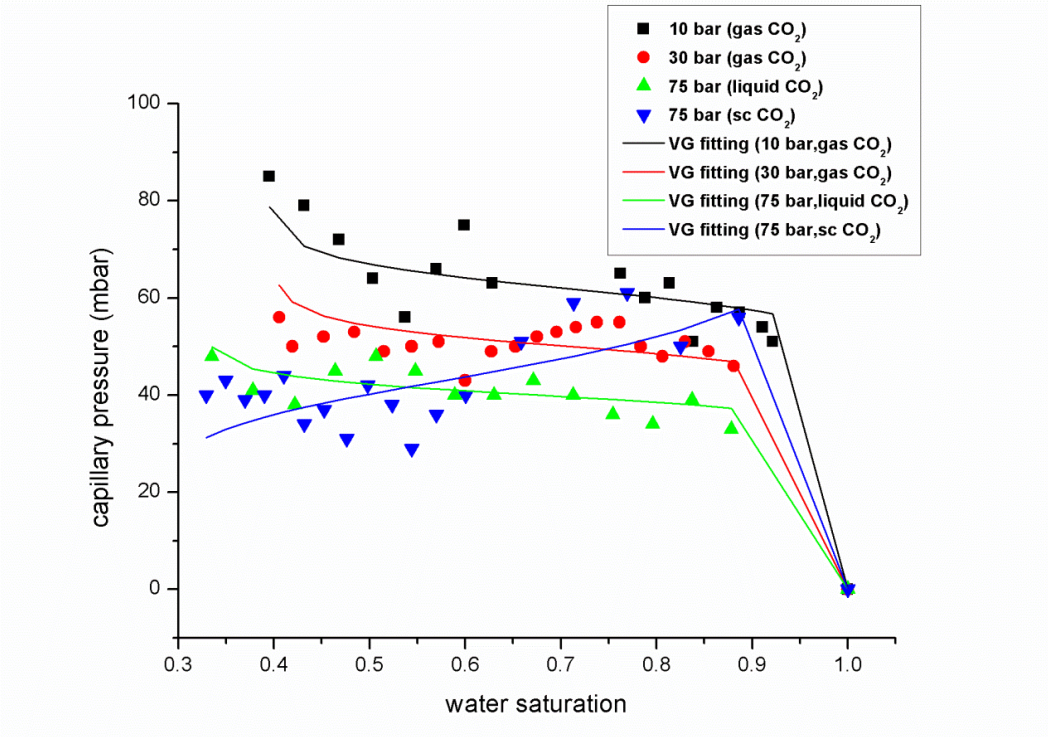

(a)

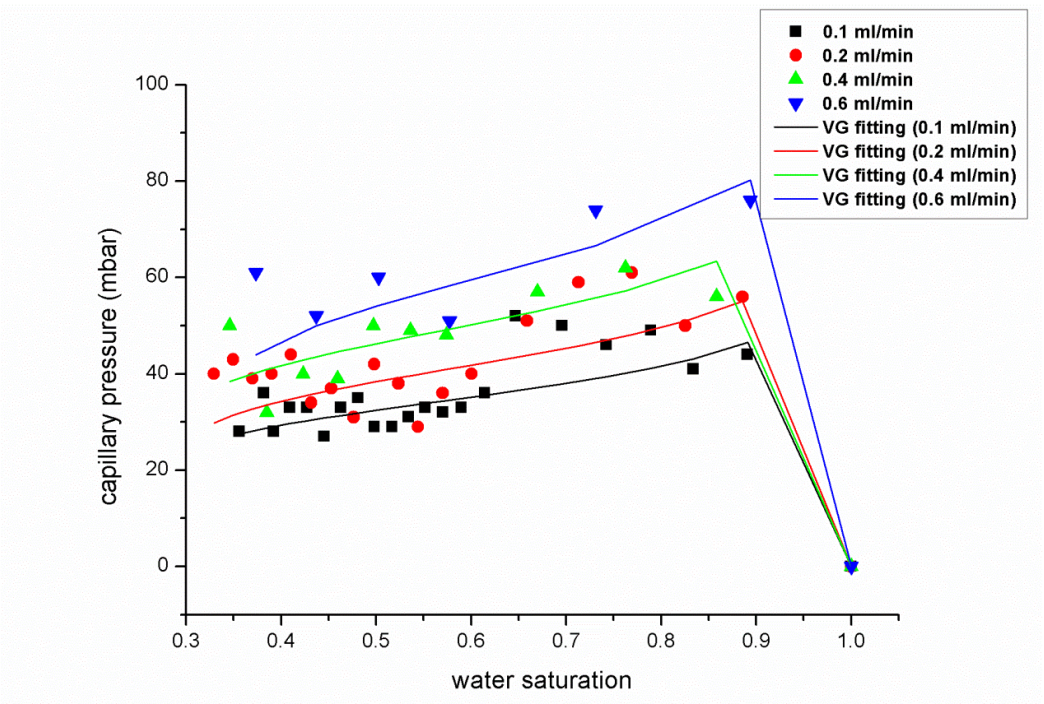

(b)

Figure 8.14 Experimental capillary pressure data and curve fitting using the van Genuchten (VG) equation for: (a) gas CO_2-water, liquid CO_2-water and supercritical CO_2-water systems at injection rate of 0.2 ml/min; and (b) supercritical CO_2-water system at various CO_2 injection rates of 0.1, 0.2, 0.4 and 0.6 ml/min

Table 8.1 Relative permeability function parameters

Systems	P_0	*m*
GasCO_2-water (10 bar, 0.2ml/min)	62	1.05
GasCO_2-water (30 bar, 0.2ml/min)	50	1.05
LiquidCO_2-water (75 bar, 0.2ml/min)	40	1.05
SuperciticialCO_2-water (75 bar, 0.1ml/min)	35	0.87
SuperciticialCO_2-water (75 bar, 0.2ml/min)	42	0.87
SuperciticialCO_2-water (75 bar, 0.4ml/min)	50	0.87
SuperciticialCO_2-water (75 bar, 0.6ml/min)	61	0.87

The fitting parameters shown in Table 8.1 are used to predict the relative permeabilities ($k_{r,water}$, $k_{r,CO2}$) of the wetting phase (water) and non-wetting phase (CO_2). Figure 8.15 shows the relative permeabilities as a function of water saturation for gas CO_2-water, liquid CO_2-water and supercritical CO_2-water displacements. It can be seen that all these three systems give similar relative permeability trends. The relative permeability of water (wetting fluid) non-linearly decreases from 1.0 to 0 with decreasing water saturation from 1.0 to the connate water saturation (S_{cw}) around 0.3~0.4. On the other hand, the relative permeability of CO_2 (non-wetting fluid) increases from 0 to 1.0 with decreasing water saturation from 1.0 to the connate water saturation (S_{cw}) around 0.3~0.4.

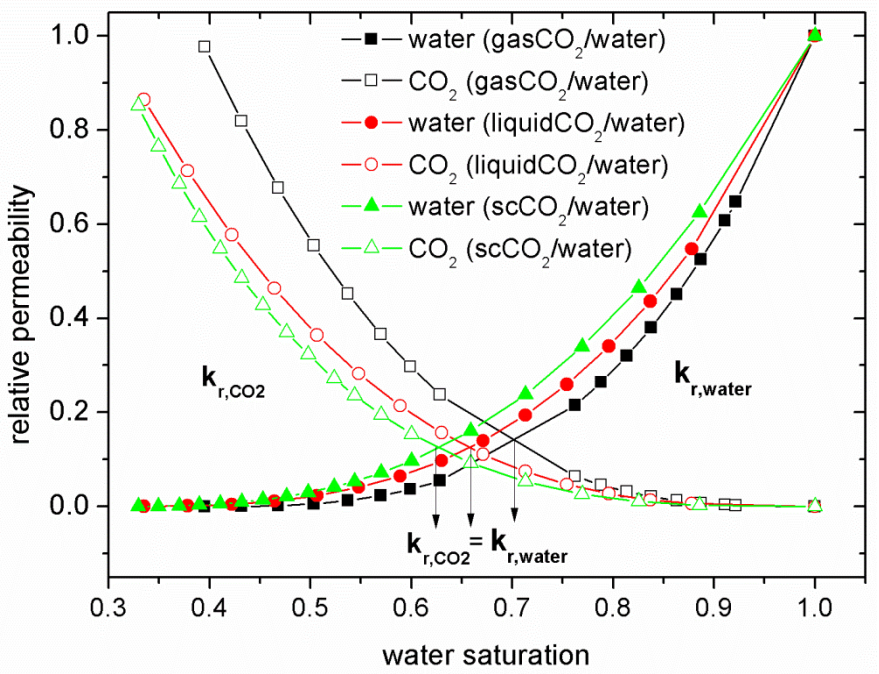

Figure 8.15 Relative permeability curves for gas CO_2-water, liquid CO_2-water and supercritical CO_2-water displacements

Some deviations can be observed in the gas CO_2-water, liquid CO_2-water and supercritical CO_2-water relative permeability curves. The supercritical CO_2-water system and the gas CO_2-water system give the highest and lowest water relative permeabilities ($k_{r,water}$) respectively, at the same water saturation. This may indicate that water can be expected to be displaced more easily by supercritical CO_2 than by liquid CO_2 and gas CO_2. It is most difficult for gas CO_2 to displace water. This also agrees with the findings concerning water production behaviour for gas CO_2-water, liquid CO_2-water and supercritical CO_2-water systems discussed in the last section. Meanwhile, the gas CO_2-water system has a higher CO_2 relative permeability ($k_{r,CO2}$) than those from liquid CO_2-water and supercritical CO_2-water systems at the same water saturation condition. In addition, the equivalent points of the relative permeabilities ($k_{r,nw}$=$k_{r,w}$) of water and CO_2 for gas CO_2-water, liquid CO_2-water and supercritical CO_2-water systems are different, at approximately 0.70, 0.66 and 0.62 respectively. Plug and Buining also studied CO_2-water drainage behaviour for gas CO_2-water, liquid CO_2-water and supercritical CO_2-water displacement in a

sand-packed bed [6]. Here, the relative permeability curves are predicted by their experimental data, as shown in Figure 8.16. Comparing Figures 8.15 and 8.16, the relative permeability of CO_2 and water trends predicted based on Plug and Buining's data are similar to the present results.

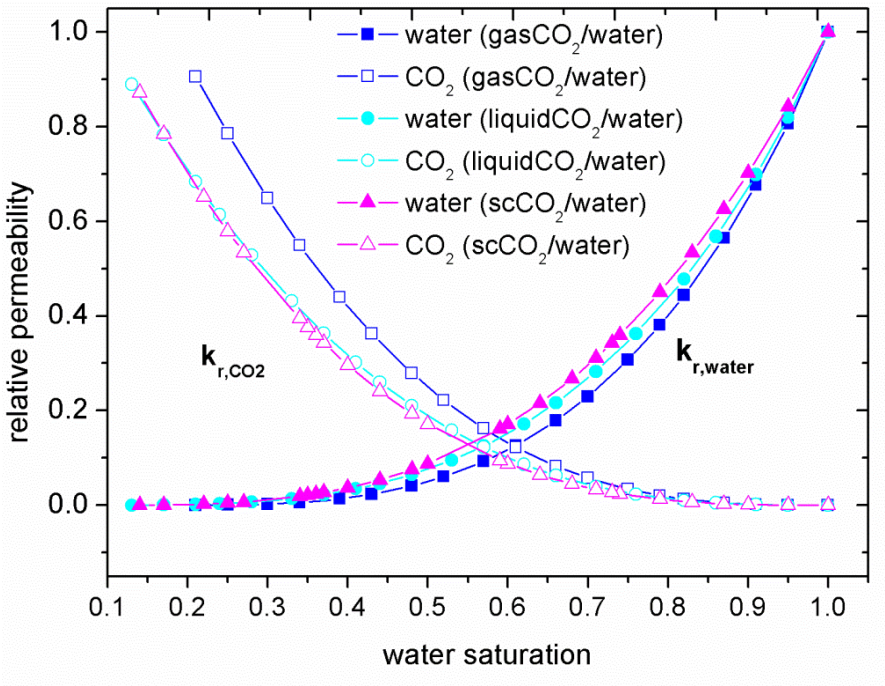

Figure 8.16 Relative permeability curves predicted based on Plug and Bruining's experimental data [6] for gas CO_2-water, liquid CO_2-water and supercritical CO_2-water displacement

8.4 Summary

Two-phase core flooding experiments for gas CO_2-water, liquid CO_2-water and supercritical CO_2-water displacements were carried out in a sandstone core sample considering the effects of CO_2 phase, pressure and CO_2 injection rate. The capillary pressure, water production behaviour and relative permeabilities have been studied. The results have good consistency with data from the literature. The results indicate the following:

- Capillary pressure-water saturation curve

Steady capillary pressure-saturation curves can be measured for gas CO_2-water and liquid CO_2-water displacement. The effect of pressure on CO_2-water capillary pressure is significant, since the capillary pressure is proportional to the interfacial tension based on the Young-Laplace equation. Significant irregular pressure-saturation behaviour is observed for the supercritical CO_2-water displacements. The complex displacement behaviour observed for supercritical CO_2 draining water could be caused by phase instabilities in the vicinity of the critical point. The complexity of the phase behaviour of CO_2 could significantly affect the density of the CO_2 [17-19], and thus its mobility in pores. The results also indicate that the drainage capillary pressure is proportional to the CO_2 injection rate. Higher drainage capillary pressure is measured when a higher CO_2 injection rate is used.

- Water production behaviour

For the gas CO_2-water system, the cumulative volume of water production is dramatically smaller than the cumulative volume of CO_2 injection. The difference becomes more and more significant as time passes. The discrepancy between the

CO_2 injection and water production for gas CO_2 displacing water can be explained by the significant dissolution of gas CO_2 in water. However, this significant deviation cannot be observed for liquid CO_2 displacing water. The liquid CO_2-water drainage gives a linear relationship between water production volume and time. The cumulative volume of water production almost equals the cumulative CO_2 injection volume. For the supercritical CO_2-water system, irregular water production curves are obtained. These further confirm the irregular pressure observations for supercritical CO_2 displacing water. The results also indicate that the time (t) consumed for the completion of CO_2-water displacement is in the order of $t_{supercritical\ CO2} < t_{liquidCO2} < t_{gasCO2}$.

- Relative permeability curve

The relative permeability curves for water and CO_2 in gas CO_2-water, liquid CO_2-water and supercritical CO_2-water systems were predicted based on the experimental capillary pressure data, using the van Genuchten (VG) model. The results indicate that the supercritical CO_2-water system gives the highest relative permeability of water and the lowest relative permeability of CO_2. Water is most easily displaced in the supercritical CO_2-water system. The gas CO_2-water system gives the lowest relative permeability of water and the highest relative permeability of CO_2. It is most difficult to drain water using gas CO_2.

The difference between the CO_2 core flooding experimental studies in this project and previous studies is that all the phases of CO_2 including gas, liquid and supercritical CO_2 are considered in this study. In addition, the water production behaviours for gas/liquid/supercritical CO_2-water displacements are also systematically investigated. This was rarely studied in previous work.

8.5 References

[1] Mito S, Xue Z, Ohsumi T. Case study of geochemical reactions at the Nagaoka CO_2 injection site, Japan. International Journal of Greenhouse Gas Control. 2008;2:309-18.

[2] Pini R, Krevor SCM, Benson SM. Capillary pressure and heterogeneity for the CO_2/water system in sandstone rocks at reservoir conditions. Advances in Water Resources. 2012;38:48-59.

[3] Bachu S, Bonijoly D, Bradshaw J, Burruss R, Holloway S, Christensen NP, et al. CO_2 storage capacity estimation: Methodology and gaps. International Journal of Greenhouse Gas Control. 2007;1:430-43.

[4] Bennion B, Bachu S. Drainage and Imbibition Relative Permeability Relationships for Supercritical CO_2/Brine and H_2S/Brine Systems in Intergranular Sandstone, Carbonate, Shale, and Anhydrite Rocks. SPE Reserv Eval Eng. 2008;11:487-96.

[5] Tokunaga TK, Wan J, Jung J-W, Kim TW, Kim Y, Dong W. Capillary pressure and saturation relations for supercritical CO_2 and brine in sand: High-pressure Pc(Sw) controller/meter measurements and capillary scaling predictions. Water Resources Research. 2013;49:4566-79.

[6] Plug WJ, Bruining J. Capillary pressure for the sand–CO_2–water system under various pressure conditions. Application to CO_2 sequestration. Advances in Water Resources. 2007;30:2339-53.

[7] Shi J-Q, Xue Z, Durucan S. Supercritical CO_2 core flooding and imbibition in Tako sandstone—Influence of sub-core scale heterogeneity. International Journal of Greenhouse Gas Control. 2011;5:75-87.

[8] Espinoza DN, Santamarina JC. Water-CO_2-mineral systems: Interfacial tension, contact angle, and diffusion—Implications to CO_2 geological storage. Water Resour Res. 2010;46:W07537.

[9] NIST. NIST Chemistry WebBook, NIST Standard Reference Database

Number 69: National Institute of Standards and Technology; 2005.

[10] Egermann P, Lombard J, Bretonnier P. A fast and accurate method to measure threshold capillary pressure of caprocks under representative conditions. International Symposium of the Society of Core Analysts. Trondheim, Norway2006.

[11] Chun B-S, Wilkinson GT. Interfacial tension in high-pressure carbon dioxide mixtures. Industrial & Engineering Chemistry Research. 1995;34:4371-7.

[12] Chalbaud C, Robin M, Lombard JM, Martin F, Egermann P, Bertin H. Interfacial tension measurements and wettability evaluation for geological CO_2 storage. Adv Water Resour. 2009;32:98-109.

[13] Kvamme B, Kuznetsova T, Hebach A, Oberhof A, Lunde E. Measurements and modelling of interfacial tension for water+carbon dioxide systems at elevated pressures. Computational Materials Science. 2007;38:506-13.

[14] Nielsen LC, Bourg IC, Sposito G. Predicting CO_2–water interfacial tension under pressure and temperature conditions of geologic CO_2 storage. Geochimica et Cosmochimica Acta. 2012;81:28-38.

[15] Saraji S, Goual L, Piri M, Plancher H. Wettability of Supercritical Carbon Dioxide/Water/Quartz Systems: Simultaneous Measurement of Contact Angle and Interfacial Tension at Reservoir Conditions. Langmuir. 2013;29:6856-66.

[16] Sutjiadi-Sia Y, Jaeger P, Eggers R. Interfacial phenomena of aqueous systems in dense carbon dioxide. The Journal of Supercritical Fluids. 2008;46:272-9.

[17] Duan Z, Sun R. An improved model calculating CO_2 solubility in pure water and aqueous NaCl solutions from 273 to 533 K and from 0 to 2000 bar. Chemical Geology. 2003;193:257-71.

[18] Fenghour A, Wakeham WA, Vesovic V. The Viscosity of Carbon Dioxide. Journal of Physical and Chemical Reference Data. 1998;27:31-44.

[19] Span R, Wagner W. A New Equation of State for Carbon Dioxide Covering the Fluid Region from the Triple‐Point Temperature to 1100 K at Pressures

up to 800 MPa. Journal of Physical and Chemical Reference Data. 1996;25:1509-96.

[20] van Genuchten MT. A Closed-form Equation for Predicting the Hydraulic Conductivity of Unsaturated Soils1. Soil Sci Soc Am J. 1980;44:892-8.

Chapter 9: Conclusions and Further Work

The ultimate goals of this study are to advance the understanding of the wetting phenomena of fluids and gas/liquid/supercritical CO_2 in micron-sized pores, and to investigate the gas/liquid/supercritical CO_2-water displacements in porous media using core flooding experiments. The results obtained are of fundamental importance for both CO_2 storage and enhanced oil recovery (EOR) processes.

Since measuring contact angles on non-flat substrates remains a challenge and few direct measurements have been carried out in a pore to determine pore wetting, a novel technique is developed in this study to directly measure the contact angles of liquids and CO_2 in a micron-sized single pore instead of conventional wetting measurements on a planar substrate. The main findings are highlighted below,

9.1 Pore Wetting of Reservoir Fluids

The contact angles of liquids were measured in single micron-sized transparent capillaries using an optical microscope. The results indicate that the pore contact angle is not $\theta=0^0$, which is commonly assumed and applied in most calculations, modeling and simulations of multiphase flow transport in porous media. Contact angles measured in a small glass capillary differ from and are larger than the contact angles measured on a flat glass surface in an open space. The effects of curved geometry or confinement, three-phase line curvature and line tension in a glass capillary might cause the difference. In addition, the different vapor saturation conditions on a flat surface and in small pores could also be one of the reasons.

The dynamic contact angles of liquids with various surface tensions and viscosities were also studied in liquid imbibition experiments in a micron-sized glass pore. The dynamic pore contact angle increases monotonically with the interfacial velocity (imbibition rate). The surface tension and viscosity of liquids do affect the dynamic contact angle in a pore. A small surface tension tends to favour the variation of dynamic contact angle with interface velocity. Liquids with higher viscosity have a more significant effect on the dynamic pore contact angle. A new empirical correlation is developed based on the experimental data which can predict the dynamic pore contact angle. In addition, the dynamic contact angle data is also described using Blake's molecular-kinetic theory.

Contact angle depends not only on surface tension but also on chemical molecular structure in some cases. In a hydrophilic glass pore, polar amphiphilic organics with functional groups have larger pore contact angles than non-polar organics, and in the order of $\theta_{-OH} > \theta_{-NH2} \approx \theta_{-COOH}$. The pore contact angle of amphiphiles increases with straight alkyl chain length. The structure of the alkyl chain of amphiphiles has an effect on glass pore wetting. The straight alkyl chain contributes most to the pore contact angle and the side chain on the carbon of backbone tends to reduce the pore contact angle. However, all these findings cannot be applied to hydrophobic surfaces. The chemical structure of amphiphiles does not contribute to the contact angle in an oil-wet pore.

9.2 Gas/Liquid/Supercritical CO_2-fluids Pore Wetting

The pore contact angles of gas/liquid/supercritical CO_2-fluid (water/brine/n-decane) systems were measured in micron-sized single oil-wet and water-wet pores. The effect of CO_2 phase on the contact angles of CO_2-fluids is considered in this study.

In an oil-wet pore, the CO_2 phase does significantly affect the CO_2-fluid pore contact angle. The effect of pressure on CO_2-fluid contact angles is not significant when there is no CO_2 phase change. The CO_2-fluid contact angles in an oil-wet pore are in the order of $\theta_{gasCO2}<\theta_{supercriticalCO2}<\theta_{liquidCO2}$.. The CO_2-brine contact angles are similar to those of CO_2-water in an oil-wet pore; $\theta_{brine} \approx \theta_{water}$. No effect of salinity on pore contact angle is observed in an oil-wet pore. On the other hand, CO_2 phase does not have a profound impact on CO_2-fluid contact angle in a water-wet pore; $\theta_{gasCO_2}\approx\theta_{supercritical\ CO_2}\approx\theta_{liquidCO_2}$ in a water-wet pore. Salinity has a significant effect on the CO_2-brine-glass pore contact angle in a water-wet pore; $\theta_{brine}>\theta_{water}$.

9.3 Gas/Liquid/Supercritical CO_2-water Displacements in Sandstone Core Sample

Gas/liquid/supercritical CO_2-water core flooding experiments were carried out in a sandstone core sample, considering the effects of CO_2 phase, pressure and CO_2 injection rate. The capillary pressure, CO_2 injection and water production behaviour and relative permeability are studied.

Significant pressure-dependent capillary pressures were measured for CO_2-water displacement, as a result of CO_2-water interfacial tension. Steady capillary pressure-saturation curves are obtained for gas CO_2-water and liquid CO_2-water systems. Significant irregular pressure-saturation curves and complex displacement behaviour are obtained for the supercritical CO_2-water displacements. This could be caused by phase instabilities in the vicinity of the critical point. The results also indicate that capillary pressure is proportional to the CO_2 injection rate. Higher drainage capillary pressure is obtained when a higher CO_2 injection rate is used.

For the gas CO_2-water system, the cumulative volume of water production is

significantly smaller than the cumulative volume of CO_2 injection. The difference becomes more and more significant over time. This is attributed to the significant level of gas CO_2 dissolution in water. On the other hand, this significant deviation cannot be observed for liquid CO_2-water displacement. Liquid CO_2-water drainage gives a linear relationship between water production volume and time. The cumulative volume of water production almost equals the cumulative volume of CO_2 injection. For the supercritical CO_2-water system, an irregular water production curve is obtained. The relative permeability curves for water and CO_2 are predicted based on the experimental capillary pressure data, using the van Genuchten equations.

9.4 Future Works

- Due to the limitations of the optical microscope used in this study, it was difficult to obtain a clear image of liquid meniscus for liquid in pores with sizes less than 100 μm. Thus, contact angle measurements for those pore sizes were not involved in this study. The measurement error of the contact angles measured in small capillaries is larger than that in large pores. Thus, the microscopic pore contact angle measurement technique will be improved in order to further minimize the effect of distortion on contact angle in a pore and thus improve the accuracy of contact angle measurement in small capillaries.

- Some conditions considered in this study are far from real-world subsurface conditions in oil reservoirs and aquifers. More systematic studies of pore contact angle and core flooding experiments need to be conducted, which should consider more factors such as high temperature and pressure, brine composition and salinity, the complexity of crude oil, porous surface roughness and pore heterogeneity.

- For the dynamic imbibition studies on dynamic pore contact angles in a single capillary, the interfaces considered in this study are liquid-air interfaces. The work can be extended to investigate liquid-liquid dynamic contact angles in a single capillary, such as in water-oil imbibition dynamics. In addition, dynamic pore wetting should also be studied at high imbibition rates at high interface velocity in a high capillary regime. Furthermore, because of the significance of the wetting line friction coefficient in Blake's molecular-kinetic theory, these coefficients for other liquids in pores in different materials need to be estimated in future work.

- Most of the contact angle measurements in this project were performed in a glass pore. Glass is a strongly water-wet, hydrophilic and high-energy material. Some findings using the glass surface here might be unique and have some limitations. In order to investigate the validation of the findings obtained in a glass pore for other surfaces, more substrates should be used, such as weakly water-wet and neutral-wet surfaces.

- Most of the contact angles measured by our pore contact angle measurement technique are equilibrium/static contact angles in a small pore. In order to describe pore wetting phenomenon more accurately and comprehensively, it is recommended that advancing and receding pore contact angles should be measured in our future work, especially for the CO_2-fluid contact angle measurements under high pressure, by further developing the pore contact angle measurement technique.

- For the CO_2 flooding experiments, a sandstone core sample was used in this study. Due to the geological complexity of CO_2 storage, other types of core samples should also be considered such as oil-wet rocks and carbonates. Furthermore, brine, oil or other reservoir fluids should also be involved in CO_2 core flooding

experiments. It would also be worth to further investigating the unstable and irregular supercritical CO_2-water displacement behaviour in the vicinity of the CO_2 critical condition.

Many industrial processes, such as fuel cell, carbon storage and enhanced oil recovery, are engineering scale processes, but they are predominantly controlled by the pore wetting and displacement of fluids in porous media. Thus, experimental studies of pore-scale wetting and displacement of CO_2 and fluids in this project could advance the understanding of long-term subsurface storage of CO_2 and oil recovery efficiency.